DEVELOPMENT OF A DIRECT MONITORING APPROACH OF CO/H_2 IN BIOREACTORS FOR SYNGAS TO BIOFUELS CONVERSION

By

JIE DANG

Bachelor of Science in Automation
Xi'an Jiaotong University
Xi'an, Shaanxi, China
2010

Master of Science in Control Science and Engineering
Xi'an Jiaotong University
Xi'an, Shaanxi
2013

Submitted to the Faculty of the
Graduate College of the
Oklahoma State University
in partial fulfillment of
the requirements for
the Degree of
DOCTOR OF PHILOSOPHY
May, 2019

DEVELOPMENT OF A DIRECT MONITORING APPROACH OF CO/H_2 IN BIOREACTORS FOR SYNGAS TO BIOFUELS CONVERSION

Dissertation Approved:

Dr. Ning Wang

Dissertation Adviser

Dr. Hasan K. Atiyeh

Dr. Yu Mao

Dr. Daqing Piao

.

ACKNOWLEDGEMENTS

I firstly give my heartfelt thanks and appreciation to my advisor, Dr. Ning Wang, for her guidance and support on my study in the Oklahoma State University. I have learned a lot of things from her instructions during the five years study and research. Dr. Wang taught me a professional method and an active attitude to overcome the difficulties in my research. She also offered me lots of opportunities to obtain new knowledge and to practice skills for my future career. I also received great encouragement and help from Dr. Wang for my life in the United States.

I greatly appreciate the guidance from my co-advisor, Dr. Hasan Atiyeh. My research could not be successful without his kindly help and tutoring. Dr. Atiyeh professional knowledge in chemistry and biological field helped me to prepare my experiment and to design my sensor. His help in my presentation and teaching skills a valuable assets for me. I am really grateful for the time and thoughts that Dr. Atiyeh had devoted to my research.

I acknowledge the financial support from the Sun Grant Program – South Center No. DOTS59-07-G-00053, USDA-NIFA Project No. OKL03005, and the Oklahoma Agricultural Experiment Station.

I also appreciate the help from my committee members, Dr. Daqing Piao and Dr. Yu Mao

for their efforts in helping me to finish my research. They provided great suggestions and instructions for my sensor development, helped me to locate and solve the challenges in my research.

In the five years, I also received lots of help from staffs, colleagues and friends. I would like to thank Mr. Mike Veldman for his training and instruction in electronical field. I greatly appreciate Mr. Wayne Kiner and the crews of BAE lab for their help to produce the special components for me. I would also like to express my appreciation to Mr. Mark Gilstrap. He trained and helped me to work in a chemistry lab, to operate equipment and devices, and to tackle safety issues.

My research also received numerical help from my colleagues. I would like to thank the help from Dr. Yeyin Shi and Dr. Yongbo Wang firstly. They gave me the valuable supports and encouragements during my first semester in OSU. They helped me to start my research from scratch and to accustom the life in the OSU when I was really shocked by the dramatically changes in the study and life. I also would like to express my appreciation to Xiao Sun and Oscar Pardo Planas. They helped me to resolve the problems in the chemistry field and to finish some chemical tests.

Finally, I would like to dedicate this dissertation to my mother and father. They are the most important people in my life. I cannot finish it without their support, encouragement, and understanding.

Name: JIE DANG

Date of Degree: May, 2019

Title of Study: DEVELOPMENT OF A DIRECT MONITORING APPROACH OF CO/H_2 IN BIOREACTORS FOR SYNGAS TO BIOFUELS CONVERSION

Major Field: BIOSYSTEMS AND AGRICULTURAL ENGINEERING

Abstract: Syngas fermentation is a novel technology to produce biofuels from syngas using acetogens. Precise monitoring of dissolved CO/H_2 concentrations helps to maintain the proper activities of the acetogens and is of great importance for a high product yield and operation stability. A new approach was developed to measure the dissolved CO/H_2 concentration with optical sensing and electrochemical methods, respectively.

An indirect mid-infrared measurement system was developed to measure dissolved CO concentration. The measurement system included a gas extraction system for dissolved CO degasification and a non-dispersive mid-infrared CO sensor for gas phase CO concentration measurement. The gas extraction system used a hollow fiber membrane contactor to extract dissolved CO in a fixed volume of liquid sample. A vacuum was applied to the contactor to accelerate the degasification. The non-dispersive mid-infrared CO sensor used a room-temperature, mid-infrared light emitting diode as a mid-infrared source. The sensor was designed to detect CO absorption in the mid-infrared range between 4.7 μm and 4.9 μm as this range has minimal spectral interference from other chemicals in the syngas fermentation. The infrared signal was detected with a thermoelectric cooled photodetector. A digital lock-in amplifier was designed to improve the quality of the collected signals from the preamplifier.

A commercial electrochemical dissolved H_2 sensor was introduced to measure the dissolved H_2 concentration. An integrated dissolved CO/H_2 measurement system was built by integrating the dissolved H_2 sensor to the developed dissolved CO measurement system. Performance evaluation of the integrated measurement system showed a maximum mean absolute percentage error of 10.83% and a root-mean-square error of 1.40 mg/L for the dissolved CO concentration measurement. The measurement on the dissolved H_2 concentration measurement was affected by the supersaturated dissolved H_2.

The developed integrated measurement system provides a new method that can measure the dissolved CO/H_2 concentrations in the syngas fermentation medium. The method would be helpful to future optimization and commercialization of the syngas fermentation technology.

TABLE OF CONTENTS

Chapter Page

Chapter Page

Chapter Page

LIST OF TABLES

LIST OF FIGURES

Figure Page

Figure Page

Figure Page

CHAPTER I

INTRODUCTION

1.1 Backgrounds

Syngas fermentation is an emerging technology which can provide renewable and sustainable fuel supply from non-sugar biomass feedstock (Maddipati et al., 2011). Biomass is converted to synthesis gas (syngas), which contains CO, CO_2, and H_2 as well as other minor gases, through gasification process. The CO and H_2 components in the syngas can be converted into ethanol, butanol, and other bioproducts by certain microorganisms (Wilkins and Atiyeh, 2011). Syngas fermentation is a hybrid technology that has many advantages compared to conventional biochemical and thermochemical technologies in biofuel production (Munasinghe and Khanal, 2010).

Many factors, including low productivity and low mass transfer rates of CO and H_2, impeded the implementation of large scale commercialized syngas fermentation (Phillips et al., 2017). Real-time monitoring and control of dissolved CO and H_2 concentrations could improve the carbon conversion rate and the operation stability (Atiyeh et al., 2017). Precise control of dissolved CO and H_2 concentrations was also important to maintain normal activities of microorganisms and enzymes (Phillips et al., 2017).

In our current research, the dissolved CO and H_2 concentrations were measured using offline gas chromatography and fermenter gas mass transfer models (Atiyeh et al., 2017), which could not provide the timely and automatic measurements. There is an urgent need for an online, real-time dissolved CO and H_2 measurement system for the further optimization of the syngas fermentation technology.

Scant research reported the measurement of dissolved CO concentration in the aqueous solution. The most related research was to measure the dissolved CO concentration in blood, which included two different measurement methods. The first method was to directly measure the dissolved CO concentration using the optical absorption spectra of CO bounded hemoglobin (COHb) (Kundu et al., 2003; Riggs and Heindel, 2006; Widdop, 2002). The second method was to release the CO from COHb and to measure the extracted CO with gas chromatography (GC) or combined gas chromatography-mass spectroscopy (GC-MS) (Collison et al., 1968; V. Varlet et al., 2012; Widdop, 2002).

Dissolved H_2 concentration can be directly measured with membrane coated electrochemical sensors (Pauss et al., 1990; Sweet et al., 1980). Another indirect method was to design a dissolved H_2 extraction apparatus and then analyze the extracted H_2 with a gas phase H_2 detector (Björnsson et al., 2001; Cord-ruwisch et al., 1997). Dissolved H_2 sensors using the direct measurement method are commercially available.

To the best of our knowledge, there is no dedicated dissolved CO sensor on the market. In this research, different CO detection methods, such as electrochemical method, conductivity method, and optical method, were compared to find an appropriate method to measure the dissolved CO concentration in the syngas fermentation medium. The comparison showed that infrared detection method was the most suitable method in this special application, which had low interference from other major chemicals in the syngas fermentation medium. Infrared method can also operate

under anaerobic fermentation environment. The developed infrared CO sensor was designed to detect CO's infrared absorption at spectral range between 4.4 μm and 5 μm based on the examination of infrared spectra of chemicals in the fermentation medium.

The selected spectral range for CO measurement was located in the mid-infrared (MIR) spectral range, which was usually detected by MIR laser sensors. There were several reports of direct infrared measurement of dissolved gases, such CO_2 (Schaden et al., 2004) and hydrocarbons (Buerck et al., 2001; Mizaikoff, 1999) with infrared laser sensors. However, the direct measurement of dissolved CO with a laser sensor would encounter several challenges: the low CO solubility (27.5mg/L, 1ATM pressure, 25°C, 100%CO, calculated by Henry's law (Sander 2015)), the weak CO infrared absorption, and the broad, strong infrared absorption from liquid water. The introduction of laser infrared radiation sources also would make the CO sensing system complicated and expensive (Popov et al., 1997; P. Werle et al., 2002).

The development of MIR light emitting diode (LED) and hollow fiber membrane (HFM) contactor provides a new solution to the measurement of dissolved CO in aqueous solution. The MIR LED could emit infrared radiation in the spectral range between 1.7 μm and 4.8 μm (Popov et al., 1997), which might replace the expensive and complicated laser infrared radiation sources for the MIR CO detection. Its disadvantage of milliwatt (mW) level of output power can be compensated by introducing sensitive photodetectors and digital signal processing techniques.

The HFM contactor is a mass transfer device that packs numerous microporous HFMs in a compact vessel (Gabelman and Hwang, 1999). The unique design of the membrane contactor resulted in a very high volumetric mass transfer (Loose et al., 2009; Sengupta et al., 1998), which was exploited in several dissolved gas measurement method (Gonzalez-valencia et al., 2014; Loose et al., 2009; Matsumoto et al., 2013).

Based on a thorough literature review and a preliminary research, an integrated dissolved CO/H_2 measurement system was designed and developed based on a MIR dissolved CO measurement system and a commercial dissolved H_2 sensor.

1.2 Research Objectives

The utmost objective of this research is to develop an integrated dissolved CO/H_2 measurement system, which utilizes an infrared method to measure dissolved CO and an electrochemical method to measure dissolved H_2 in water based medium. The specific objectives include:

1) To design, develop and test a MIR CO sensor to measure gas phase CO concentration;
2) To design, develop and test a dissolved CO measurement system to measure dissolved CO concentration in water based medium with a dissolved gas extraction system and the developed mid-infrared CO sensor;
3) To evaluate the performance of a commercial dissolved H_2 sensor; and
4) To develop an integrated dissolved CO/H_2 measurement system to measure dissolved CO and H_2 concentrations in water based medium and to evaluate the performance of the integrated system.

CHAPTER II

LITERATURE REVIEWS

2.1 Introduction to syngas fermentation

Syngas fermentation is a novel technology to produce biofuel from renewable lignocellulosic biomass instead of sugar or starch based feedstock (Devarapalli and Atiyeh, 2015; Maddipati et al., 2011). The traditional techniques to utilize lignocellulosic biomass for biofuel production are biochemical conversion and thermochemical conversion (Devarapalli and Atiyeh, 2015; Munasinghe and Khanal, 2010). Syngas fermentation is a hybrid technique that incorporates the gasification process from thermochemical conversion and biological fermentation from biochemical conversion (Devarapalli and Atiyeh, 2015; Maddipati et al., 2011). Lignocellulosic biomass is gasified to produce syngas, a mixture of CO, CO_2, H_2, and minor gases such as CH_4, NH_3, H_2S, and HCl (Wilkins and Atiyeh, 2011). Then, the CO and H_2 components in syngas are converted to ethanol, butanol, and other products by biocatalysts, which are extremely anaerobic microorganisms such as *Clostridium ljungdahlii, C. autoethanogenum, and C. carboxidivorans* (Wilkins and Atiyeh, 2011).

Syngas fermentation avoids the disadvantages of biochemical and thermochemical conversion by circumventing biomass pretreatment process in biochemical conversion and Fischer-Tropsch process in thermochemical conversion (Munasinghe and Khanal, 2010). Fermentation with

microorganisms avoids the expensive chemical catalysts, high pressure/temperature operation condition, and low product specificity in thermochemical conversion (Daniell et al., 2012; Tirado-Acevedo et al., 2010).

However, commercialization of syngas fermentation was hindered by low productivity (Devarapalli and Atiyeh, 2015; Maddipati et al., 2011) and low mass transfer rates of CO and H_2 (Bredwell et al., 1999). The mass transfer rates of CO and H_2 could be improved with precise measurement and control of dissolved CO and H_2 concentrations (Devarapalli and Atiyeh, 2015). Appropriate dissolved CO and H_2 concentrations in a fermentation medium could improve carbon conversion rate and product specificity, which in turn maintained the normal activity of microorganisms and enzymes (Phillips et al., 2017). The dissolved CO and H_2 concentrations were measured with a method using offline gas chromatography and fermenter gas mass transfer models in our previous research (Atiyeh et al., 2017), which was complicated and time-consuming. It was of great value to monitor and control the dissolved CO and H_2 concentrations in bioreactors to improve the product yield and specificity, which can be achieved by developing a real-time online measurement system to avoid the inhibition on the microorganisms by above dissolved gases.

2.2 Dissolved gas measurement methods

2.2.1 Dissolved CO/H_2 measurement methods

2.2.1.1 Dissolved CO measurement methods

To the best of our knowledge, scant research reported methods to measure dissolved CO concentration in aqueous solution. The most related method was to measure the concentration of carboxyhemoglobin (COHb), a CO bounded hemoglobin, in the blood (Widdop, 2002). The

difference of the optical absorption spectra from COHb and CO-free hemoglobin was used to measure COHb concentration (Ramieri et al., 1974; Riggs and Heindel, 2006). This method could be further modified to directly measure dissolved CO concentration by establishing a fitting model between the dissolved CO concentration and the hemoglobin absorption spectra (Kundu et al., 2003; Riggs and Heindel, 2006; Widdop, 2002). The CO concentration was then obtained by comparing the absorption spectra of the unknown sample to the absorption spectra of COHb and CO-free hemoglobin (Riggs and Heindel, 2006; Ungerman and Heindel, 2007).

Another method to measure dissolved CO concentration in blood was performed with gas chromatography (GC) or combined gas chromatography-mass spectroscopy (GC-MS) techniques (Collison et al., 1968; Varlet et al., 2012; Widdop, 2002). This method was an indirect approach as it utilized chemical liberation agents to release CO from COHb. The extracted CO gas was then analyzed by GC (Collison et al., 1968) or combined GC-MS technique (Varlet et al., 2012). The chemical liberation agents were only effective to COHb; therefore, this dissolved CO measurement method had limited applications.

2.2.1.2 Dissolved H_2 measurement method

Dissolved H_2 concentration in aqueous solution can be measured with two common methods: the direct method and indirect method. The direct method was to design a sensor that can measure dissolved H_2 concentration in the liquid (Pauss et al., 1990; Sweet et al., 1980). The indirect method was to design a dissolved H_2 extraction apparatus and then to analyze the extracted H_2 with a gas phase H_2 detector (Björnsson et al., 2001; Cord-ruwisch et al., 1997).

Membrane coated electrochemical sensors had been used in the direct measurement of dissolved H_2 concentration in an aqueous solution (Hara and Macdonald, 1997; Kuroda et al., 1991; Sweet et al., 1980). Selective permeable membranes, such as Teflon and silicone membrane, were used to separate sensors' electrolytes from the liquid samples and to allow the selective diffusion of H_2

to the electrodes (Pauss et al., 1990). Two types of H_2 detection principles were used in these sensors. The first type utilized the oxidation of H_2 with oxygen (O_2) as shown in Equation 2.1 and 2.2 (Hara and Macdonald, 1997):

$$\frac{1}{2}O_2 + 2e^- + H_2O \rightarrow 2OH^- \quad (2.1)$$

$$H_2 \rightarrow 2H^+ + 2e^- \quad (2.2)$$

The overall reaction was that H_2 was oxidized to H_2O as shown in Equation 2.3:

$$\frac{1}{2}O_2 + H_2 \rightarrow H_2O \quad (2.3)$$

The second type of dissolved H_2 sensors had different electrode materials and polarization voltages (Mislov et al., 2015; Sweet et al., 1980); therefore, they didn't need O_2 in measurement:

$$2AgCl + 2e^- \rightarrow 2Ag + 2Cl^- \quad (2.4)$$

$$H_2 \rightarrow 2H^+ + 2e^- \quad (2.5)$$

AgCl (Silver chloride) was reduced to Ag (silver) by H_2 in these sensors as shown in Equation 2.6:

$$2AgCl + H_2 \rightarrow 2Ag + 2HCl \quad (2.6)$$

Another method for dissolved H_2 measurement was to extract the dissolved H_2 with gas extractors and measure the extracted H_2 (Björnsson et al., 2001; Lovley and Goodwin, 1988). Dissolved H_2 in the aqueous solution could be extracted by static headspace equilibrium method (Lovley and Goodwin, 1988), gas stripping technique (Björnsson et al., 2001), and membrane extractor (Pauss et al., 1990). The extracted H_2 was measured by common gas measurement methods such as GC

(Lovley and Goodwin, 1988), conductivity sensor (Björnsson et al., 2001), and electrochemical gas sensor (Pauss et al., 1990).

2.2.2 Review of dissolved gas measurement methods

The literature reviews on the methods to measure dissolved CO and H_2 concentrations showed two types of measurement methods:

1) Direct method: measure dissolved CO/H_2 in the aqueous solution directly.
2) Indirect method: measure extracted in gas phase and then calculate dissolved CO/H_2 concentrations.

Direct method included the electrochemical dissolved H_2 sensors and the dissolved CO measurement methods using COHb, which utilized the chemical or biological properties of the dissolved gases. Indirect dissolved gas measurement method included the GC/MS-GC methods with headspace equilibrium, membrane extraction, and chemical gas extraction techniques. Chemical (breakdown of hemoglobin) or physical (headspace equilibrium, membrane extractor) gas extraction methods were used to extract the dissolved gases.

Further search on the commercial dissolved CO and H_2 sensor showed that there was commercial dissolved H_2 sensor in the market. However, no dedicated dissolved CO sensor was available currently. It was necessary to develop a specific dissolved CO sensor for this research. Therefore, a review on the dissolved gas measurement methods was performed to help the design of the dissolved CO sensor.

2.2.2.1 Direct dissolved gas measurement methods

Electrochemical sensors can be modified to directly measure concentration of dissolved gases (Ramamoorthy et al., 2003; Sweet et al., 1980). The Clark type of electrochemical sensors, with

hydrophobic membrane coated on the electrodes or the surface of sensors, were reported to measure dissolved O_2 (Nei and Compton, 1996), H_2 (Sweet et al., 1980), H_2S (Jeroschewski et al., 1996), N_2O (Revsbech et al., 1988), and SO_2 (Schiavon et al., 1991). Membranes in the Clark type of electrochemical sensors allowed selective gas-only diffusion while isolated electrolyte from liquids (Mislov et al., 2015; Schiavon et al., 1991). Silicone membrane (Krämer and Conrad, 1993) and Polytetrafluoroethylene (PTFE) membrane (Hara and Macdonald, 1997) were the most commonly used membranes.

The pH sensors can be used to measure dissolved acidic or alkaline gases, such as CO_2 (Severinghaus and Freeman, 1958) and NH_3 (Thomas and Booth, 1973), through the pH changes from the dissolution of these gases. The pH sensors used in these applications were electrochemical sensors with gas permeable membranes coated on the surface (Thomas and Booth, 1973). The Henderson-Hasselbalch equation was used to determine dissolved gases concentration according to the pH value and sample temperature (Severinghaus and Freeman, 1958).

Optical sensors, such as colorimetric and fluorescence sensors, can be used to measure dissolved gases in aqueous solution. Colorimetric sensors utilize the optical absorption change in the spectra of the sensing materials to detect dissolved gases. The sensing materials included chemical dyes (Mills and Chang, 1994; Stangelmayer et al., 1998) or biological materials, such as hemoglobin (Chung et al., 1995; Kundu et al., 2003). They were reported to detect dissolved CO_2 (Mills and Chang, 1994), SO_2 (Stangelmayer et al., 1998), CO (Kundu et al., 2003), and O_2 (Chung et al., 1995). Fluorescence sensors were reported to detect dissolved gases such as dissolved O_2 (Chu and Lo, 2010; McEvoy et al., 1996) and CO_2 (Liu et al., 2010) with gas-binding fluorescence dyes or dissolved CO_2 (Burke et al., 2006; Muller and Hauser, 1996; Wolfbeis et al., 1998) and NH_3 (Lobnik and Wolfbeis, 1998; Waich et al., 2008) with fluorescence pH indicators.

2.2.2.2 Indirect dissolved gas measurement methods

Indirect dissolved gas measurement methods can be categorized by their principles for dissolved gas extraction. As Henry's law stated that the solubility of gases was related to the partial pressure of the gases (Robbins et al., 1993; Wiesenburg and Guinasso Jr, 1979), most dissolved gas extractions were performed by reducing the partial pressure to extract dissolved gases. Temperature factor was also utilized as it could change the Henry's law coefficient, thus further affected the dissolution of gases (Sander, 2015).

Gas stripping technique, or named as dynamic headspace equilibration technique, had been used for dissolved gas measurement since 1960s (Swinnerton et al., 1962). Carrier gases, such as N_2 or He, were forced to pass through the liquid and to strip the dissolved gas from the liquid by reducing the partial pressure of the dissolved gas (Cohen, 1977; Cosgrove and Walkley, 1981; Salonen, 1981; Swinnerton et al., 1962). Carrier gases were also used to transport the stripped gas samples to gas analyzers in these reports.

Static headspace equilibration method is another common method for dissolved gas extraction (B'Hymer, 2003). Automatic static headspace equilibration samplers were available to measure dissolved gas concentrations continuously and automatically (Butler and Elkins, 1991; Jalbert et al., 2001; Kampbell and Vandegrift, 1998). However, its sensitivity on dissolved gas concentrations was lower than the gas stripping technique (B'Hymer, 2003). The operation of static headspace equilibration method included two steps: firstly, a portion of liquid sample was stored in a sealed vial; secondly, a new equilibrium was established in the vial and the equilibrated gas in headspace of the vial was used for analysis (Jalbert et al., 2001; Johnson et al., 1990). The establishment of new equilibrium can be accelerated by heating liquid sample, reducing headspace pressure, or decreasing headspace volume (B'Hymer, 2003; Johnson et al., 1990; Tsurushima et al., 1999).

Vacuum extraction systems, such as the Van Slyke apparatus, were reported in measurements of dissolved gas concentrations in blood or environmental water sample manometrically (Brix, 1981; Van Slyke and Neill, 1924). The mercury manometer inside the apparatus generated a controllable vacuum in the headspace for quantitative dissolved gas extraction. Vacuum extraction system could also be implemented as a gas stripping system, using high vacuum instead of carrier gases to extract dissolved gas (Lammers and Suess, 1994).

Heating the liquid sample was not commonly considered for dissolved gas measurement because of the generated water vapor in the extracted gas. However, this method could achieve a rapid and efficient gas extraction (Leonard et al., 1998). A cold condenser or a membrane filter was usually used in this method to separate the extracted gas from the water vapor (Noij et al., 1987).

2.2.2.3 Membranes in dissolved gas measurement

Gas permeable membranes were used in several dissolved gas measurement systems (Duval, 2003), such as membrane coated electrochemical sensors (Sweet et al., 1980), membrane introduction mass spectroscopy (Hillman et al., 1985), and membrane extraction gas chromatography (Pratt and Pawliszyn, 1992). The gas concentration gradient between the two sides of membrane provided the force for gas diffusion (Pandey and Chauhan, 2001; Xu and Mitra, 1994). Hydrophobic membranes, such as silicone, Teflon, and Nafion membrane, were preferred as they would stop the diffusion of liquids through the membranes (Davey et al., 2011; Gabelman and Hwang, 1999). Carrier gas and/or high vacuum were also introduced to accelerate the process of dissolved gas extraction with membranes (Davey et al., 2011; Pratt and Pawliszyn, 1992).

The unique design of HFM contactors, which packed numerous microporous HFMs in a small chamber, resulted in very high volumetric mass transfer coefficient by maximizing the contact surface area in a given volume (Gabelman and Hwang, 1999; Loose et al., 2009; Sengupta et al.,

1998). The flow rate and the pressure of liquids or gases in the HFM contactors could be maintained at different levels (Gabelman and Hwang, 1999). The modular design of the contactors also facilitated easy scale-up and replacement of the contactors (Sengupta et al., 1998).

HFM contactors were primarily used in industry for gas-liquid or liquid-liquid mass transfer, because they reduced problems such as emulsion, foaming, and flooding from conventional mass transfer techniques. (Gabelman and Hwang, 1999). The high mass transfer efficiency of HFM contactors was exploited in dissolved gas measurements (Sengupta et al., 1998). The application of HFM contactor had demonstrated its capability in building an real-time, fast response dissolved gas measurement system (Gonzalez-valencia et al., 2014; Loose et al., 2009; Matsumoto et al., 2013).

2.2.2.4 Liquid sample preparation method

The design of a dissolved gas sensor required to obtain liquid samples with a precise dissolved gas concentration for sensor calibration. Henry's law was a common method to determine the dissolved gas concentration in the aqueous solution (Kampbell and Vandegrift, 1998; Sanford et al., 1996). Another method was to prepare standard liquid sample with saturated dissolved gases, then add gas-free water to the prepared standard liquid sample to obtain liquid samples with different dissolved gas concentrations (Riggs and Heindel, 2006; Widdop, 2002). It was also possible to use certain chemicals to prepare liquid samples with known dissolved gas concentration (Fukushi and Hiiro, 1987; Varlet et al., 2013). The reaction between the chemicals could release a certain amount of gases into the liquid sample, thus the dissolved gas concentrations in the liquid samples could be obtained. A correlation equation between the extracted gas concentration and the dissolved gas concentration could be obtained based on the design of the sensor; however, the equation was seldom reported (Cohen, 1977).

2.3 Sensors for CO detection

A review of different CO detection methods was performed to determine the CO detection principle. There were several requirements on the ideal CO detection principle summarized from the syngas fermentation environments. The most important one was the selectivity of the CO sensor. The sensor should have the least interference from other chemicals in the syngas fermentation medium, such as H_2 and alcohols. The sensitivity of the CO sensor should be high, as it was known that CO has a very low solubility in water (27.5 mg/L at 25 °C). Fast response time as well as reversible detection were also preferred for a real-time, continuous measurement of dissolved CO concentration.

2.3.1 Electrochemical sensors

Electrochemical CO sensors utilize the chemical reaction of CO to detect its presence and to measure its concentration. They can be categorized as potentiometric sensors and amperometric sensors based on the physical properties employed for detection (Vashist et al., 2011).

Potentiometric CO sensors monitor the electromotive force (emf) between the electrodes to detect CO (Okamoto et al., 1980). The measured emf between the two electrodes is generated by the mixed potential from the oxidation of CO and reduction of oxygen (Fergus, 2007). The reactions occurred at both electrodes with oxygen and CO are shown in Equation 2.7 and 2.8 (Fergus, 2007; Sorita and Kawano, 1997).

$$\frac{1}{2}O_2 + 2e^- \Leftrightarrow O^{2-} \tag{2.7}$$

$$CO + O^{2-} \Leftrightarrow CO_2 + 2e^- \tag{2.8}$$

Overall, CO was oxidized to CO_2 by oxygen as shown in Equation 2.9:

$$CO + \frac{1}{2}O_2 \Leftrightarrow CO_2 \quad (2.9)$$

Disadvantages of the potentiometric sensors include low sensitivity, low selectivity between CO and H_2, and high electrode operation temperature (Fergus, 2007; Sorita and Kawano, 1997). Novel electrode materials or catalysts were reported to improve sensitivity and selectivity to CO, such as metal oxide catalyst (Li et al., 1993; Park et al., 2010) and metal oxide electrode (Goto et al., 2015; Sorita and Kawano, 1997). However, abovementioned materials need to be heated to 400~700°C for the best selectivity and sensitivity to CO. Nanomaterials were reported with improved CO sensitivity and lower operation temperature at about 130°C. (Wu et al., 2003).

Amperometric CO sensors measure the current changes between the working and counter electrodes to determine the CO concentration (Stetter and Li, 2008). A constant or variable potential applied between the two electrodes triggers electrochemical reactions. The reaction rate, which can be measured as an external circuit current, is proportional to the concentration of CO. Practical amperometric CO sensors with liquid electrolyte were firstly reported in 1970s (Bay et al., 1974). These sensors a three-electrode structure with a working electrode, a counter electrode, and a reference electrode. The electrodes and the liquid electrolyte were covered with a layer of gas permeable Teflon membrane. The reference electrode was used to maintain a constant electrochemical potential at the working electrode. CO was oxidized on the working electrode as shown in Equation 2.10:

$$CO + H_2O \rightarrow CO_2 + 2H^+ + 2e^- \quad (2.10)$$

On the counter electrode, the oxygen was reduced to water as shown in Equation 2.11:

$$\frac{1}{2}O_2 + 2H^+ + 2e^- \rightarrow H_2O \quad (2.11)$$

Overall, CO was oxidized to CO_2 as shown in Equation 2.12:

$$CO + \frac{1}{2}O_2 \rightarrow CO_2 \quad (2.12)$$

Improvements on the original design by Bay et al. (1974) included replacing the liquid electrolyte with solid electrolytes and simplifying the sensor structure. CO sensors with solid electrolytes such as Nafion conducting polymer (Yan and Liu, 1994) or protonic conduction film (Alberti et al., 1993) were reported. Compact planar design of sensor was reported , which greatly simplified the structure of the sensor (van der Wal et al., 1996).

Disadvantages of amperometric CO sensors include high humidity influence and high cross sensitivity to other gases. Gas flows with a low relative humidity would greatly reduce the CO response of a solid electrolyte sensor (Alberti et al., 1993; van der Wal et al., 1996). The applied potential for CO oxidation could also trigger the oxidation reaction on other reducing gases, such as NO_x, H_2 and hydrocarbons (Stetter and Li, 2008; van der Wal et al., 1996).

In summary, electrochemical CO sensors have low detection limits to CO (1ppm, Takeda et al., 2015), high CO sensitivity and fast response and recovery time (Fouletier, 1982; Stetter and Li, 2008). However, they have two disadvantages in syngas fermentation environment: the requirement of oxygen and the low selectivity to H_2. The electrodes of the potentiometric CO sensors need to be heated to several hundred degree Celsius for the best sensitivity and selectivity.

2.3.2 Conductivity sensors

Conductivity CO sensors include metal-oxide CO sensors and conducting polymer CO sensors (Arshak et al., 2004). These sensors are built with a layer of sensing material enclosed between two electrodes. When the sensing material is exposed to CO gas, an electrical resistance change will occur as the result of the interaction between the sensing material and CO. The change of

sensor resistance is used to determine CO concentration (Bai and Shi, 2007; C. Wang et al., 2010).

The metal-oxide CO sensors, or semiconductor CO sensors, are fabricated with semiconducting metal-oxide based on the phenomena that the conductivity of semiconductors changes in contact with gases (Morrison, 1953, 1982; Yamazoe et al., 2003). Primitive metal-oxide CO sensors were reported to have cross-sensitivity to H_2, because sensing materials used to improve sensitivity to CO also increased the sensor's sensitivity to H_2 (Kobayashi et al., 1988; Morrison, 1982). Efforts to improve the sensitivity and selectivity of CO detection included applying new metal-oxide materials (Kobayashi et al., 1988; Wu et al., 2006; Yamaura et al., 2000) or novel doping materials (Choi et al., 2005; Kundu et al., 2003; Yamaura et al., 2008), and modification of the surface nanostructure of the sensing materials (Ansari et al., 2002). However, these metal-oxide CO sensors need high operation temperature (80°C~250°C) for optimal CO sensitivity and selectivity. Room temperature metal-oxide CO sensor was reported with the cost of poor selectivity to other reducing gases, such as NO, H_2 and CH_4 (Wu et al., 2009).

Detection mechanism of metal-oxide CO sensors is complicated because of the complicated nature of the metal-oxide structure (Wang et al., 2010; Yamazoe et al., 2003). A widely accepted theory stated that the electrons trapping and the band bending of the sensing materials associated with CO and/or oxygen changed the materials' conductivity (Morrison, 1982; Wang et al., 2010). Absorbed oxygen molecules in the surface of metal-oxide sensing materials attracted electrons from the surface (Eq.2.13) and generate an electron-depleted region.

$$O_2 + 2e^- \longrightarrow 2O^- \tag{2.13}$$

When CO was exposed to the sensor, it would be oxidized by the absorbed O^- and release electrons back to the metal-oxide surface as reaction in Equation 2.14.

$$CO + O^- \longrightarrow CO_2 + e^- \quad (2.14)$$

Therefore, the thickness of the electron-depleted region would decrease and in turn reduced the resistance of the metal-oxide sensing materials. Other theories, such as CO absorption on sensing material (Wu et al., 2008) and collapsed charge order restoration with CO (Ghosh et al., 2016), were also proposed for different type of sensing materials.

Metal-oxide CO sensors are preferred for their advantages such as solid state structure, low cost, and simple structure (Wang et al., 2010). However, their disadvantages such as high optimal operation temperature and cross sensitivity to other chemicals are not desired in many applications. Also, the sensitivity of metal-oxide CO sensors were influenced by relative humidity around the sensors (Barsan and Weimar, 2003; Morrison, 1982; C. Wang et al., 2010; Yamaura et al., 2008). Their response was not very fast, ranging from several seconds (Ansari et al., 2002) to several minutes (Wu et al., 2008).

Conducting polymer CO sensors are preferred over metal-oxide CO sensors because of their high sensitivity and quick response at room temperature (Bai and Shi, 2007). Polyaniline was the most popular conducting polymer for CO detection (Dixit et al., 2005; Misra et al., 2004; Ram et al., 2005) and was often doped with other materials for enhanced sensitivity (Liu et al., 2012; S. Pandey, 2016; Sen et al., 2016; Wang et al., 2017).

The detection mechanism of polyaniline can be explained by the electrons transfer between CO and the polymer itself (Sen et al., 2016). Polyaniline is a P-type semiconductor with majority charge carriers of holes (Bai and Shi, 2007). CO molecules extract electrons from the polyaniline, thus increase the number of charge carrier in the polyaniline and the conductivity of polyaniline (Liu et al., 2012). Other theories included CO physical absorption to polyaniline (Misra et al., 2004) and redox reaction between CO and polyaniline (Ram et al., 2005).

Room temperature operation is one of the biggest advantages of conducting polymer CO sensors (Bai and Shi, 2007). Their response time for CO at low concentration fall in several seconds, which is faster than that of metal-oxide ones (Liu et al., 2012; Pandey, 2016). However, few researcher reported the selectivity of conducting polymer CO sensors. Liu et al. (2012) reported a sensor with no cross sensitivity to H_2 and Sen et al. (2016) reported a sensor with good selectivity to liquefied petroleum gas and CH_4. Polyaniline based conducting polymer sensors were also used for H_2 and alcohols detection (Pandey, 2016), which may imply that these sensors may have cross sensitivity to H_2 and alcohols.

In summary, conductivity CO sensors are preferred for their simple structure, easy fabrication and high sensitivity and CO selectivity with proper sensing materials (Bai and Shi, 2007; C. Wang et al., 2010). Some of them can operate at anaerobic environment (Liu et al., 2012; Wu et al., 2008), which is required in syngas fermentation application. However, metal-oxide CO sensors would also response to reducing gases, such as H_2 and CH_4 (Kobayashi et al., 1988). They also need high temperature for optimal CO sensitivity (Wu et al., 2009). Conducting polymer CO sensors can work at room temperature, but scant research reported their selectivity, especially to the reducing gases (Liu et al., 2012). In syngas fermentation with H_2 and alcohol rich environment, conductivity sensors are not an optimal choice.

2.3.3 Optical CO sensors

Optical CO sensors are based on the spectral responses of CO or CO related chemicals in the ranges of ultraviolet, visible, and infrared. In general, optical CO sensors have many advantages compared to other CO sensors, such as fast response, high gas selectivity, wide measurement range, minimal drift, and noninvasive measurement (Hodgkinson and Tatam, 2013).

Vacuum ultraviolet resonance fluorescence (VURF) CO sensors measured the CO concentration by detecting a spectral response located in the fourth positive band of CO vacuum ultraviolet

spectrum, which was excited by fluorescent sources (Volz and Kley, 1985). The VURF sensors were as fast and sensitive as tunable laser spectroscopy sensors in CO measurements (Gerbig et al., 1996). The detection limits of VURF sensors could reach to parts per billion by volume (ppbv) level at a response time within a few seconds (Gerbig et al., 1999; Scharffe et al., 2012). Water vapor affected accuracy of VURF sensors, thus should be removed completely (Gerbig et al., 1996). High concentration of CO_2 also affected VURF CO sensors because of the ultraviolet photolysis of CO_2 to CO (Gerbig et al., 1996; Volz and Kley, 1985). Hence, the rich CO_2 presence in the syngas fermentation environment limits the application of VURF CO sensors.

Colorimetric CO sensors were built based on the visible or near-infrared absorption spectra generated from the interaction between CO and specific chemicals. The chemicals used in colorimetric CO sensors could be metal-oxide thin films (Ando et al., 1995; Cantalini et al., 2005; Ghodselahi et al., 2011), metal complex (Courbat et al., 2011; Moragure et al., 2011; Park et al., 2014), or biological materials (Blyth et al., 1995).

The oxidization of CO on the metal-oxide thin film generated a change of the film's absorption spectra, which was correlated to CO concentration (Ando and Group, 2000; Ghodselahi et al., 2011). Colorimetric sensors based on metal-oxide thin film generally operated in temperature around 250°C ~ 350°C for optimal CO sensitivity and selectivity (Ando et al., 1997; Cantalini et al., 2005; Nam et al., 2006). However, metal-oxide colorimetric sensors had poor selectivity to other reducing gases, such as H_2 (Ando et al., 1997; Cantalini et al., 2005). Metal complex colorimetric sensors exhibited an obvious color change when exposed to CO (Benito-Garagorri et al., 2008; Marín-Hernández et al., 2016). The coordination between CO and the specific metal complex changed the spin-state or the electron density, thus resulted in color changes observable to the naked eyes (Marín-Hernández et al., 2016). Advantages of metal complex colorimetric sensors include room temperature detection, fast response, low detection limit, and fully reversible detection (Benito-Garagorri et al., 2008; Courbat et al., 2011; Moragure et al., 2011).

However, scant research reported the selectivity of metal complex colorimetric CO sensors to gases or organic chemicals, especially to H_2 (Marín-Hernández et al., 2016; Moragure et al., 2011; Peter et al., 2012).

Fluorescent CO sensors were built to utilize the luminescence response of metal complex (Matkovich et al., 2006; Rogers and Wolf, 2002), organic substrates (Yan et al., 2014; Zheng et al., 2014), and fluorescent proteins (Michel et al., 2012) for room temperature CO detection and concentration measurement. Fluorescent CO sensors had better sensitivity than the colorimetric CO sensors because of the strong luminescence response (Rogers and Wolf, 2002). They were also capable to detect CO molecules in living cells or tissues by having the cells or tissues incubated with the fluorescent indicators (Michel et al., 2012; Zheng et al., 2014), which imply a possibility to design a dissolved CO fluorescent sensor.

Fluorescent CO sensors were reported with a parts-per-million (ppm) level detection limit and good selectivity to multiple gases, such as CO_2, SO_2, NO_x, H_2S, and organic vapors like acetone and ethanol (Toscani et al., 2015). However, most fluorescent sensors were fabricated based on irreversible reaction from metal complex fluorescent indicator or fluorescent proteins (Marín-Hernández et al., 2016; Matkovich et al., 2006; Toscani et al., 2015), which made them less attractable in continuous real-time measurements.

Infrared CO sensors include non-dispersive infrared sensor, tunable diode laser spectroscopy and spectrophotometry (Hodgkinson and Tatam, 2013). These sensors utilize the unique infrared absorption spectra of CO for sensitive and selective detection of CO (Borisov and Wolfbeis, 2008; Hodgkinson and Tatam, 2013; Werle et al., 2002). The wavelengths used in infrared CO sensors correspond to the fundamental, 1st overtone, and 2nd overtone infrared absorption band of CO at 4.6 μm, 2.3 μm, and1.57 μm respectively (Li et al., 2015).

Non-dispersive infrared (NDIR) sensors measure CO concentration by detecting the infrared absorption of CO. Broadband infrared sources are usually used in the NDIR sensors. Narrowband bandpass optical filters or gas correlation filters were introduced for CO selectivity (Silver and Chen, 2006). The sensitivity of the NDIR sensors was mainly determined by its gas cell pathlength according to the Beer-Lambert law (Hodgkinson and Tatam, 2013). The photodetector properties and signal processing designs affect its sensitivity as well.

Tunable diode laser spectroscopy (TDLS) is a highly sensitive and selective technology in the detection of traces gases in atmosphere (Schiff et al., 1994; P. Werle et al., 2002; Peter Werle, 1998). The TDLS CO sensors were reported using 4.6 μm (Barron-Jimenez et al., 2006; Miller et al., 1993), 2.3 μm (Ebert et al., 2004; Wang et al., 2000), or 1.57 μm (Cai et al., 2011) lasers in the measurement of CO infrared absorption. The TDLS CO sensors scanned an individual gas absorption line at very high resolution to provide high CO selectivity (Schiff et al., 1994; Werle et al., 2002). Lasers' good directionality promotes very long optical pathlength sensor design, which greatly improves their sensitivity to CO (Tittel et al., 2003). TDLS can be categorized as direct absorption spectroscopy and wavelength modulation spectroscopy (Hodgkinson and Tatam, 2013; Werle et al., 2002). Direct absorption spectroscopy has similar structure to NDIR sensors (Werle et al., 2002). Wavelength modulation spectroscopy was introduced to improve the signal-to-noise (SNR) ratio of direct absorption spectroscopy (Schiff et al., 1994).

Infrared spectrometers, such as dispersive infrared spectrometers and Fourier transform infrared (FTIR) spectrometers, have the capability to measure the infrared absorption of the sample in a wide wavelength range (Hodgkinson and Tatam, 2013). FTIR spectrometers had much better SNR compared to traditional dispersive infrared spectrometers (Hodgkinson and Tatam, 2013). Although infrared spectrometers were not specific designed for CO measurement, spectrometers with an open optical path design were reported to measure CO concentration in environment (Childers et al., 2001; Twiss et al., 1955; Zhao et al., 2002).

Photoacoustic CO sensors, or optoacoustic CO sensors, were built to detect the pressure wave generated from infrared absorption of CO, which was known as photoacoustic effect (Gerlach and Amer, 1978; Hodgkinson and Tatam, 2013; Patimisco et al., 2014; Tam, 1986). Lasers were the best infrared radiation source for photoacoustic sensors as the photoacoustic signal strength was proportional to absorbed infrared radiation strength (Harren et al., 2000). The narrow bandwidth and high energy density of lasers resulted in high CO sensitivity and selectivity of photoacoustic sensors (Chen et al., 2009; Gerlach and Amer, 1978).

Advantages of photoacoustic CO sensors include its short optical pathlength for trace gas measurement (Gerlach and Amer, 1978; Hök et al., 2000) and free of sensitive photodetector (Patimisco et al., 2014). Detection limit of less than one ppm in volume was reported with a laser with milliwatt output power (Gerlach and Amer, 1978). The improved Quartz enhanced photoacoustic (QEPAS) CO sensors had a detection limit at ppbv level with a mid-infrared 4.55 μm (Kosterev et al., 2005) or 4.61 μm laser (Stefanski et al., 2013).

2.3.4 Other CO sensors

Thermoelectric sensors, piezoelectric sensors, and microelectronic sensors can also be used to detect CO.

Thermoelectric CO sensors utilize the thermoelectric (Seebeck) effect, which converts heat to electricity, to measure the CO concentration (Nagai et al., 2013). The heat generated by the catalytic combustion of CO is proportional to the CO concentration (Matsumiya et al., 2004). The temperature change from the generated heat is further converted to a voltage signal, which is used to determine CO concentration.

The catalysts in thermoelectric CO sensors determined the sensitivity, selectivity, and optimal operation temperature of the sensors (Nagai et al., 2013; Xu et al., 2008). The detection limit of thermoelectric sensors could reach ppm level (Nagai et al., 2013) while the minimal operation

temperature was reported around 90°C ~125°C (Xu et al., 2008). Thermoelectric sensors had a good selectivity as no significant responses from H_2, CH_4, and alcohols were reported (Matsumiya et al., 2004; Nagai et al., 2013; Xu et al., 2008).

Disadvantages of thermoelectric CO sensors include high operation temperature, oxygen required in CO detection, and complicated signal processing (Nagai et al., 2013; Xu et al., 2008). The catalytic combustion of CO requires oxygen, which is strictly prohibited in syngas fermentation application. Thermoelectric CO sensors also need sophisticated circuit design, as the raw voltage signal was only several microvolts (Nagai et al., 2013).

Piezoelectric CO sensors were built based on the phenomena that the resonance frequency of the piezoelectric crystal was affected by the crystal mass changes from absorbed gases (Alder and McCallum, 1983; Ho and Gullbault, 1982). The resonance frequency change was linear to the mass change according to the Sauerbrey equation (Fung and Wong, 2002). These sensors could have high sensitivity and selectivity to certain gases with selective absorption coatings (Fung and Wong, 2002; Ho and Gullbault, 1982).

Piezoelectric CO sensors were reported with specific coatings on piezoelectric crystals that could directly absorb CO gas in room temperature (Fung and Wong, 2002; Guimarães et al., 2006; Kuo and Shih, 2005). Theses sensors were also reported free of interference from H_2, SO_2, H_2S (Fung and Wong, 2002) and had a moderate interference from NO_2 (Kuo and Shih, 2005). However, the reported piezoelectric CO sensors, especially those based on absorption coating, were non-reversible, single-use ones. (Fung and Wong, 2002; Guimarães et al., 2006). Therefore, piezoelectric CO sensors are inappropriate for repeated CO measurement in syngas fermentation applications.

Microelectronic CO sensors include the field-effect-transistor (FET) based CO sensors and the diode-based CO sensors. The FET CO sensors exploited semiconducting metal oxides as gate

material, whose carrier concentration could be altered in contact with CO (Dobos and Zimmer, 1985). The change of the carrier concentration alters the threshold gate voltage. The diode-based CO sensors measured the change of current-voltage (*I-V*) characteristic to determine the CO concentration (Gurbuz et al., 1999; Salehi and Nikfarjam, 2004). The *I-V* change of the diode-based sensor was generated from the conductivity change of the semiconducting materials, which was the result of CO oxidation (Gurbuz et al., 1999) or CO absorption (Salehi and Kalantari, 2007).

FET CO sensors usually worked at an elevated temperature, ranging from 75°C (Fukuda et al., 2001) to 160°C (Dobos and Zimmer, 1985). Their sensitivity and selectivity were greatly affected by the gate material and the gate surface nanostructure (Fukuda et al., 2001; Maclay et al., 1988). Like other CO sensors using semiconducting metal oxide material, FET sensors also had poor selectivity to H_2 (Formoso and Maclay, 1990), CH_4 (Maclay et al., 1988), and ethanol (Dobos and Zimmer, 1985). Their response time ranged from 75 seconds (Fukuda et al., 2001) to several hundred seconds (Formoso and Maclay, 1990).

Diode-based CO sensors were reported with a response time within a few seconds (Gurbuz et al., 1999; Salehi and Nikfarjam, 2004). Diode-based CO sensors in room-temperature were also reported with no interference from O_2, H_2, and CO_2 as well as moderate interference from NO (Salehi and Kalantari, 2007).

In summary, thermoelectric sensors, piezoelectric sensors, and microelectronic sensors are not suitable in syngas fermentation applications. Thermoelectric sensors and microelectronic sensors have poor selectivity and operate at elevated operation temperature. Piezoelectric sensors are non-reversible, single-use sensors, which need to be replaced frequently.

2.3.5 Comparison of CO sensors

A comparison on the described CO detection methods was performed to determine the appropriate CO detection principle for the design of the dissolved CO sensor (Table.2-1). The primary comparison criteria included sensor selectivity, oxygen requirement, optimal operation temperature, and maturity of the technique. The reversibility of the CO detection was also considered in the comparison.

The presence of H_2 and other reducing gases in the fermentation medium was a big challenge for the CO detection. Most common methods, such as electrochemical sensors and conductivity sensors, also responded to these gases. There were several reports of new sensing materials to improve the CO selectivity; however, the maturity or available of the sensors was questionable. The requirement of oxygen in the detection of CO was also problematic, since the microorganisms were highly anaerobic.

Vacuum ultraviolet resonance fluorescence senor (VURF) might be a good choice in syngas fermentation. However, its reaction to CO_2 greatly limited its application. The syngas contains CO_2 and the microorganisms will also produce CO_2 in the fermentation process.

Colorimetric and fluorescent sensors were promising techniques to detect dissolved CO in the aqueous solution. However, these sensors were still in the laboratory development stages and their detection might be affected by the color or the debris of the fermentation medium. The highly selective fluorescent sensors were based on irreversible reactions.

Table.2-1 Comparison of CO sensors in syngas fermentation application

CO Sensor Type	CO Selectivity (Interference Chemicals)	Oxygen Required?	Optimal Operation Temperature	Maturity of Sensor
1. Electrochemical sensor	Low (H_2)	Yes	Room temperature	High
2. Conductivity sensor: Semi-conductor	Low (H_2)	Yes	High	High
3. Conductivity sensor: Conducting polymer	Low (Reducing gases)	Yes	Room temperature	Low
4. Vacuum ultraviolet resonance fluorescence senor (VURF)	Low (CO_2)	No	Room temperature	High
5. Colorimetric sensor	High[1]	No	Room temperature	Low
6. Fluorescent sensor	High[1,3]	No	Room temperature	Low[3]
7. Infrared sensor	High[2]	No	Room temperature	High
8. Thermoelectric sensor	Low (H_2)	Yes	High	Low
9. Piezoelectric sensor	High[3]	No	Room temperature	Low[3]
10. Microelectronics sensor	Low (H_2)	No	Room temperature	Low

* 1) The color of the fermentation medium may interference; 2) Selectivity can be high when properly select the absorption band; 3) Non-reversible CO detection (one-time detection only).

Infrared sensor was the only choice for development a dissolved CO sensor for the syngas fermentation application. It did not have the disadvantages, such as interference from H_2 or requirement of O_2, from abovementioned methods. The sensitivity to CO of an infrared sensor was among the highest in all kinds of CO detection methods. The response time and repeatability of an infrared sensor were also satisfactory. Also, the maturity of the infrared detection

technology was high with commercial components available in the market to develop an in-house infrared sensor.

2.4 Infrared spectroscopy

2.4.1 Principle of infrared spectroscopy

Infrared spectroscopy is a technique to identify and measure chemicals through their interactions with infrared radiation. The infrared radiation is one portion of electromagnetic radiation with higher wavelength than visible light. It can be categorized as near-infrared (NIR: 0.76 μm-2.5 μm), mid-infrared (MIR: 2.5 μm-25 μm) and far-infrared (NIR: >25 μm) (Stuart, 2004).

Molecules absorb infrared radiation when they demonstrate a change of dipole moment from molecular vibration or rotation (Stuart, 2004). Symmetric diatomic molecules, such as H_2, N_2, and O_2, are transparent to infrared radiation; because their dipole moments remain unchanged in molecular vibration. The infrared absorption spectrum is obtained by measuring the absorbed infrared radiation over a radiation wavelength range. The wavelength position of an infrared absorption peak in the spectrum is related to the vibrational molecular energy of certain molecules. The infrared spectrum usually used the unit of wavenumber, which is the spatial frequency of the infrared radiation.

The wavelengths, or in frequencies form of wavenumber, of infrared absorption peaks can be estimated with a classic mass and spring model (Williams and Norris, 2001). The vibrational energy E of a molecule contains two atoms (mass) connected with a bond (spring) in harmonic vibration can be expressed in Equation 2.15:

$$E = \frac{h}{2\pi}\sqrt{\frac{k}{\mu}} \tag{2.15}$$

where k is the bond force (spring) constant and h is the Planck's constant. The reduced mass of the system μ is defined as $\mu = \frac{m_1 m_2}{m_1 + m_2}$, in which m_1 and m_2 are the mass of the two atoms.

It is the energy coupling between photons and the molecular vibrational energy that generates the specific infrared absorption (Williams and Norris, 2001). The frequency of the radiation absorbed by the molecule can be calculated by the difference between two vibrational energy states E_1 and E_0 as Equation 2.16 (Stuart, 2004):

$$\bar{\nu} = (E_1 - E_0)/h \tag{2.16}$$

The quantum theory states that actual vibrational energy of molecule is fixed in a series of discrete, quantized energy levels as in Equation 2.17:

$$E_\upsilon = (\upsilon + 1/2)h\nu_f \tag{2.17}$$

where υ is the vibrational quantum number for the vibration and E_υ is the energy of the υth quantum level of that specific vibration. ν_f is the fundamental frequency of the vibration as $\frac{1}{2\pi}\sqrt{k/\mu}$.

The absorption of infrared radiation occurs when the energy of a light photon is equal to the energy difference between two quantum levels. Therefore, specific molecules only interact with infrared radiation energy at certain frequencies. The specific infrared absorption makes the infrared spectroscopy a very selective tool in detection of chemicals (Williams and Norris, 2001). The infrared absorption can be more complicated by factors such as multi-atoms molecules, anharmonic vibration, presence of functional group, and Fermi resonance (Williams and Norris, 2001).

The fundamental absorption bands in an infrared spectrum are the products of harmonic molecule vibrations. The overtone bands in an infrared spectrum are generated because the actual molecular vibration is not strictly harmonic and the energy differences between quantum levels are not constant. Since the energy difference is smaller when the vibrational quantum number is larger than one; it is possible that the energy from a single photon matches the required energy between multiple quantum levels. The frequency of overtone bands are roughly the multiples of the fundamental frequency ν_f , but the absorption intensity of the overtone bands are one magnitude smaller than the fundamental bands (Stuart, 2004; Williams and Norris, 2001). For example, the 1st overtone band is approximately located at $2\nu_f$ frequency, in which ν_f is the fundamental frequency of the vibration. The frequencyν_f can be represented in wavelength λ as $\nu_f = \frac{c}{\lambda}$, where c is the speed of light.

The above discussion on the quantum theory of infrared absorption suggests that the infrared absorption in fundamental infrared absorption bands of CO is the strongest. The wavelength of the fundamental bands is also higher than the overtone bands. This theory matches with observations on actual infrared spectrum of CO (Li et al., 2015).

2.4.2 Review of infrared spectroscopy instruments

Infrared spectroscopy can be categorized as transmission spectroscopy and reflectance spectroscopy (Stuart, 2004). Transmission spectroscopy directs the infrared radiation pass through a sample and utilizes the infrared absorption spectrum to detect and identify chemicals in the sample. Reflectance spectroscopy indirectly analyzes the infrared absorption of chemicals through the measurement of reflected infrared radiation (Khoshhesab, 2012). Photoacoustic infrared spectroscopy is a different technique and utilizes the photoacoustic effect generated by infrared absorption to detect chemicals (Michaelian, 2010; Tam, 1986). In general, transmission spectroscopy is the most widely used method in the design of infrared spectroscopy instruments.

2.4.2.1 Transmission spectroscopy

Dispersive spectrometers and Fourier transform infrared (FTIR) spectrometers are commonly used instruments for dispersive spectroscopy. Traditional dispersive spectrometers use diffraction gratings to disperse the infrared radiation to a wide spectral range (Schrader, 1994); then the infrared radiation at individual wavelength is separately detected. The design of dispersive spectrometers decreases the radiation energy in each wavelength while increases the measurement time. Diffraction gratings also need frequent calibration to ensure accuracy (Thermo Nicolet Corporation, 2002).

Fourier transform infrared (FTIR) spectrometers are more advanced and accurate than dispersive spectrometers (Saptari, 2003). FTIR spectrometers utilize a Michelson interferometer instead of the diffraction gratings in dispersive spectrometers to generate the dispersed wavelengths. The obtained interference pattern, called as interferogram, is calculated by a Fourier transform algorithm to obtain infrared spectra (Stuart, 2004). FTIR spectrometers are the most prevailing instruments in infrared spectrum analysis as they had fast measurement speed, good spectral resolution and high signal-to-noise ratio (Bacsik et al., 2004).

Non-dispersive infrared (NDIR) sensors are designed to measure the infrared absorption of a sample (primarily gas) at certain spectral ranges (Hodgkinson and Tatam, 2013). The basic components of a NDIR sensor include a broadband infrared source, a sample cell, and an infrared detector (Silver and Chen, 2006). The NDIR sensors measure the quantity of infrared absorption from sample to determine the sample's concentration according to the Beer-Lambert law. The application of broadband IR sources often requires a narrowband infrared filter to improve sensor selectivity to certain chemicals (Dakin et al., 2003; Silver and Chen, 2006).

Tunable diode laser spectroscopy (TDLS) sensors exclusively utilize lasers as the infrared sources (Schiff et al., 1994; Werle, 1998). TDLS sensors are similar to NDIR sensors since both sensors

utilize the attenuation of infrared radiation to measure sample concentration. The narrow bandwidth characteristics of the laser ensure the high selectivity of TDLS sensors, especially for measurement of single component in complex chemicals (Schiff et al., 1994). The spatial coherence of lasers, resulting in strong directionality, allows for long and/or multipass optical pathlength design; thus greatly improves the sensors' sensitivity on trace amount gases (Werle et al., 2002). TDLS sensors are mostly used in gas measurement at atmosphere pressure or vacuum condition when the width of infrared absorption lines is not dramatically increased by high pressure (Werle et al., 2002).

2.4.2.2 Reflectance spectroscopy

Reflectance spectroscopy includes internal reflectance spectroscopy and external reflectance spectroscopy (Khoshhesab, 2012; Stuart, 2004). External reflectance spectroscopy can be further divided to specular reflectance spectroscopy and diffuse reflectance spectroscopy (Stuart, 2004). The reflectance spectroscopy emerges to study the chemicals that are not suitable for being analyzed by transmittance spectroscopy, such as solids and liquids (Khoshhesab, 2012).

Internal reflectance spectroscopy is also named as attenuated total reflection (ATR) spectroscopy (Khoshhesab, 2012). ATR spectroscopy measures evanescent waves generated by total reflectance between a sample and a reflection medium (Fahrenfort, 1961; Khoshhesab, 2012). The reflection medium is infrared transparent and has a higher reflection index than that of the sample to generate the total reflectance. The evanescent waves penetrate through the sample and reflect back to the medium; therefore, the infrared absorption of the sample can be measured through the intensity of the reflected radiation (Fahrenfort, 1961; Khoshhesab, 2012). ATR spectroscopy is most commonly used along with FTIR spectrometers to investigate the infrared absorption spectra of surface layer of materials, such as coatings or thin films (Khoshhesab, 2012; Mirabella, 1998).

External reflectance spectroscopy measures specular reflectance and diffuse reflectance (Khoshhesab, 2012). Specular reflectance occurs when the angle of incidence and the angle of reflectance are equal. The intensity of the reflected radiation is determined by the angle of incidence and the sample's properties: refractive index, surface roughness, and absorption coefficient (Khoshhesab, 2012). Infrared absorption coefficient and spectrum can be calculated from the specular reflection spectrum by the Kramers-Kronig equation (Khoshhesab, 2012; Roessler, 1965). Therefore, specular spectroscopy is suitable to measure the surface properties of materials (Khoshhesab, 2012).

Diffuse spectroscopy is commonly used to measure materials in particle forms, such as soil or minerals (Torrent and Barrón, 2008). Diffuse spectroscopy is usually integrated into a FTIR spectrometer; therefore, it is also termed as diffuse reflectance infrared Fourier transform spectroscopy (DRIFTS) (Stuart, 2004). The diffuse spectroscopy measures the reflected radiation by diffuse scattering. An integrating sphere is usually used in DRIFTS to collect the reflected radiation at every direction (Torrent and Barrón, 2008). The reflectance spectrum can be processed by the Kubelka-Munk theory to a spectrum analogous to the absorption spectrum (Khoshhesab, 2012; Torrent and Barrón, 2008).

2.4.2.3 Photoacoustic infrared spectroscopy

Photoacoustic infrared spectroscopy is designed based on the photoacoustic effect (Tam, 1986). The design of the photoacoustic sensors is focused on generating and detecting acoustic waves. The acoustic waves are generated by selective infrared absorption of a sample or a medium next to a sample. Modulated infrared lasers are commonly used in the photoacoustic sensors while applications of LED infrared radiation sources were also reported (Kuusela et al., 2009). The sample, mostly in gas form, is sealed in a sample cell with microphone, piezoelectric transducer, or capacitor transducer as acoustic wave detectors (Tam, 1986). The applications of cantilever

microphones, quartz-enhanced piezoelectric detectors, and resonance sample cells had greatly improve the sensitivity of photoacoustic sensors (Bozóki et al., 2011).

2.4.3 Mid-infrared radiation source and photodetectors

Mid-infrared (MIR, 2.5 μm-25 μm) wavelength range is preferred in gas detection as it includes the fundamental absorption bands of most gases. The infrared absorption intensity at fundamental absorption bands is one magnitude larger than that at overtone absorption bands in the near-infrared wavelength range (Williams and Norris, 2001). The strong infrared absorption is favorable in gas detection to achieve lower detection limit, stronger response and compact design. Mid-infrared radiation sources include tungsten-halogen lamps, narrowband infrared emitters, mid-infrared lasers, and light emitting diodes. Mid-infrared photodetectors include commercially available lead selenide (PbSe), indium antimonide (InSb), and mercury cadmium telluride (MCT) photodetectors.

2.4.3.1 Mid-infrared radiation sources

Tungsten-halogen lamps are traditional infrared radiation sources for near-infrared spectroscopy (Hodgkinson and Tatam, 2013). The tungsten filament in the lamp bulb is heated near 3000K to emit light (MacIsaac et al., 1999). Halogen gases are added to reduce the vaporization of tungsten. Tungsten-halogen lamps can be used as MIR radiation sources, but most of their radiation resides in visible and near-infrared wavelength range (MacIsaac et al., 1999; Williams and Norris, 2001). These lamps cannot be modulated at a high frequency directly (Hodgkinson and Tatam, 2013); therefore, optical choppers are usually required to achieve a high modulation frequency.

Micro-machined narrowband thermal emitters are novel mid-infrared radiation sources (Chan et al., 2006; Lin et al., 2003). These emitters are excited to surface plasma state to emit narrowband mid-infrared radiations (Chan et al., 2006). The surface plasma state is generated by engraving

the emitter's surface with holes, cavities, or gratings (Miyazaki et al., 2008; Pralle et al., 2002; Tsai et al., 2006). The engraved patterns are within several micrometers or nanometers and directly affect the emission spectrum of the emitters (Chan et al., 2006; Miyazaki et al., 2008). The emission spectrum was reported to have a peak in far infrared wavelength range, around 7 μm wavelength (Inoue et al., 2014; Miyazaki et al., 2008). The micro-machined thermal emitters have significant advantages over the tungsten-halogen lamps as the emission is more efficiently concentrated in a narrower wavelength range (Chan et al., 2006). Therefore, they can be used to design NDIR sensors without narrowband infrared filters (Inoue et al., 2014; Miyazaki et al., 2014). However, these emitters still need to operate at a very high temperature and are not designed to be modulated at a high frequency (Inoue et al., 2014).

Mid-infrared lasers include semiconductor lasers, doped insulator lasers, and quantum cascade lasers (Werle et al., 2002). Mid-infrared lasers can also be generated from near-infrared lasers by difference frequency generation (DFG) method (Tittel et al., 2003). However, the output power from a DFG laser is inherently low and the highest emission is limited at up to 5 μm wavelength (Kosterev and Tittel, 2002).

Semi-conductor lasers utilize the transition between conduction band and valence band in semiconductor materials to generate emission (P. Werle et al., 2002). The band gaps of the semiconductor materials determine the laser's emission spectrum (Capasso et al., 1999). Therefore, most semiconductor lasers have an emission spectrum in the near-infrared wavelength (less than 2.5 μm) (Werle et al., 2002). Certain semiconductor lasers fabricated with specific materials have emission spectra in the mid-infrared wavelength range at lower operation temperature, such as the antimonide lasers fabricated with III-V compounds and the lead-salt lasers fabricated with IV-VI semiconducting materials (Werle et al., 2002). The antimonide lasers could generate emission in 3-4 μm wavelength range when it was cooled with liquid nitrogen (P. Werle and Popov, 1999). Lead-salt lasers were reported with emissions in 3-30 μm wavelength

range (Tittel et al., 2003); however, they need to be operated under cryogenic cooling conditions (Tacke, 2003).

Doped insulator lasers emit infrared radiation in near-infrared and mid-infrared wavelength range (Godard, 2007; Tittel et al., 2003). They were fabricated of semiconductor materials (II-VI compounds) doped with metal ion, such as Cr^{2+} and Fe^{2+} (Godard, 2007). The Cr^{2+} doped lasers have an emission in 3-4 μm wavelength range while the Fe^{2+} doped laser can reach to 4-5 μm wavelength under room temperature. However, their emission spectrum are much wider than that of other lasers (Godard, 2007).

The most widely used quantum cascade (QC) lasers are based on the intersubband transitions between quantized states in a multiple-quantum-well heterostructure to emit laser (Gmachl et al., 2001; Kosterev and Tittel, 2002). Electrons cascade down through these states and generate the laser emission (Capasso et al., 1999). The wavelength of the emission is determined by the size of quantum wells instead of the material band gaps; therefore, it is possible to design lasers with specific emission wavelength by adjusting the size of quantum wells (Capasso et al., 1999). The QC lasers can have emission spectrum up to terahertz range with a miniwatt level of output power (Gmachl et al., 2001; Williams et al., 2006). They can also be operated at room temperature in pulsed mode with an emission up to 16 μm wavelength (Gmachl et al., 2001). The distributed feedback QC lasers (QC-DFB laser) are particular useful for trace gas measurements; because of their advantages of single-frequency emission spectrum, room temperature operation, and high output power (Godard, 2007; Kosterev and Tittel, 2002). TDLS sensors with QC-DFB lasers provide a sensitivity of several parts-per-billion by volume (ppbv) on gases (Kosterev and Tittel, 2002).

Mid-infrared light emitting diodes (MIR LEDs) can provide infrared emission up to 6μm wavelength (Alexandrov et al., 2002). The MIR LEDs have many advantages over lasers or

tungsten-halogen lamps, such as narrowband emission spectrum, room-temperature operation, high modulation frequency, low power consumption, and low cost (Fanchenko et al., 2016; Hodgkinson and Tatam, 2013; Sotnikova et al., 2010). However, the biggest disadvantage of MIR LEDs is their low output power of several hundred milliwatt (mW) in pulsed mode or several mW in continuous wave mode (Abell et al., 2014; Fanchenko et al., 2016). Meanwhile, the emission spectrum of MIR LEDs is affected by their temperature (Smith et al., 2002). Therefore, it is essential to precisely control their temperature during operation (Hodgkinson and Tatam, 2013).

2.4.3.2 Mid-infrared photodetectors

Commercially available mid-infrared photodetectors include PbSe, InSb, and MCT photodetectors, which are named after their fabrication materials (Downs and Vandervelde, 2013; Rogalski, 2012). They are most sensitive to infrared radiations in 3-5 μm, 2-6 μm, and 2-14 μm wavelength range, respectively (Downs and Vandervelde, 2013). PbSe, InSb and MCT photodetectors are categorized as intrinsic quantum photodetectors, since their intrinsic properties altered by excitations from received photons (Potter and Eisenman, 1962). Extrinsic quantum photodetectors include several type of Si and Ge based photodetectors, whose IR sensitivity is generated from the impurities inside the semiconductor (Sclar, 1984). Extrinsic photodetectors are sensitive to infrared radiations in a wide wavelength range (up to several hundred micrometers), but they need to operate at extremely low temperature (Rogalski, 2002). There are some mid-infrared photodetectors under development, such as quantum well (QW) infrared photodetectors and strained layer superlattices (SLS) photodetectors (Downs and Vandervelde, 2013).

PbSe photodetectors are photoconductive detectors, which have a detectable conductance change when they receive infrared radiations (Nudelman, 1962). The spectral response of PbSe

photodetectors is dramatically influenced by its operation temperature (Kaye, 1955). The photodetectors can be sensitive to infrared radiations at around 6 μm wavelength when they are liquid nitrogen cooled (Potter and Eisenman, 1962). PbSe photodetectors are still preferred for their low cost, fast response and room-temperature operation in detection of infrared radiations within 5 μm wavelength (Rogalski, 2012). The primary noise source of PbSe photodetectors is the flicker noise at low frequencies (Emmons et al., 1975); therefore, it is necessary to use high-frequency modulated infrared radiation sources to improve signal-to-noise ratio of PbSe photodetectors.

InSb photodetectors are photovoltaic detectors with p-n junctions, which generate voltaic signal from received infrared radiations (Pagel and Petritz, 1961). InSb photodetectors are commonly used to detect infrared radiations within 6μm wavelength (Downs and Vandervelde, 2013; Emmons et al., 1975). Since the photodetectors operate in photovoltaic mode, the primary noise source is the temperature related thermal noise (Johnson noise) (Pagel and Petritz, 1961). Therefore, InSb photodetectors are usually cooled to extreme low temperature by dry ice or liquid nitrogen to achieve a highest possible signal-to-noise ratio (Emmons et al., 1975; Potter and Eisenman, 1962). The photovoltaic mode makes InSb photodetectors suitable to detect low-frequency modulated infrared radiations (Emmons et al., 1975).

MCT photodetectors are the most popular detectors in mid-infrared applications (Downs and Vandervelde, 2013; Rogalski, 2012). They can be fabricated to detect infrared radiation in a wide wavelength range with an operation temperature from 77K (liquid nitrogen) to room temperature (Rogalski, 2005). MCT photodetectors can be designed as photoconductive or photovoltaic detectors by adjusting the components composition in MCT alloy (Norton, 2002; Rogalski, 2005). MCT photodetectors are the most sensitive photodetectors in 3-5μm wavelength range (Downs and Vandervelde, 2013).

Quantum well (QW) infrared photodetectors are designed to replace the MCT photodetectors in mid-infrared detection (Rogalski, 2011). They detect infrared radiation with a series of tiny quantum wells to form discretized quantum energy level in these wells. Therefore, QW infrared photodetectors can be fabricated with common III-V semiconductor materials instead of the MCT alloy (Downs and Vandervelde, 2013). However, QW infrared photodetectors are only sensitive to infrared radiation in very narrow spectral range (Rogalski, 2011) and they cannot detect normally incident infrared radiation (Karim and Andersson, 2013).

Strained layer superlattices (SLS) photodetectors are fabricated with lattice matched layers of different semiconductors (Rogalski, 2011). The quantum wells are formed within the lattice boundary between different materials (Karim and Andersson, 2013). SLS photodetectors can be made with well researched III-V semiconductors with a performance similar to MCT photodetectors in 3-18μm wavelength range (Downs and Vandervelde, 2013; Razeghi et al., 2002; Rogalski, 2012).

2.4.4 Data processing methods for infrared sensors

The Beer-Lambert law is the basis to determine a sample concentration in infrared transmittance spectroscopy. It stated that infrared absorption of a sample is determined by the attenuation coefficient of the sample at a specific wavelength α (cm^{-1}) and the optical pathlength L (cm) as in Equation 2.18 (Hodgkinson and Tatam, 2013):

$$I = I_o e^{-\alpha L} \tag{2.18}$$

in which I is the intensity (watt) of infrared radiation transmitted by the sample; I_o is the intensity (watt) of the infrared emission from the infrared radiation source. The attenuation coefficient of the sample α is the product of the molar attenuation coefficient ε ($L \cdot cm^{-1} mol^{-1}$) and the concentration of the sample C ($mol \cdot L^{-1}$): $\alpha = \varepsilon C$.

When a sample's concentration is very low, the ratio between the infrared emission intensity I_o and absorbed radiation intensity $\Delta I = I_o - I$ can be approximated to a linear function of sample concentration C as Equation 2.19:

$$\frac{\Delta I}{I_o} = \frac{I_o - I}{I_o} = 1 - e^{-\varepsilon LC} \approx \varepsilon LC \tag{2.19}$$

The infrared transmittance T and absorbance A (both dimensionless) were defined as (Stuart, 2004; Swinehart, 1962):

$$T = \frac{I}{I_o} = e^{-\varepsilon LC} = 10^{-A} \tag{2.20}$$

Therefore, the infrared absorbance A could be obtained from Equation 2.19 and Equation 2.20 as:

$$A = \frac{\varepsilon LC}{ln10} \approx \frac{1}{ln10} \cdot \frac{\Delta I}{I_o} \tag{2.21}$$

For gas measurements, the infrared absorbance is actually related to the number of molecules in the gas cell. Therefore, the ideal gas law is required to calculate the actual gas concentration (Hodgkinson and Tatam, 2013; Stuart, 2004). Pressure and temperature of the gas sample need to be recorded to convert the number of molecules to gas concentration.

Calibration of a transmission type infrared sensor can be performed by measuring samples with known concentrations (Schiff et al., 1994; Stuart, 2004). The sensor outputs and the sample concentrations generate a calibration equation for analyzing unknown concentration samples. Based on the approximation in Equation 2.21, the calibration equation for an IR sensor is linear when the sample concentration is low. Therefore, it can be approximated by a linear model with the least square method as Equation 2.22 (Williams and Norris, 2001):

$$y = mx + b \tag{2.22}$$

in which y is the sensor response (the infrared absorbance, dimensionless) and x is the sample concentration (mol·L^{-1}). The slope of the linear equation m is often called as the sensitivity (1/ mol·L^{-1}). The intercept b (dimensionless) represents the sensor's background response when no sample is presented.

Sensitivity is defined as the sensor's response over the concentration by the International Union of Pure and Applied Chemistry (IUPAC) (Long and Winefordner, 1983). Therefore, the slope m is usually used as the sensitivity. However, this definition requires two assumption: 1) there is a liner relationship between the sample concentration and the sensor's response; 2) the concentration values are correct (Skoog et al., 2017).

The limit of detection DL (mol·L^{-1}) is defined as the minimal concentration that can be detected with confidence (Long and Winefordner, 1983; Skoog et al., 2017). It can be calculated from the measurements of the background response of the sensor:

$$DL = \frac{KS_{bl}}{m} \tag{2.23}$$

where m is the sensitivity and S_{bl} is the standard deviation of background response measurement. K is a constant and usually set at $K = 3$ (Kaiser, 1978; Mocak et al., 1997). The measurement of background response of sensor gives the mean value $\bar{X}_{bl}$ and the standard deviation S_{bl} as:

$$\bar{X}_{bl} = \frac{\sum_{j=1}^{n_b} X_{blj}}{n_b} \tag{2.24}$$

$$S_{bl} = \sqrt{\frac{\sum_{j=1}^{n_b} \left(X_{blj} - \bar{X}_{bl}\right)^2}{n_b - 1}} \tag{2.25}$$

in which n_b is the number of measurement and X_{blj} represents the jth measurement on blank response.

2.5 Summary

Reviews of related literatures suggested that the mid-infrared spectroscopy method might be the best method to measure dissolved CO concentration in the syngas fermentation. However, the infrared absorption spectra of syngas were required to verify the conclusion on the selectivity of mid-infrared spectroscopy method. It was also necessary to evaluate the infrared absorption spectrum of liquid water to determine the possibility of a direct, dissolved CO infrared measurement system. Preliminary experiments would be performed to answer these questions. The final design of the mid-infrared dissolved CO measurement system would be determined based on the results from the preliminary experiments.

The principle of the infrared detection had ruled out the possibility of detecting H_2 with infrared method. Therefore, a standalone dissolved H_2 sensor was purchased and integrated with the dissolved CO measurement system to establish an integrated dissolved CO/H_2 measurement system.

CHAPTER III

PRELIMINARY EXPERIMENTS FOR DISSOLVED CO INFRARED MEASUREMENT

Abstract

An infrared CO detection method was selected as the measurement principle for the syngas fermentation process based on the previous literature reviews. However, the feasibility of infrared CO detection in syngas fermentation was still unknown. Preliminary experiments were designed to verify the infrared absorption properties of major chemicals in syngas fermentation process. The syngas samples, in gas phase and dissolved phase, were measured with a Fourier transform infrared (FTIR) spectrometer to obtain their infrared absorption spectra. A further review on the infrared absorption spectra database was also performed. The results from the FTIR spectrometer and the database showed that CO had strong spectral response in wavelength range of 4.42 μm to 5 μm. The infrared method could be used to detect CO in syngas fermentation environment. It was also found that other chemicals in the fermentation medium did not have strong spectral responses in the CO wavelength range. However, the infrared measurement of dissolved CO was challenging because of the strong water interference.

Key Words: Infrared absorption spectra; FTIR spectroscopy, CO infrared detection

3.1 Introduction

Syngas fermentation is a promising solution to produce biofuels, such as ethanol and butanol, by extremely anaerobic microorganisms with CO (carbon monoxide) and H_2 (hydrogen) in the syngas (Wilkins and Atiyeh, 2011). Measurement and control of dissolved CO and H_2 concentrations in the syngas fermentation medium are of great importance to improve the products yield and specificity (Atiyeh et al., 2017).

Currently, there were some commercial dissolved H_2 sensors available on the market. However, based on our knowledge, there was no dedicated dissolved CO sensor suitable for the syngas fermentation application. A dissolved CO sensor needs to be designed for this specific application. Previous reviews on the CO detection methods suggested that infrared CO detection method should be the best choice. Infrared method is not affected by H_2 and require no oxygen in measurement (Stuart, 2004). Its measurement is also rapid, sensitive, and reversible (Hodgkinson and Tatam, 2013). However, the infrared absorption bands for CO detection as well as the influence of water on infrared detection need to be determined before the design of the infrared dissolved CO sensor.

Infrared CO sensors usually utilize infrared absorption bands of CO at 4.6 μm, 2.3 μm, and 1.57 μm in wavelength (Li et al., 2015). It was also known that the CO infrared absorption at 4.6 μm was the strongest. The concentration of CO was determined based on Beer-Lambert law, which correlated the infrared absorption strength to the CO's concentration (McDonagh et al., 2008). Therefore, the measurement of CO concentration would be inaccurate if other chemicals had infrared absorption spectra overlapped with CO. The infrared absorption bands for CO detection should be selected at a wavelength range with the least interference from those of other chemicals. Hence, it was necessary to examine the infrared absorption of major chemicals in syngas fermentation.

The influence of water on infrared CO detection includes two aspects: the water in vapor form and in liquid form. Water in vapor form has three infrared detection windows in near and mid infrared spectral range, allocated around 4 μm, 2.13 μm, and 1.59 μm in wavelength (Shine et al., 2016). Water in liquid form has strong and broad infrared absorption bands between 2.5 μm and 10 μm in wavelength (Downing and Williams, 1975). The influence from water vapor can be ignored by using desiccant to remove water vapor in the sample. However, the strong infrared absorption from liquid water cannot be circumvented in the design of infrared dissolved CO sensor.

The available reports on infrared dissolved gas measurement method showed that direct measurement of dissolved gases, such CO_2 (Schaden et al., 2004) and hydrocarbons (Buerck et al., 2001; Mizaikoff, 1999), was possible. More conventional indirect infrared measurement methods were reported with the aid of gas extraction apparatuses (Boulart et al., 2010; Fietzek et al., 2014). Therefore, the preliminary experiments were designed to examine the infrared absorption spectra (primary in the mid-infrared range) of syngas in gas phase and in aqueous solution. The experiment results would be further used to determine the appropriate infrared absorption band(s) for CO detection and to decide the design of the infrared dissolved CO sensor. The specific objectives of the preliminary experiments included:

1) To examine the infrared spectra of syngas components and other chemicals in the fermentation medium;

2) To determine the appropriate infrared absorption band(s) for CO measurement.

3.2 Material and Methods

3.2.1 Gas phase syngas measurement experiment setup

The gas phase syngas experiment was designed to measure the infrared absorption spectra of the following three types of gas samples:

1) Pure gases: CO, CO_2 (carbon dioxide), H_2, and N_2 (nitrogen);
2) CO/N_2 mixtures: CO/N_2 ratio from 0.3%/99.7% to 80%/20%;
3) Syngas samples: Type I: 40% CO, 30% CO_2, and 30% H_2; type II: 20% CO, 15% CO_2, 5% H_2, and 60% N_2; Producer gas: 14.22% CO, 16.9% CO_2, 11.54% H_2, 53.98% N_2, 2.74% CH_4 (methane), 0.07% C_2H_2 (acetylene), 0.39% C_2H_4 (ethylene), and 0.15% C_2H_6 (ethane).

The gas samples were prepared in a gas station and stored in 250 mL serum bottles at 20 psig pressure. Three replicates were prepared for each type of gas sample. The accurate gas composition of each sample was determined by gas chromatography (GC) (Agilent 6890 N GC, Agilent Technologies, Wilmington, DE, USA) before the experiment. A gas tight syringe was used to take a portion of the gas sample from the serum bottle and deliver it to the GC.

A flow-through, transmission type gas cell (0024-117, Thermo Spectra-Tech, Madison, WI, USA) was used for infrared measurements. The cell has an optical pathlength of 100 mm and mounted with uncoated CaF_2 windows. A gas delivery system (Fig.3-1) was used to load the gas samples to the gas cell. The gas cell was vacuumed to -25 inHg with a manual vacuum pump before loading each sample. After the serum bottle was connected with the gas cell, the Cell Inlet Valve was open firstly to load the gas cell. Then the Cell Outlet Valve was open to purge the gas cell with the desired gas sample before the measurements. The Cell Inlet Valve and the Cell Outlet Valve were closed when the pressure inside the serum bottle was around 0.3 psig. The loaded gas cell was placed into the sample chamber of a Fourier transform infrared (FTIR)

spectrometer (Nicolet 6700, Thermo Scientific, Madison, WI, USA) for infrared absorption spectra measurement. The FTIR spectrometer was thoroughly purged with N_2 before each measurement.

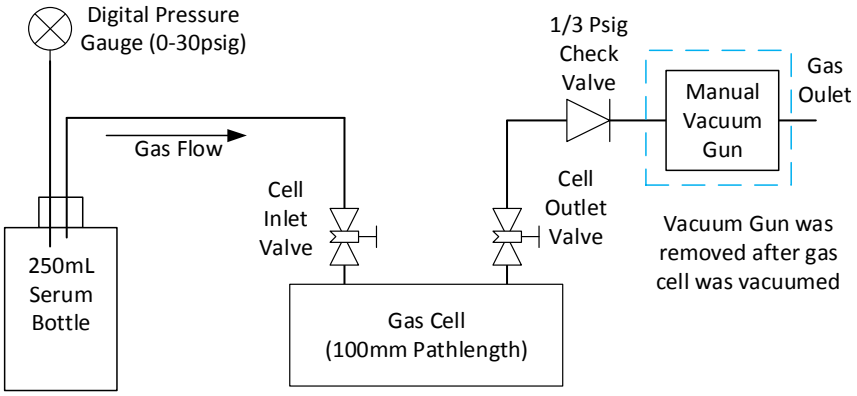

Fig.3-1. Illustration of experimental setup for loading/purging gas cell with desired gas sample

The FTIR spectrometer was set to measure infrared absorption spectra between 1,110 cm^{-1} and 4,000 cm^{-1} in wavenumber (2.5 μm to 9.009 μm in wavelength) at a resolution of 1 cm^{-1}. Each sample was scanned for 32 times to perform average filtering for better measurement quality. The background spectrum was obtained by measuring the infrared absorption spectra of pure N_2 in the gas cell, which would be used to generate infrared absorption spectra of gas samples. The obtained infrared absorption spectra were analyzed by OMNIC® (version 8.0, Thermo Scientific, Madison, WI, USA) software provided along with the FTIR spectrometer. Infrared absorption spectral libraries in the OMNIC software were used to compare the obtained infrared absorption spectra and to identify chemicals in the obtained spectra.

An analysis was performed on the obtained infrared absorption spectra of CO/N_2 mixtures to determine the relationship between CO concentrations and the infrared absorbance. The CO concentration in these samples was prepared to be evenly distributed between 0 to 400 mg/L

under the experimental condition. The exact CO concentrations in the samples were calculated using the ideal gas law from the sample pressure in the gas cell, ambient pressure, room temperature, and percentage of CO in the gas sample. The absorbance data in the infrared absorption spectra were further analyzed by a program (Appendix II) written in MATLAB® (Release 2013b, The MathWorks, Inc., Natick, MA, USA) to obtain the absorbance data at a single wavelength and the accumulated absorbance data in a specific wavelength range. The absorbance data at a single wavelength was used to simulate the measurement of a tunable diode laser spectroscopy (TDLS) sensor, which measured the infrared absorption at certain absorption wavelength. The accumulated absorbance data in a specific wavelength range was used to simulate the response of a non-dispersive infrared (NDIR) sensor, which measured the infrared absorption in a broad spectral range. The single wavelength was selected 4.63 μm (2161 cm^{-1} in wavenumber) while the wavelength rage was selected as 4.46 μm to 4.95 μm (2020 cm^{-1} to 2240 cm^{-1} in wavenumber). These two values were selected where the CO infrared absorption was the strongest and had the least interference from other gases.

The CO concentration C (mol/L) in the CO/N_2 mixtures was calculated based on ideal gas law:

$$C_G = \frac{n}{V} = \frac{P_{CO}}{RT} \tag{3.1}$$

where P_{CO} was the partial pressure of CO in the gas cell (kPa). R was the gas constant ($8.3144 L \cdot kPa \cdot K^{-1} \cdot mol^{-1}$) and T was the temperature of gas sample (K). The partial pressure P_{CO} was calculated from the molar percentage, M, of the CO in the gas sample and the absolute pressure P_{abs} (kPa) in the gas cell: $P_{CO} = MP_{abs}$.

3.2.2 Dissolved syngas measurement experiment setup

The dissolved syngas measurement experiment was designed to measure the infrared absorption spectra of following two liquid samples:

1) Distilled water with pure N_2;
2) Distilled water with CO/N_2 gas mixture (80%C O, 20% N_2).

The 250 mL serum bottles were used to prepare the liquid samples. The bottles were filled with 100 mL of distilled water, then the water and the headspace of the bottles were purged with the desired gas samples for at least five minutes. After the purge process, the headspace of the bottle was pressurized to 20 psig with the desired gases. The serum bottles were shaken and stored for at least 24 hours before the measurements. Three replicates were prepared for each type of the liquid samples. The headspace gas composition in each replicate was measured with a GC before the experiment.

A flow-through, transmittance type liquid cell (DLC-S25, Harrick Scientific Products Inc., Pleasantville, NY, USA) was used in the experiment. The liquid cell had an optical pathlength of 100 μm and was mounted with uncoated zinc selenide (ZnSe) windows. A gas-tight syringe was used to load the liquid sample from a serum bottle to the liquid cell without dissolved gases depressurization.

The FTIR spectrometer was set to use the same configuration as the previous gas phase experiment, which measured the infrared absorption spectra between 1,110 cm^{-1} and 4,000 cm^{-1} in wavenumber at a resolution of 1 cm^{-1}. Each liquid sample was scanned for 32 times as well. However, the output power of the spectrometer was adjusted to the "Turbo" mode to maximize the output of the infrared source in the spectrometer. The background spectrum used to compare the liquid sample infrared absorption was collected with gas-free distilled water loaded in the liquid cell. The OMNIC software was used to process the obtained infrared absorption spectra.

A review of the major components in the syngas fermentation medium was also performed by checking the OMNIC software infrared spectral libraries. The chemicals in syngas fermentation medium included two groups: nutrients for microorganisms such as vitamins and minerals;

fermentation products, including alcohols and organic acids. The chemicals with higher than 1g/L concentration in the medium were investigated as they may have significant influence on the infrared absorption. The examined nutrients included glucose, MES (4-morpholineethanesulfonic acid) , and cysteine. The examined products included ethanol, butanol, hexanol, acetic acid, butyric acid, and hexanoic acid.

3.3 Results and Discussions

3.3.1 Gas phase syngas measurement experiment

1) Determination of the CO infrared detection band(s)

The obtained infrared absorption spectra of the gas sample were shown in Fig.3-2. The spectra of pure gases, CO/N_2 mixtures, and syngas were demonstrated in the same wavelength scale. The obtained infrared absorption spectra showed that the CO infrared absorption bands located between 2000 cm^{-1} and 2260 cm^{-1} position (4.42 μm to 5 μm in wavelength) were free of interference from CO_2, CH_4, C_2H_2, C_2H_4, and C_2H_6 gases in the syngas.

H_2 and N_2 in the syngas were known to be transparent to infrared radiation because of their symmetric diatomic molecular structure, which had no dipole moment change in molecular vibration (Stuart, 2004). A further investigation of the infrared absorption spectra of CO, CO_2, and the minor components (CH_4 and hydrocarbons) were performed by checking the infrared absorption spectral library of OMNIC software (Fig.3-3). The obtained infrared absorption spectra from the gas phase FTIR experiment was similar to the high-resolution infrared spectra in the library. Therefore, it was concluded that the wavelength range between 4.4 μm and 5 μm was the best choice for infrared CO detection in syngas fermentation.

2) Infrared absorption spectra analysis

The results of the infrared absorption spectra analysis on the CO/N_2 mixture samples were shown in Fig.3-4. A linear regression analysis was performed on the infrared absorbance data and the CO concentrations in the mixture samples. The linear regression model was used in the analysis, because the Beer-Lambert law stated that the absorbance A (dimensionless) was proportional to the concentration C ($mg \cdot L^{-1}$) when the infrared attenuation coefficient ε ($m^{-1} \cdot mg^{-1} \cdot L$) and optical pathlength L (m) were fixed.

The result of the regression analysis performed on the absorbance data on single wavelength (4.63 μm, 2161 cm^{-1} in wavenumber) showed that there was a good linear relationship between the prepared CO concentrations and the measured absorbance (Fig.3-4a):

$$y = 0.0030x + 0.2510 \tag{3.2}$$

The coefficient of determination was $R^2 = 0.9724$.

The regression analysis performed on the absorbance data on a wavelength range (4.46 μm to 4.95 μm, 2020 cm^{-1} to 2240 cm^{-1} in wavenumber) had a better fit as it had fewer interference from outliers in the measurement (Fig.3-4b):

$$y = 0.3098x + 13.483 \tag{3.3}$$

The coefficient of determination was $R^2 = 0.9909$.

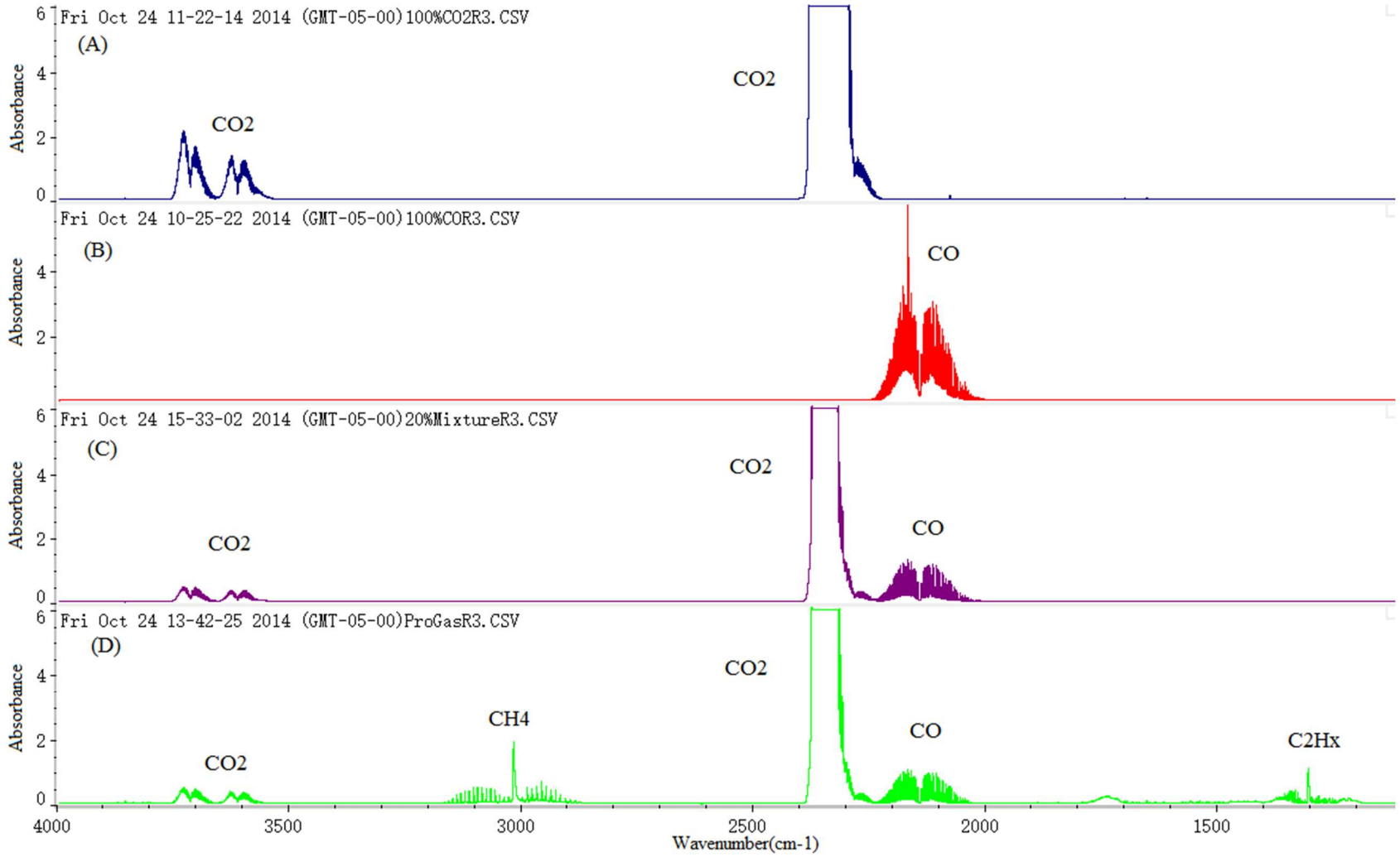

Fig.3-2 Obtained infrared absorption spectra from FTIR measurements: a) 100% CO_2; b) 100% CO; c) syngas type II; d) producer gas.

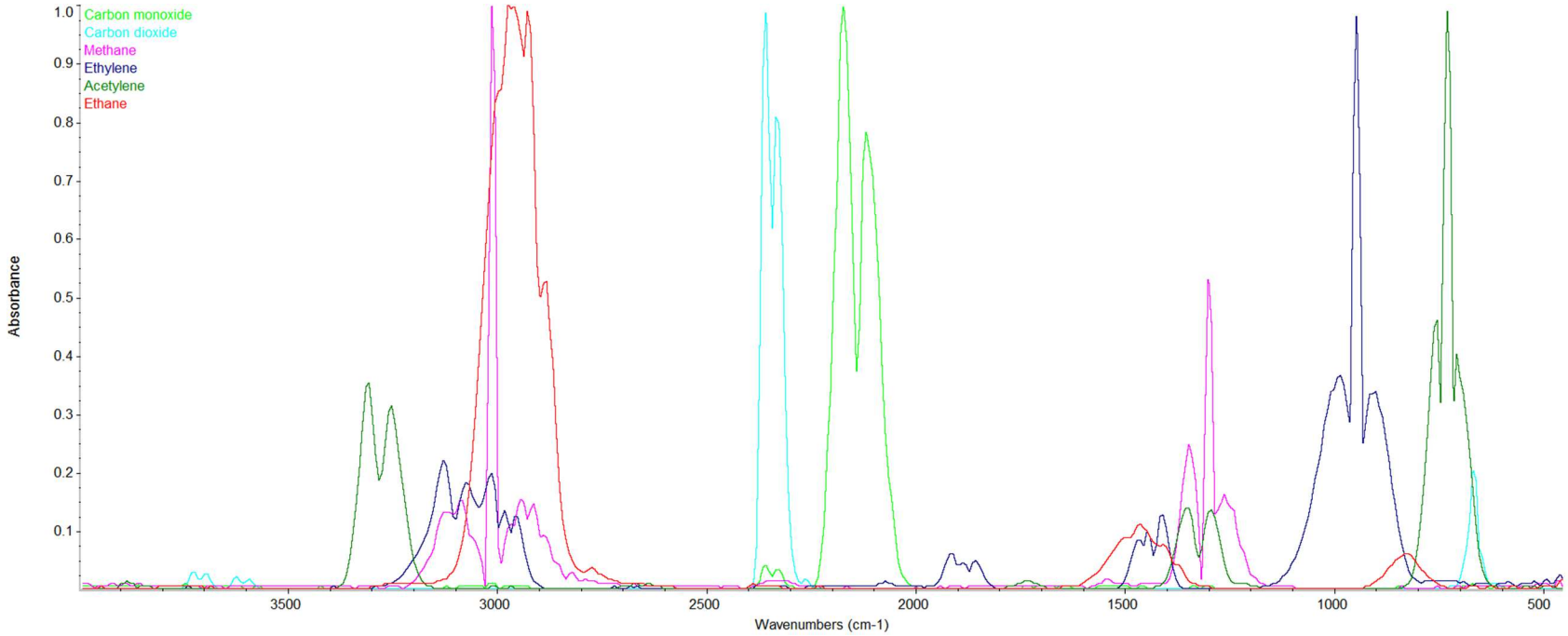

Fig.3-3 Infrared absorption spectra of syngas components obtained from OMNIC® software infrared spectral library. (CO was represented in light green color. Library used: Nicolet Vapor Phase Library)

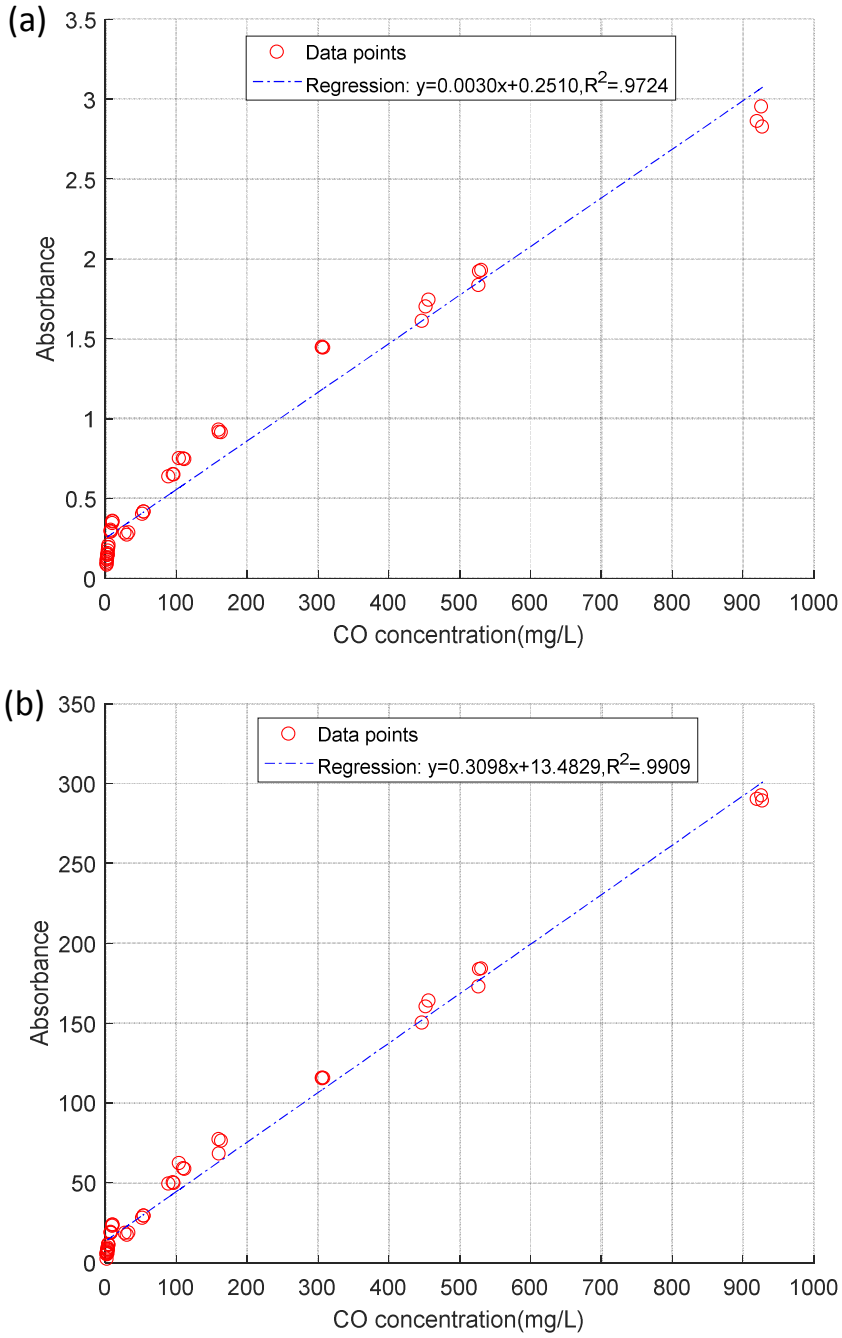

Fig.3-4 Regression analysis between CO concentrations (x-axis) and infrared absorbance data (y-axis): a) absorbance at single wavelength 4.63 μm ($y = 0.0030x + 0.2510, R^2 = 0.9724$); b) accumulated absorbance data within 4.46 μm to 4.95 μm wavelength range ($y = 0.3098x + 13.4829, R^2 = 0.9909$).

3.3.2 Dissolved syngas measurement experiment

The results of the dissolved syngas measurement experiment were not satisfactory. The FT-IR spectrometer could not obtain an obvious infrared absorption spectra even it was set at Turbo mode. The background single beam spectra, whose y-axis represented the normalized strength of the received infrared radiation at the detector of the spectrometer, showed that liquid water had a strong infrared absorption across the entire mid-infrared range (Fig.3-5a). The strength of the received infrared radiation was much higher when the same liquid cell was loaded with gas phase N_2 (Fig.3-5a). The interference fringe in the single beam spectra of the gas phase N_2 sample was generated by the parallel placed liquid cell windows, according to the liquid cell manufacturer's instruction.

The measurement on the liquid sample with dissolved CO/N_2 mixture (80% CO, 20%N_2) showed that there was no obvious infrared absorption exist in the known position of CO infrared absorption band (Fig.3-5b). The zero absorbance at the CO infrared absorption band suggested that it was not possible to detect dissolved CO with the current experiment setup. The abnormal infrared absorbance at 2.70 μm to 3.45 μm (3,700 cm^{-1} to 2,900 cm^{-1} in wavenumber) and 5.88 μm to 6.66 μm (1,700 cm^{-1} to 1,500 cm^{-1} in wavenumber) were generated from the division of sample signal and background signal, which were both zero. The single beam spectra indicated that the majority of the infrared radiation from the infrared source was absorbed by water under the experiment setup. The strong infrared absorption from water, along with the tiny optical pathlength (100 μm) and low solubility of CO in water (27.5 mg/L at 25 °C), leaded to the unsuccessful dissolved syngas measurements.

An analysis was performed to theoretically calculate the infrared absorption of liquid water in the selected spectral range for CO detection (4.17μm to 4.95 μm, 2,020 cm^{-1} to 2,400 cm^{-1} in wavenumber). The infrared attenuation coefficients of liquid water, μ_w (cm^{-1}), at each wavelength

were obtained from data in the literature review (Downing and Williams, 1975). The infrared transmittance T was calculated based on the attenuation coefficient data of liquid water (Eq.3.4). The optical pathlength L_C of the liquid water was assumed as 100 μm (0.01 cm) (Fig.3-6a).

$$T = \frac{I}{I_o} = e^{-\mu_w L_c} \tag{3.4}$$

where I_o was the infrared emission intensity (watt) from the infrared radiation source, I was the transmitted infrared radiation intensity (watt) by the water sample.

In the range of interest, 2,020 cm^{-1} to 2,400 cm^{-1} in wavenumber (4.17 μm to 4.95 μm in wavelength), the calculation showed that less than 5% of the original infrared emission in CO's absorption band (2,020 cm^{-1} to 2,260 cm^{-1}) could pass through the 100 μm thickness cell containing water. This number further decreased when the transmittance of the liquid cell materials (uncoated ZnSe glass) was considered, which was around 70% per window according to its specification. The transmittance dropped to less than 2% in above spectral range when the windows were considered (Fig.3-6b).

The calculation of the transmittance data for liquid water and the liquid cell materials suggested that a very powerful laser should be used to directly measure dissolved CO concentration in the aqueous solution. If the infrared absorbance of CO at 4.63 μm (2,161 cm^{-1}) would be used, the infrared transmittance would be close to 0.9% from the infrared absorption simulation (Fig.3-6b). Therefore, an approximate power of 9 mW would be received by the photodetector from a 1 W infrared radiation source. A less powerful infrared radiation source would have the majority of its output power attenuated by the liquid water; thus, the signal corresponding to the CO infrared absorption would be too small to detect. The high output from a laser could compensate the absorption of the liquid water and generate a detectable CO signal for the photodetector to measure CO concentration in the liquid sample.

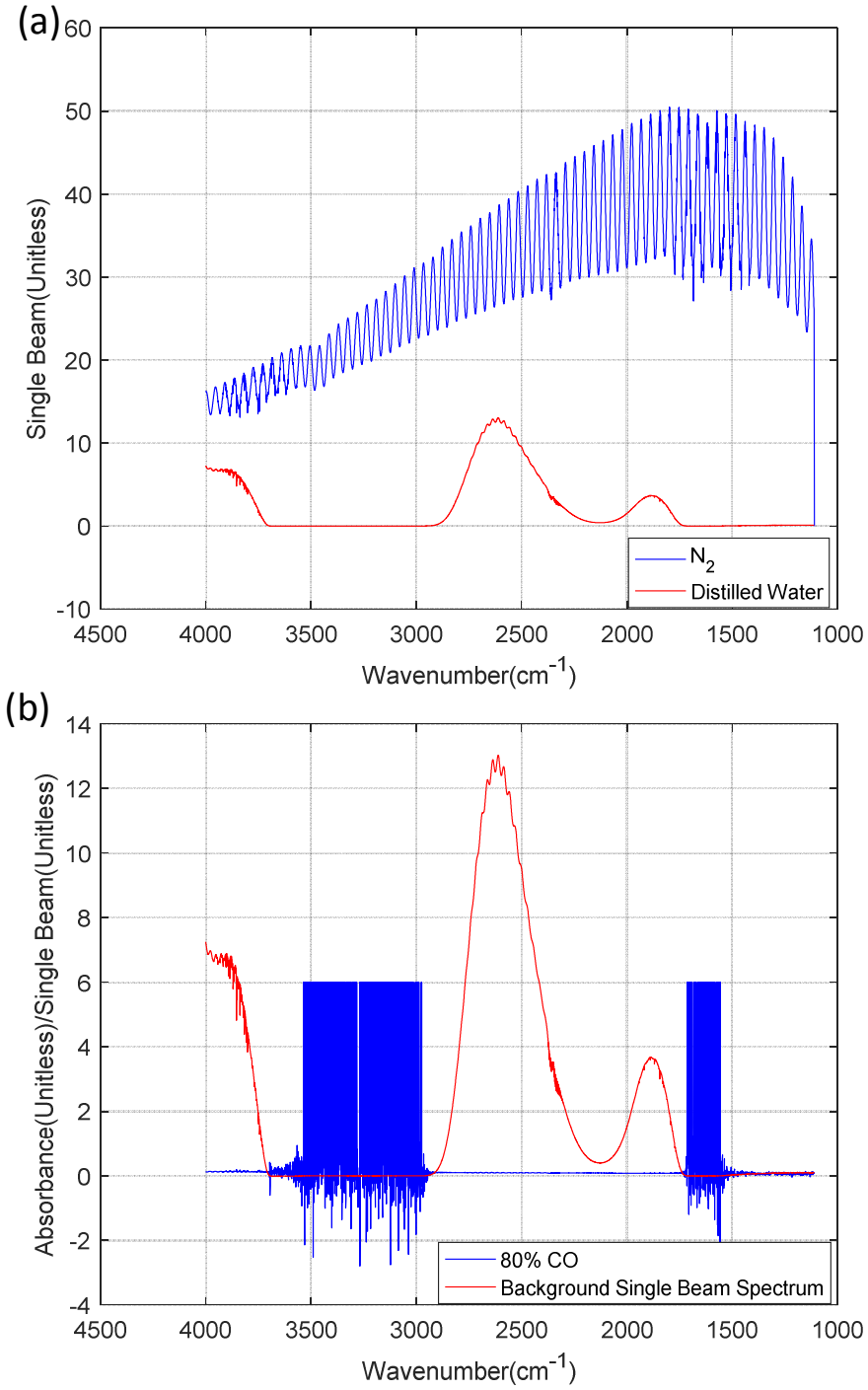

Fig.3-5 Infrared absorption spectra obtained from dissolved syngas experiment: a) background single beam spectra with gas phase N_2 and distilled water as the sample, respectively; b) the measured spectrum of liquid sample with dissolved CO/N_2 mixture (80% CO, balance with N_2) and the background single beam spectrum of liquid water.

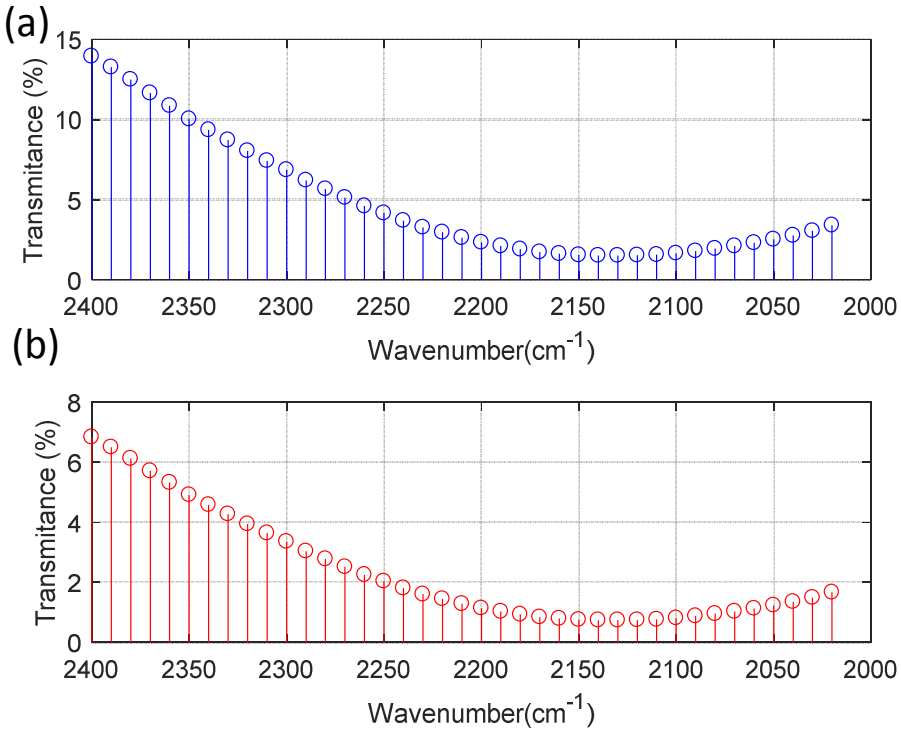

Fig.3-6 Calculated transmittance of liquid water based on coefficient data from Downing and Williams (1975): a) liquid water (100 μm optical pathlength); b) liquid water in liquid cell with two ZnSe windows (100 μm optical pathlength; ZnSe windows' transmittance was 70% per window according to specifications).

The review of the infrared absorption spectra of major chemicals in the fermentation medium showed that there was no strong interference from these chemicals to the selected CO detection bands (Fig.3-7). Therefore, it was possible to design a method to directly measure dissolved CO concentration.

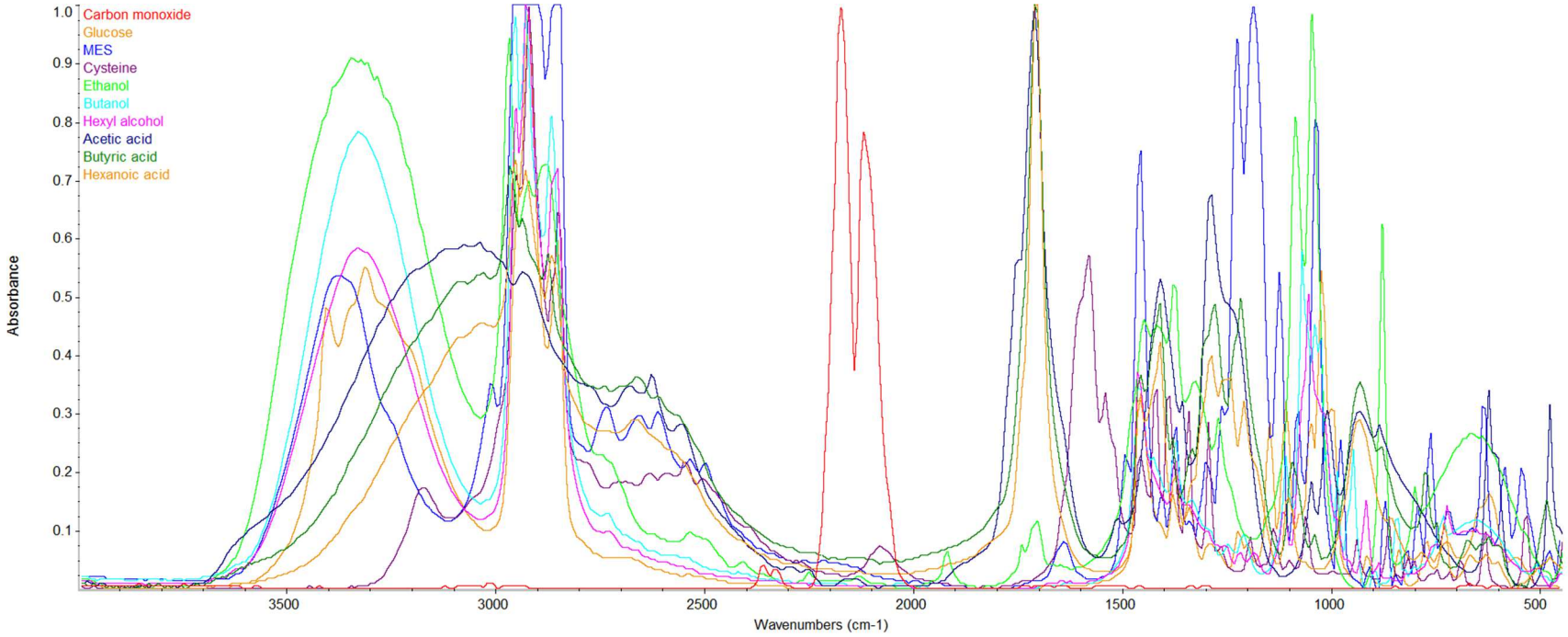

Fig.3-7 Infrared absorption spectra of major chemicals in the obtained from OMNIC software infrared spectral libraries. (CO is represented in red color in the center. Libraries used: Aldrich Collection FT-IR Spectra Edition II, Nicolet Vapor Phase Library.)

3.4 Conclusions

The preliminary experiments obtained several infrared absorption spectra from gas phase and dissolved syngas samples. The analysis of the spectra showed that the mid-infrared spectral range between 4.42 μm to 5 μm (2,000 cm^{-1} and 2,260 cm^{-1} in wavenumber) was the best choice for infrared CO measurement. Other chemicals in syngas and fermentation medium showed nearly no infrared absorption in this spectral range. Also, the infrared spectra obtained from gas samples with different CO concentration showed that it was possible to measure CO concentration in gas phase from its infrared absorbance.

However, the results from dissolved syngas samples demonstrated that it would be challenging to directly measure dissolved CO concentration in aqueous solution. The liquid water had a very strong infrared absorption in the above spectra range for CO measurement, which resulted in the unsuccessful measurements of dissolved syngas samples with the FTIR spectrometer. The calculation of liquid water infrared transmittance data showed that less than 2% of infrared radiation could pass through the liquid cell used in the experiment.

These results suggested two possible methods to measure dissolved CO concentration: 1) directly measure dissolved CO concentration with a powerful infrared radiation source, such as a quantum cascade laser; 2) extract dissolved CO from the liquid sample, then measure the gas phase CO with an infrared sensor and estimate the dissolved CO concentration in the liquid sample.

CHAPTER IV

MID-INFRARED CARBON MONOXIDE SENSOR

Abstract

An infrared CO detection method was selected to indirectly measure dissolved CO concentration in syngas fermentation medium based on a comparison of CO detection methods. The CO's mid-infrared (MIR) absorption bands located between 4.42 μm and 5 μm were used. The developed indirectly dissolved CO measurement system contained an infrared CO sensing unit and a dissolved gas extraction system. A gas phase MIR CO sensor was developed as a sensing unit. The CO sensor used a MIR light emitting diode (LED) as its infrared source, whose emission spectrum was appropriate for the MIR CO measurements in syngas fermentation environment. A highly sensitive, thermoelectrically cooled photodetector was used. The optical pathlength of the sensor was selected as 50 mm. A digital lock-in amplifier was introduced to improve the sensor's sensitivity. The MIR CO sensor was calibrated with standard calibration gases. The validation tests on the sensor demonstrated a mean absolute percentage error of 5.67% and a root-mean-square error of 0.47mg/L in CO measurements.

Key words: Mid-infrared CO sensor, Infrared light emitting diode, Non-dispersive infrared sensor

4.1 Introduction

An infrared carbon monoxide (CO) detection method was selected to measure dissolved CO concentration in syngas fermentation medium based on the results from preliminary experiments and literature reviews. The infrared method had a high CO sensitivity and showed less interference from other chemicals than other CO detection methods in syngas fermentation environment. The CO infrared absorption bands in a spectral range from 4.42 μm to 5 μm (in mid-infrared region) was determined for CO detection after thoroughly examination of the infrared absorption spectra of major chemicals in the syngas fermentation medium.

Two possible approaches were considered for the mid-infrared (MIR) measurement of dissolved CO concentration:

1) Directly measure dissolved CO concentration in the fermentation medium with a modified MIR tunable diode laser spectroscopy (TDLS) sensor;
2) Measure gas phase CO with a MIR CO sensor after the dissolved CO was extracted from fermentation medium.

The first approach was considered as there were several reports of direct infrared measurement of dissolved gases, such CO_2 (Schaden et al., 2004) and hydrocarbons (Buerck et al., 2001; Mizaikoff, 1999) with MIR TDLS sensors. Gas extraction system was not required in this approach, which shortened the response time of the sensor and simplified the overall measurement system. However, the CO sensing part would be complicated and expensive due to the utilization of lasers (Popov et al., 1997; P. Werle et al., 2002). The solubility of CO was extremely low (27.5 mg/L, 1ATM pressure, 25℃, 100% CO, calculated by Henry's law (Sander, 2015)) and its infrared absorption was weaker than CO_2, which made the CO detection more challenging. Also, the water had a broad, strong infrared absorption in the same spectral range, which further attenuated the infrared signals. The results from the preliminary experiments had

showed the difficulties of detecting dissolved CO in the aqueous solution. Therefore, the second approach was selected as the method to measure the dissolved CO concentration. The development of a MIR CO sensor was described in this chapter while the development of dissolved gas extraction system and the integration of the MIR CO sensor were stated in Chapter 5.

The MIR CO sensor was developed to measure the gas phase CO concentration based on the Beer-Lambert law (Swinehart, 1962), which stated that the infrared absorbance of CO was related to the molar CO absorption coefficient, the concentration of CO and the optical pathlength of the sensor. TDLS sensors and non-dispersive infrared (NDIR) sensors were the most common infrared sensors to measure the concentration of gas phase chemicals (Hodgkinson and Tatam, 2013). Distributed feedback quantum cascade (QC-DFB) lasers were usually used as the infrared radiation sources for the TDLS sensors (Werle et al., 2002) while Tungsten-halogen lamps were usually used in NDIR sensors (Williams and Norris, 2001). The structure of NDIR sensors were simpler than the TDLS sensors; however, they required optical choppers to modulate the infrared radiation and the Tungsten-halogen lamps had most of their emissions in the near-infrared (NIR) spectral range (Hodgkinson and Tatam, 2013; MacIsaac et al., 1999). The emission spectra of the infrared radiation sources in NDIR sensors limited their application in MIR applications.

The commercialization of the MIR light emitting diodes (LED) provided alternative choice of infrared sources in NDIR sensors. The LEDs could emit infrared radiation in the spectral range between 1.7 μm and 4.8 μm (Popov et al., 1997). They usually have one single emission spectrum with a narrow spectral bandwidth, which is around one tenth of its peak emission wavelength (Sotnikova et al., 2010). Their emission was electronically modulated by controlling the driving current of the LEDs (Alexandrov et al., 2002), which made an optical chopper unnecessary. There were several reports of NDIR sensors with MIR LEDs as the infrared

radiation sources for the measurement of CH_4 (methane), CO_2, CO, and NO (nitric oxide) (Alexandrov et al., 2002; Haigh et al., 2007; Sotnikova et al., 2010).

The most obvious disadvantage of the MIR LEDs was their low output power, which were several hundred milliwatt (mW) in the pulsed mode and several mW in the continuous wave mode (Abell et al., 2014; Fanchenko et al., 2016). The low output power resulted in a noisy signal and further reduced the detection capability of NDIR sensors. This drawback could be compensated by introducing highly sensitive photodetector and digital signal processing technology. A digital lock-in amplifier could be introduced to significantly improve the signal-to-noise ratio, since the emission of the LEDs was electronically modulated at a very high frequency (Davies and Meuli, 2010).

Therefore, the objective of this research was to develop a NDIR CO sensor with MIR LED as its infrared radiation source to measure gas phase CO concentration. The specific objectives included:

1) To develop a MIR CO sensor;

2) To determine the optimal parameters of the MIR CO sensor; and

3) To evaluate the performance of the developed MIR CO sensor.

4.2 Materials and Methods

4.2.1 Overall design of the MIR CO sensor

A mid-infrared (MIR) CO sensor was developed for measuring gas phase CO with a typical NDIR sensor structure (Fig.4-1). The infrared radiation source (the MIR LED) and the photodetector was placed on the opposite sides of the gas cell. The photodetector was installed on

a preamplifier by its manufacturer. A converging lens was used to focus the infrared radiation on the photodetector. The sensor had a short optical pathlength (50mm length) design to omit the collimating lens for the infrared radiation source. The optical chopper in typical NDIR sensors was not necessary as the infrared emission from the LED was electronically modulated. A narrowband infrared filter was used to provide the CO selectivity. The entire MIR CO sensor was installed in a cage system (Thorlabs Inc., Newton, NJ, USA).

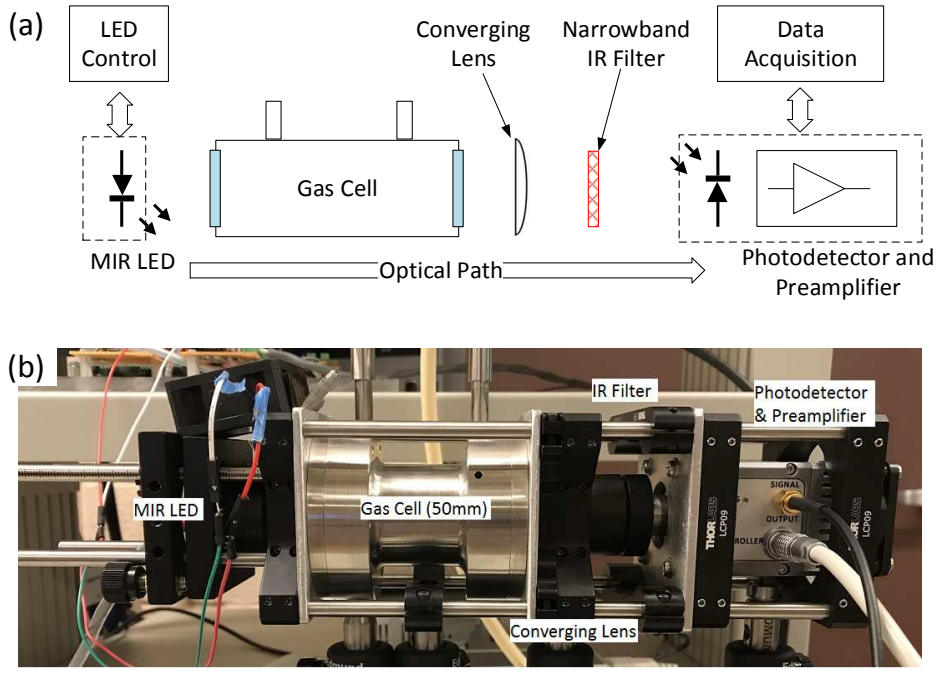

Fig.4-1 Illustration of the developed MIR CO sensor: a) schematic diagram of the MIR sensor; b) assembled MIR sensor in a cage system.

A data acquisition (DAQ) system was designed to control the LED temperature and to collect the output signal from the preamplifier. The DAQ system was programmed using LabVIEW® (Release 2015, National Instruments Co., Austin, TX, USA) software. The signal processing algorithm for the infrared sensor was also included in the developed LabVIEW® program.

4.2.1.1 Infrared radiation source

The sensor used a mid-infrared light emitting diode (LED) (Lms46LED-TEM-R, LED Microsensor NT, LLC, Saint-Petersburg, Russia) as the infrared radiation source. The LED had a typical peak emission spectrum wavelength at 4.45 µm and a typical spectral bandwidth about 0.9 µm (full width at half maximum, FWHM). The actual emission spectrum of the LED was greatly influenced by its internal temperature and driving current (Fig.4-2).

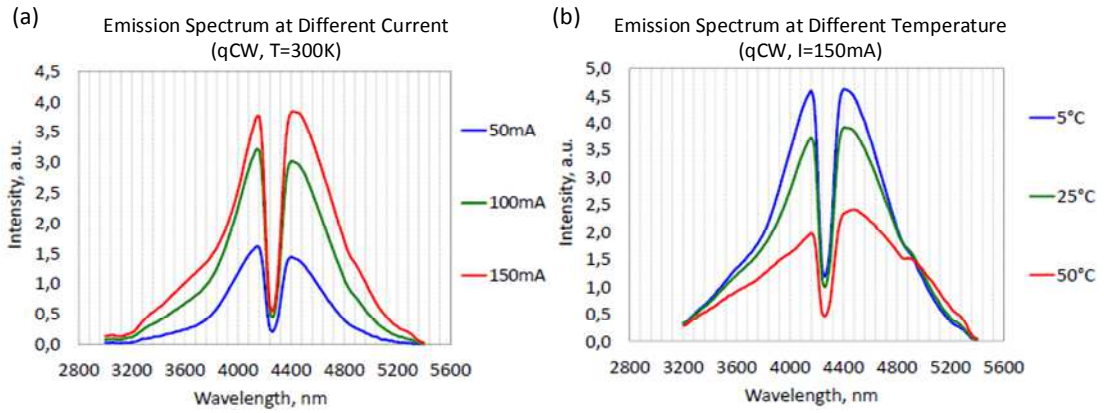

Fig.4-2 Illustration of the LED emission spectrum with different driving currents (a) and under different temperatures (b) in quasi continuous wave (qCW) mode (Graphs adopted from the LED's specification document. LED was set at the quasi continuous wave mode).

However, the data shown in Fig.4-2 was obtained in the quasi continuous wave (qCW) mode, which had an inferior output radiation power. The maximum LED's output power was obtained when the LED was operated under a pulse mode. Therefore, it was necessary to determine the temperature and driving current of the LED in the pulse mode to obtain a highest, stable output power.

The LED included a thermoelectric cooler and a temperature sensor for LED temperature control as well as a parabolic reflector to form a collimated light beam. A LED thermoelectric cooling

(TEC) controller (TEC controller, LED Microsensor NT, LLC, Saint-Petersburg, Russia) was used to provide the LED's p-n junction temperature control.

A LED driver board (D-41, LED Microsensor NT, LLC, Saint-Petersburg, Russia) was used to power the LED. The LED driver was designed by the manufacturer to operate the LED in a pulse mode, thus the emitted infrared radiation from the LED would be a series of pulses with a fixed pulse width (Fig.4-3a). The pulse frequency and pulse width were controlled by the jumpers on the LED driver board. The amplitude of the pulse was determined by the selected LED driving current from the LED driver. However, the heat generated during the LED operation limited the combination of LED driving current, pulse frequency, and pulse width (Fig.4-3b).

(a)

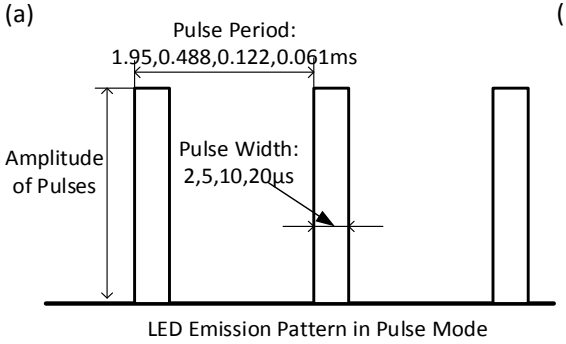

(b)

Current, A		Frequency			
		512 Hz	2 kHz	8 kHz	16 kHz
Pulse duration, µs	2	1.9	1.9	1.5	0.6
	5	1.9	1.9	0.6	0.2
	10	1.9	1.5	0.2	0.2
	20	1.9	0.6	0.2	0.2

Fig.4-3 Illustration of the LED's emission pattern in time domain: a) LED emission pattern demonstration (The pulse period is the reciprocal of pulse frequency); b) allowable combinations of LED driving current, pulse frequency, pulse width from the manual of the LED driver (Graphs adopted from the LED's specification document).

4.2.1.2 Infrared photodetector

A photovoltaic photodiode (PVI-4TE-5, VIGO System S.A., Ozarow Mazowiecki, Poland) was selected as the photodetector of the MIR CO sensor. The photodiode was attached with a programmable preamplifier (PIP-DC-20M-F-M4, VIGO System S.A., Ozarow Mazowiecki,

Poland). A thermoelectric cooling (TEC) unit (PTCC-01-BAS, VIGO System S.A., Ozarow Mazowiecki, Poland) was used to provide the temperature control (around 196K) function for the photodiode. The working condition of the photodiode and the parameters of preamplifier were controlled by a preamplifier management software (SmartManager, VIGO System S.A., Ozarow Mazowiecki, Poland).

The selected photodiode had a typical peak detectivity of 2.0E+11($cm \cdot \sqrt{HZ}/W$) at 5 μm wavelength. The typical spectral response bandwidth (in FWHM) was about 2.1 μm; thus the photodiode had a strong response to infrared radiation in the spectral range between 4 μm and 6 μm. Therefore, a narrow passband infrared filter (INBP4800, Electro Optical Components Inc., Santa Rosa, CA, USA) was used to block the infrared radiation outside the spectral range assigned for CO measurements. The filter was preferred to be transparent for the infrared radiation located in the spectral range between 4.7 μm and 4.9 μm, which would not have interference issue from CO_2. The spectral characteristics of the selected filter were presented along with the actual CO fundamental infrared absorption band obtained from previous Fourier transform infrared spectroscopy (FTIR) experiment (Fig.4-4). The filter had a typical central wavelength of 4.8 μm and a passband width (in FWHM) of 0.25 μm. The minimal transmittance of the filter in the passband was 85%. The typical transmittance of the filter in the stopband was smaller than 1%.

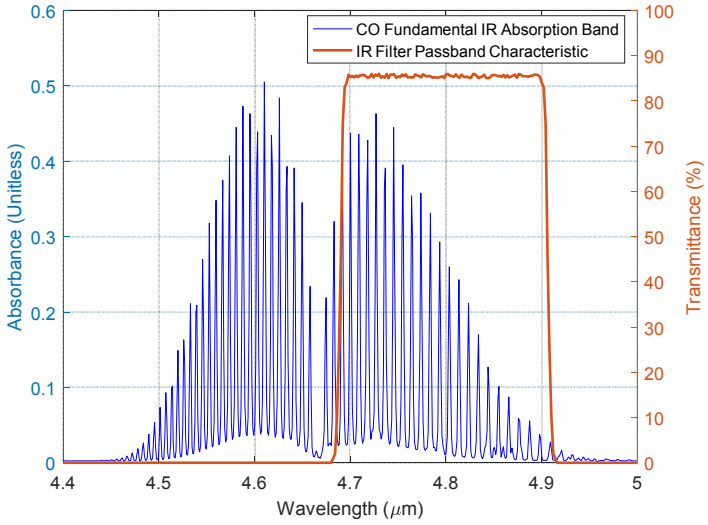

Fig.4-4 Illustration of the CO fundamental infrared absorption band (from FTIR experiment data shown as Fig.3-2) and the spectral characteristics of the selected infrared bandpass filter.

4.2.1.3 Optical path design

The MIR CO sensor was designed without collimating lens. Therefore, the position arrangement of the LED and photodetector was determined by the converging lens' parameters (Fig.4-5).

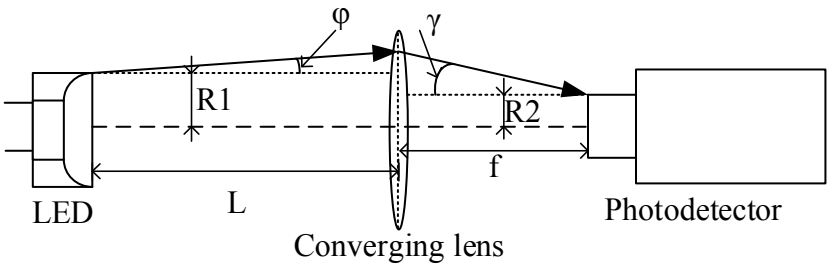

Fig.4-5 Simplified illustration of the optical path design of the developed MIR CO sensor (R_1: LED's beam radius; R_2: beam diameter at the focus point; L: maximum distance between the converging lens and the LED; φ: half value of the LED beam divergence angle; f: focal length of converging lens; γ: acceptance angle of photodetector).

The optical theory about a converging lens stated that the beam diameter was the smallest at the focus; thus the photodetector should be placed at the focus of the converging lens. The optical invariant stated the relationship between the optical parameters of the LED and the photodetector optical parameters as:

$$R_2 = f\varphi \tag{4.1}$$

$$\gamma = R_1/f \tag{4.2}$$

where R_2 was the beam diameter at the focus , f (mm) was the focal length of the lens and φ was the half value of the LED beam divergence angle. The LED had a typical beam divergence angle at about 10°, thus φ was around 5°. γ was the acceptance angle of photodetector, which was the maximal deviation angle of the radiation from the optical axis that could be received by the photodetector (which was 18° according to its specification). R_1 was the LED's beam radius, which was obtained from the radius of the LED's reflector (was 7.5 mm according to LED's specification).

Equation 4.1 and 4.2 were used to estimate the focal length of the converging lens and the available position for the LED. The radius of the converging lens was determined by the LED position and the size limitation of the infrared sensor. The size limitation of the selected cage system determined the maximal radius r of the converging lens was 12.7 mm. The maximum distance L_M (mm) between the converging lens and the LED was calculated as:

$$L_M = (r - R_1)/\varphi \tag{4.3}$$

The maximum distance L_M was calculated from Equaiton.4.3 as 60 mm, which was obtained when the maximal radius r and beam divergence angle φ were used. Therefore, a stainless steel, transmission gas cell with 50 mm pathlength and 38mm window diameter (164-2500, PIKE Technologies, Inc., Madison, WI, USA) was selected based on above calculation on maximum

distance L_M. A plano-convex lens (88-163, Edmund Optics Inc., Barrington, NJ, USA) with a focal length of 35 mm and a diameter of 25.4 mm was selected for as the converging lens. The lens' beam pattern matched with the acceptance angle of photodetector. The minimal transmittance of the plano-convex lens was 90%.

The design of the MIR sensor was simpler than the typical NDIR sensors (Silver and Chen, 2006). The developed optical design didn't have the reference channel to provide the real-time feedback on the initial output power of the infrared source (Jacobs et al., 1959). The initial output power of the LED was obtained by measuring background signal strength (when gas cell filled with nitrogen or air) before and after the CO measurements.

4.2.1.4 Data acquisition system and signal processing

The DAQ system was primarily used to control the LED's temperature and collect the preamplifier output signal. It was also used to collect the values of some parameters, such as the temperature or the pressure of the gas sample in the gas cell, for the calibration of the MIR CO sensor. The detailed description of the DAQ system was provided in Section 6.2.1.

Meanwhile, the preamplifier output (PO) signal required signal processing procedures to be converted to the corresponding gas phase CO concentration. The PO signal was directly related to the intensity of the infrared radiation received at the photodetector. Since the MIR CO sensor didn't have the reference channel to measure the intensity of the emitted infrared radiation from the infrared radiation source (Silver and Chen, 2006), additional procedure was required to calculate the infrared absorbance from the PO signal. The infrared absorbance would be used to calculate the CO concentration in gas phase based on the results from the sensor's calibration.

A signal enhancement method was also required for the PO signal as the MIR LED had only an output power of several hundred milliwatt (mW) in the pulsed mode (Abell et al., 2014; Fanchenko et al., 2016). Since the driving mode of the LED naturally modulated the LED's

infrared emission, a lock-in amplifier was used as the primary signal enhancement method (Scofield, 1994). The details of signal processing for the PO signal were provided in Chapter 6.

4.2.2 MIR CO sensor experiment setup

4.2.2.1 Parameter determination of the MIR CO sensor

The settings of the preamplifier and the LED need to be determined before further tests of the MIR CO sensor. Because there was no detailed reference document for these settings, tests were designed to determine the parameters by analyzing the preamplifier output (PO) signal. The objective of these tests was to find the best preamplifier and LED settings to obtain a stable PO signal with a highest possible strength.

1. System setup

The developed MIR sensor was to be tested with different gas samples, such as air, nitrogen (N_2), and CO. Therefore, a simple test setup was established to transport the N_2 and CO to the gas cell of the MIR CO sensor (Fig.4-6).

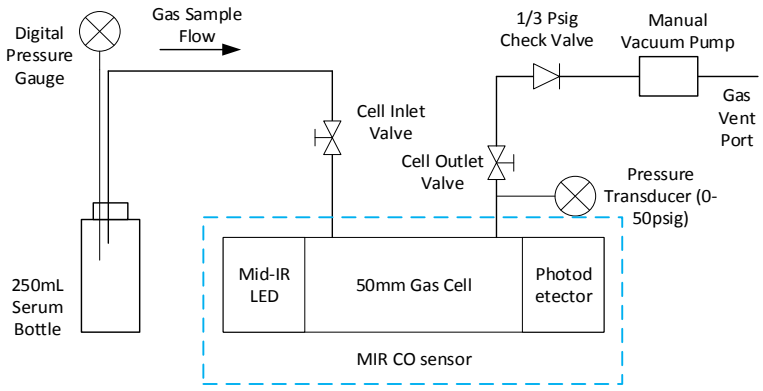

Fig.4-6. Schematic diagram of the parameter determination test setup (blue dashed lines indicated the main body of the MIR CO sensor).

The gas samples were prepared and stored in 250 mL serum bottles beforehand in the laboratory. The samples inside the serum bottles were pressurized to 20 psig before the test. The pressure was used to flush and fill the gas cell with the desired gas samples. The gas cell was vacuumed to -25 inHg before the filling to remove the remaining gas inside the gas cell. When air was used as a gas sample, the serum bottle was removed from the setup and the vacuum pump was used to fill the gas cell with air.

The prepared gas samples included pure N_2 and CO/N_2 mixtures. The concentrations C_G (mol/L) of CO in the mixture samples were calculated based on the idea gas law as shown in Equation 4.4:

$$C_G = \frac{n}{V} = \frac{M(P_s + P_A)}{RT} \tag{4.4}$$

in which n was the amount of CO molecules (mol), V was the volume of the gas cell (L). M was the molar percentage of CO in the gas samples, P_s was the pressure of the gas sample (psig) and P_A was the ambient atmosphere pressure (psi). R was the ideal law gas constant ($8.3144 L \cdot kPa \cdot K^{-1} \cdot mol^{-1}$) and T was the temperature of the gas sample (K).

An oscilloscope (MSO8104a, Agilent, Santa Clara, CA, USA) was used to examine the amplitude of the PO signal. The sampling rate of the oscilloscope was set to 1 billion sample per second (GS/s) and the built-in oscilloscope signal measurement function was used to measure the amplitude. The PO signal was also collected with the DAQ system to examine its waveform.

The alignment of the infrared sensor was performed before the test to place the LED and the photodetector in their optimal positions. The alignment included the orientation of the LED and the axial position of the photodetector. The LED was installed in a kinetic mount (KC1, Thorlabs Inc., Newton, NJ, USA) in the cage system. The orientation was adjusted by changing the direction of the kinetic mount. The position of the photodetector was adjusted by sliding the

photodetector and the preamplifier along the rods of the system in order to place the photodetector in the focus of the converging lens. The amplitude measurement from the oscilloscope was used as the criterion to determine if the alignment of the LED and photodetector was correct. The position with the highest PO signal amplitude should be the appropriate alignment.

2. System tests

A. Photodetector/Preamplifier test

The objective of the photodetector/preamplifier test was to find the appropriate settings of the preamplifier. The frequency bandwidth and the gain were the two major parameters to be determined. Above settings were controlled through a manufacturer provided preamplifier control software (SmartManager, VIGO System S.A., Ozarow Mazowiecki, Poland). The photodetector itself was cooled to 196K during the operation by the controller and other parameters of the photodetector were preset by the manufacturer.

The frequency bandwidth of the preamplifier affect the preamplifier response time and the noise in the PO signal (Boreman, 2001; Hall et al., 1975). The frequency bandwidth of the preamplifier Δf is the reciprocal of response time t_s as shown in Equation 4.5 (Boreman, 2001). The coefficient C is determined by different preamplifier or detector settings (Eppeldauer and Martin, 2001; Hall et al., 1975). An estimation of C was given at 0.35 by the manufacturer of the photodetector.

$$\Delta f = C/t_s \tag{4.5}$$

The frequency bandwidth Δf along with the detection area A, and the normalized detectivity of photodetector D^* decide the noise equivalent power (NEP) of combination of photodetector and preamplifier as shown in Equation 4.6 (Boreman, 2001; Crawford, 1998). Noise equivalent power

is defined as the signal have a signal-to-noise ratio of one ($SNR = 1$), which is usually used to describe the minimal detectable optical power (Hall et al., 1975).

$$NEP = \frac{\sqrt{A} \cdot \sqrt{\Delta f}}{D^*} \tag{4.6}$$

The preamplifier gain $G = G_1 G_2$ was determined by the 1st stage transimpedance amplifier gain G_1 and the 2nd stage amplifier gain G_2 (preamplifier gain in the software) in the preamplifier. The photodetector was operated at photovoltaic mode, thus a transimpedance amplifier was required to transfer the current output signal to a voltage output signal. The gain of the transimpedance amplifier was determined by its transimpedance resistance. For both the 1st and 2nd stage amplifiers, the gain could not be infinitely large due to the gain-bandwidth product of the amplifiers was a fixed value.

A high preamplifier gain resulted in a higher PO signal amplitude, but it would increase the response time of the preamplifier by lowering the bandwidth (Eq.4.5), which was shown in a form of waveform distortions. Thus, the preamplifier might be too slow to respond the fast changing signal. The high gain's negative effect on the frequency bandwidth of the amplifiers was also considered in the selection of the 1st and 2nd amplifiers' gain. Therefore, the photodiode/preamplifier test was designed to find the optimal gain settings (1st stage transimpedance amplifier resistance and the 2nd stage amplifier gain) to provide a PO signal with highest possible amplitude and free of waveform distortion.

The mid-infrared LED was set with a LED driving current of 0.6A, a pulse frequency of 512 Hz, a pulse width of 10 μs, and a LED operating temperature 20 °C during the test. The PO signal was monitored by the high-speed oscilloscope (MSO8104a), which was capable of a maximum 4 GS/s sampling rate and had a precise signal measurement function. The oscilloscope was set at DC coupling during the test and an average of 256 data points were used in the signal measurements.

A sampling rate of 1 GS/s was used in the test. The effect of the different preamplifier settings was compared based on oscilloscope's measurements on the PO signal amplitude and waveform.

B. LED test

After the settings of the preamplifier was determined, the LED was tested with the objective to maximize the intensity of its emitted infrared radiation while keeping the LED's temperature stable. The LED had four parameters to be determined: LED operating temperature, driving current, pulse frequency, and pulse width. The LED operating temperature was known to affect the LED's infrared radiation intensity (Fig.4-2b). Meanwhile, the LED driving current directly determined the intensity of the emitted infrared radiation from the LED (Fig.4-2a).

The pulse frequency and pulse width did not affect the intensity of the emitted infrared radiation, but they determined to the output power of the LED as they defined the duty cycle of the LED. When a lock-in amplifier was used, the pulse frequency and pulse width were also related to the strength of the lock-in amplifier output signal (Scofield, 1994). A combination of high LED driving current, high pulse frequency and wide pulse width theoretically generated the largest LED output power. However, the generated heat during the LED operation limited the selection of combinations (Fig.4-3b).

Thus, the test on the LED included three parts: i. Test of the LED driving current; ii. Test of the LED operating temperature; iii. Test of the LED driving settings (driving current, pulse frequency and pulse frequency). The designed gas sample delivery system was used to fill the gas cell with different gas samples (Fig.4-6). Three types of gas samples were used in the test: air, pure N_2, and N_2/CO mixture.

The PO signal was collected with the DAQ system to record its waveform for time domain and frequency domain analysis. The sampling rate of the DAQ system was selected as 2MS/s. A total of 20 million data points (10 seconds length) were collected for each measurement to have a

better understanding of the characteristics of the PO signal. For the test i on the LED driving current, the high-speed oscilloscope (MSO8104a) was used to examine the PO signal.

A derivative method was used to calculate the amplitude of the PO signal. The method used the derivatives between data points to locate the position of the pulse and to calculate the amplitude. The calculated amplitude of the PO signal was the average of all the located pulses. For the discrete PO signal, the derivative $\dot{x}(i)$ of the ith data point $x(i)$ was obtained as the difference between the ith and $i+1$th data points:

$$\dot{x}(i) = x(i+1) - x(i) \tag{4.7}$$

The derivative $\dot{x}(i)$ was used to determine the start and the end of a pulse. A large positive derivative indicated the start of a pulse while a large negative derivative indicated the end of a pulse (Fig.4-7). A threshold was used to find these large derivatives to locate the pulses.

i. LED driving current test

The LED driver provided five levels of driving current: 0.2 A, 0.6 A, 1 A, 1.5 A, and 1.9 A, which could be selected by a jumper on the driver. All of these current settings were tested since there was no instruction on the behavior of the LED under these settings. Air samples were used in the test. The LED operating temperature was controlled at 20 °C. The pulse frequency was selected as 512 Hz while the pulse width was 2 μs.

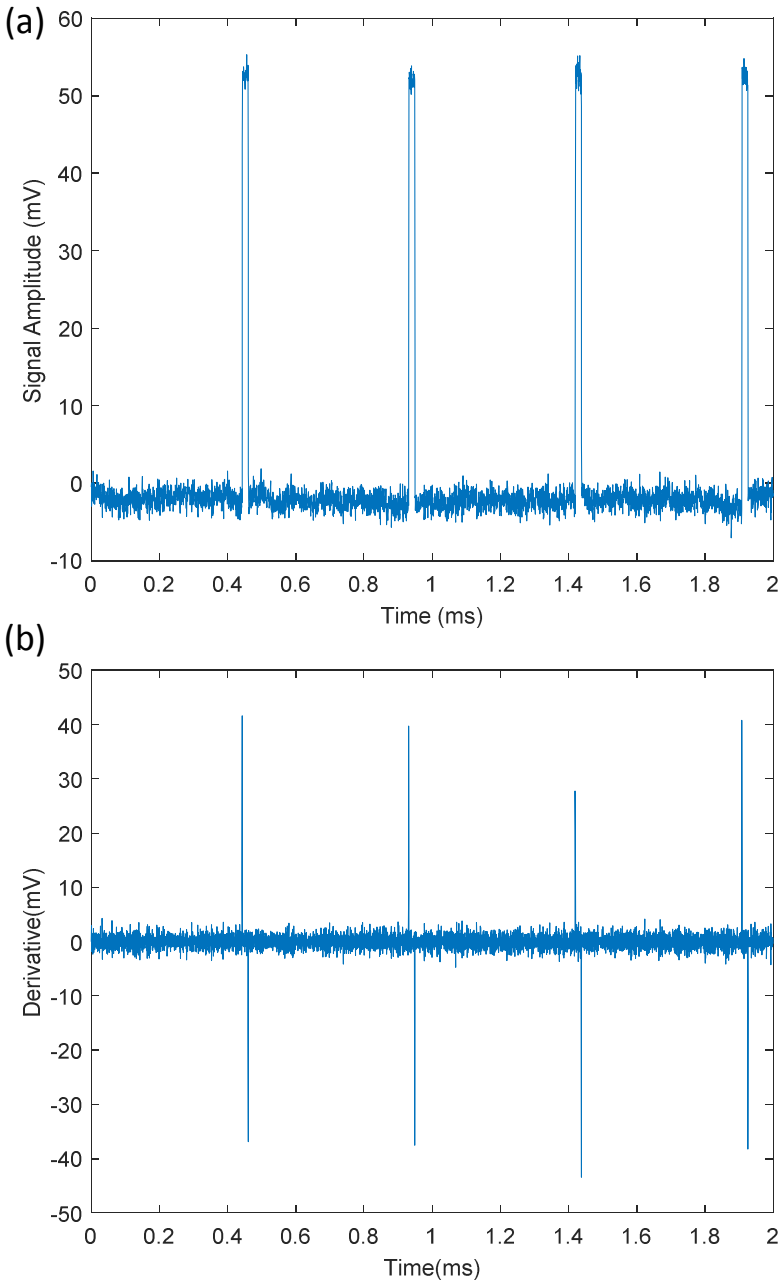

Fig.4-7 Demonstration of the derivative method to locate the pulses in the PO signal: a) original PO signal; b) calculated derivative (A duration of 2 ms of PO signal was shown in the graph. The LED setting (driving current, pulse frequency, and pulse width) was 0.6 A, 2 kHz, and 20 μs).

ii. LED operating temperature test

The LED operating temperature test examined the PO signal's amplitude with different gas samples at different temperatures. Air, N_2, and N_2/CO mixture samples were used in the test. Four operating temperature were tested: -10 °C, 0 °C, 10 °C, and 20 °C. The LED was set with a LED driving current of 0.6 A, a pulse frequency of 512 Hz, and a pulse width of 10 μs. The described derivative method was used to calculate the amplitude of the PO signal.

iii. LED driving settings test

The LED driving settings test used air as the gas sample. The LED operating temperature was set at 20 °C. Four LED driving settings were evaluated in the test to provide the data for the design of a lock-in amplifier (Table.4-1). Above settings were selected based on the allowable combination graph (Fig.4-3b). A pulse frequency of 16 kHz was not selected as it was known that the LED did not have a stable temperature under this frequency from the preliminary test on the LED. A Fast Fourier Transform (FFT) method was used to analyze the PO signals to evaluate their frequency characteristics.

Table.4-1 List of the LED driving settings tested for lock-in amplifier design

Setting No.	LED Settings		
	LED Driving Current (A)	LED Pulse Frequency (kHz)	LED Pulse Width (μs)
1	0.2	8	20
2	0.6	2	20
3	0.6	8	5
4	1.5	2	10

4.2.2.2 Calibration of the MIR CO sensor

1. Experimental setup

The developed MIR CO sensor was calibrated to obtain its response curve. A calibration experiment was performed using two types of calibration gases (34LS-49, Cal Gas Direct, Inc., Huntington Beach, CA, USA) with verified CO molar percentages of 0.1005% and 0.4950% (balance with N_2), respectively. The calibration gases were named as CalGas1 (0.1005% CO) and CalGas2 (0.4950% CO) in this dissertation. Different CO concentrations in the gas cell were obtained by adjusting the pressure of the calibration gases. A pressure transducer (PX509-050GC2IS, Omega, Norwalk, CT, USA) was used to measure the pressure of the calibration gases in the gas cell. A type-T thermocouple was attached to the stainless steel gas cell to measure the gas temperature. The atmosphere pressure was recorded from a pressure gauge installed in the laboratory.

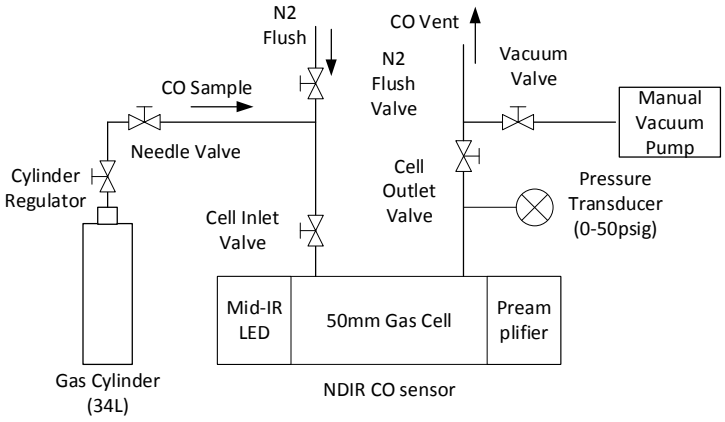

Fig.4-8 Schematic diagram of the MIR CO sensor calibration experimental setup

The settings of LED, preamplifier, and lock-in amplifier in the MIR CO sensor were determined and listed as follows:

a. LED settings: operating temperature: 20 °C; LED driving current: 0.6 A; pulse frequency: 2 kHz; pulse width: 20 μs;

b. Preamplifier: 1st stage transimpedance: High (5 kΩ); Coupling mode: AC; Frequency bandwidth: Low (150 kHz); Preamplifier (2^{nd} stage amplifier) gain: 124 (approximate to 37.5 V/V);

c. Lock-in amplifier: Reference frequency: 8192Hz; Lowpass filter: three-order Butterworth filter with a cutoff frequency of 2Hz.

Gas samples with different CO concentrations were obtained by filling the gas cell with calibration gas between 0 and 50 psig. An approximate 10 psig pressure interval was designed between adjacent pressure levels. The gas cell was pressurized to 50 psig firstly, then the pressure was gradually decreased to 5 psig by releasing syngas to obtain a series of gas samples with descending CO concentrations. The gas cell was pressurized to 50 psig again to obtain a series of gas samples with ascending CO concentrations. Above sample preparation method was designed to test if the MIR CO sensor had a hysteresis error. Each calibration gas was used three times in the calibration to generate three independence sets of gas samples. A total of 32 data points were obtained for each calibration gas.

Validation tests were performed after the calibration to evaluate the accuracy of the obtained calibration model. The first validation test was performed immediately after the calibration model was obtained. The second validation test was performed about six months after the initial calibration to evaluate the long-term stability of the MIR CO sensor. A set of known concentration of CO samples was prepared and measured by the MIR CO sensor in the validation tests. The CO samples with different concentrations were prepared with the same method as the calibration experimental setup; however, the gas samples were only prepared with a descending CO concentrations. The differences between the measured CO concentration and prepared CO concentration were compared.

The calibration of the MIR CO sensor included following steps:

a. The gas cell of the MIR CO sensor was vacuumed to -25 inHg with a manual vacuum pump. Then the cell was purged with N_2 for two minutes. An infrared measurement was performed on the N_2 sample to obtain the pre-measurement infrared emission intensity of the LED;

b. The gas cell was vacuumed to -25 inHg and purged with the calibration gas three times by pressurizing the cell to 50 psig then releasing the pressure to 0 psig. The cell was pressurized to 50 psig with the desired calibration gas after the purge. The pressure in the gas cell was decreased to 5 psig and increased to 50 psig again to obtain gas samples with descending and ascending CO concentrations. Infrared measurements were performed to obtain the transmitted infrared radiation intensity passing through the gas samples.

c. After all gas samples were measured, the gas cell was vacuumed (to -25inHg) and purged with N_2 for two minutes. An infrared measurement was performed to obtain the after-measurement infrared emission intensity. The two measurements on N_2 were used to estimate the original infrared radiation intensity used for infrared absorbance calculation.

d. The infrared absorbance was calculated from the transmitted infrared radiation intensity and the infrared emission intensity of the LED. A linear regression analysis was performed to set up a calibration model between CO concentrations and the infrared absorbance, which was used as the response of the MIR CO sensor. The detailed calculation process was described in Section 6.2.3.

2. Data processing

The prepared CO concentration C_G (mg/L) in the gas samples was calculated using Equation 4.4. The measured CO concentration C_M (mg/L) for each gas sample was obtained through the validation tests.

An absolute percentage error and a root-mean-square (RMS) error were used to evaluate the measurement accuracy of the MIR CO sensor. The absolute percentage error E_{AP} was used to compare the difference between the measured C_M and prepared C_G CO concentration:

$$E_{AP} = |1 - C_M/C_G| \times 100\% \tag{4.8}$$

A mean absolute percentage error (MAPE) $\bar{E}_{AP}$ and corresponding standard deviation were calculated for each calibration gases in the two validation tests.

A root-mean-square error (RMSE) E_{RMS} was calculated to evaluate the measurement accuracy over all the data points. It was obtained by calculating the distance between the measured and the prepared CO concentration as Equation 4.9:

$$E_{RMS} = \sqrt{\frac{\sum_{i=1}^{N}(C_M - C_G)^2}{N}} \tag{4.9}$$

in which N was the number of the data points.

4.3. Results and Discussions

4.3.1 Parameter of the MIR CO sensor

4.3.1.1 Photodetector/Preamplifier settings

The parameters of the preamplifier were determined as following:

a. 1st stage transimpedance resistance: High (5 kΩ);

b. Frequency bandwidth: Low (150 kHz);

c. Preamplifier gain: 124 (approximate to 37.5 V/V).

Due to the limitation made by the manufacturer of the preamplifier, the 1st transimpedance resistance could only be selected as High (5 kΩ) or Low (1 kΩ) and the smallest frequency bandwidth was 150 kHz. The measurement on the PO signal showed that above settings had the highest PO signal amplitude. The waveform analysis did not find a distorted waveform with the selected bandwidth setting, which suggested the photodetector and the preamplifier were fast enough for this application.

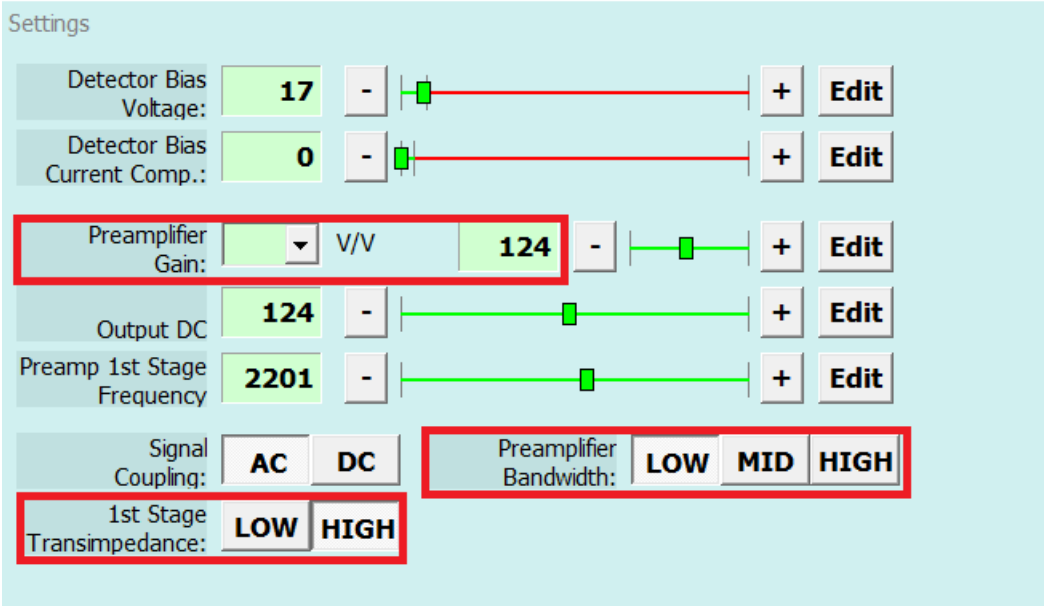

Fig.4-9. Screenshot of the preamplifier setting software with the selected preamplifier settings (shown in red blocks).

4.3.1.2 LED settings

1. LED driving current test

The result of the LED driving current test showed that ripples appeared in the PO signal when the current was set at 1.0 A and above (Fig.4-10). The ripples greatly affected the measurement of the amplitude of the PO signal. To verify the ripples were not generated by the DAQ system, an

oscilloscope was directly connected to the preamplifier to monitor the signal. The signal collected with the oscilloscope also had the ripples when the current was set higher than 1.0A.

A further examination was performed to evaluate the effect of different pulse frequency and pulse width (Table.4-2). It might be possible that the ripples would disappear with a different pulse frequency and/or pulse width. The results showed that the PO signal still had the ripples when the pulse frequency or pulse width was changed (Fig.4-11). Therefore, the LED driving current was selected as 0.6A since it would not generate the ripples in the PO signal.

Table.4-2 List of the LED driving settings tested for additional LED driving current evaluation

Setting No.	LED Settings		
	LED Driving Current (A)	LED Pulse Frequency (kHz)	LED Pulse Width (μs)
1	1.0	0.512	10
2	1.0	2	2
3	1.0	2	5
4	1.0	8	2

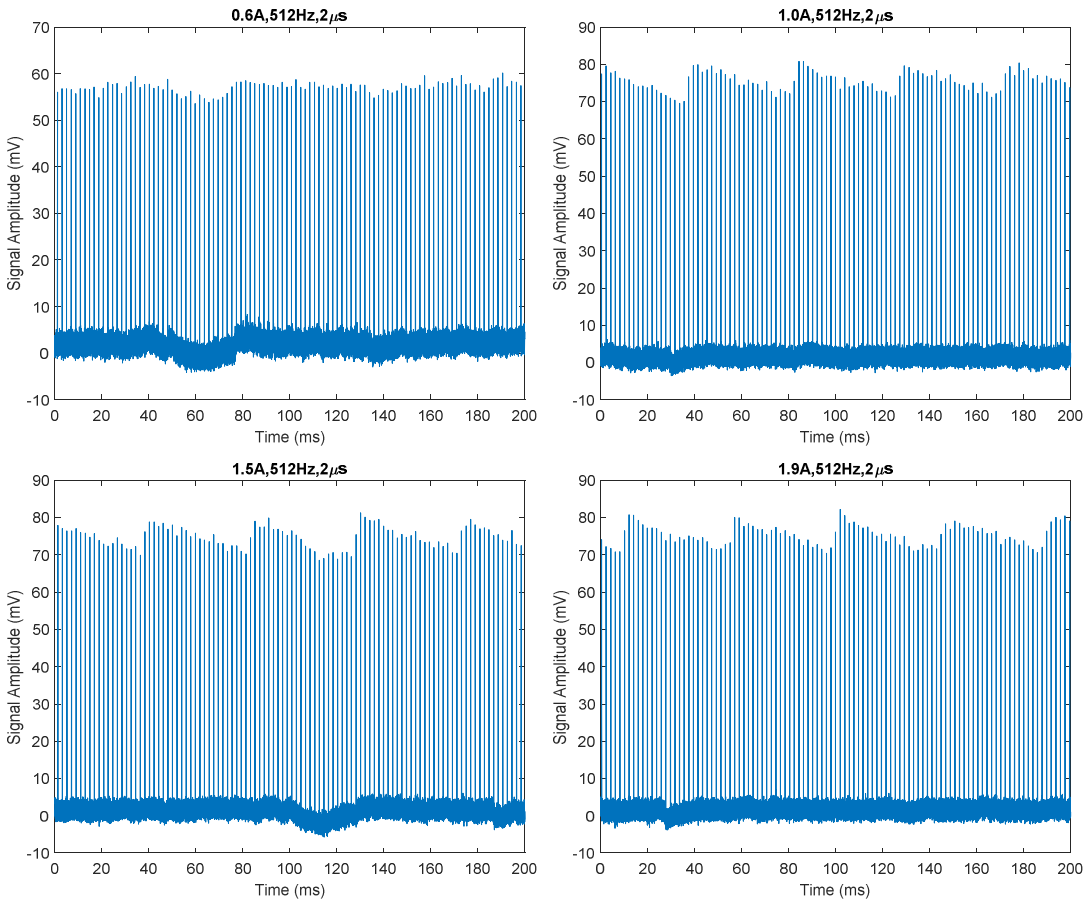

Fig.4-10 Illustration of the PO signal collected with the DAQ system at different LED driving current (LED pulse frequency: 512 Hz; Pulse width: 2μs)

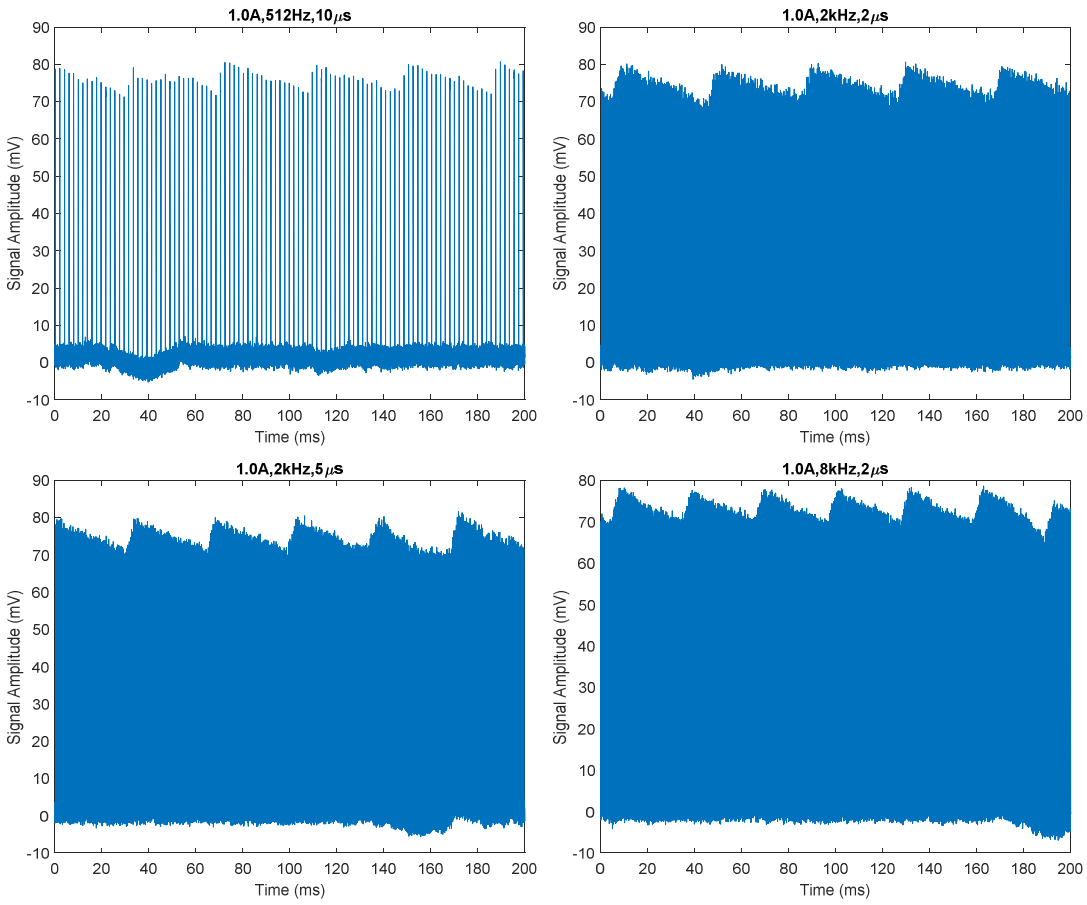

Fig.4-11 Illustration of the PO signal collected with the DAQ system at different LED settings (shown in Table.4-2).

2. LED operating temperature test

The results of the LED operating temperature test showed that the amplitude of the PO signal was the highest when the LED was operated at -10 °C (Table.4-3). However, the heat generated from the LED made it difficult to maintain the -10 °C setting for an extended time with the MIR CO sensor placed at room temperature (21 °C ± 2 °C). A cooling fan was added to the MIR CO sensor to improve the heat dissipation of the LED.

The measurements of the PO signal amplitude were found to be strongly affected by the instable LED temperature, which had a negative effect on the stability of the sensor measurement. Since the measured amplitude had a maximal difference less than 20% between the -10 °C setting and 20 °C setting, the improvement of the LED output power from a lower operation temperature did not justify the consequent poor measurement stability. Therefore, it was decided to set the LED operation temperature at 20 °C.

Table.4-3 List of average amplitude calculation of the PO signal at different LED temperature set points

LED Temperature Set Points (°C)	Average Amplitude of Signal (mV)			
	Gas Samples			
	Air	N_2	N_2/CO Mix1	N_2/CO Mix2
-10	58.2061 (0.5313)	59.9182 (0.5468)	45.1910 (0.5382)	49.1301 (0.4949)
0	54.7775 (0.5110)	58.1923 (0.4255)	44.5451 (0.4703)	48.3855 (0.4758)
10	50.5762 (0.5418)	56.7302 (0.4914)	43.3080 (0.5068)	46.9369 (0.5129)
20	48.0382 (0.4692)	53.4801 (0.4780)	41.2175 (0.4622)	44.6457 (0.4686)

*Standard deviation of measurement was shown in the parenthesis. CO concentration in N_2/CO Mix1 sample: 115.1 mg/L; CO concentration in N_2/CO Mix2 sample: 77.7 mg/L.

3. LED driving settings test

The PO signal was a periodic pulse signal, so it could be decomposed by a Fourier Series Expansion to a weighed sum of several sinusoidal components at discrete frequencies ($mf, m = 1,2,3,\cdots$), which was the integer times of the pulse frequency f (Hz) (Smith, 1999). The theory of the lock-in amplifier suggested that the amplitude of the sinusoidal component would determine the strength of the output signal of the lock-in amplifier (Section 6.2.2.2). The amplitude of these

sinusoidal components could be calculated by frequency domain (FFT) analysis of the PO signal. Therefore, a FFT analysis was performed to measure the peak amplitude of the PO signal at each LED driving settings.

The results showed that the No.1 setting in Table.4-4 had the highest peak amplitude. Meanwhile, the calculated amplitudes from No.2 and No.3 settings were 31% and 37%, respectively, smaller than No.1 settings. The No.4 setting, which used a LED current of 1.5 A, had unfavorable small peaks around the sinusoidal components from the previous discovered ripples (Fig.4-13).

The comparison of the No.1, No.2, and No.3 settings in time domain indicated that a 0.2 A current might had a pulse amplitude too small (nearly one-third of that under 0.6 A) for time domain amplitude measurement (Fig.4-14). Meanwhile, the short pulse width in setting No.3 might be problematic for the data acquisition. Because the DAQ system only had a maximum sampling rate of 2MS/s, a 5 μs pulse width would result in only 10 data points collected per pulse. Thus, the No.2 setting was selected.

Table.4-4 List of the LED settings and the peak amplitude in 0-20 kHz frequency range

No.	LED Driving Settings	Peak Amplitude in 0-20 kHz Frequency Range	Difference (%)
1	0.2 A, 8 kHz, 20 μs	3.394E-3	0
2	0.6 A, 2 kHz, 20 μs	2.332E-3	-31%
3	0.6 A, 8 kHz, 5 μs	2.149E-3	-37%
4	1.5 A, 2 kHz, 10 μs	1.571E-3	-54%

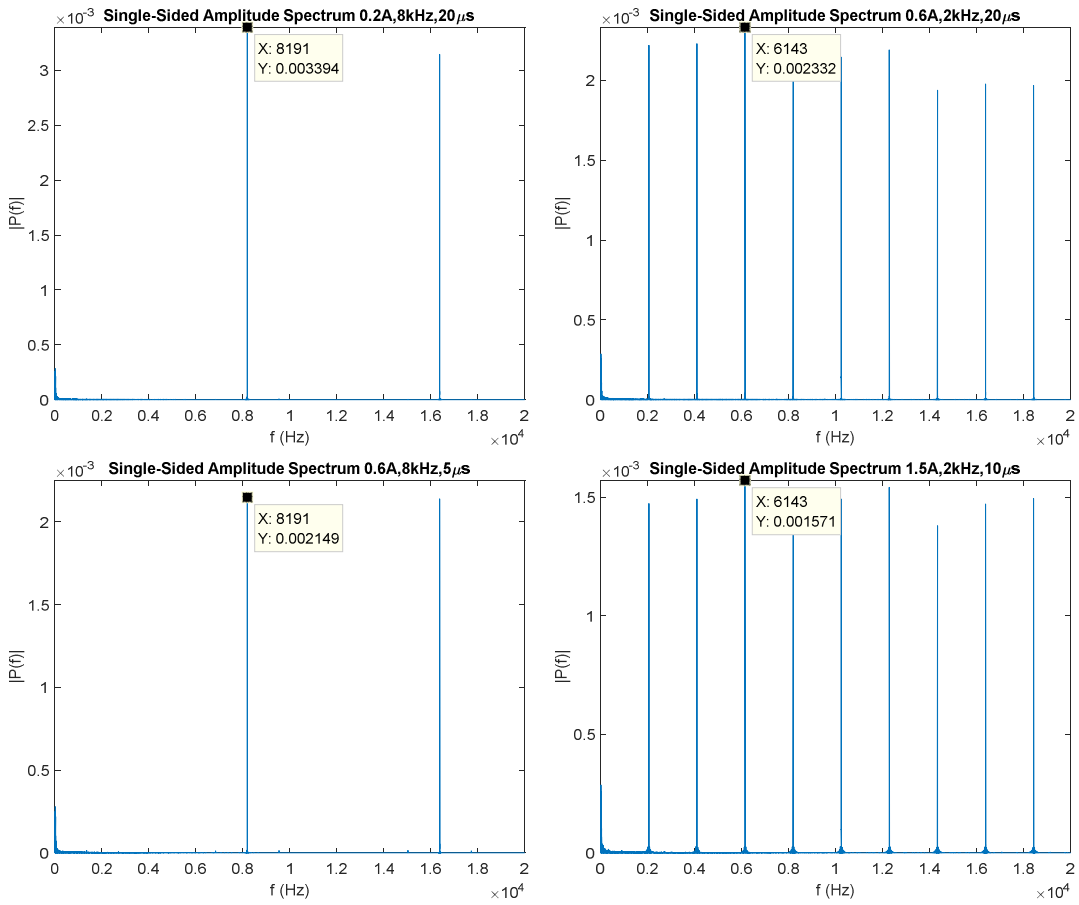

Fig.4-12 Spectral analyses (in 0-20 kHz frequency range) of the PO signal under different LED settings described in Table.4-4 (Peak amplitude was measured with MATLAB® software as the markings in the figures, where X represented the frequency (Hz) and Y represented the measured peak amplitude).

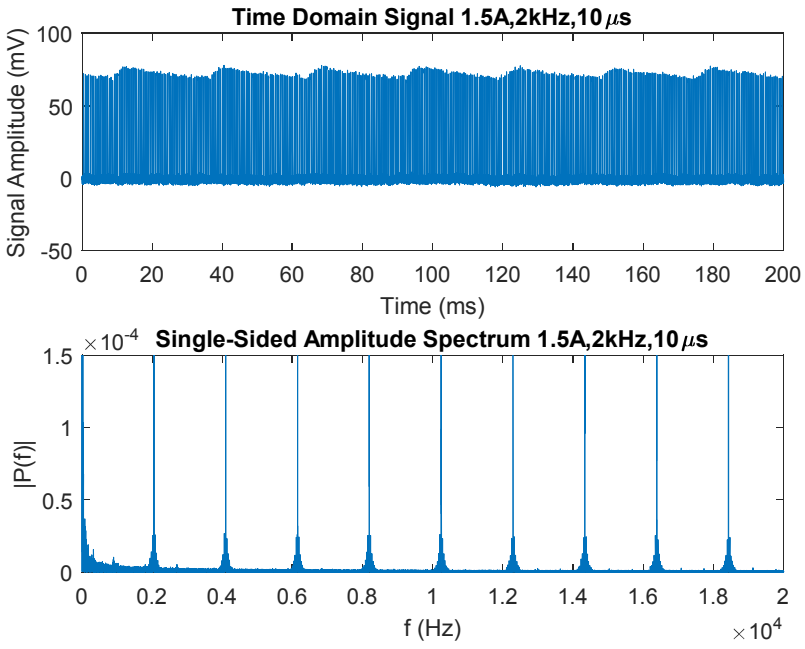

Fig.4-13 Time domain (in 200 ms) and frequency domain (in 0-20 kHz frequency range) analyses of the PO signal generated with a LED setting (No.4) of 1.5 A, 2 kHz, 10 μs.

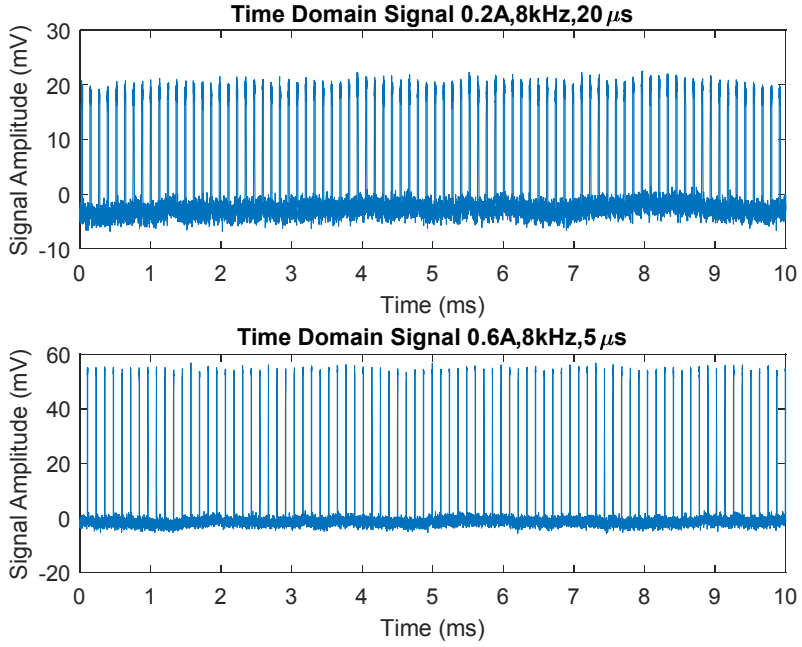

Fig.4-14 Comparison of the PO signal generated with LED current set at 0.2 A (No.1 setting) and 0.6 A (No.3 setting) in time domain (in 10 ms).

4.3.2 MIR CO sensor calibration

The calibration of the developed MIR CO sensor used gas samples with a CO concentration ranged from 1.26 mg/L to 24.80 mg/L. In total, 33 gas samples were prepared at different pressures from the two type of calibration gases, CalGas1 and CalGas2, respectively. The obtained infrared absorbance and the corresponding prepared CO concentration for each gas sample were shown in Fig.4-15. The infrared absorbance was calculated based on the procedures described in Section 6.2.3. The prepared CO concentration was calculated using Equation 4.4. A regression analysis was performed to obtain a calibration model between the infrared absorbance A and the CO concentration C_G in gas phase:

$$A = 0.0019974C_G + 0.00022867, R^2 = 0.9971 \quad (4.10)$$

The obtained model provided a sensitivity of 1.9974E-3 (infrared absorbance) per 1 mg/L of CO (gas phase).

The results of the two validation tests were shown in Fig.4-16. The prepared and measured CO concentrations of the gas samples were displayed as the x-axis and y-axis, respectively. The examination of the validation tests showed that the data obtained from the 1st test had a tendency of underestimation at lower CO concentrations and overestimation at higher CO concentrations. The examination of the raw data showed that the after-measurement infrared emission intensity was slightly higher (less than 0.5%) than the pre-measurement infrared emission intensity. Because the average of these two intensities was used as the infrared emission intensity of the LED in the infrared absorbance calculation (shown in Section 6.2.3). The samples measured at the beginning of the test (with higher CO concentrations) would have a higher than actual infrared absorbance while the samples measured at the end of the test (with lower concentrations) would have a lower one. Therefore, the sensor underestimated the samples with lower

concentrations and overestimated the samples with higher ones. This problem could be partially solved by controlling the LED warm-up time (one to two minutes) as performed in the 2nd test.

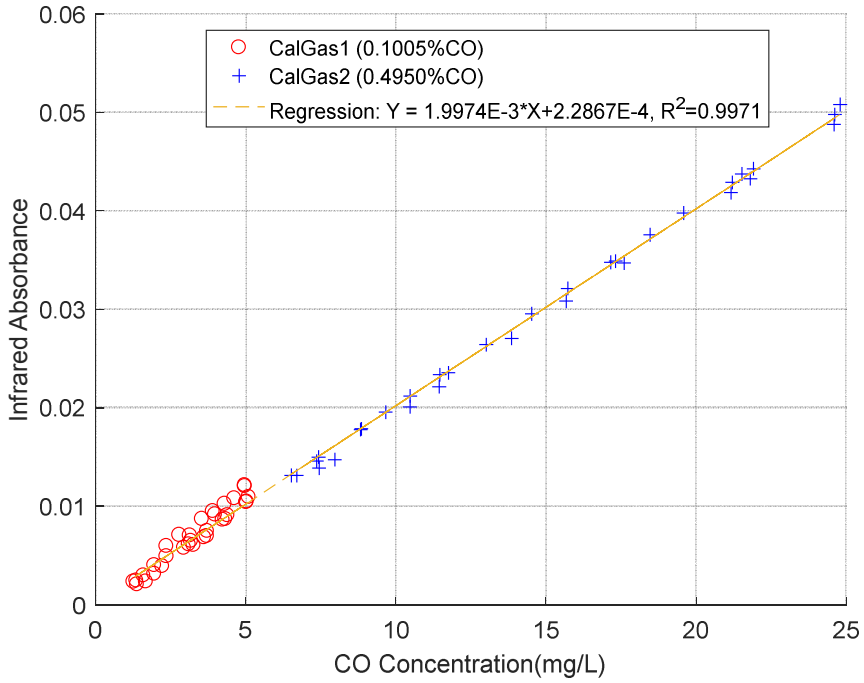

Fig.4-15 Calibration test results of the MIR CO sensor (Data from CalGas1 (0.1005% CO, balance with N_2) were shown in "o" markers. Data from CalGas2 (0.4950% CO, balance with N_2) were shown in "+" markers).

The prepared CO concentrations in the 1st validation test were in the range of 1.88-4.73 mg/L for CalGas1 and 5.94-23.35 mg/L for CalGas2. The prepared CO concentrations in the 2nd test were 1.38-4.95 mg/L and 6.21-24.43 mg/L for CalGas1 and CalGas2, respectively.

The MAPE and the RMSE for individual validation test were shown in Table.4-5. The MAPE and RMSE for all the data points in the two tests were 5.67% (standard deviation: 7.06%) and 0.47 mg/L, respectively.

Table.4-5 Calculation of the MAPE and RMSE for the validation tests

No.	Calibration Gas	1st Validation Test			2nd Validation Test		
		MAPE	MAPE S.D.	Test RMSE	MAPE	MAPE S.D.	Test RMSE
1	CalGas1	4.76%	5.10%	0.28mg/L	15.71%	11.37%	0.61mg/L
2	CalGas2	2.12%	2.07%		4.10%	2.52%	

*S.D. was the abbreviation of standard deviation; MAPE was the abbreviation of mean absolute percentage error; RMSE was the abbreviation of root-mean-square error. CalGas1: 0.1005% CO, balance with N_2. CalGas2: 0.4950% CO, balance with N_2.

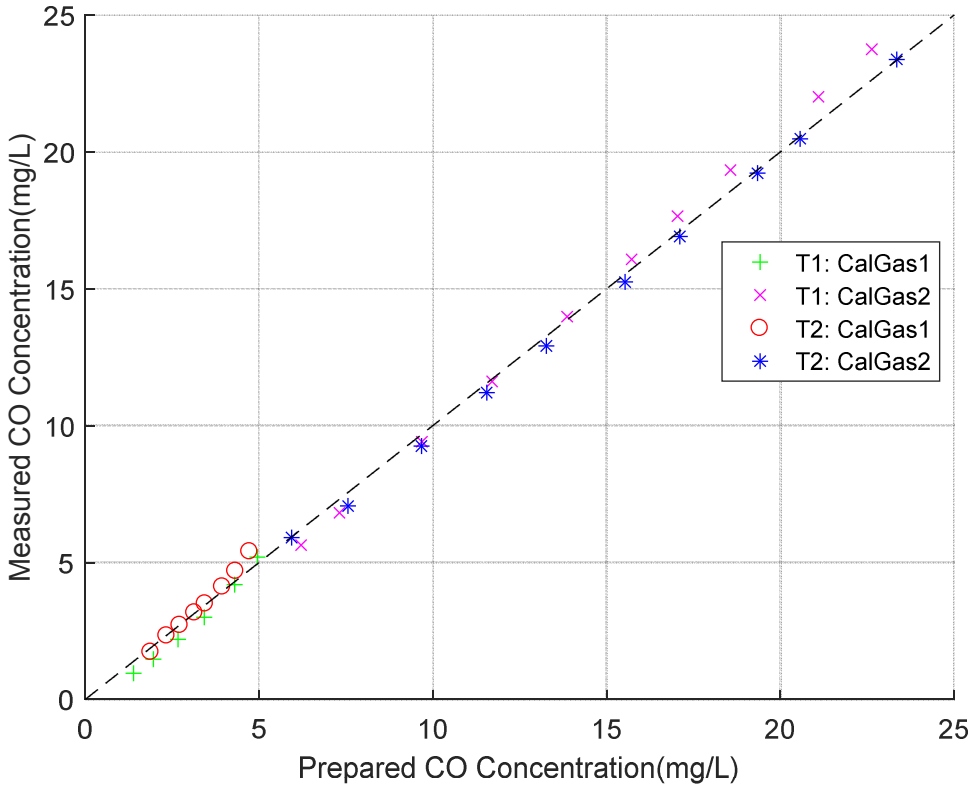

Fig.4-16 Validation tests results of the MIR CO sensor (T1 represented the 1st validation test, which was performed instantaneously after the calibration. T2 represented the 2nd validation test, which was performed six months after the calibration. Data from CalGas1 (0.1005% CO, balance with N_2) were shown in "o" and "+" markers. Data from CalGas2 (0.4950% CO, balance with N_2) were shown in "*" and "X" markers).

4.4. Conclusions

A MIR CO sensor was designed and implemented with a MIR LED and a MIR photodetector. The parameters of the LED and the preamplifier were adjusted based on the time domain and frequency domain (FFT) analysis on the preamplifier output signal. A calibration on the MIR CO sensor was performed to obtain its calibration model. Two validation tests were performed to evaluate the calibration model with gas samples at known CO concentrations. The results demonstrated that the MIR LED could be used as the infrared radiation source for MIR CO measurement. The developed MIR CO sensor could be applied as the CO sensing unit for the developed dissolved CO measurement system with a mean absolute percentage error of 5.67% and a root-mean-square error of 0.47 mg/L.

CHAPTER V

DISSOLVED CARBON MONOXIDE MEASUREMENT EXPERIMENT

Abstract

The concentration of dissolved carbon monoxide (CO) in the syngas fermentation medium has a substantial influence on the fermentation process by regulating the activities of enzymes and microorganisms. Precise measurement and control of the dissolved CO concentration can improve the fermentation process efficiency and stability. A dissolved CO concentration measurement system was developed based on an indirect method, which measured the extracted, gas phase CO to determine the dissolved CO concentration. The dissolved CO in a liquid sample with known volume was extracted with a hollow fiber membrane contactor. The amount of extracted CO was measured by a MIR CO sensor and used to estimate the dissolved CO concentration. The performance of the developed dissolved CO measurement system was evaluated. The results demonstrated that the developed system could measure dissolved CO concentration with a maximal mean absolute percentage error of 6.18%. The measurement took 20 minutes per sample, but could be reduced by further improvements on the gas extraction process. The system can be ultimately integrated with a fermenter controller to provide real-time measurement and control of dissolved CO concentrations during syngas fermentation.

Key words: Dissolved carbon monoxide, Hollow fiber membrane contactor, MIR CO sensor

5.1 Introduction

Dissolved carbon monoxide (CO) concentration is a vital parameter in syngas fermentation process. Microorganisms in fermentation medium utilize dissolved CO through the acetyl-CoA pathway to produce bioethanol or other bioproducts (Wilkins and Atiyeh, 2011). CO concentration greatly affected the conversion rate of other syngas components, namely hydrogen (H_2) and CO_2, by regulating the activities of enzymes and microorganisms (Devarapalli and Atiyeh, 2015). Appropriate dissolved CO concentration was important to improve the fermentation process efficiency and stability (Atiyeh et al., 2017).

However, methods to measure dissolved CO concentration were scantly reported. Riggs and Heindel (2006) developed an optical method to measure the optical absorption spectra of CO-myoglobin and to determine the dissolved CO concentration. Jang et al. (2018) measured the dissolved CO concentration by heating the fermentation medium samples to release CO and then measuring the released CO with a gas chromatography equipped with a thermal conductivity detector. Offline gas chromatography combined with fermenter gas mass transfer models was also used to estimate the dissolved CO concentration based on partial pressure of CO in fermenter headspace and the mass transfer of CO (Atiyeh et al., 2017). It was also possible to measure the dissolved CO concentration with the help of general, indirect dissolved gas measurement methods, such as gas stripping technique (Schelter et al., 2014) and static headspace equilibration method (Butler and Elkins, 1991). These general methods firstly separated the dissolved gases from liquid samples, then measured the extracted gases with gas chromatography or mass spectroscopy techniques. However, the research of syngas fermentation required a measurement method that could automatically measure the dissolved CO concentration in a timely manner to

optimize the fermentation process. None of abovementioned methods could meet the requirements in syngas fermentation application, such as sensor response time, chemical interference, and reversible measurement. Therefore, it is of great value to develop a new, real-time system to measure the dissolved CO concentration in syngas fermentation process.

Measurement of dissolved CO concentration in a syngas fermentation medium confronted many challenges, such as low CO solubility, low chemical reactivity of CO in room temperature, anaerobic fermentation environments, and interference from other chemicals, like H_2 (hydrogen), CO_2 (carbon dioxide), CH_4 (methane), and alcohols. Review on available CO measurement methods showed that infrared method was the best method to measure CO at room temperature and in oxygen-free environment. The method also had the least interference from chemicals in the fermentation medium.

Using infrared sensors for dissolved CO measurement had to overcome the challenge from the strong, broad water infrared absorption, which limited the penetration depth of infrared radiation to a few micrometers (Boulart et al., 2010; Downing and Williams, 1975). Schaden et al. (2004) reported a direct method to measure dissolved CO_2 with a high power mid-infrared laser in a short optical pathlength (119 μm) transmission cell. However, this method was not feasible for dissolved CO measurement because CO has much lower solubility and weaker infrared absorption than CO_2. Hence, an indirect method was selected to measure the dissolved CO concentration, which measured gas phase CO extracted from the fermentation medium to determine the dissolved CO concentration.

The design of the dissolved CO measurement system was based on the evaluation of various dissolved gas detection methods, such as gas striping (Swinnerton et al., 1962), headspace equilibrium (B'Hymer, 2003), and liquid sample evaporation (Jang et al., 2018). Hydrophobic membrane was preferred because it would block liquid water into the extracted gases and was

easier to set up than the gas stripping or the headspace equilibrium technique. A hollow fiber membrane (HFM) contactor was selected due to its high efficiency in gas-liquid mass transfer (Gabelman and Hwang, 1999). The usage of HFMs improved the contact surface of the liquid sample and reduced the diffusion path length of dissolved gases (Peng et al., 2008). The contactor was superior to the widely used single-layer membrane gas extraction method for its better gas extraction efficiency at high liquid flow rate (Matsumoto et al., 2013). The applications with this type of contactors were recently reported in the detection of dissolved gases, such as N_2, O_2, CO_2, CH_4, Ar (Argon), and Xe (Xenon), in ground water with satisfactory results (Gonzalez-valencia et al., 2014; Loose et al., 2009; Matsumoto et al., 2013).

The main objective of this research was to develop a dissolved CO measurement system which included a gas extraction system and the developed MIR CO sensor. The specific objectives included:

1) To design a dissolved gas extraction system using a HFM contactor and find the suitable operation procedure for gas extraction;

2) To design a dissolved CO measurement system with the dissolved gas extraction system and the developed MIR CO sensor; and

3) To evaluate the performance of the dissolved CO measurement system.

5.2 Materials and Methods

5.2.1 Measurement system setup

The dissolved CO measurement system was composed of a dissolved gas extraction system and a MIR CO sensor (Fig.5-1). The dissolved gas extraction system was designed to degas a liquid

sample with known volume and transport the extracted gases to the MIR CO sensor. The MIR CO sensor was used to measure the gas phase CO concentration of the extracted gas samples to estimate the total amount of dissolved CO in the liquid sample. The dissolved CO concentration was then calculated from the amount of the dissolved CO and the volume of liquid sample used in the gas extraction.

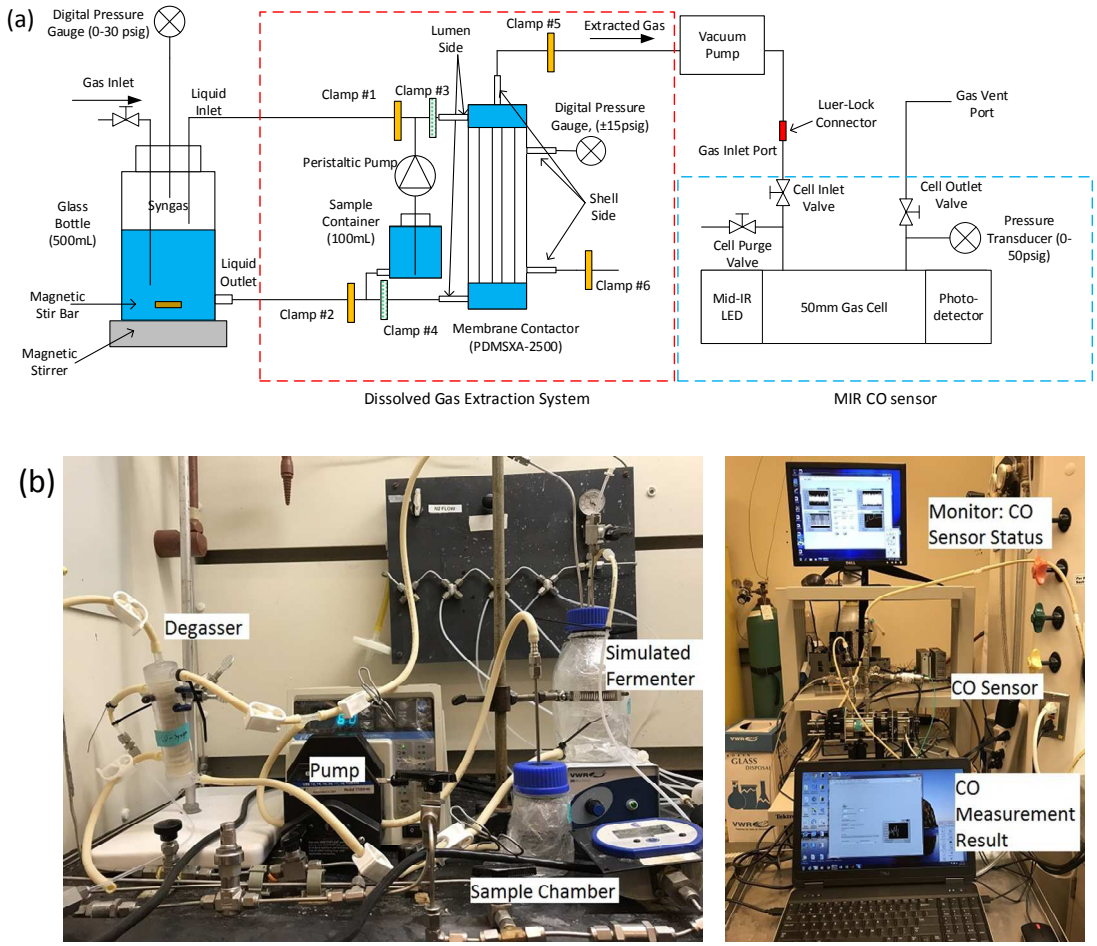

Fig.5-1 Illustration of the developed dissolved CO measurement system: a) schematic diagram of the designed system; b) assembled dissolved CO measurement system with the dissolved gas extraction system shown in the left and the MIR CO sensor in the right.

5.2.1.1 Dissolved gas extraction system

The primary objective of the dissolved gas extraction system was to completely extract the dissolved gases from a liquid sample. The system used a HFM contactor to extract dissolved gases, a vacuum pump to establish vacuum in the contactor, and a peristaltic pump to circulate the liquid sample in the contactor. The system was designed to continuously circulate a known volume of liquid sample through the HFM contactor to extract dissolved gases. The vacuum was established inside the contactor to accelerate the degassing. The vacuum pump was also designed to transport the extracted gases to the MIR CO sensor.

The core component of the dissolved gas extraction system was the HFM contactor (PDXMA-2500, PermSelect, Ann Arbor, MI, USA). The contactor had a surface area of 2,500 cm^2 with 3,200 silicone membrane microfibers. The membrane fiber separated the contactor into two chambers, the lumen side chamber and the shell side chamber. The volumes of the two chambers were 21 mL and 26 mL, respectively. The lumen side chamber of the contactor was assigned to store the liquid sample because of its higher transmembrane pressure limit than that of the shell side. The shell side chamber contained the extracted gases and was connected to the MIR CO sensor through the vacuum pump. A digital pressure gauge (DPG5600B, Omega, Norwalk, CT, USA) was installed to the shell side chamber to monitor pressure changes during the gas extraction.

The volume of the liquid sample was essential to calculate the dissolved CO concentration. However, the gas diffusion through the HFMs would always occur when there was a pressure difference between the two sides of the membrane. Thus, the dissolved gases in the liquid sample would diffuse through the membrane until an equilibrium was reached between the two sides of the membrane. This characteristic of the membrane made it impossible to precisely control the volume of liquid sample for degassing if the contactor was directly filled with liquid samples. The

liquid samples would release the dissolved gases through the filling process, which made it difficult to calculate the dissolved CO concentration. Therefore, a 100 mL glass bottle was introduced as a sample container to store a liquid sample with known volume for degassing. Meanwhile, the lumen side of the contactor was filled with gas-free water beforehand to avoid the loss of dissolved gases during the filling process.

A diaphragm type vacuum pump (7011-0252, Gardner Denver Thomas, Inc., Sheboygan, WI, USA) was installed between the contactor and the MIR CO sensor to generate the required vacuum in the contactor. The inlet of the pump was connected to the shell side chamber while the outlet of the pump was connected to the inlet port of the gas cell of the MIR CO sensor. The vacuum pump was set at a flow rate of 7.5 L/min and a maximal vacuum of -900 mbar (-13.05 psig, 85 torr in standard atmosphere pressure) at the inlet. Meanwhile, it could generate a maximal pressure of 2.3bar (33.36 psig) in its outlet. The pump was also used to transport the extracted gases to the MIR CO sensor by feeding the extracted gases into the gas cell of the sensor. The diaphragm structure of the pump prevented the backflow of the gases from high pressure side (the gas cell of the MIR CO sensor) to the low pressure side (the shell side chamber of the contactor).

For testing purposes, a 500 mL glass bottle was used to prepare liquid samples with known dissolved CO concentration. The dissolved CO concentration was calculated from the headspace pressure in the 500 mL bottle and the liquid temperature based on the Henry's law. A digital pressure gauge (DPG5600B, Omega, Norwalk, CT, USA) was used to measure the headspace pressure. A magnetic stirring bar was placed in the 500 mL bottle beforehand and a magnetic stirrer (200 Mini-Stirrer, VWR, Radnor, PA, USA) was used to agitate the liquid sample, which would shorten the time to reach an equilibrium between the gas phase and dissolved syngas.

A peristaltic pump (7523-30, Cole-Parmer, Vernon Hills, IL, USA) was installed at the outlet of the liquid sample container (the 100 mL glass bottle) to transport the liquid sample between different vessels. By controlling the pump flow direction, the liquid sample could be circulated between the 500 mL bottle and the sample container or between the sample container and the lumen side chamber at a desired flow rate.

5.2.1.2 Mid-infrared CO sensor

The developed MIR CO sensor was used to measure the gas phase CO concentration in the extracted gases. The details of the settings of the MIR CO sensor setup were described in Chapter 4. The measurements of the CO concentration in the extracted gases were based on the calibration model (Eq.4.10) described in Section 4.3.2, which described the relationship between infrared absorbance and the gas phase CO concentration. The infrared absorbance of the gas sample was calculated from the attenuation of the infrared radiation intensity ΔI and the infrared emission intensity of the LED I_o. The detailed calculation procedures for the infrared absorbance of the gas samples were discussed in Section 6.2.3.

5.2.2 Dissolved CO measurement experimental setup

5.2.2.1 Preliminary test setup

A preliminary test was performed for the following purposes:

1) To determine the volume V_L (mL) of a liquid sample and the volume V_G (mL) of the gas cell for the calculation of the dissolved CO concentration;

2) To develop the operating procedures of the gas extraction system to achieve the best gas extraction.

1. Volume measurement test

The volume of the sensor gas cell V_G (mL) was measured by connecting the gas cell with a bottle pressurized with nitrogen (Figure.5-2). The pressure inside the gas cell was set at atmosphere pressure beforehand. The volume calculation was based on the principle that the total amount of gas would not change when the two vessels were connected to each other:

$$n_1 + n_2 = n_3 \tag{5.1}$$

where n_1 and n_2 represented the amounts (in mole) of gas in the bottle and in the gas cell before the connection. n_3 represented the total amount (in mole) of gas in the two vessels after the connection. According to the ideal gas law, the pressure P (psia) of certain amount n (in mole) of gas was determined by its volume V (mL) and temperature T (K):

$$n = \frac{PV}{RT} \tag{5.2}$$

in which R was the ideal gas law constant (8.3144L·kPa·K^{-1}·mol^{-1}). The temperature of the gas was maintained at around 23°C during the test. By substituting Equation 5.2 to Equation 5.1, the volume of the gas cell V_G could be obtained as:

$$(P_1 + P_A)V_1 + P_A V_G = (P_A + P_2)(V_1 + V_G) \tag{5.3}$$

where P_1 and V_1 were the initial pressure (psig) and the volume (mL) of the bottle respectively. P_2 was the new stabilized pressure (psig) in the two vessels. P_A was the recorded atmosphere pressure (psia) during the measurement. The volume V_1 of the bottle was measured with water for three times. Three different initial pressures P_1 (2.52 psig, 6.04 psig, and 9.43 psig) were used in the test to measure the volume of the gas cell V_G.

The volume V_L (L) of the liquid sample inside the sample container was measured by filling the entire bottle and tubing with water. The volume of water inside the bottle was then measured with

a graduated cylinder. Three independent measurements were performed to measure the volume of the water.

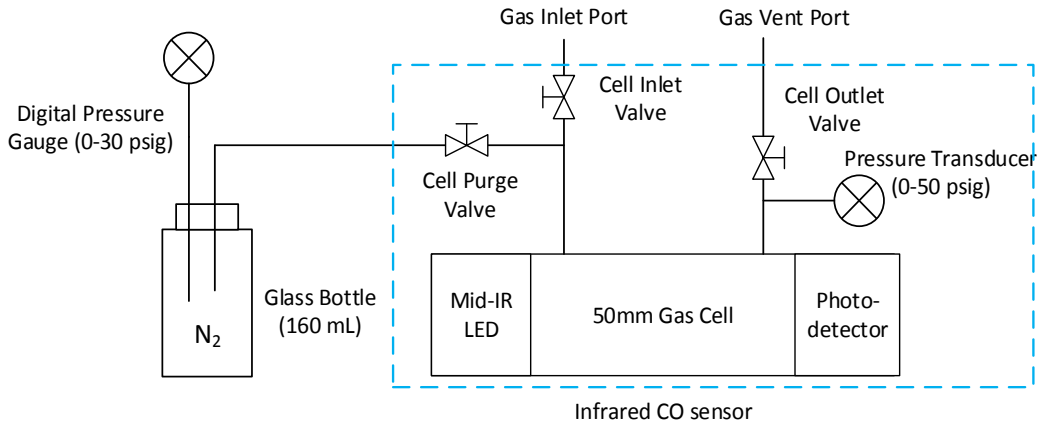

Fig.5-2 Illustration of the experimental setup for measuring the volume of the gas cell of the MIR CO sensor.

2. Dissolved gas extraction system test

The test on the dissolved gas extraction system was designed to develop the appropriate operating procedures to achieve the best gas extraction. The primary factors related to the gas extraction included:

1) The liquid sample flow rate;

2) The time duration of the gas extraction; and

3) The vacuum pump's capability to transport extracted gases to the MIR CO sensor.

The specification of the HFM contactor stated that its gas extraction efficiency was inversely proportional to the liquid sample flow rate. Matsumoto, et al. (2013) also reported that a slower liquid sample flow rate had better gas extraction efficiency. However, above conclusions were

obtained when the HFM contactors were installed in a flow-through system. In this research, the contactor was installed in a circulation system. The flow rate of liquid sample might have less impact on the gas extraction because the liquid samples would circulate in the HFM contactor for multiple times and alleviate the corresponding low gas extraction efficiency from a high flow rate.

The time duration of the gas extraction process had a direct influence on the gas extraction ratio R_E, which was calculated as the ratio between the measured C_{CO} and prepared C_{CO}^{aq} dissolved CO concentration:

$$R_E = C_{CO}/C_{CO}^{aq} \tag{5.4}$$

The details of the calculation of dissolved CO concentrations were described in Section 6.2.3.

The gas extraction ratio R_E was used to evaluate different extraction process settings. A longer gas extraction process should have a better gas extraction ratio as it increased the time duration of the degassing. However, it might have a negative effect on the capability of the vacuum pump to transport extracted gases to the MIR CO sensor. Because the vacuum pump was directly connected to the gas cell of the MIR CO sensor, a longer gas extraction process might generate a high backflow pressure for the vacuum pump when the extracted gas was accumulated in the gas cell. Thus, the high backflow pressure would affect the normal operation of the vacuum pump and impede the transport of the extracted gases. As a result, the amount of CO measured by the MIR CO sensor would be smaller than expected.

Therefore, the test of the gas extraction system was performed to evaluate the effect of the liquid sample flow rate and the time duration of the gas extraction. A further test was performed to compare the obtained gas extraction ratio R_E between a single long gas extraction cycle and several short gas extraction cycles (total time durations of gas extraction were the same).

Liquid samples were prepared with an initial headspace syngas pressure of 5 psig for the most part of the test. A liquid sample with an initial syngas pressure of 10 psig was prepared for the test with multiple gas extraction cycles to evaluate the gas extraction ratio R_E at different dissolved gas concentrations. The detailed test contents were listed as follows:

1) Compare the setting of the liquid sample flow rate at 50 mL/min (low setting) and 160 mL/min (high setting), respectively, with a length of gas extraction of four minutes.

2) Compare the effect of a single long-time gas extraction cycle and multiple short-time gas extraction cycles with a liquid sample flow rate of 60 mL/min. The single gas extraction cycle lasted ten minutes. Multiple short-time gas extraction cycles included three five-minute extraction cycles.

The details of the setup was described in Section 5.2.1. The operation steps of the developed dissolved CO measurement system were described as follows:

1) The measurement system was purged with N_2 (nitrogen) for two to three minutes before the test. Liquid samples with dissolved CO were prepared by introducing pressurized syngas to the container with CO-free water in the test. A total volume of 500 mL reverse osmosis (RO) water was used for each test and was injected to the 500 mL bottle before the pressurization. The lumen side chamber of the contactor and the 100 mL bottle were fully filled with RO water by the peristaltic pump before the introduction of syngas. After the vessels were filled with RO water, the Clamp #1, #2, #3, #4, and #5 were applied to isolate the three vessels (Fig.5-1a). The Clamp #6 would be closed for the whole test unless explicitly mentioned.

2) The syngas used in the test contained 40% CO, 30% CO_2, and 30% H_2 in molar percentage. The headspace of 500 mL bottle and the RO water inside was purged with the syngas before pressurization for three minutes. The headspace of the 500 mL bottle was

pressurized to 5 psig after the purge. A magnetic stirrer was used to accelerate the establishment of equilibrium between gas phase and dissolved syngas in the bottle. It was assumed that an equilibrium between the gas phase and the dissolved syngas was achieved when the headspace pressure did not change in ten minutes.

3) After the equilibrium was achieved, the liquid sample was mixed with RO water inside the sample container (the 100 mL bottle). The Clamp #1 and #2 was removed from the setup to allow the peristaltic pump to circulate the liquid sample in a counter-clockwise direction. The water was circulated (at 100 mL/min flow rate) between the 500 mL bottle and the sample container until a new equilibrium was established. The Clamp #1 and #2 were applied after the new equilibrium was established. The liquid sample containing dissolved CO was stored in the sample container and ready for gas extraction. The Clamp #3, #4, and #5 were applied in the setup during this step to isolate the RO water inside the lumen side chamber of the HFM contactor from the liquid sample.

4) The Clamp #3 and #4 was removed to allow the circulation of the liquid sample between the sample container and the lumen side chamber of the contactor with the peristaltic pump. The liquid flow was set at a clockwise direction and maintained during the entire extraction process. The liquid flow rate was set at the specific values based on the test contents. The Clamp #5 was applied to evaluate the natural diffusion of the dissolved gases, which was represented by the pressure change in the shell side chamber. When the pressure was stabilized, the Clamp #5 was removed and the Cell Inlet valve between infrared CO sensor and the vacuum pump was open.

5) The vacuum pump was turned on to extract dissolved gases and to transport the extracted gases to the MIR CO sensor. When the desired gas extraction time duration was reached, the vacuum pump was turned off and the Cell Inlet valve was closed. The CO

concentration in the extracted gas sample was measured with the MIR CO sensor. The gas cell of the sensor was vacuumed to -25 inch of mercury (inHg) with a manual vacuum pump before the gas transportation. The MIR CO sensor was operated based on the settings described in Chapter 4. The original infrared radiation intensity was measured based on the method described in Section 6.2.3.

6) The test with multiple gas extraction cycles had additional operations after step 5):

   i. The gas cell of the MIR CO sensor and the vacuum pump was temporally disconnected to vent the gas cell. The gas cell was vented and vacuumed to -25 inHg pressure. An infrared measurement was performed on the remaining gases in the gas cell to determine the residual CO concentration, which was used to calculate the total amount of extracted CO.

   ii. The procedures stated in step 5) were performed again to measure the CO concentration in the extracted gases during the 2nd cycle.

   iii. Repeat step i and ii until the desired number of cycles were completed.

5.2.2.2 Dissolved CO measurement experiment setup

1. Experimental setup and procedures

A dissolved CO measurement experiment was designed to evaluate the performance of the developed dissolved CO measurement system. Liquid samples with different dissolved CO concentrations were measured during the experiment. The setup of the dissolved CO measurement system was described in the Section 5.2.1.

The operating procedures of the experiment were developed based on the results from previous dissolved gas extraction system test, which showed that the method with multiple, short gas extraction cycles had better capability to completely extract dissolved CO from the liquid samples and transport the extracted CO to the MIR CO sensor. Therefore, the experiment was performed with a gas extraction setup of three five-minute gas extraction cycles. The liquid sample flow rate during gas extraction was set at 60 mL/min as previous test showed the flow rate did not have obvious influence on the gas extraction ratio. The detailed operation procedures were stated in Section 5.2.2.1 and Fig.5-3.

2. Liquid sample preparation method

Liquid samples with five levels of dissolved CO concentrations were prepared in the experiment. The liquid samples were prepared with the same method stated in Section 5.2.2.1. The syngas contained 40% CO, 30% CO_2, and 30% H_2 (in molar percentage). The initial headspace pressures in the bottles were controlled at 5 psig, 7.5 psig, 10 psig, 12.5 psig, and 15 psig to generate liquid samples with different dissolved CO concentrations. Liquid samples were prepared from RO water before each measurement and discarded after the measurement to avoid changes in syngas composition. Dissolved CO measurement at each pressure was repeated for three times.

The dissolved CO concentration C_{CO}^{aq} (mg/L) in the prepared liquid samples was calculated based on Henry's law as Equation 5.5:

$$C_{CO}^{aq} = kH_{T_s}P_{CO} \tag{5.5}$$

where H_{T_s} (mol/L·psi) was the Henry's law constant at the certain temperature T (K) and k was the constant to transfer the unit from mol/L to mg/L. P_{CO} (psi) was the partial pressure of the CO in the headspace of the 500 mL bottle, which was calculated from the CO molar percentage in the syngas and the headspace pressure of the 500 mL bottle.

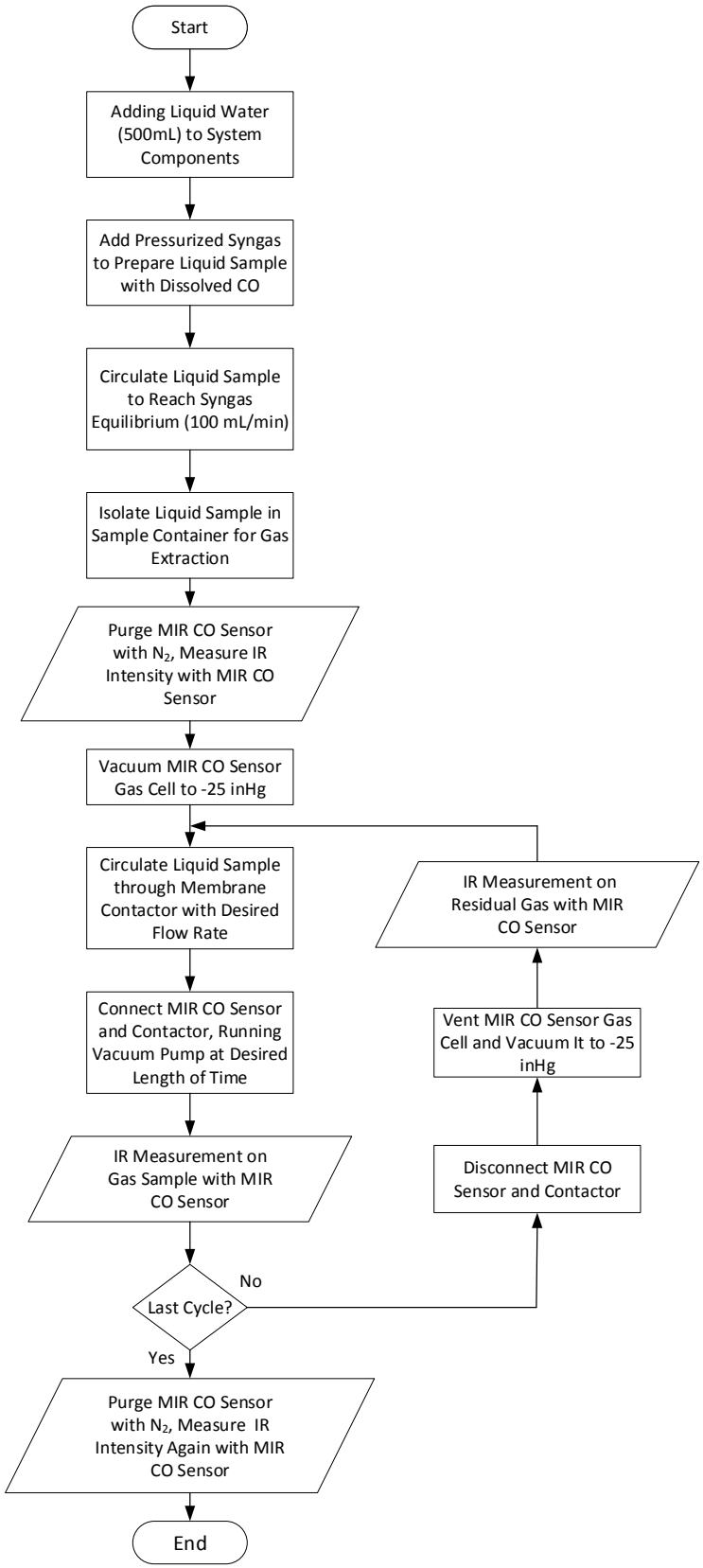

Fig.5-3. Flowchart of the dissolved CO measurement experiment operation procedures

The Henry's law constant was adjusted with the liquid sample temperature T_s measured during each test. The adjusted value was calculated from the standard Henry's law constant at reference temperature $T_\theta = 298K$ (Sander, 2015):

$$H_{T_s} = H_\theta \times exp\left[\frac{-\Delta_{sol}H}{R}\left(\frac{1}{T_s} - \frac{1}{T_\theta}\right)\right] \quad (5.6)$$

where $\frac{-\Delta_{sol}H}{R} = 1300$ was the temperature dependent terms (K) from van 't Hoff equation (for CO) and $H_\theta = 9.7E-6$ was the Henry's law constant for CO ($mol \cdot m^{-3} \cdot Pa^{-1}$) at reference temperature (Sander, 2015).

3. Data processing methods

The dissolved CO concentration C_{CO} (mg/L) was measured in an indirect approach, which utilized the measurement of the amount (in mass) of gas phase CO, m_{CO} (mg), and the volume V_L (L) of the liquid sample to calculate the dissolved CO concentration:

$$C_{CO} = m_{CO}/V_L \quad (5.7)$$

The amount of gas phase CO m_{CO} was calculated from the accumulated gas phase CO concentration, C_G (mg/L), in the gas cell and the volume of the gas cell, V_G (L), as

$$m_{CO} = C_G V_G \quad (5.8)$$

The calculation of the dissolved CO concentration shown in Equation 5.7 assumed a dissolved CO extraction ratio of 100%. Thus, the accuracy of the obtained dissolved CO concentration was largely depending on the degassing capability of the dissolved gas extraction system. Meanwhile, the accurate values of the volume V_L and V_G should also be measured before the calculation of the dissolved CO concentration. The detailed procedure to obtain the accumulated gas phase CO concentration C_G was described in the Section 6.2.3.

The comparison on the prepared C_{CO}^{aq} and measured C_{CO} dissolved CO concentration (mg/L) would be used to evaluate the performance of the measurement system. The mean absolute percentage error (MAPE) $\bar{E}_{AP}$ defined in Section 4.2.2.2 were calculated to compare the repeatability of the measurement system. The root-mean-square error (RMSE) E_{RMS} (Eq.4.9) was used to evaluate the measurement accuracy for all the data points (with a dissolved CO concentration in range of 13.7-21 mg/L).

5.3 Results and Discussions

5.3.1 Preliminary test

1. Volume measurement test

The average value of the gas cell volume V_G was calculated as 55.27 mL (Table.5-1).

Table.5-1 Result of the gas cell volume V_G measurements

Sample No.	Pressure in Bottle Before Connection (psig)	Pressure in Bottle After Connection (psig)	Calculated Volume of the Gas Cell (mL)
Bottle 1	2.52	1.86	56.66
Bottle 2	6.04	4.50	54.64
Bottle 3	9.43	7.03	54.51

*Atmosphere pressure: 750 mmHg; Temperature: 23 ℃; Gas bottle volume: 159.67 mL

The volume of the liquid sample inside the sample container V_L was actually measured in two parts: the volume of the sample container and the volume of the rubber tubing inside the peristaltic pump (Table.5-2). The average value of the liquid sample volume was calculated as 128.7 mL.

Table.5-2 Result of the liquid sample volume V_L measurements

Measurement No.	Sample Container Volume (mL)	Tubing Volume inside Peristaltic Pump (mL)	Total Volume of Liquid Sample (mL)
1	118	10.3	128.3
2	118	10.1	128.1
3	120	9.8	129.8

II. Dissolved gas extraction system test

The results from the tests demonstrated that the liquid sample flow rate did not have an obvious effect on the gas extraction ratio R_E , which was calculated as the fraction between the measure and prepared dissolved CO concentration.

The gas extraction ratios obtained with flow rate changed from 160 mL/min to 50 mL/min were close to each other when the gas extraction processes had a four-minute length (Fig.5-4). The result could be explained by the design to circulate the liquid sample in the contactor, which compensated the lower gas extraction efficiency from a higher flow rate with more circulation cycles.

The test results showed that when the total gas extraction time duration was the same (ten minutes), multiple short gas extraction cycles had a better gas extraction ratio than one single long gas extraction cycle (Fig.5-5). The gas extraction ratio obtained from two five-minute gas extraction cycles were obviously higher than that from one single ten-minute gas extraction cycle. When three five-minute gas extraction cycles were performed, the gas extraction ratio could reach 90%.

The design of the gas extraction system used a vacuum pump to establish vacuum in the contactor and to transport the extracted gases. Therefore, the capability of the vacuum pump to establish vacuum would deteriorate when there was an excessive backflow pressure built up in the gas cell

of the MIR CO sensor, which would resist the flow of the extracted gases to the gas cell. Early tests on the vacuum pump had showed that the rotation of the vacuum pump would slow down when the pressure inside the gas cell reached 20 psig. A single long extraction cycle was prone to reach a high backflow pressure while multiple short extraction cycles could avoid the high backflow pressure built up by the vent and the vacuum of the gas cell between cycles. The release of the pressure inside the gas cell helped to restore the performance of the vacuum pump. As a result, the multiple short extraction cycles had a larger gas extraction ratio than the single long extraction cycle with the same total gas extraction time duration.

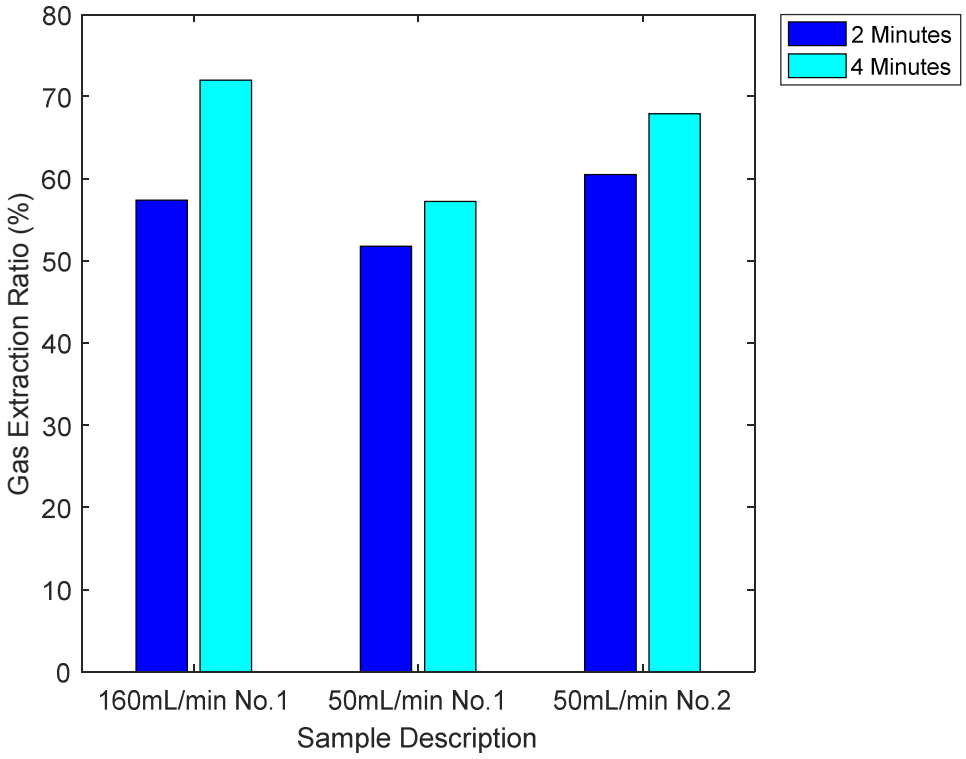

Fig.5-4 Comparison of the gas extraction ratios at different liquid flow rate (Gas extraction ratios were measured at two minutes and four minutes from the start of test).

Since the multiple gas extraction cycles procedure only tested three five-minute gas extraction cycles, it might be helpful to test procedures with shorter gas extraction time duration (for example, two or three minutes) and more extraction cycles (more than three) in a future research. In addition, it would be helpful to revise the current setup by replacing the manual clamps with automatic solenoid valves, which would reduce operation errors during the measurement.

The preliminary tests of the dissolved gas extraction system also showed that there was a variation of the gas extraction ratio among different samples with the same dissolved CO concentrations, even the operation procedures were exactly the same. As few samples were tested, a further research on the variation might be needed.

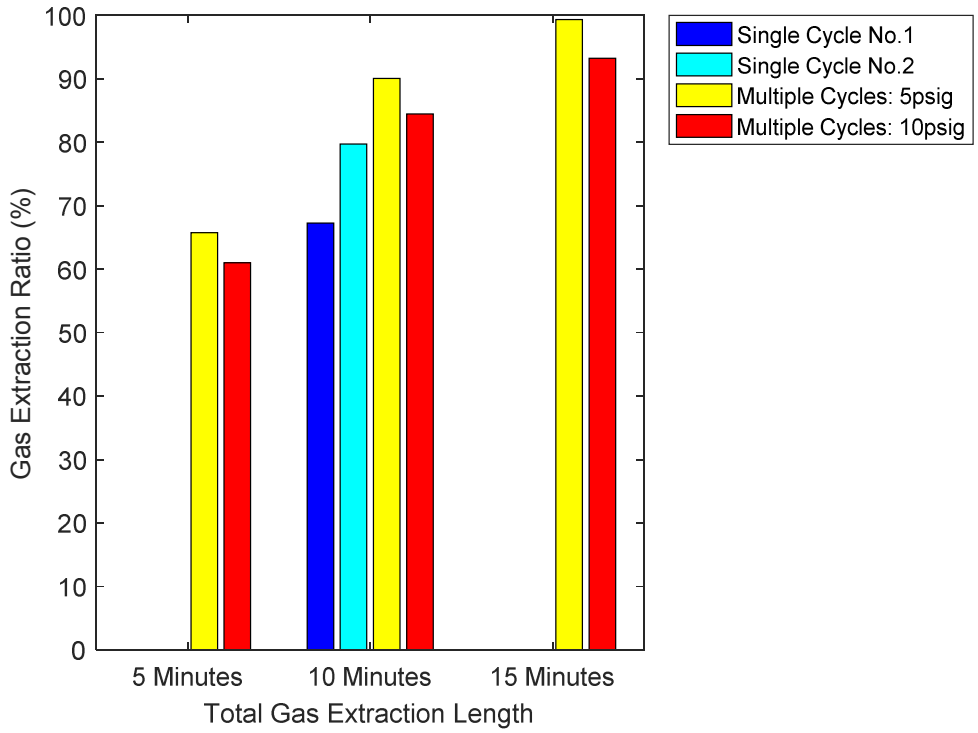

Fig.5-5 Comparison of the gas extraction ratios between single extraction cycle (initial syngas pressure: 5 psig) and multiple extraction cycles (initial syngas pressure: 5 psig and 10 psig).

5.3.2 Dissolved CO measurement experiment

The results of the dissolved CO concentration measurement experiment were shown in Fig.5-6. The prepared and measured dissolved CO concentration were calculated based on equations stated in Section 5.2.2.2. The measured dissolved CO concentration was close to the prepared dissolved CO concentration for the samples prepared with 5 and 7.5 psig initial headspace pressures. The samples prepared with 10 psig, 12.5 psig, and 15 psig initial headspace pressures showed a tendency of underestimation of dissolved CO concentration. It was suspected that a higher dissolved CO concentration would require more cycles for complete degassing. Therefore, a fourth cycle was added during the measurement of 15 psig samples to verify the assumption. The results with four cycles were also demonstrated in Fig.5-6, which showed a better estimation of the prepared dissolved CO concentration. The analysis of the mean absolute percentage error (MAPE) $\bar{E}_{AP}$, across different pressure level was shown in Fig.5-7 and Table.5-3. The variation of the $\bar{E}_{AP}$ was shown as the error bar, which represented one standard deviation. The root-mean-square error (RMSE) was listed in Table.5-3.

Table.5-3 Calculation of the MAPE and RMSE for each pressure level

No.	Sample Initial Pressure	MAPE	MAPE S.D.	RMSE after 3rd Cycle (mg/L) for Entire Test
1	5 psig	2.61%	2.45%	0.83
2	7.5 psig	3.06%	1.49%	
3	10 psig	4.64%	3.54%	
4	12.5 psig	3.58%	0.65%	
5	15 psig	6.18%	0.84%	
6	15 psig*	2.40%	1.11%	

*Results after the 4th gas extraction cycle. S.D. was the abbreviation of standard deviation.

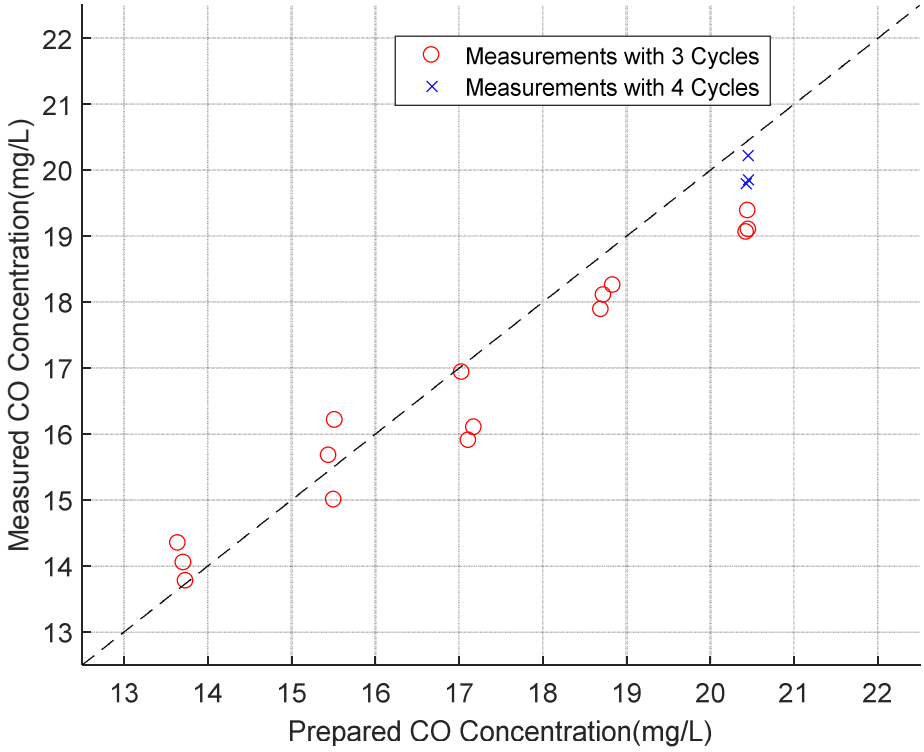

Fig.5-6 Demonstration of the measured dissolved CO concentrations versus the prepared dissolved CO concentrations (Data points obtained with three extraction cycles were shown in "o" markers. Data points (liquid samples with 15 psig initial pressure) obtained with four extraction cycles were shown in "x" markers.)

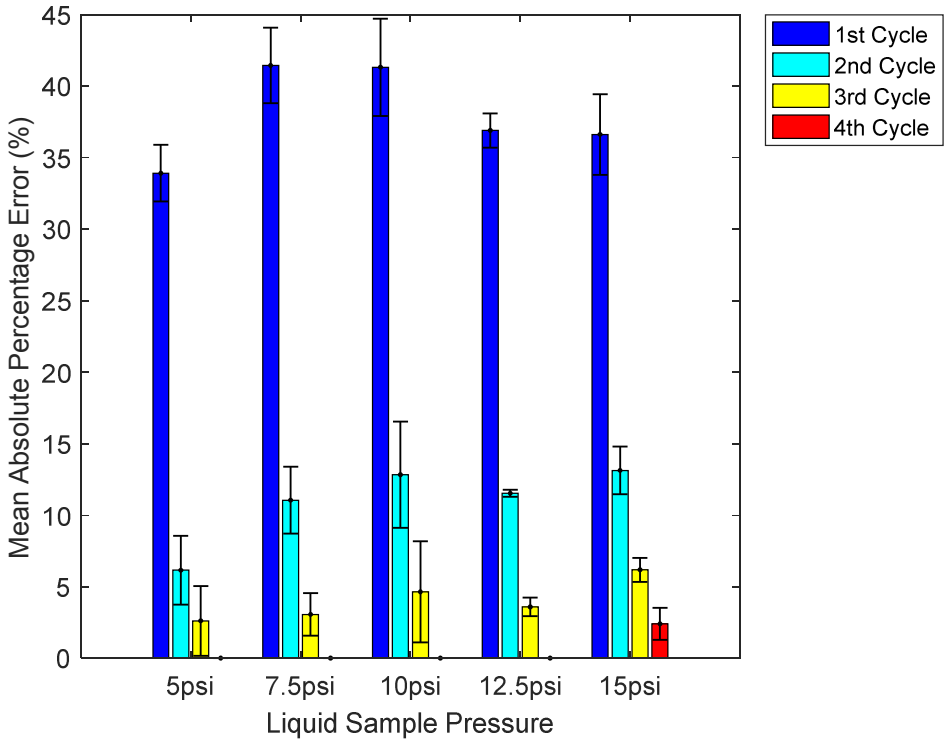

Fig.5-7 Mean absolute percentage errors (MAPE) and corresponding standard deviations in four gas extraction cycles for each pressure level

The maximum MAPE was 6.18% (from dataset of 15 psig samples) after three cycles of gas extraction. The RMSE for the measurement of dissolved CO concentration was 0.83 mg/L. The measurement time for one sample under three extraction cycles was around 20 minutes in the current experiment setup and condition. The standard deviations of the MAPEs, shown as the error bar in Fig.5-7, were randomly distributed during the experiment ranged from 0.65% to 3.54%.

The experiment setup used rubber tubing to connect different vessels, which might have some deformations during the experiment. There were several manual clamps applied in the tubing to block the liquid samples. The position of these clamps might also have tiny changes during the

experiment. The tubing deformations and the clamp position changes could alter the actual volume of the liquid sample to be degassed and further affect the calculation of the gas extraction ratio.

Therefore, the future improvement of the developed dissolved CO measurement system was suggested to replace current manual system setup with an automatic system. The clamps should be replaced with solenoid valves while the rubber tubing should replace with stainless steel tubing, which would have better control on the volume of the liquid sample to be degassed. Meanwhile, an automatic controller should be used to control the operation sequence, which referred to the open or close of the valves and the liquid flow direction. It would be more convenient to test different gas extraction procedures and to reduce the measurement time of the system.

5.4 Conclusions

A dissolved CO measurement system was developed with a dissolved gas extraction system and a MIR CO sensor. The design and the performance of the system was evaluated with liquid samples containing different dissolved CO concentrations. The results demonstrated that dissolved CO concentration could be measured with the developed system, which measured the extracted CO to determine the dissolved CO concentration. The maximal mean absolute percentage error in dissolved CO concentration measurement was less than 7% and the measurement time for one sample was around 20 minutes.

The designed dissolved gas extraction system was built on a hollow fiber membrane (HFM) contactor that could reach more than 90% extraction ratio with three five-minute gas extraction cycles on around 128 mL of liquid sample with a liquid circulation rate of 60mL/min. The future improvement of dissolved CO measurement system could include the automation of the system to

improve the measurement repeatability. The designed multiple cycle gas extraction procedures also could be tested to determine if a revised procedure with more gas extraction cycles and shorter gas extraction per cycle could reduce the measurement time of the system.

CHAPTER VI

SIGNAL PROCESSING PROCEDURES FOR DISSOLVED CO MEASUREMENT SYSTEM

Abstract

Signal processing procedures were developed for the designed dissolved CO measurement system to convert the measurements from the mid-infrared (MIR) CO sensor to the corresponding dissolved CO concentrations. A data acquisition system was built to collect the output signals from the MIR CO sensor. The collected signals were then processed by a digital lock-in amplifier, which was implemented with LabVIEW® software, to improve the signal-to-noise ratio. The parameters of the lock-in amplifier was determined based on theoretical and Fourier analysis of the collected signals. The design of the MIR CO sensor did not include the reference channel in traditional non-dispersive infrared sensors. Thus, a calculation procedure was specially developed to convert the processed signals to gas phase CO concentrations. The obtained gas phase CO concentrations were then used to calculate the dissolved CO concentrations in liquid samples according to the designed gas extraction process.

Keywords: Dissolved CO concentration, Data acquisition system, Lock-in amplifier

6.1 Introduction

The developed dissolved CO measurement system was designed to measure the total amount of dissolved CO in a liquid sample of known volume to indirectly estimate the dissolved CO concentration. A mid-infrared (MIR) CO sensor was used to measure the gas phase CO concentration in the extracted gas sample, which was used to calculate the total amount of dissolved CO in the liquid sample.

The MIR CO sensor used a MIR light emitting diode (LED) as its infrared radiation source. A photodetector was used to measure the transmitted infrared radiation after passing through gas samples. In most non-dispersive infrared (NDIR) sensors, a reference channel was included to exclusively measure the intensity of the emitted infrared radiation from the infrared radiation sources (Burt and Minkoff, 1956; Dinh et al., 2016; Koppius, 1951). The measured infrared radiation intensities from the gas sample and the infrared radiation source were compared to obtain the infrared absorbance, which was related to the CO concentration according to the Beer-Lambert law.

Because of the highly stabilized LED output, the MIR CO sensor was designed without a reference channel. It was plausible to use the intensity of the pre-measured LED emission to estimate the actual intensity of the LED emission during the CO measurements. The intensity of the pre-measured LED emission was obtained by measuring the infrared radiation intensity with N_2 sample in the gas cell. Therefore, the infrared absorbance could be calculated from the obtained infrared radiation intensities of CO samples and the estimated intensity of the LED emission. This unique design of the MIR CO sensor required a special signal processing procedure to calculate gas phase CO concentrations based on the raw signals collected by the photodetector of the MIR CO sensor.

Signal enhancements were required to improve the signal-to-noise ratio of the raw signals before the calculation of the gas phase CO concentrations. The low output power (in several hundred milliwatt in pulse mode) of the LED resulted in a very noisy signal received by the photodetector (Abell et al., 2014; Fanchenko et al., 2016). Although a preamplifier was used as a preliminary signal processing unit, the obtained preamplifier output (PO) signal was still not suitable for direct calculation of the CO concentrations. Thus, a signal enhancement method was required to selectively amplify the PO signal. Based on theoretical and Fourier analysis of the PO signal, a lock-in amplifier was introduced to process the PO signal.

The dissolved CO concentrations were obtained from the gas phase CO concentrations according to the gas extraction process. The complexity of the gas extraction required a procedure to describe the process of calculating the dissolved CO concentrations from the measurements of the MIR CO sensor.

The primary objective of this research was to establish the signal processing procedures for the developed dissolved CO measurement system. The specific objectives included:

1) To design the signal processing procedures to convert the measurements from the MIR CO sensor to actual dissolved CO concentrations;
2) To design and implement a signal enhancement method to improve the preamplifier output signal.

6.2 Material and Methods

6.2.1 Data acquisition system

The data acquisition (DAQ) system was designed to have following functions (Fig.6-1):

1) Measure and control the temperature of the MIR LED;
2) Measure the pressure and the temperature of gas samples inside the gas cell of the MIR CO sensor; and
3) Measure and record the preamplifier output signal to determine the gas phase CO concentration.

The first two functions were achieved by using a compact data acquisition (cDAQ) controller (cDAQ-9133, National Instruments Co., Austin, TX, USA) with three DAQ modules. An analog input (AI) module (NI 9205, National Instruments Co., Austin, TX, USA), an analog output (AO) module (NI 9264, National Instruments Co., Austin, TX, USA), and a thermocouple input (TI) module (NI 9212, National Instruments Co., Austin, TX, USA) were installed in the cDAQ controller. The TI module was connected with an isothermal terminal block with screw terminals (TB-9212, National Instruments Co., Austin, TX, USA) to provide the connection interface for thermocouples. The compact DAQ controller had a built-in embedded processor (Intel Atom® E3825, 1.33GHz); therefore, it can operate independently without connecting to a host computer.

The third function was achieved by using an external DAQ device (USB-6366, National Instruments Co., Austin, TX, USA) with a highest sampling rate of two million samples per second (2MS/s). The DAQ device was connected to a high-performance host computer instead of the cDAQ controller due to the insufficient performance of the controller's processer. Therefore, two LabVIEW® (Release 2015, National Instruments Co., Austin, TX, USA) programs were developed for the data acquisition system. One program was running on the cDAQ controller to achieve the first two functions. The other one was running on the host computer for the preamplifier output signal collection and processing.

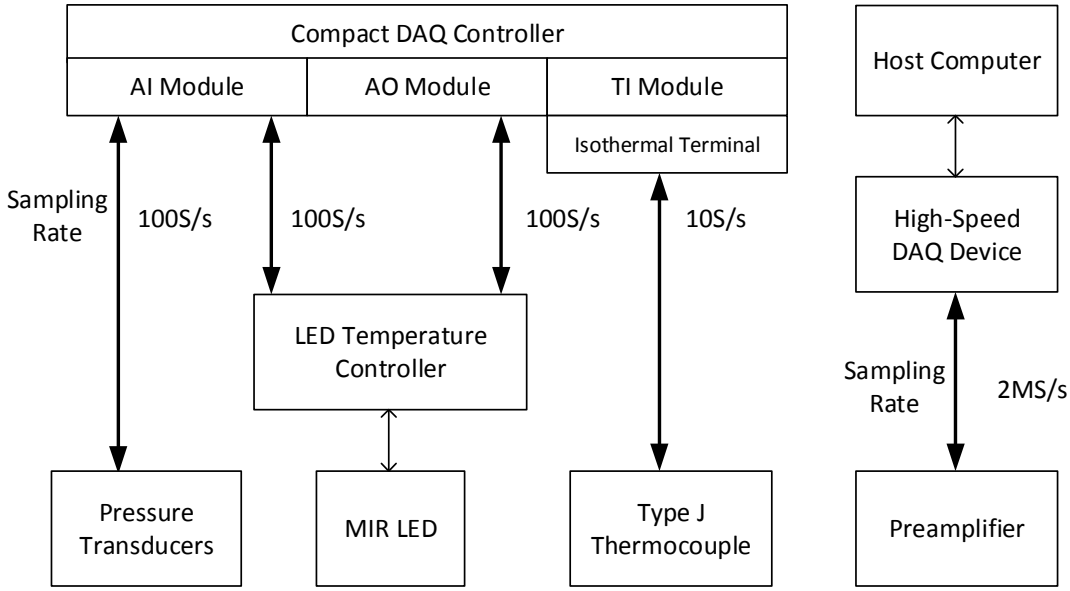

Fig.6-1 Diagram of the data acquisition system of the MIR CO sensor (AI: analog input; AO: analog output; TI: thermocouple input; S/s: sample per second; MS/s: million sample per second.)

6.2.1.1 LED temperature measurement and control

The temperature of the MIR LED (Lms46LED-TEM-R, LED Microsensor NT, LLC, Saint-Petersburg, Russia) affected the LED's infrared emission intensity and spectra. Therefore, it was important to stabilize the LED temperature during CO measurements. The LED had a built-in thermoresistor to measure its p-n junction temperature and a thermocooler to adjust its temperature, which could be connected to a LED thermoelectric cooling (TEC) controller (TEC controller, LED Microsensor NT, LLC, Saint-Petersburg, Russia) to measure and control its temperature.

The cDAQ controller was used to obtain the real-time measurement of the LED temperature and to adjust the LED temperature setpoint (Fig.6-2). The measurement of the LED temperature was performed by connecting the AI module of the cDAQ controller with the temperature signal

output terminal of the LED TEC controller. The adjustment of the LED temperature setpoint was achieved by outputting an analog voltage signal from the AO module of the cDAQ controller to the external temperature control input of the LED TEC controller.

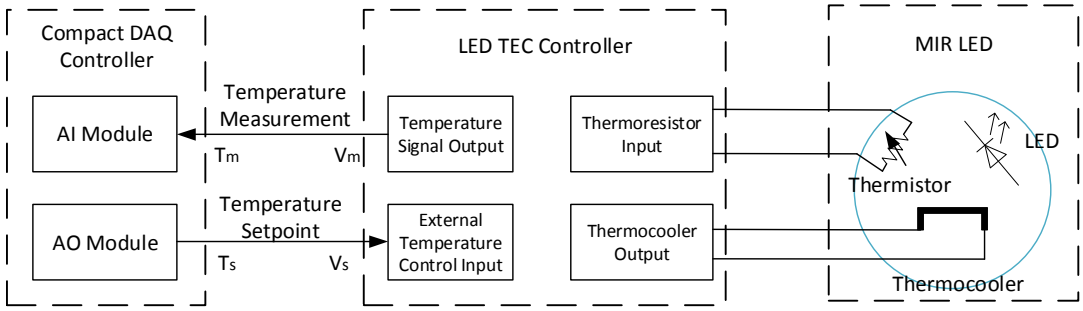

Fig.6-2 Hardware connection diagram for LED temperature measurement and control function

The LED temperature measurement was converted from the measured analog voltage signal by following equation (Eq.6.1) according to the manual of the LED TEC controller:

$$T_m = V_m/10 \tag{6.1}$$

where T_m was the measured LED temperature (°C), V_m was the voltage of the signal (mV). Equation 6.1 was only valid in the temperature range between -15 °C and 25 °C.

An analog voltage signal was required for external adjustment of the LED temperature setpoint. The LED temperature could be set between -10 °C to 22 °C based on the manual of the LED TEC controller. The temperature setpoint was converted to an analog output voltage signal as:

$$V_s = 0.1364 \times (22 - T_s) \tag{6.2}$$

where T_s was the LED temperature setpoint (°C), V_s was the voltage (V) of the external temperature control signal.

6.2.1.2 Gas sample pressure and temperature measurements

The pressure and the temperature of the gas samples were used during the calibration of the MIR CO sensor. Therefore, two pressure transducers with a measurement range of 0-50 psig (PX509-050GC2IS, Omega, Norwalk, CT, USA) and 0-30 psia (PX509-030AC2IS, Omega, Norwalk, CT, USA) were installed, respectively, on the gas cell of the MIR CO sensor. A type-J thermocouple was attached to the outside wall of the gas cell to measure the temperature of the gas sample.

The measurements of the pressure transducers was output as current signals (4-20mA). A 4 mA signal represented the zero point and a 20 mA signal represented the maximal pressure measurement (50 psig or 30 psia depending on the pressure transducer). Two 500 Ω resistors (R_1 and R_2) were connected to the transducers in series to convert the current signals to two voltage signals. The voltage signals (of gas pressure) were then collected with the AI module of the cDAQ controller at a sampling rate of 100 S/s. Two conversion equations (Eq.6.3 and Eq.6.4) were established to convert the voltage signals to the pressure measurement readings. The pressure transducers were powered by a 24 V DC power supply to improve their pressure resolution.

For the 0-50 psig pressure transducer:

$$P_{m1} = 6.25 \times V_{m1} - 12.5 \tag{6.3}$$

where P_{m1} was the measured pressure (psig), V_{m1} was the voltage (V) over its resistor R_1.

For the 0-30 psia pressure transducer:

$$P_{m2} = 3.75 \times V_{m2} - 7.5 \tag{6.4}$$

where P_{m2} was the measured pressure (psia), V_{m2} was the voltage (V) over its resistor R_2.

The isothermal terminal block (TB-9212) was used to provide the cold junction compensation (CJC) function for the thermocouple. The terminal block had two build-in CJC channels (CJC0 channel was used) to adjust the temperature measurement, T_c (ºC), from the thermocouple. The sampling rate of the temperature was set at 10 S/s.

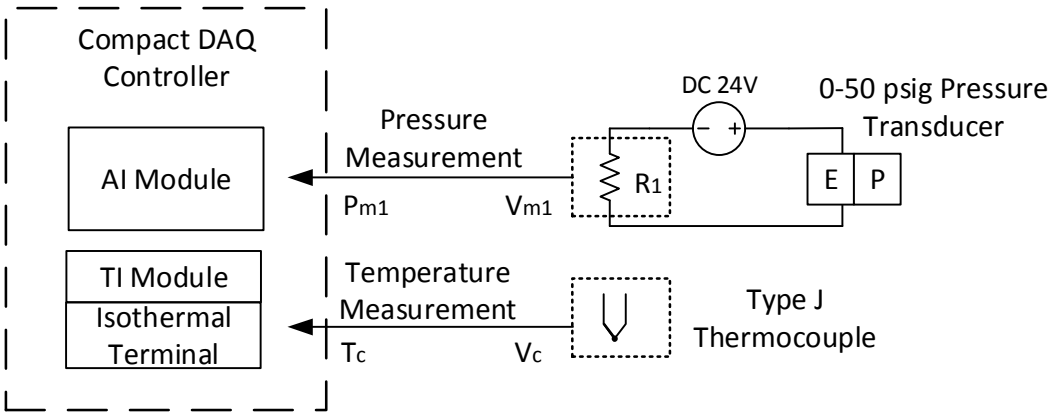

Fig.6-3 Hardware connection diagram for gas pressure and temperature measurement function (Only the connection for the 0-50 psig pressure transducer was shown in the graph. The connection for the 0-30 psia pressure transducer was similar to the 0-50 psig transducer.)

6.2.1.3 Preamplifier output signal collection

The MIR CO sensor used a photovoltaic photodetector (PVI-4TE-5, VIGO System S.A., Ozarow Mazowiecki, Poland) to measure the intensity of the transmitted infrared radiation to determine the CO concentration in the gas sample. When the photodetector was illuminated by an infrared radiation, it output a current signal which was magnified and converted to a voltage output signal by a preamplifier (PIP-DC-20M-F-M4, VIGO System S.A., Ozarow Mazowiecki, Poland). The amplitude of the PO signal was determined by the intensity of the infrared radiation, the IR sensitivity of the photodetector, the gain setting of the preamplifier, and the optical design. The waveform of the PO signal was determined by the modulation pattern of the infrared radiation.

The LED, as the infrared radiation source, was operated at a pulse mode by switching its power supply on and off continuously with a LED driver (D-41, LED Microsensor NT, LLC, Saint-Petersburg, Russia). Therefore, the generated infrared radiation would be a series of pulses, whose frequency related to the speed of the switching. The pulse width was determined by the time when the LED was powered on during one pulse.

The frequency of the LED infrared radiation could be selected at four frequency, namely 512 Hz, 2 kHz (2,048 Hz actually), 8 kHz (8,192 Hz), or 16 kHz (16,384 Hz). The pulse width could be selected at 2 μs, 5 μs, 10 μs, or 20 μs. Therefore, the sampling rate of the DAQ device should be high enough to catch up the very short pulse width. A sampling rate of 1 MS/s sampling rate would record data in a 1μs interval, which equaled to record two data points for one pulse when the pulse width was selected at 2 μs. Thus, the sampling rate of the DAQ device was selected at its highest value of 2 MS/s.

The high sampling rate would record a huge number of data points in a short time, which was too large to store if the PO signal was collected continuously. Thus, the developed LabVIEW® program only collected the PO signal in a limited length, which was ten million data points per signal (equal to a signal length of five seconds).

The preamplifier was connected to the DAQ device through a coaxial cable to provide a good interference resistance. A 50 Ω pass-through BNC terminator was installed on the terminal of the DAQ device to provide the required 50 Ω load for the preamplifier.

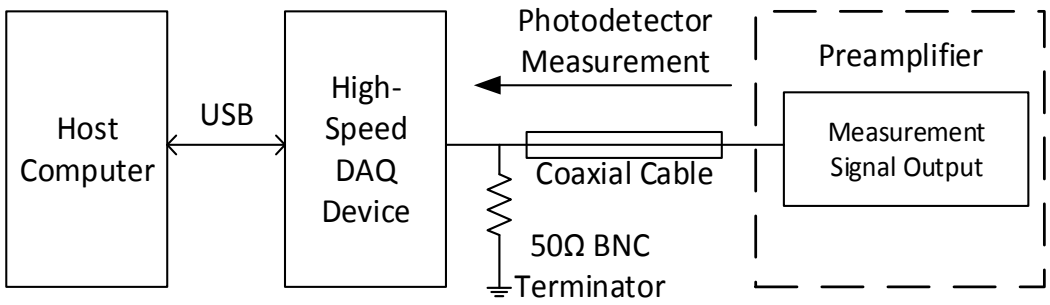

Fig.6-4 Hardware connection diagram for preamplifier output signal collection function

6.2.2 Signal enhancement method

The PO signal carried the information of the CO concentrations in the gas samples. However, the infrared radiation source of the MIR CO sensor , the MIR LED, had a very small output power. As a result, the obtained PO signal had a very low signal-to-noise ratio (SNR), which made the direct utilization of the PO signal problematic. The tiny change resulted from the change of CO concentration would easily mixed up with the noise when the signal had a low SNR. Therefore, a signal enhancement method was required.

Meanwhile, the amplitude of the PO signal was directly related to the transmitted infrared radiation intensity. However, measurement of the amplitude of each pulse would be hard to achieve when the pulse frequency was very high. Hence, the signal enhancement method was also used to convert the amplitude into a more appropriate format for further calculation of the CO concentration.

6.2.2.1 Preamplifier output signal analysis

The PO signal $x(t)$ under an ideal condition would be a series of pulses with the same frequency and duty cycle as those of the infrared radiation from the LED, which could be described in time domain as Equation 6.5:

$$x(t) = \begin{cases} A, & |t| \le \tau/2 \\ 0, & \tau/2 < |t| \le T/2 \end{cases} \qquad (6.5)$$
$$x(t) = x(t \pm nT), n = 0,1,2,\cdots$$

where T was the pulse period (second) of the signal and the reciprocal of the pulse frequency $f = 1/T$ (Hz). τ was the pulse width (second). A was the amplitude (dimensionless), which was related to the LED driving current, the gain of the preamplifier, the optical design of the MIR CO sensor, and the CO concentration in the gas cell. The pulse frequency f and the pulse width τ were determined by the LED driver, which were 2kHz and 20μs (a duty cycle of 4%), respectively.

In real applications, the PO signal was mixed with a noise signal $n(t)$, which mainly included the thermal noise from the photovoltaic photodetector itself and the Flicker noise from the resistance of the preamplifier circuit components (Nudelman, 1962). The thermal noise was evenly distributed in all frequency components while the Flicker noise primarily resided in the low frequency (Voss and Clarke, 1976). Therefore, the actual PO signal $X(t)$ (V) could be described as:

$$X(t) = n(t) + x(t) \qquad (6.6)$$

in which $n(t)$ represented the noise signal generated from the photodetector and the preamplifier circuits, $x(t)$ was the PO signal under the ideal condition.

The theoretical analysis of the PO signal showed that the direct calculation of the amplitude in time domain was problematic. Two methods, the derivative method and the external synchronization method, were considered in the direct measurement of the amplitude. They were designed to locate the accurate position of the pulses in the PO signal and calculate their amplitude. The derivative method used the derivative between data points to locate the position of the pulses while the external synchronization method used an additional data channel to inform the preamplifier to collect signal when the LED was lit up.

The first problem encountered was the low signal-to-noise ratio of the PO signal. The amplitude of the signal $x(t)$ itself, was around 50 to 80 mV when no CO was presented in the gas cell (with higher than 0.6 A LED driving current). However, the noise signal $n(t)$ had an approximate 2 to 3 mV amplitude. This would made the derivative method particular unreliable, as the derivative calculation might falsely recognize a peak generated by the noise as a pulse. The simple amplification of the PO signal was useless as it would simultaneously magnify signal and noise.

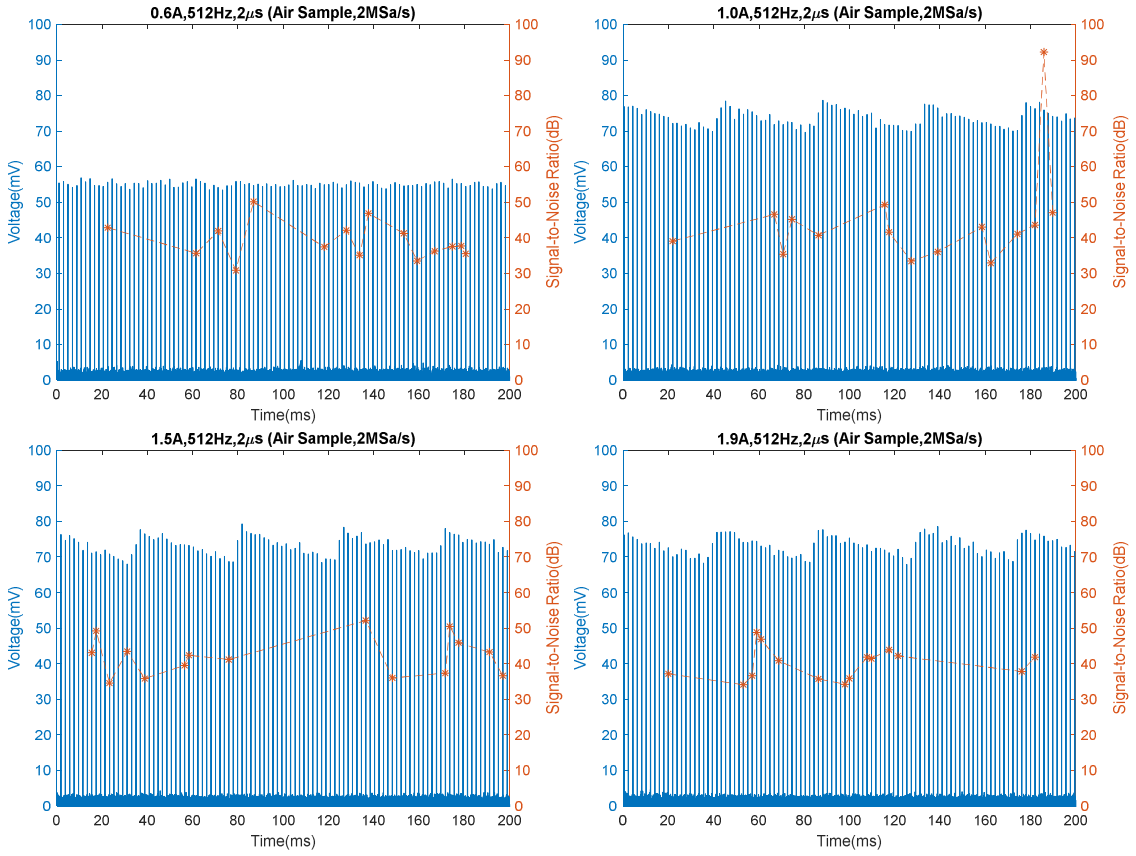

Fig.6-5. Illustration of the PO signal in time domain and SNR calculation at random pulses (LED current was selected as 0.6 A, 1 A, 1.5 A, and 1.9 A. Fifteen random pulses were selected to demonstrate the fluctuation of SNR across time.)

The second problem was the incapability to remove noise signal $n(t)$ from the PO signal $X(t)$. This problem was applied to both of the methods. The locating of the pulses simplified the amplitude calculation and measurement; however, it also made further noise reduction impossible by removing the modulation of the infrared radiation.

The third problem was the ripples in the PO signal generated from the LED driver. When the LED driving current was set at higher than 1.0A, the driver cannot provide smooth current. Therefore, ripples were detected in the corresponding PO signals (Fig.6-5).

A spectral analysis program was written with MATLAB® software to analyze the PO signal in frequency domain with Fast Fourier Transform (FFT) method (Fig.6-6). The Fourier expansion of a pulse signal included three parts: the DC component, the fundamental sinusoidal component, and the harmonic sinusoidal components (Smith, 1999). Therefore, the PO signal could be written as follows (Eq.6.7):

$$X(t) = n(t) + A\tau f + \sum_{m=1}^{\infty} \frac{2A}{m\pi} sin(\pi m\tau f)\, cos(2\pi f m t) \tag{6.7}$$

The obtained spectra would have strong frequency components at discrete frequency positions ($mf, m = 1,2,3,\cdots$), which was the integer times of the pulse frequency, f (Hz). Meanwhile, the noise signal $n(t)$ resulted in frequency components that resided in the whole frequency range. The strength of the noise signal decreased at higher frequency positions because of the characteristics of Flicker noise (Voss and Clarke, 1976). The power spectral density analysis of the PO signal supported this conclusion as the peaks positioned at the integer times of the fundamental frequency. Meanwhile, the power density of the noise decreased when the frequency increased (Fig.6-6).

Since the signal part and the noise part in the PO signal could be more clearly separated in frequency domain, it was necessary to find a suitable method to utilize this characteristic to amplify the signal $x(t)$ while suppress the noise signal $n(t)$.

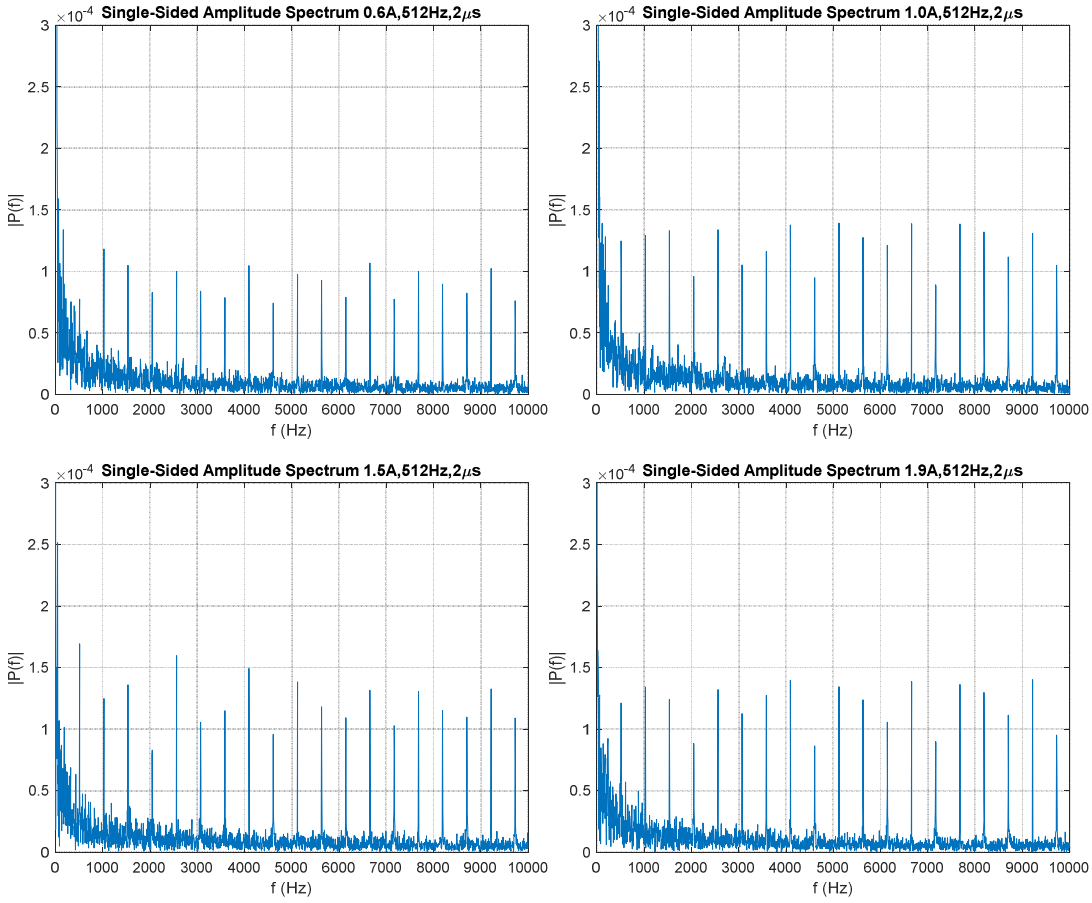

Fig.6-6 Illustration of spectral analyses of the PO signals shown in Fig.6-5 in 0-10 kHz frequency range

6.2.2.2 Design of a lock-in amplifier

Lock-in amplifiers were commonly used to process signals from infrared sensors to improve the sensors' performance by their selectively amplification of the signals (Silver and Chen, 2006). Optical choppers were used to modulate the infrared emission from the infrared radiation sources. Therefore, the useful, infrared measurement signal could be distinguished from the noise in the frequency domain. A lock-in amplifier could utilize this difference to amplify the infrared measurement signal with desired frequency components. Since most part of the noise signal was not amplified, the sign-to-noise ratio of the measurement signal was improved. In the designed MIR CO sensor, the LED's infrared emission was naturally modulated. Therefore, the optical chopper was not required.

The phase sensitive detection method was the basis of a lock-in amplifier (Scofield, 1994). A periodic reference signal was generated by the amplifier and was multiplied to the periodic input signal. When the two signals had the same frequency, the product was only related to the phase difference between the signals. Therefore, the lock-in amplifier could selectively amplify a signal with a certain frequency components by minimizing the bandwidth of the noise signal to a very tiny intervals. The output value of a lock-in amplifier was determined by the amplitudes and the phase difference of the two signals.

In practice, two reference signals with a phase shift of $\pi/2$ was used, so the measurement of the phase differences between the input signal and the reference signals would be unnecessary (Sonnaillon and Bonetto, 2005). Lock-in amplifiers could be designed in either digital or analog form (D'Amico et al., 2010; Davies and Meuli, 2010). A digital lock-in amplifier was more favorable as it had better performance (lower phase noise, better frequency range, and flexibility) than its analog counterpart (Dixon and Wu, 1989) and it could be implemented as a dedicated signal processer (Gaspar et al., 2004) or written as a program (Davies and Meuli, 2010).

1. Theoretical derivation of lock-in amplifier

A theoretical derivation was performed for the MIR CO sensor, as the input signal to the lock-in amplifier, the PO signal, was a pulse signal (Eq.6.6) instead of a sinusoidal signal in most literature (Dixon and Wu, 1989; Scofield, 1994). The Fourier expansion (Eq.6.8) of the PO signal showed that it contained periodic components of $\sum_{m=1}^{\infty} \frac{2A}{m\pi} sin(\pi m\tau f)\, cos(2\pi f m t)$, which could be applied in the theoretical derivation of lock-in amplifier.

Two sinusoidal reference signals (shown in Eq.6.8), $R(t)$ and $\bar{R}(t)$, were introduced and multiplied with the PO signal $X(t)$. The reference signals were designed with a phase shift of $\pi/2$ to remove the procedure to measure the phase differences between the PO signal and the reference signals.

$$R(t) = cos(2\pi\Omega t + \phi), \bar{R}(t) = sin(2\pi\Omega t + \phi) \tag{6.8}$$

where Ω was the frequency (Hz) of the reference signals and ϕ was the phase (radian) difference between the reference signals and the original signal. When the frequency, Ω, of the reference signals equaled to the frequency (Hz), kf, of a certain sinusoidal component in the PO signal $X(t)$, the products would contain two DC components as shown in Equation 6.9 and Equation 6.10:

$$\begin{aligned} X(t)R(t) = {} & \frac{2A}{k\pi} sin(\pi k\tau f) cos(2\pi f k t) cos(2\pi\Omega t + \phi) \\ & + \left[n(t) + A\tau f \; + \sum_{m=1}^{\infty} \frac{2A}{m\pi} sin(\pi m\tau f)\, cos(2\pi f m t) \right] cos(2\pi\Omega t \\ & + \phi) = \frac{A}{k\pi} sin(\pi k\tau f)[cos(\phi) + cos(4\pi f k t + \phi)] + \cdots \end{aligned} \tag{6.9}$$

$$X(t)\bar{R}(t) = \frac{2A}{k\pi} sin\left(\pi k \frac{\tau}{T}\right) cos(2\pi fkt) sin(2\pi\Omega t + \phi)$$
$$+ \left[n(t) + A\tau f + \sum_{m=1}^{\infty} \frac{2A}{m\pi} sin(\pi m\tau f)\, cos(2\pi fmt) \right] sin(2\pi\Omega t) \qquad (6.10)$$
$$= \frac{A}{k\pi} sin(\pi k\tau f)[sin(\phi) + sin(4\pi fkt + \phi)] + \cdots$$

The multiplication of the reference signals and the PO signal altered the original spectra distribution of the PO signal. One sinusoidal component in the PO signal was relocated to the DC position, while the remaining frequency components would move to higher frequency positions. The useful DC components in the products $X(t)R(t)$ and $X(t)\bar{R}(t)$ could be separated using low-pass filters (LPFs):

$$Y(t) = X(t)R(t)|_{DC} = \frac{A}{k\pi} sin(\pi k\tau f) cos(\phi) \qquad (6.11)$$

$$\bar{Y}(t) = X(t)\bar{R}(t)|_{DC} = \frac{A}{k\pi} sin(\pi k\tau f) sin(\phi) \qquad (6.12)$$

The separated DC components, $Y(t)$ and $\bar{Y}(t)$, were only related to the phase difference ϕ (rad) between the PO signal and the reference signals. The phase difference could be removed by adding the squares of the $Y(t)$ and $\bar{Y}(t)$, which made it possible to obtain the amplitude of the PO signal, A (Eq.6.13):

$$A = \frac{k\pi}{sin(\pi k\tau f)} \sqrt{[Y(t)]^2 + [\bar{Y}(t)]^2} \approx \frac{1}{\tau f} \sqrt{[Y(t)]^2 + [\bar{Y}(t)]^2} \qquad (6.13)$$

where the form of $sin(\pi k\tau f)$ was approximated to $\pi k\tau f$, since the product τf was very small based on the LED settings.

In practice, the form of $\sqrt{[Y(t)]^2 + [\bar{Y}(t)]^2}$ was used as the output signal of the lock-in amplifier (LO signal). The value of the LO signal was determined by the pulse frequency f, pulse width τ,

and pulse amplitude A of the PO signal. As a result, a gain of τf was added to the amplitude while the gain for noise part was close to zero.

2. Lock-in amplifier software implementation

A lock-in amplifier was written in LabVIEW software and was added to the developed data acquisition program for the preamplifier as a signal processing algorithm. Since the PO signal was a discrete time signal with limited length, the reference signals were generated as two discrete, sinusoidal signals with the same length of the PO signal. The phase difference of $\pi/2$ between the two reference signals was generated by using a Hilbert transform on one of the sinusoidal signal. The amplitude of the reference signals was selected as one. The frequency of the reference signals was determined based on the spectral analysis of the PO signal under different LED driving settings.

The DC components $Y(t)$ and $\bar{Y}(t)$ (Eq.6.11 and Eq.6.12) were separated by two LPFs with the same parameters. The LPFs in the lock-in amplifier were critical for the overall amplifier performance. The LPFs should have a very low cutoff frequency and a very narrow transient band to effectively separate the DC components, $Y(t)$ and $\bar{Y}(t)$, from other frequency components. Ripples in the passband or stopband were not favored, as the ripples in passband might generate an unexpected fluctuation of the LO signal when the LED's driving frequency changed slightly. Ripples in the stopband might coincide with some of the non-DC spectral peaks and resulted in unexpected noise, especially for the FIR filter, which had multiple stopband ripples (Lim and Parker, 1983).

The LabVIEW software could easily implement a finite impulse response (FIR) filter or an infinite impulse response (IIR) filter with its built-in functions. However, the requirement of ripples in passband and stopband removed the FIR filter or some IIR filters (Chebyshev and elliptical filter) from the candidate list, because of the ripples in their stopband or passband

(Smith, 1999). Butterworth filter was the only type of IIR filter with smooth response in both passband and stopband. Therefore, Butterworth filter was selected as the LPFs used in the lock-in amplifier algorithm. The settings of Butterworth filter, such as the cutoff frequency and the order of the filter, would be determined by analyzing the spectral characteristics of the signals $X(t)R(t)$ and $X(t)\bar{R}(t)$.

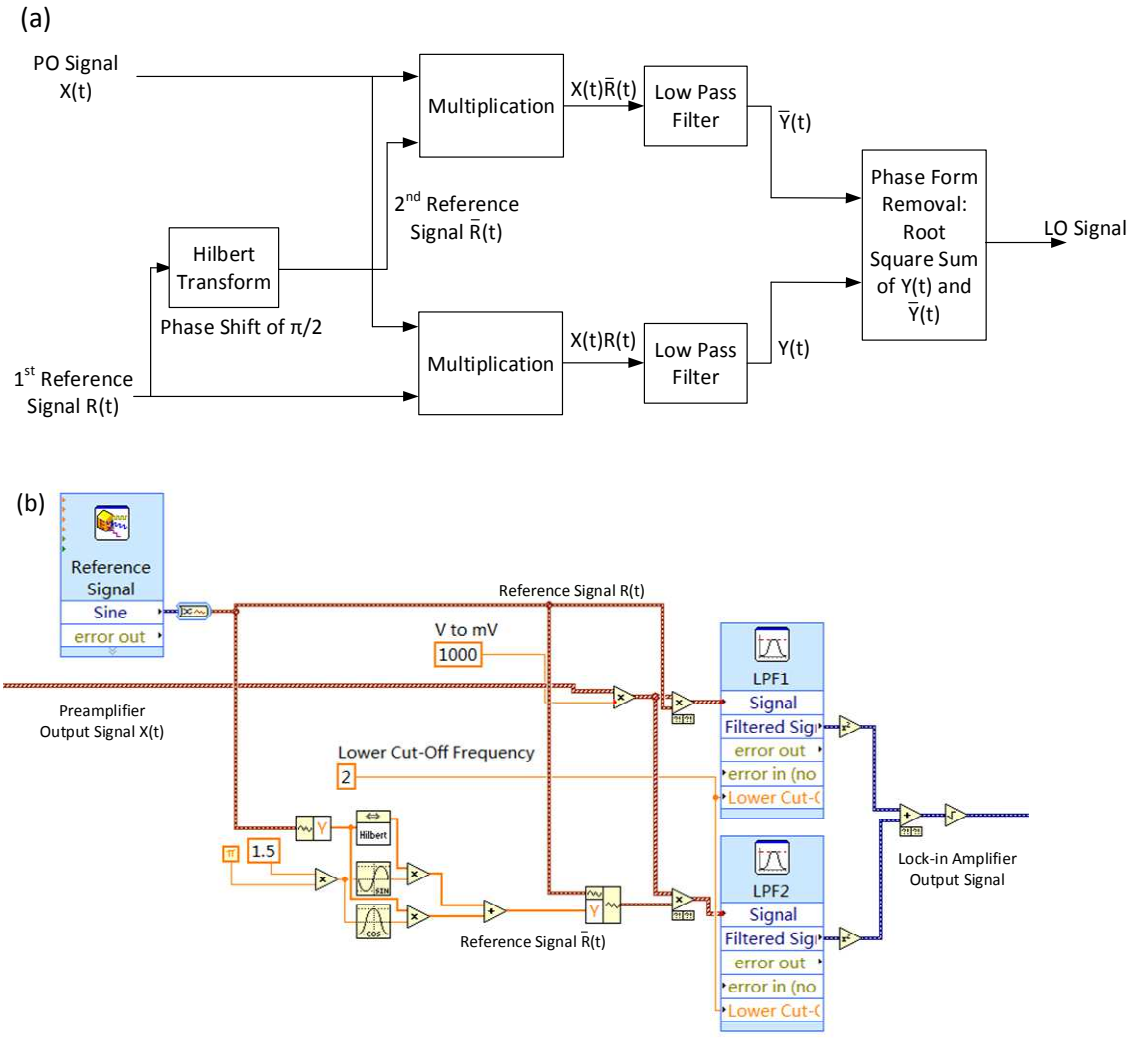

Fig.6-7 Implementation of a lock-in amplifier algorithm in the data acquisition program: a) block diagram of the lock-in amplifier algorithm; b) the lock-in amplifier algorithm written with LabVIEW® software.

6.2.3 Signal processing procedures

The designed lock-in amplifier algorithm was used to amplify the signal and suppress the noise in the PO signal. The LO signal, whose amplitude was related to the intensity of the received infrared radiation at the photodetector, was used in the signal processing procedures to calculate CO concentration.. However, the infrared absorbance A (dimensionless) was the value that directly related to the CO concentration C (mol·L^{-1}) according to the Beer-Lambert law (Eq.6.14). The LO signals required additional processing to obtain the infrared absorbance.

The analysis described in the Section 2.4.4 demonstrated that the infrared absorbance A was calculated from the attenuation of the infrared radiation intensity ,ΔI (mV), and the infrared emission intensity of the LED, I_o (mV):

$$A \approx \frac{1}{ln10}\frac{\Delta I}{I_o} \tag{6.14}$$

The design of the MIR CO sensor did not include a reference channel to measure the real-time intensity of the infrared emission from the LED. Therefore, the infrared emission intensity of the LED could be only measured before or after the CO measurement by filling the gas cell with infrared transparent gases, such as pure N_2. By comparing the LO signal with N_2 sample and CO samples, the infrared absorbance could be determined.

A calibration on the MIR CO sensor was then performed to determine the relationship between infrared absorbance and the CO concentration, which required to measure the infrared absorbance of the gas samples with known CO concentrations. The obtained calibration model was used to determine the CO concentrations in unknown gas samples. The measured gas phase CO concentrations were then used in the calculation of the dissolved CO concentrations according to the designed gas extraction process.

Therefore, the signal processing procedures of the MIR CO sensor included two steps to convert the LO signal to a dissolved CO concentration (Fig.6-8):

1) Calculate the gas phase CO concentration from the infrared absorbance of a CO gas sample;
2) Calculate the dissolved CO concentration based on the volume of the liquid sample and the amount of the extracted CO.

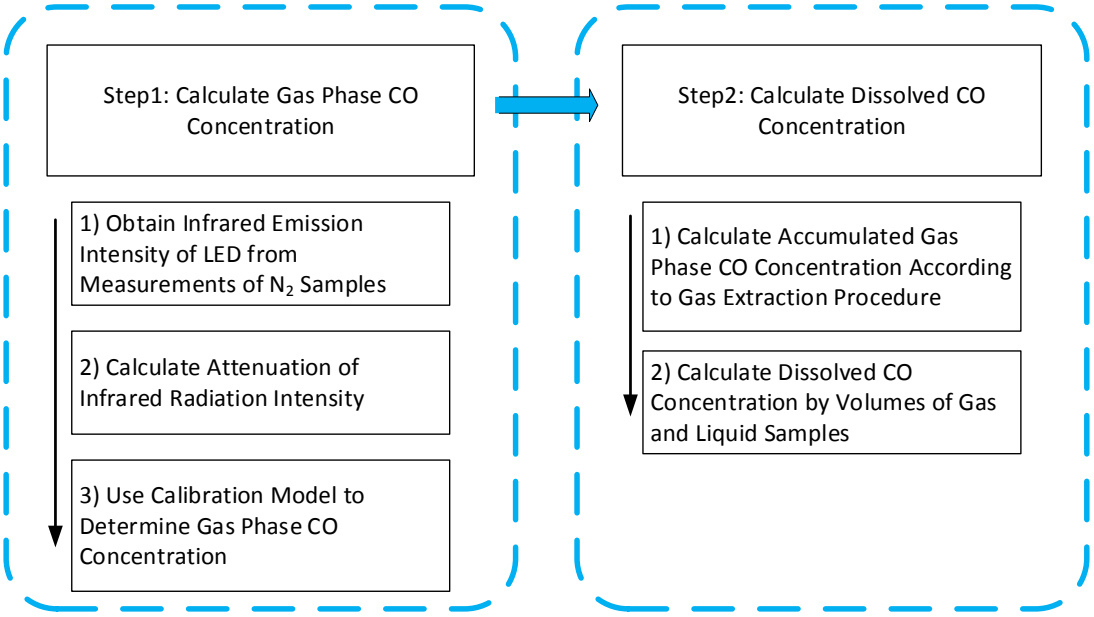

Fig.6-8 Overview of the signal processing procedures for the dissolved CO measurement system

Step1: Gas phase CO concentration calculation

1) Calculation of the infrared emission intensity of the LED

The data acquisition program collected a signal contained 10 million data points in each infrared measurement. Thus, the LO signal would have the same number of data points. However, the LPFs in the lock-in amplifier algorithm would introduce to a settling time to the LO signal. Therefore, only the last five million data points were used in data analysis (Fig.6-9b). The mean

and standard deviation of the five million data points were used as the measurement result of the gas sample.

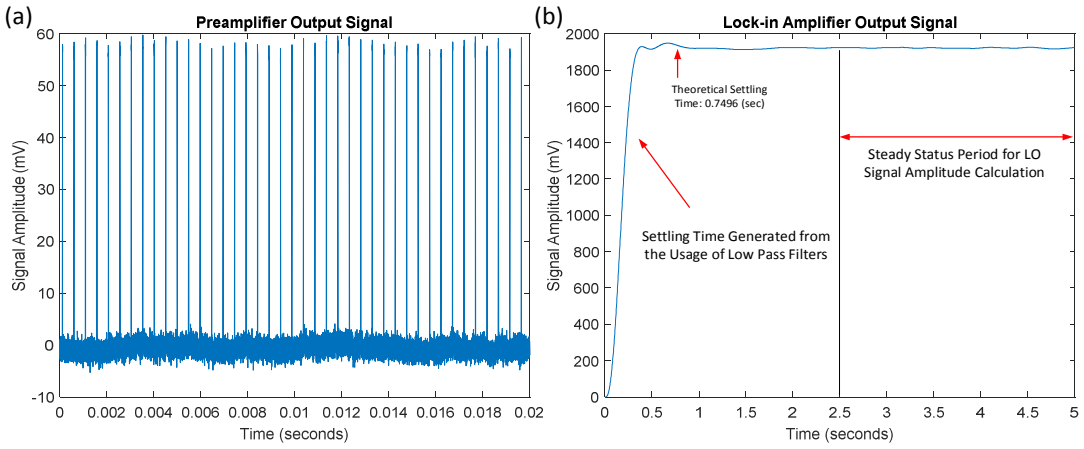

Fig.6-9 Demonstration of the PO signal and the corresponding LO signal (The PO signal was only shown in 0.02 second lengths to display the pulses. Length of the PO signal was five seconds).

Because there was no reference channel in the design of the MIR CO sensor, the infrared emission intensity of the LED was measured with N_2 as the gas sample. Although the lock-in amplifier greatly improved the SNR of the signal, it still had some variations in the measurement results. Therefore, each N_2 sample was measured five times to had a better estimation of the infrared emission intensity of the LED. The five measurements were then processed by a weighted average method shown in Equation 6.15 to obtain an averaged value $\bar{x}$ and standard deviation $\bar{\sigma}$:

$$\bar{x} = \frac{\sum_{i=1}^{5} \frac{x_i}{\sigma_i^2}}{\sum_{i=1}^{5} \frac{1}{\sigma_i^2}}, \bar{\sigma} = \frac{1}{\sqrt{\sum_{i=1}^{5} \frac{1}{\sigma_i^2}}} \tag{6.15}$$

in which x_i was the mean value of the ith measurement and σ_i was the corresponding standard deviation.

The average value $\bar{x}$ in Equation 6.15 was used as the infrared emission intensity of the LED. Two measurements of N_2 samples were performed before and after the CO measurements to determine the change of the LED infrared emission intensity during the CO measurements. The average of these two measurements were used as the infrared emission intensity I_o for absorbance calculation (Eq.6.16).

$$I_o = (I_{o1} + I_{o2})/2 \tag{6.16}$$

where I_{o1} was the infrared emission intensity obtained before the CO measurement, I_{o2} was the infrared emission intensity obtained after the CO measurement.

2) Calculation of infrared absorbance

The infrared absorbance used to determine CO concentration was calculated based on Equation 6.14. The transmitted infrared radiation intensity I by the gas samples was obtained with the same method as that of the infrared emission intensity of the LED I_o. The gas samples were measured five times with the MIR CO sensor. The five measurements were then processed with the described weighted average method (Eq.6.15) to obtain the average value, which represented the transmitted infrared radiation intensity I and was used to calculate the infrared absorbance A of the gas samples.

3) Calculation of CO concentration from calibration model

The calibration of the MIR CO sensor generated a calibration model between the infrared absorbance and corresponding CO concentration (Eq.6.17), which would be used to calculate the CO concentration, C (mg/L), in gas phase.

$$A = 0.0019974C + 0.00022867, R^2 = 0.9971 \quad (6.17)$$

The infrared absorbance A (dimensionless) of the unknown sample was obtained based on the procedure stated in the Step1.

Step 2: Dissolved CO concentration calculation

The dissolved CO concentration was calculated by estimating the total amount of CO in a liquid sample with known volume, V_L (L). The total amount of CO was obtained by using the accumulated gas phase CO concentration, C_G (mg/L), and the volume of the MIR CO sensor gas cell, V_G (L):

$$C_{CO} = C_G V_G / V_L \quad (6.19)$$

A gas extraction system was used for the purpose of completely degassing the dissolved CO in a liquid sample. A special, three-cycle gas extraction procedure was used in the measurement to achieve a maximum gas extraction ratio. The procedure was designed to vacuum the gas cell between intervals of gas extraction periods to improve the gas transportation from the gas extraction system to the MIR CO sensor (Fig.6-10).

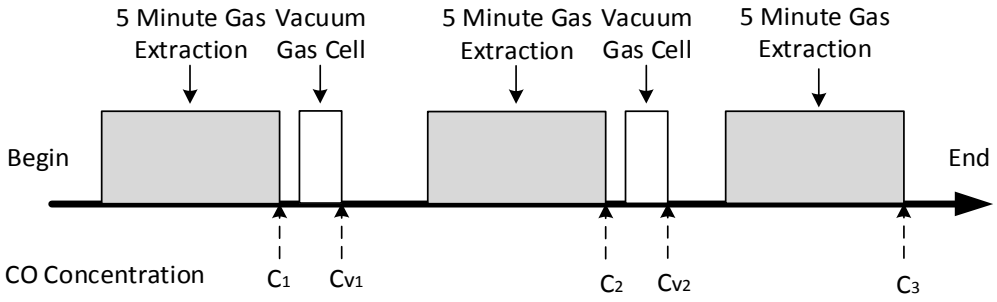

Fig.6-10. Illustration of the designed gas extraction process for the accumulated gas phase CO concentration C_G calculation.

Therefore, the accumulated gas phase CO concentration C_G was calculated from the repeated measurements during the three gas extraction cycles as Equation 6.20:

$$C_G = C_1 + C_2 + C_3 - (C_{V1} + C_{V2}) \quad (6.20)$$

where C_i $(i = 1,2,3)$ represented the measured CO concentration (mg/L) in the gas sample after the ith extraction cycle and C_{Vi} $(i = 1,2)$ represented the measured CO concentration (mg/L) in the residual gas sample after vacuum sweep in the ith cycle. The subtraction of C_{V1} and C_{V2} was applied as these residual CO concentrations were included in the measured CO concentration C_2 and C_3 of the next gas extraction cycles, respectively.

6.3 Results and Discussions

6.3.1 Lock-in amplifier parameters

The parameters of the designed lock-in amplifier was listed as follows:

1) The frequency of the reference signal was determined as 8,192 Hz;
2) The LPFs in the lock-in amplifier were a pair of three-order Butterworth filters with a cutoff frequency of 2 Hz.

The PO signals with three different LED frequencies: 512 Hz, 2 kHz (2,048 Hz actually), and 8 kHz (8,192 Hz), were analyzed with the FFT method (Fig.6-11) to determine the frequency of the reference signals. The results showed that the 8,192Hz was a suitable reference frequency for the three types of LED settings. This reference frequency also was relatively free of the noise interference as the majority of the noise signal existed in the lower frequency positions.

The calculation of the response time (in the form of settling time of the filter) of Butterworth filter was shown in Table.6-1. The results showed that a small cutoff frequency and a high order

of filter would dramatically increase the settling time of the filter and decrease the response time of the lock-in amplifier.

The order of an IIR filter determined the width of the transition band between the filter's passband and stopband. A higher order filter had a narrower transition band, which resulted in a faster attenuation over the cutoff frequency. For the lock-in amplifier, a narrower transition band resulted in fewer noise in the LO signal. An evaluation was performed by comparing the ratio between the standard deviation and the mean value of the LO signal with different PO signals used as the input to the lock-in amplifier. The ratio was used to examine whether the wide transition band introduced unnecessary noise to the DC part. The order of the LPF was compared in four discrete levels from two to five as shown in Table.6-2. The results in Table.6-1 and Table.6-2 showed that a three-order Butterworth LPF would be appropriate with acceptable settling time and transition band width.

Table.6-1 List of settling time of Butterworth LPF at different order of filter and cutoff frequency

Order of Filter	Settling Time (seconds)				
	Cutoff Frequency (Hz)				
	1	2	10	25	100
2	1.0483	0.5241	0.1048	0.0419	0.0105
3	1.4992	0.7496	0.1499	0.0060	0.0150
4	1.6589	0.8295	0.1659	0.0664	0.0166
5	2.2065	1.1033	0.2207	0.0883	0.0221

* Sampling rate was 2 MS/s

Table.6-2 List of the ratio between standard deviation and the mean value of steady state LO signal under different LED settings

Order of Filter	S.D./Mean (%)				
	LED Driver Settings				
	0.6 A, 512 Hz, 10 μs	0.6 A, 2 kHz, 10 μs	1.5A, 2 kHz, 10 μs	0.2 A, 8 kHz, 10 μs	0.6 A, 8 kHz, 5 μs
2	1.2720	0.2033	0.1637	0.0612	0.1325
3	1.2546	0.1897	0.1619	0.0599	0.1311
4	1.2484	0.1779	0.1639	0.0584	0.1308
5	1.2478	0.1722	0.1685	0.0568	0.1313

*Standard deviation (S.D.) and mean value was obtained from output signals in 2.5 seconds to 5 seconds. Lowpass filter cutoff frequency was 2 Hz.

The spectral analysis of the input signals to the LPF, which were the products $X(t)R(t)$ and $X(t)\bar{R}(t)$ in Equation 6.9 and Equation 6.10, was performed to determine the cutoff frequency of the filter (Fig.6-12). The PO signals $X(t)$ were selected with different LED pulse frequencies and pulse widths to examine whether there was a frequency change of the DC components in different LED settings. The result showed that DC components of the products were located at about 1 Hz position in the spectra, which implied that there was a slight frequency difference between the reference signals and the PO signal. The frequency responses of three LPFs with cutoff frequency set at 1 Hz, 2 Hz, and 2.8 Hz and an order of filter of 3 were generated (Fig.6-13). The spectral analysis of the LPFs and the input signals to the LPFs showed that 2 Hz was an appropriate cut-off frequency. A cutoff frequency set at 1 Hz would remove part of the useful frequency components.

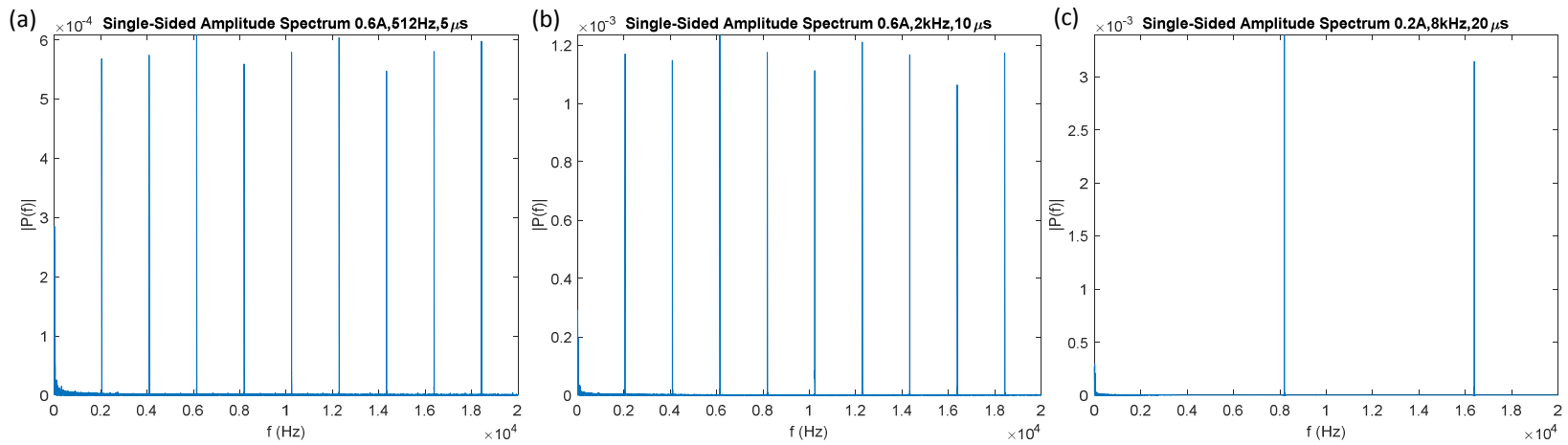

Fig.6-11. Illustration of spectral analyses of the PO signal with FFT method in 0-20 kHz frequency range (LED driving current, Pulse Frequency, Pulse Width: a) 0.6 A, 512 Hz, 5 μs; b) 0.6 A, 2 kHz, 10 μs; c) 0.2 A, 8 kHz, 20 μs.)

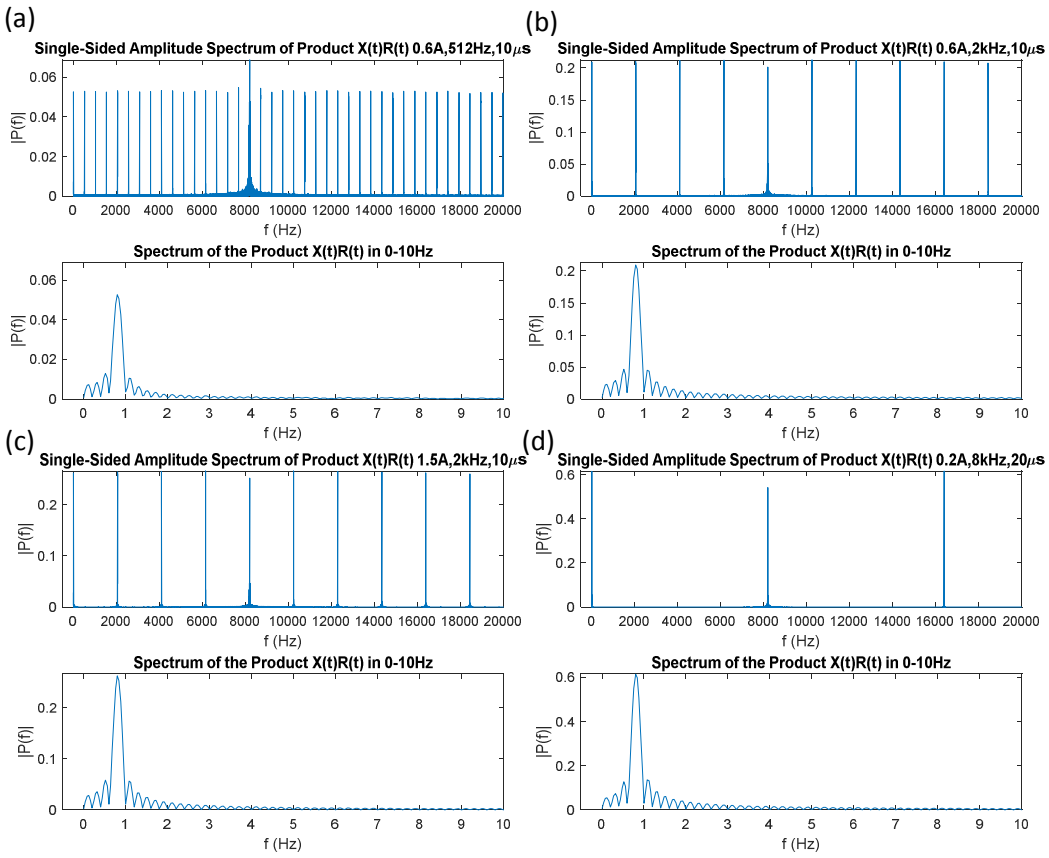

Fig.6-12 Spectral analyses of the signal of product $X(t)R(t)$ under different LED settings (LED driving current, Pulse Frequency, Pulse Width: a) 0.6 A, 512 Hz, 10 μs; b) 0.6 A, 2 kHz, 10 μs; c) 1.5 A, 2 kHz, 10 μs; d) 0.2 A, 8 kHz, 20 μs.)

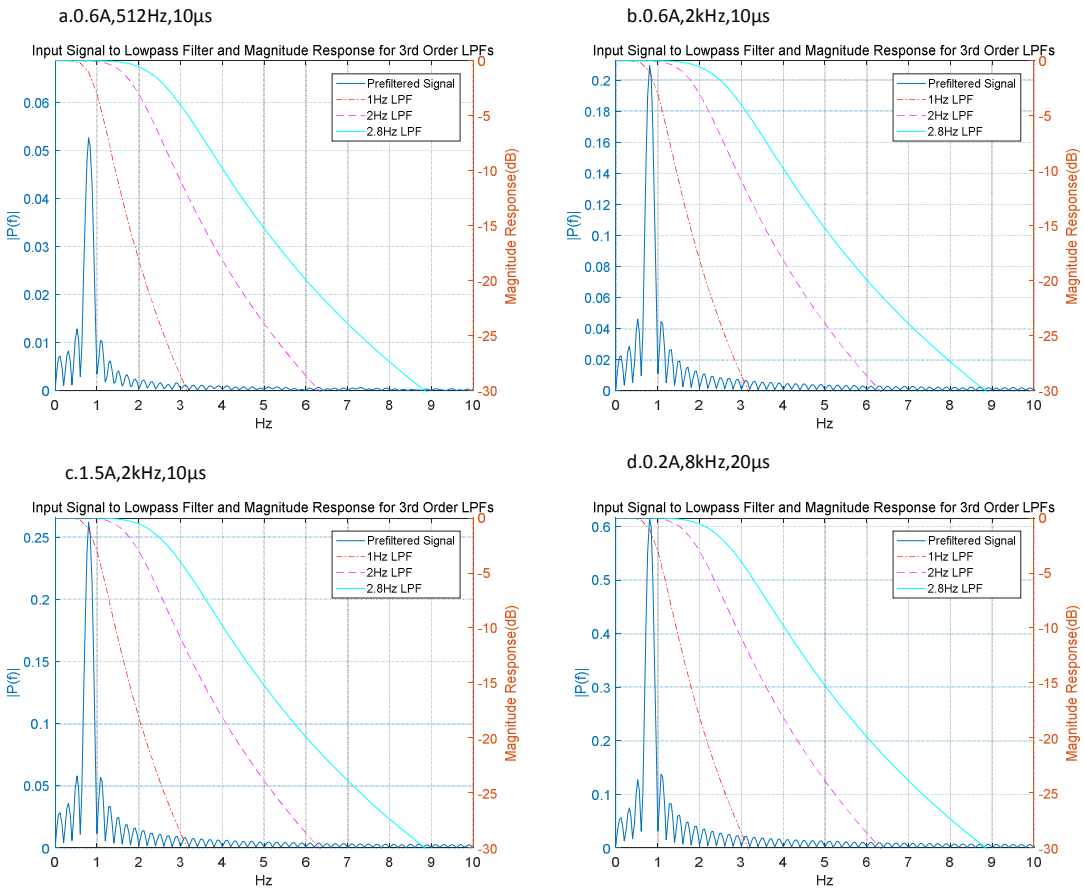

Fig.6-13 Spectral analyses of the signal of product $X(t)R(t)$ under different LED settings with different LPF cutoff frequency (LED driving current, Pulse Frequency, Pulse Width: a) 0.6 A, 512 Hz, 10 μs; b) 0.6 A, 2 kHz, 10 μs; c) 1.5 A, 2 kHz, 10 μs; d) 0.2A, 8 kHz, 20 μs.)

6.3.2 Performance evaluation of the lock-in amplifier

The performance of the designed lock-in amplifier was compared by calculating the amplitude of the PO signals and the LO signals to show the signal change from the lock-in amplifier (Fig.6-14). The amplitude of the PO signals was calculated by the derivative method, which used the amplitude change between adjacent data points to detect the position of the pulses. The amplitude of the LO signals was obtained when the LO signals entered a stable status. The PO signals and the LO signals used had a signal length of five seconds and a total data points of ten millions. The

amplitude measurements were performed on the rear part of the signals, from the 2.5 seconds to 5 seconds, which included the last five million data points.

The results showed that the amplitude of the LO signals followed the theoretical derivation in Equation 6.13, which stated the amplitude was determined by the LED driving current, the LED pulse frequency, and the LED pulse width (Table.6-3, Figure.6-14). It was found that the ripples in the PO signal, which might disrupt the amplitude measurement with the derivative method, could be overcome by the lock-in amplifier (Figure.6-14c). Meanwhile, the introduction of the lock-in amplifier selectively amplified the PO signal, which was shown by the relative unchanged standard deviation of the LO signal. Therefore, the design of the lock-in amplifier had achieved its primary objective: to amplify the modulated signal while to suppress the noise in the PO signal.

Table.6-3 Comparison of the amplitude measurement results of the PO signal and the LO signal under different LED settings

No.	LED Settings	PO Signal		Steady State LO Signal	
		Mean (mV)	Standard Deviation (mV)	Mean (mV)	Standard Deviation (mV)
a	0.2 A, 512 Hz, 10 μs	22.96	1.91	103.94	2.16
b	0.6 A, 512 Hz, 10 μs	58.59	1.82	264.11	2.29
c	1.5 A, 512 Hz, 10μs	74.79	2.97	343.52	2.37
d	0.6 A, 2 kHz, 20 μs	52.26	1.86	1920.79	2.09

*1) Lock-in amplifier: 8,192Hz reference frequency. LPF: 2 Hz cutoff frequency, three-order Butterworth filter; 2) The data (d) with 2 kHz pulse frequency had less PO signal amplitude to that of data (b) with 512 Hz frequency due to the limitation of the LED driver; 3) The standard deviation of the PO signal for data (c) was higher because of the ripples generated by the LED driver.

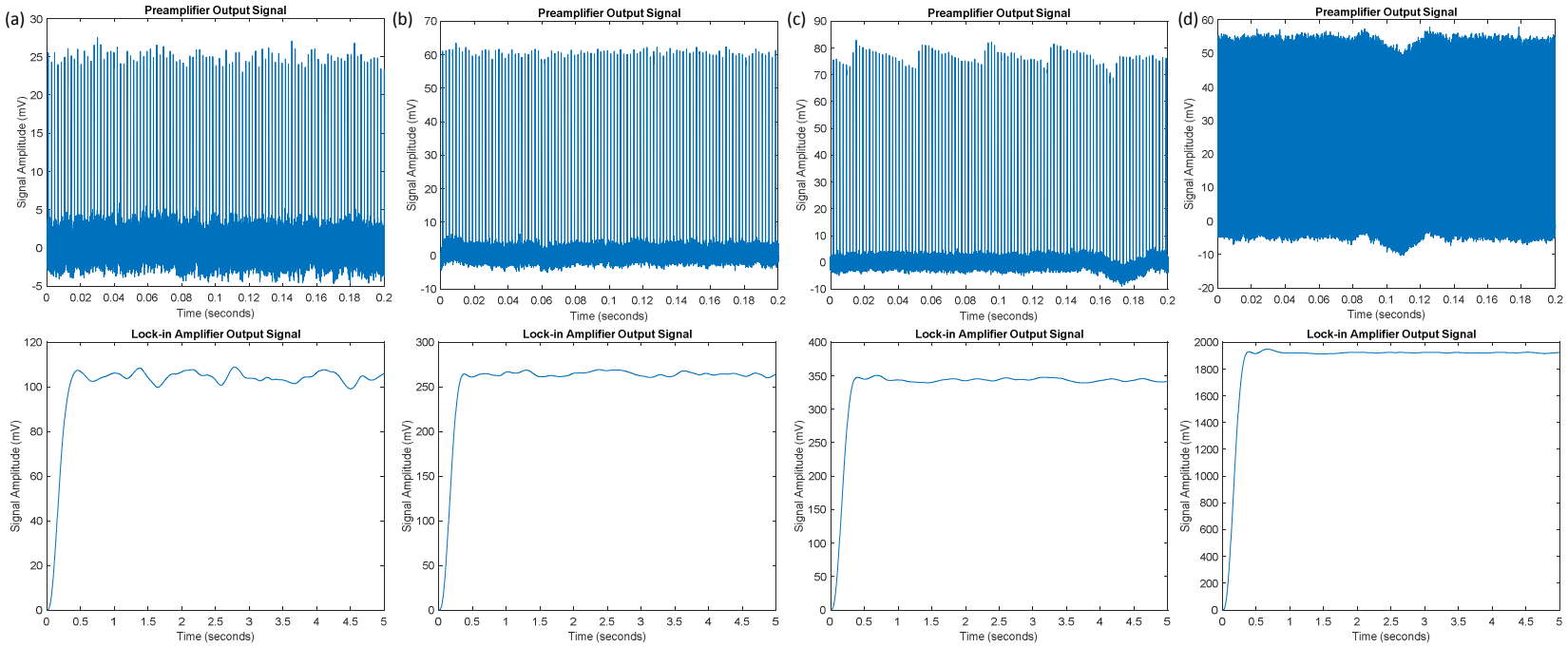

Fig.6-14 Time domain PO signals and LO signals comparison (LED driving current, Pulse Frequency, Pulse Width: a) 0.2 A, 512 Hz, 10 μs; b) 0.6 A, 512 Hz, 10 μs; c) 1.5 A, 512 Hz, 10 μs; d) 0.6A, 2 kHz, 20 μs.)

6.4 Conclusions

Signal processing procedures were developed for the developed dissolved CO measurement system, which were used to calculate dissolved CO concentration from the PO signal. The data acquisition system was described firstly as the basis of the signal processing procedures. A signal enhancement method, which was implemented as a lock-in amplifier, was designed and evaluated to overcome the special obstacles generated by the low power LED of the developed MIR CO sensor. The developed procedures included two major steps. The first step was to measure the gas phase CO concentration from the PO signal. The second step was to calculate the dissolved CO concentration from the obtained gas phase CO concentration based on the designed gas extraction procedure.

CHAPTER VII

EVALUATION OF A COMMERICAL DISSOLVED H_2 SENSOR

Abstract

The ratio between dissolved CO and H_2 concentrations affects the final product composition and CO/H_2 conversion efficiencies. Therefore, it is of practical significance to monitor and control the dissolved H_2 concentration in the syngas fermentation process. A commercial, electrochemical dissolved H_2 sensor was tested to find an appropriate method to integrate it into the developed dissolved CO measurement system. Two installation methods, the flow-through cell setup and the submerged probe setup, were compared. The comparison results showed that the submerged probe setup was the appropriate method to integrate the dissolved H_2 sensor with the developed dissolved CO measurement system. It was also demonstrated that the liquid preparation method with a magnetic stirrer would generate supersaturated H_2 in the liquid sample. The mean absolute percentage error (MAPE) of the dissolved H_2 concentration was around 11% with the submerged probe setup.

Keywords: Syngas fermentation, Electrochemical dissolved H_2 sensor, Dissolved H_2 concentration

7.1 Introduction

The ratio between dissolved CO and H_2 concentrations affected the dominant chemical reactions in the syngas fermentation and further determined the composition of final products and the conversion rates of CO and H_2 (Devarapalli and Atiyeh, 2015). Therefore, the measurement and control of the dissolved H_2 concentration during the syngas fermentation process were important and necessary.

The dissolved H_2 concentration could be measured by a direct method with membrane coated electrochemical dissolved H_2 sensors (Hara and Macdonald, 1997; Kuroda et al., 1991; Sweet et al., 1980) or an indirect method which measured the extracted H_2 concentrations with dissolved H_2 extractors (Björnsson et al., 2001; Lovley & Goodwin, 1988). The details of these methods were described in Section 2.2.1.2. Currently, the electrochemical dissolved H_2 sensors were commercially available and had been reported being used in several fermentation scenarios (Adessi et al., 2012; Revsbech, 2005). Based on a thorough literature review, an electrochemical dissolved H_2 sensor (H_2 microsensor, AMT Analysenmesstechnik GmbH, Rostock, Germany) was chosen to measure dissolved H_2 concentration in this research.

The selected dissolved H_2 sensor was claimed to be free of interference from major chemicals in syngas fermentation medium by its manufacturer. It was also capable of operating under an anaerobic environment. However, there was no information from the manufacturer on the installation of this sensor into a small-size fermenter. Therefore, it was necessary to find an appropriate method to install the dissolved H_2 sensor for syngas fermentation and to integrate the sensor with the developed dissolved CO measurement system. The overall objective of this research was to determine a method to integrate the dissolved H_2 sensor into the dissolved CO measurement system and to evaluate the H_2 sensor's performance in syngas fermentation applications.

7.2 Material and Methods

7.2.1 Dissolved H_2 Sensor

The dissolved H_2 sensor included a H_2 detection probe, a pH/temperature probe, and a sensor controller. The H_2 detection probe contained three electrodes and the electrolyte for the electrochemical measurement of the dissolved H_2 concentration. The pH/temperature probe was used to provide temperature compensation during the measurement of the dissolved H_2 concentration (The pH data was not used in H_2 measurement). The sensor controller contained a preloaded program to operate the two probes and calculate the dissolved H_2 concentration. It also provided an operation interface to check the probes status and adjust the sensor parameters. The sensor controller used a RS-232 interface to upload measurement data to a computer or other data acquisition devices.

In the experiment, the sensor controller was directly connected to a laptop with a null modem RS-232 cable. A data acquisition program was developed in LabVIEW® (Release 2015, National Instruments Co., Austin, TX, USA) software to record the dissolved H_2 concentration and the liquid sample temperature every two seconds.

The primary specifications of the commercial dissolved H_2 sensor from the manufacturer were listed as follows:

a. Measurement range: 0.0002 mg/L to 3 mg/L;

b. Accuracy: < 2% of the measuring value;

c. Response time: < 2 seconds.

The sensor experiment was designed to verify the above specifications, mainly focused on the accuracy of the dissolved H_2 concentration measurement.

7.2.2 Experiment setup

7.2.2.1 Liquid sample preparation

In general, the liquid samples were prepared with the same method used to prepared liquid samples with dissolved CO described in Section 5.2.2.2. The liquid samples with dissolved H_2 were prepared by adding pressurized syngas (40% CO, 30% CO_2, and 30% H_2 in molar percentage) to reverse osmosis (RO) water in a 500 mL glass bottle. The RO water and the remaining headspace of the bottle were purged with the syngas for five minutes before adjusting the pressure to the desired value.

The dissolved H_2 concentration in a liquid sample was controlled by adjusting the syngas headspace pressure. A digital pressure gauge (DPG5600B, Omega, Norwalk, CT, USA) was used to measure the headspace pressure in the 500 mL bottle. The precise dissolved H_2 concentration C_H^{aq} (mg/L) in the liquid sample was calculated based on the Henry's law as Equation 7.1:

$$C_H^{aq} = kH_{T_s}P_H \tag{7.1}$$

in which H_{T_s} was the Henry's law constant at a certain temperature T_s, P_H was the partial pressure of H_2 in the headspace of the 500 mL bottle, k was the coefficient to convert the concentration unit from mol/L to mg/L. The temperature, T_s (K), was obtained from the pH/temperature probe. The partial pressure, P_H (psi), was calculated from the headspace pressure, P_H (psig), in the 500 mL bottle, the molar percentage M (%) of H_2, and the atmosphere pressure, P_A (mmHg), as shown in Equation 7.2:

$$P_H = M(P_H + k_P P_A) \tag{7.2}$$

in which k_P was the coefficient to transfer the unit of pressure from mmHg to psi.

The Henry's law constant, H_{T_s} (mol/L·psi), at temperature T was calculated from the standard Henry's law constant at a reference temperature $T_\theta = 298K$ (Sander, 2015):

$$H_{T_s} = H_\theta \times exp\left[\frac{-\Delta_{sol}H}{R}\left(\frac{1}{T} - \frac{1}{T_\theta}\right)\right] \quad (7.3)$$

in which $\frac{-\Delta_{sol}H}{R} = 500$ was the temperature dependent terms (K) from van 't Hoff equation for H_2 and $H_\theta = 7.8E-6$ was the Henry's law constant for H_2 ($mol \cdot m^{-3} \cdot Pa^{-1}$) at the reference temperature T_θ (Sander, 2015).

The calculation of the prepared dissolved H_2 concentration was valid when the gas phase syngas and dissolved syngas reached an equilibrium. The equilibrium was accessed by monitoring the change of the headspace pressure in a 500 mL bottle. When the headspace pressure was stabilized for a certain length of time (10-15 minutes in experiment), it was assumed the equilibrium was reached. Two methods, a stirring method and a circulation method, were used in the experiment to accelerate the process to reach equilibrium.

The circulation method was designed to establish an outside circulation path to circulate liquid samples. The circulation would facilitate the contact between the water and the syngas in the headspace, which in turn reduced the time to reach equilibrium. It would also accelerate the mass transfer within the liquid sample to obtain a sample with homogenized dissolved H_2. However, the circulation method required a large liquid sample flow rate in the system.

The stirring method was designed to use a magnetic stirrer to speed up the equilibrium. The whirlpool generated by the magnetic stirring bar would increase the contact surface of syngas to the water. The stirring also helped to get a homogenized liquid sample with same dissolved H_2 concentration. This method, however, might generate some syngas bubbles during the process, which might affect the dissolved H_2 measurements.

7.2.2.2 Sensor installation

Two flow-through cells were provided along with the dissolved H_2 sensor by the manufacturer. The cells were customized for the H_2 detection probe and the pH/temperature probe, respectively. They were connected in series to establish a liquid sample path. Because of the tendency that the flow-through cells would leak slightly when the liquid sample was pressurized, the pH/temperature probe was not installed into its specific flow-through cell. Only the H_2 detection probe was installed into its specific flow-through cell. The pH/temperature probe was placed in a vessel containing RO water and next to the simulated fermenter.

The two probes of the dissolved H_2 sensor could be also directly submerged into the liquid sample. The submerged probe setup was designed to mount the probes in rubber stoppers and installed the stoppers into a bottle with liquid samples. However, due to the limitation of the rubber stopper diameter, only the H_2 detection probe was installed into the bottle. The pH/temperature probe was placed in a different vessel like the flow-through cell setup.

Both the flow-through cell setup and the submerged probe setup were established and tested to determine the appropriate method to integrate the dissolved H_2 sensor with the dissolved CO measurement system.

1) The flow-through cell setup

The experiment setup with the flow-through cell was shown in Fig.7-1. The H_2 detection probe was vertically inserted into the flow-through cell. Two clamp holders were used to hold the cell and the probe in their relative positions to avoid liquid sample leakage. The pH/temperature probe was placed in a separate beaker (400 mL) filled with approximate 350 mL of RO water as its flow-through cell tended to leak under pressure. The H_2 detection probe and the pH/temperature probe were placed close together to avoid significant temperature difference. The flow-through cell was connected to a 500 mL bottle with a flexible rubber tubing. A peristaltic pump (7523-30,

Cole-Parmer, Vernon Hills, IL, USA) was installed between the cell and the bottle to provide a constant liquid flow rate for the dissolved H_2 measurements. Two clamps (Clamp #1 and #2) were used to control the liquid flow during the preparation of the liquid samples.

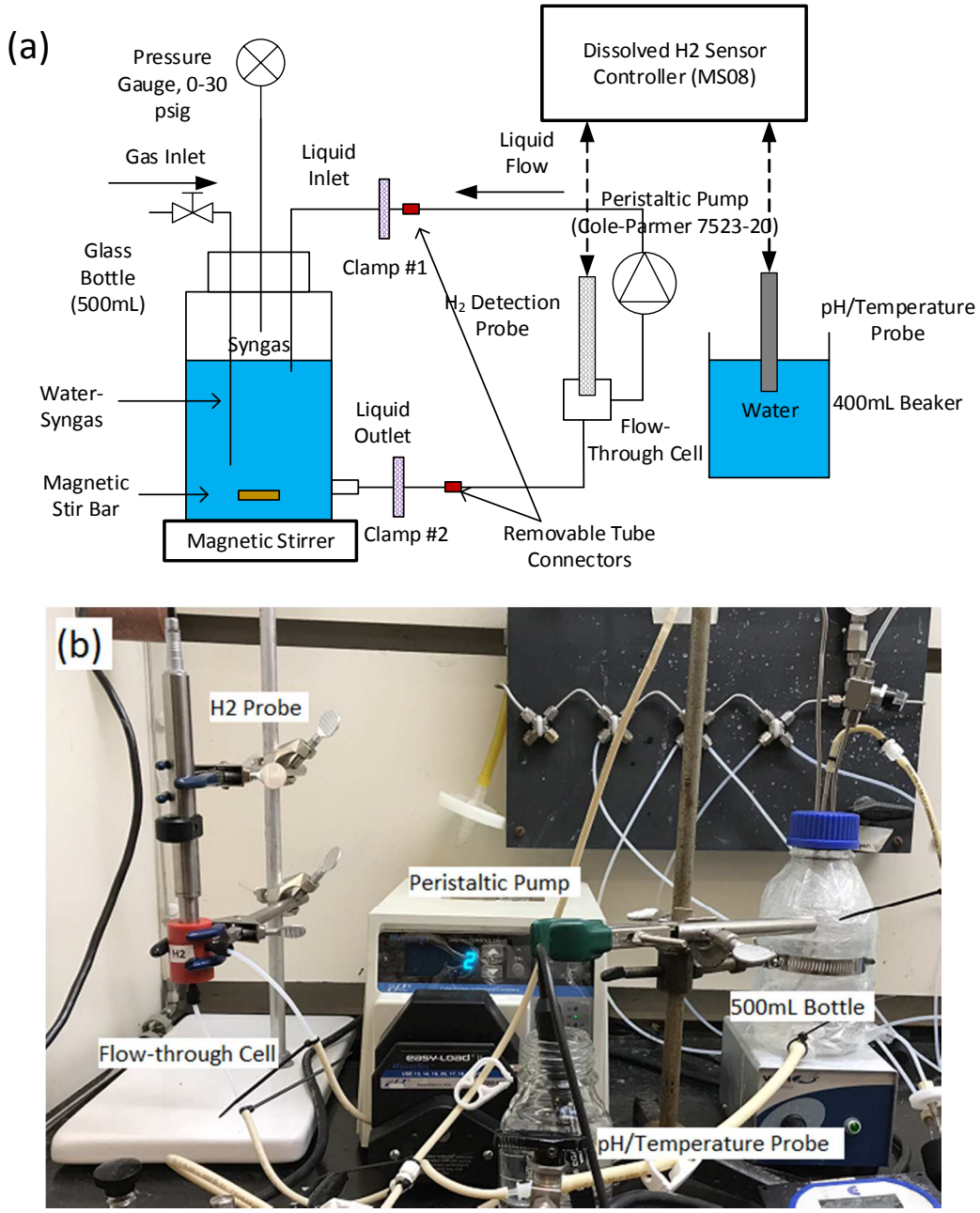

Fig.7-1 Illustration of the flow-through cell setup of the dissolved H_2 sensor: a) the schematic diagram of the test setup; b) the assembled experiment setup.

2) The submerged probe setup

The experiment setup was shown in the Fig.7-2. The H_2 detection probe was mounted on a rubber stopper (size No.6). The rubber stopper was then installed into a 100 mL glass bottle used as a sample container for the developed dissolved CO measurement system. The pH/temperature probe was placed in a beaker (400 mL) with 350 mL RO water. The two bottles were connected together with a flexible rubber tubing. A peristaltic pump (7523-30, Cole-Parmer, Vernon Hills, IL, USA) was used to circulate the liquid sample between the two bottles. Two clamps (Clamp #1 and #2) were installed on the tubing to control the liquid flow.

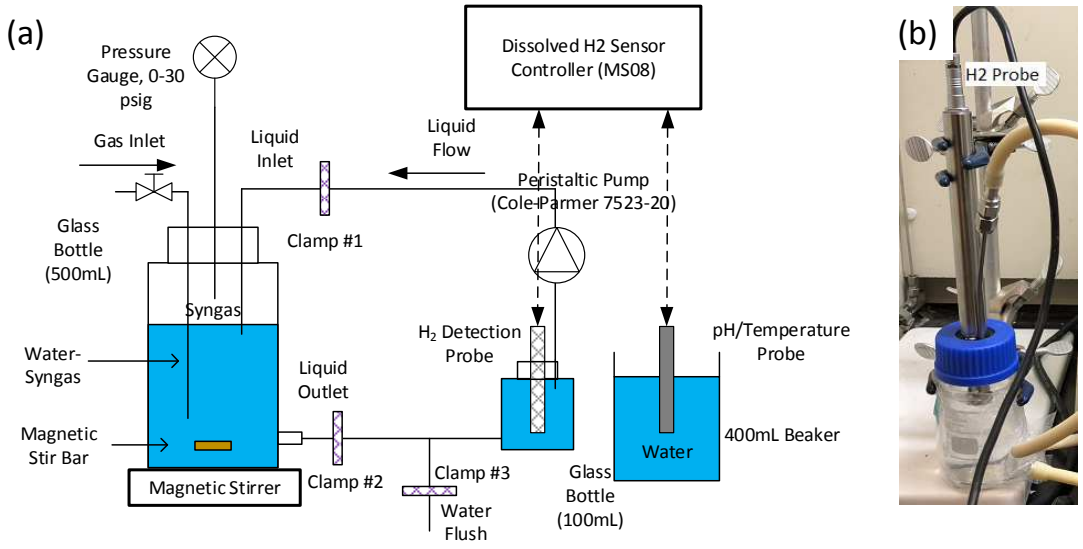

Fig.7-2 Illustration of the submerged probe setup of the dissolved H_2 sensor: a) the schematic diagram of the test setup; b) the 100 mL bottle with the H_2 detection probe.

7.2.2.3 Experiment procedures

1) The flow-through cell setup

The liquid sample was prepared firstly as the method stated in Section 7.2.2.1. The total volume of the used RO water was 400mL. The time for purging the RO water and the headspace of the

500 mL bottle with syngas was five minutes. The syngas in the headspace was pressurized to two levels, 5 psig and 15 psig, respectively. Only the stirring method was used for this setup due to the flow rate limitation of the flow-through cell. The rotation speed of the magnetic stirrer was set at the smallest (position No.1) to avoid generating strong whirlpool in the bottle. It was assumed that the equilibrium was reached when the headspace pressure inside the 500mL bottle was stable (less than 0.01 psig pressure change) for more than ten minutes.

Before each measurement, the H_2 detection probe required to be polarized with H_2-free water. Thus, the flow-through cell was separated from the 500 mL bottle to establish a path to polarize the probe with H_2-free water. The peristaltic pump was used to pump H_2-free water through the cell with a flow rate of 10 mL/min. The time for the polarization was about 60 minutes.

The dissolved H_2 sensor was ready for measurement after the equilibrium was reached and the H_2 detection probe was polarized. The prepared liquid sample was pumped through the flow-through cell at a fixed 2 mL/min flow rate by the peristaltic pump. Three independent measurements were performed for each headspace pressure. The minimal time duration for the three dissolved H_2 measurements was 50 minutes.

2) The submerged probe setup

The liquid sample in the submerged probe setup was prepared with 500 mL RO water. The extra 100 mL RO water was used to fully fill the 100 mL bottle, which contained the H_2 detection probe. The two bottles were isolated with Clamp#1 and #2 after the 100 mL bottle was full of H_2-free RO water. The preparation of liquid samples was performed in the 500 mL bottle while the polarization of the H_2 detection probe was performed in the 100 mL bottle with steady state RO water. The time for the polarization was around 30 to 40 minutes. The submerged probe setup had a short polarization time, because the H_2 detection probe was completely submerged in huge

amount of H_2-free water (around 100 mL). The sufficient water contact helped to accelerate the polarization.

The remaining RO water in the 500 mL bottle was used to prepare the liquid samples with the same procedures described in the flow-through cell setup. However, the syngas was only pressurized to 5 psig in this setup. Both the stirring method and the circulation method were used in this setup to shorten the time to reach equilibrium. The equilibrium in both methods was judged by monitoring the headspace pressure. The equilibrium was believed to be obtained when the headspace pressure was stabilized (had less than 0.01 psig pressure change) for ten minutes.

For the stirring method, the speed setting of the magnetic stirrer was selected at the smallest (position No.1). The polarization of the H_2 detection probe and the preparation of liquid samples were performed simultaneously. After the equilibrium was reached and the H_2 detection probe was polarized, the liquid sample was pumped to the 100 mL bottle at a flow rate of 100 mL/min. Only one measurement was performed with this method as the stirrer might generate tiny H_2 babbles in the liquid sample , which would result in a supersaturated dissolved H_2 concentration (Kikuchi et al., 2001). The dissolved H_2 concentration was measured for at least 100 minutes.

For the circulation method, the preparation of liquid samples was performed after the H_2 probe detection was polarized. The connection between the 100 mL bottle and the 500 mL bottle provided the path to circulate liquid sample. The flow rate was maintained by the peristaltic pump at 100 mL/min. Three independent measurements were performed on liquid samples, which were freshly prepared for each test. Because of the additional time required to reach equilibrium, each measurement lasted at least 100 minutes, which was longer than that of the flow-through cell setup.

7.3 Results and Discussions

7.3.1 The flow-through cell setup

The results of the dissolved H_2 concentration measurement were shown in Fig.7-3. The solid line represented the average of the prepared dissolved H_2 concentration, $\bar{C}_H^{aq}$ (mg/L), in the liquid sample from the three replicate measurements. The concentrations C_H^{aq} in each measurement were calculated as the method stated in Section 7.2.2.1 from the Henry's law. The maximal standard deviation of C_H^{aq} among the three measurements was smaller than 0.01mg/L. Therefore, the averaged value $\bar{C}_H^{aq}$ was used.

The dotted line with markers represented the measured dissolved H_2 concentration, C_H (mg/L), in the three measurements. The results from liquid samples with syngas pressurized at 5 psig and 15 psig were shown in Fig.7-3a and Fig.7-3b, respectively. The result showed the measurements of C_H in a time duration of 50 minutes.

The comparison of the prepared and measured dissolved H_2 concentration in this experiment demonstrated three obvious problems:

1) An overestimation of the measured dissolved H_2 concentration at the beginning of the testing;

2) A rapid decrease of the measured dissolved H_2 concentration during the testing; and

3) An inconsistency of measured dissolved H_2 concentration between replicate tests.

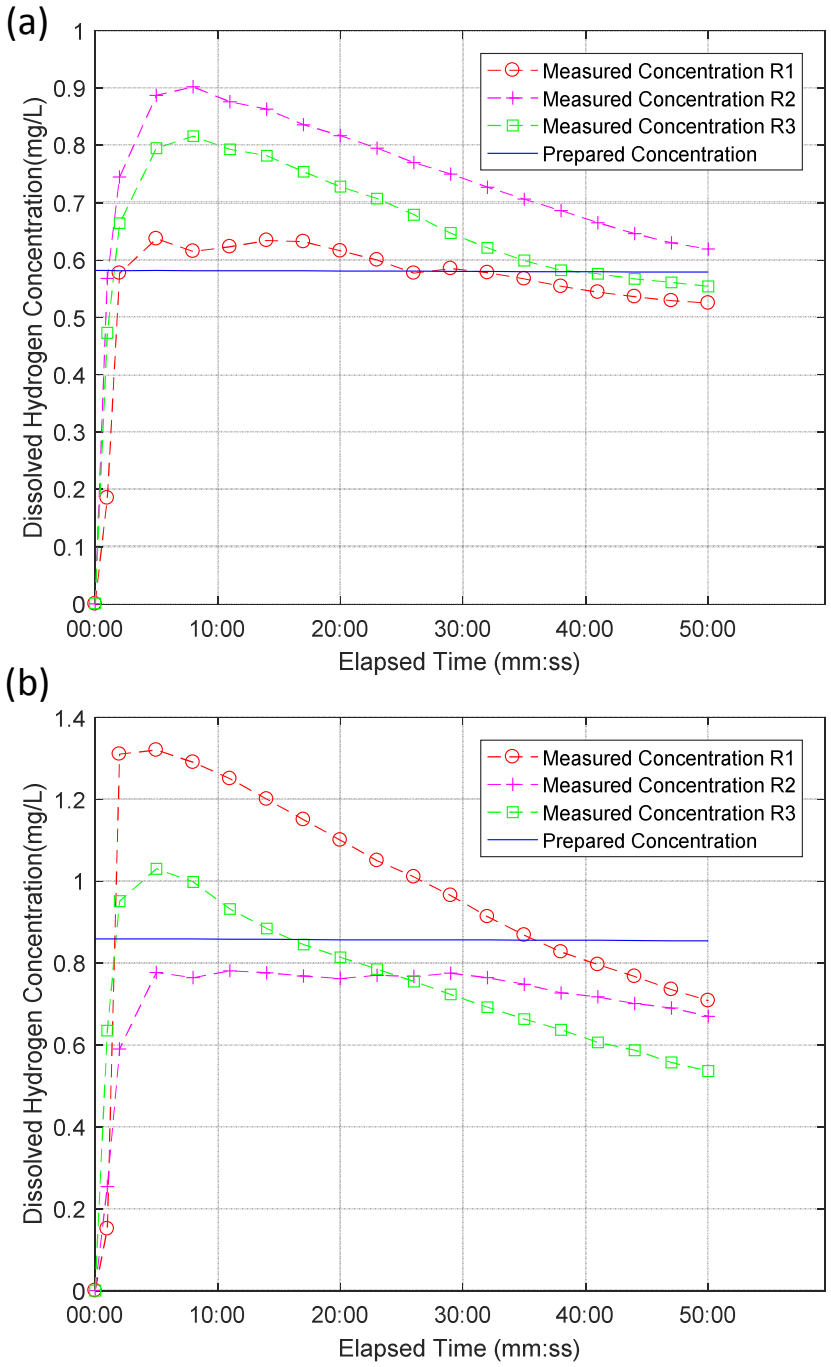

Fig.7-3 Measurement results of the dissolved H_2 concentrations with the flow-through cell setup at initial pressures of 5 psig (a) and 15 psig (b) (R1, R2, and R3 represented the three independent measurements. The time point 00:00 represented the time when liquid samples were introduced to the dissolved H_2 sensor).

According to the specification of the dissolved H_2 sensor, the sensor should have a measurement error less than 2% of the measuring value. However, the results showed in the Fig.7-3 had a maximal absolute percentage measurement error of 55.12% for the 5 psig group and 52.52% for the 15 psig group. It was also impossible to determine the dissolved H_2 concentration because the dissolved H_2 sensor could not provide a stable dissolved H_2 concentration reading.

The first problem of the dissolved H_2 sensor was the overestimation of the dissolved H_2 concentration. According to the manufacturer of the dissolved H_2 sensor, the overestimation might be the result of H_2 supersaturation in the liquid samples. The Henry's law used to calculate the prepared dissolved H_2 concentration would no longer valid under this condition. The possible cause of the supersaturation was the stirring method used to shorten the equilibrium time. The magnetic stirrer generated a whirlpool in the bottle and resulted in large amounts of tiny H_2 bubbles in the liquid sample. This assumption was made based on reports of similar H_2 supersaturation scenarios during the production of H_2 from water electrolysis (Kikuchi et al., 2001) or fermentation of organic waste (Kraemer and Bagley, 2006). The limitation of the mass transfer between the dissolved and gas phase H_2 generated the supersaturation in above situation (Kraemer and Bagley, 2006). Kikuchi et al. (2001) stated that there was a supersaturation status existed around the H_2 bubbles in the water, which was similar to the scenario in this experiment as the magnetic stirrer generated tiny H_2 bubbles by forming great whirlpool in the water. Therefore, it was reasonable to suspect that the stirring method generated the supersaturation.

The second problem of rapidly decreased readings and the third problem of inconsistency were believed to be the result of the flow-through cell design. The flow-through cell used two rubber O-rings as the sealing between the cell body and the probes, which were already found to be problematic. The cell for the pH/temperature probe was leaking during the pressure test before the experiment. In the initial test, it was also found that the measurement of the dissolved H_2

concentration would have an obvious change when the flow-through cell and H_2 detection probe were pressed together.

It was assumed that the small volume of the flow through cell (around 1 mL) and the leakage contributed to the rapid decrease of the sensor reading. The tiny amount of H_2 inside the cell was prematurely released to the environment, thus generated the decrease of the readings. Meanwhile, the installation of the H_2 detection probe to the flow-through cell also resulted in different sealing conditions between three measurements, which led to the inconsistency of the dissolved H_2 concentration measurements.

In summary, the experiment on the dissolved H_2 sensor with the flow-through cell setup demonstrated several problems regarding the liquid sample preparation and the cell design. The next experiment with the submerged probe setup was designed to correct these problems.

7.3.2 The submerged probe setup

The results of the dissolved H_2 concentration measurement with the submerged probe setup were shown in Fig.7-4. The solid dark blue line represented the average of the prepared dissolved H_2 concentration $\bar{C}_H^{aq}$ in the liquid sample from the three measurements (using circulation method) which were calculated as the method stated in Section 7.2.2.1 from the Henry's law. The concentration $\bar{C}_H^{aq}$ was adjusted based on the change of headspace pressure during the process. The maximal standard deviation of C_H^{aq} between the three measurements was smaller than 0.01mg/L. The solid cyan line with "X" markers represented the prepared dissolved H_2 concentration $\bar{C}_H^{aq}$ for the measurement with the stirring method. It was calculated with the same method stated in Section 7.2.2.1.

The dotted lines with markers represented the measured dissolved H_2 concentration C_H. The results included one measurement with the stirring method (black dotted line with "X" markers) and three measurements with the circulation method (with circle, cross, and square markers). The two methods to accelerate the equilibrium were compared in Fig.7-4 to verify previous assumption that the stirring method generated the H_2 supersaturation. The liquid samples used in all measurements were prepared with an initial syngas pressure of 5 psig. The tendency of the measured and prepared dissolved H_2 concentration in 100 minutes were illustrated in Fig.7-4.

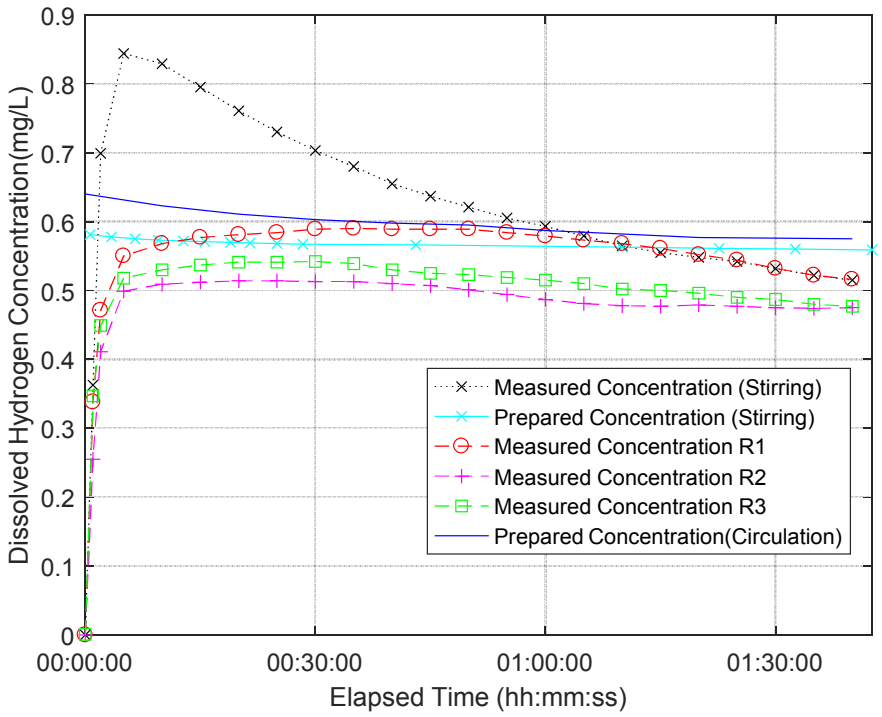

Fig.7-4 Measurement results of the dissolved H_2 concentrations with the submerged H_2 probe setup (Black dotted line with "X" markers was obtained with the stirring method to speed up equilibrium. The other three dotted lines were obtained with the circulation method. The two solid lines represented the average prepared dissolved H_2 concentration from the circulation method and the stirring method. R1, R2, and R3 represented the three independent measurements with the circulation method).

The results in Fig.7-4 demonstrated that:

1) An overestimation of the measured dissolved H_2 concentration only occurred with the stirring method;

2) The measurements on the dissolved H_2 concentration with the circulation method showed relative stable readings and have less deviation among different replicate; and

3) The prepared dissolved H_2 concentration C_H^{aq} (from the Henry's law) with the stirring method was lower than that with the circulation method.

The first finding showed that the stirring method was the primary cause of the overestimated dissolved H_2 concentration. The stirrer generated a supersaturated dissolved H_2 in the liquid samples, which resulted in an invalid condition to use the Henry's law to calculate the dissolved H_2 concentration. Thus, the measured dissolved H_2 concentration was always higher than the prepared one. Meanwhile, the circulation method did not generate the whirlpool; thus, it didn't generate a supersaturation H_2 in the liquid sample. The measured dissolved H_2 concentrations did not show the peak in the start of the measurement and were more close to the prepared concentration than the measurement with stirring method.

The second finding confirmed the suspicion on the flaw of the flow-through cell design. The measurement results were consistent with the submerged probe setup due to the better sealing in the setup. The variations among measurements was smaller and the rapid decrease of the sensor's reading was not obvious. However, the measured dissolved H_2 concentration C_H was 1.01% to 18.30% (average 11.43%) lower than the prepared concentration C_H^{aq} from Henry's law calculation.

The third finding on the comparison of the prepared dissolved H_2 concentration C_H^{aq} might be useful to explain the underestimated measured dissolved H_2 concentration C_H with the stirring

method to prepare the liquid sample. The stirring method had a lower prepared concentration C_H^{aq} than the circulation method suggested that the circulation method might not able to sufficiently dissolve the H_2 gas into the water. As a result, the measured dissolved H_2 concentration was underestimated with the stirring method.

In summary, the setup with the submerged H_2 probe provided more reliable measurements of the dissolved H_2 concentrations. The magnetic stirrer should not be used in liquid sample preparation to generate the supersaturated H_2 in the liquid samples.

7.4 Conclusions

A commercial dissolved H_2 sensor was evaluated to determine the appropriate installation and operation methods. Two installation methods, the flow-through cell setup and the submerged probe setup, were compared. The comparison of the installation methods showed that the submerged setup was the appropriate setup to integrate the dissolved H_2 sensor with the dissolved CO measurement system. The submerged probe setup could achieve consistent, stable dissolved H_2 concentration measurements. Meanwhile, based on the available measurement results on the dissolved H_2 concentration, the circulation method was considered as the appropriate method to prepare the liquid samples with dissolved H_2. The method did not result in supersaturated H_2 in the liquid samples as the stirring method.

The mean absolute percentage error (MAPE) between the measured and prepared dissolved H_2 concentration with the submerged probe setup and the circulation method was 11.43%. For the experiment performed with the stirring method and the flow-through cell setup, the MAPE could not be properly calculated as the measurement readings from the H_2 sensor were unstable and constantly decreasing.

CHAPTER VIII

PERFORMANCE EVALUATION OF THE INTEGRATED DISSOLVED CO/H_2 MEASUREMENT SYSTEM

Abstract

Monitoring and control of dissolved CO and H_2 concentrations in syngas fermentation medium are important to improve the fermentation efficiency. An integrated dissolved CO/H_2 measurement system was developed based on a dissolved CO measurement system and a commercial dissolved H_2 sensor. Experiments were performed to evaluate the performance of the integrated system. Two liquid sample preparation methods, the circulation method and the stirring method, were used in the experiment to address the problems during the integration. The CO measurement results showed that the previous determined circulation method failed to have sufficient CO dissolved the liquid samples, with a mean absolute percentage error between 41.21% and 45.84%. The CO measurement results with the stirring method was close to that of previous experiment, with a mean absolute percentage error between 8.67% and 10.83%. A mean absolute percentage error around 20% was reported for dissolved H_2 concentration measurement with the circulation method. The H_2 measurement showed that a supersaturated H_2 generated with the stirring method.

Keywords: Syngas fermentation, Electrochemical dissolved H_2 sensor, Infrared dissolved CO measurement

8.1 Introduction

Appropriate dissolved CO and H_2 concentrations were critical to maintain the normal activities of microorganisms and enzymes during syngas fermentation (Devarapalli and Atiyeh, 2015; Hurst and Lewis, 2010). Precise measurement and control of the dissolved CO and H_2 concentrations could improve mass transfer rates of CO and H_2 in the fermentation medium (Devarapalli and Atiyeh, 2015), the final product yield, and fermentation process stability (Atiyeh et al., 2017). Therefore, measurement and control of the dissolved CO and H_2 concentrations had great practical significance in optimization of syngas fermentation. In previous chapters, the measurements of dissolved CO and H_2 concentrations were performed separately. This chapter presented an integrated dissolved CO/H_2 measurement system with an objective to simultaneously measure CO and H_2 concentrations.

The dissolved CO/H_2 measurement system was established by integrating an off-the-shelf dissolved H_2 sensor to a developed dissolved CO measurement system. Two integration setups, the flow-through setup and the submerged probe setup, were tested and compared in previous chapter to determine the appropriate integration method for the dissolved H_2 sensor. The flow-through setup had less influence on the CO measurements as it established a new, separate liquid sample circulation path for the dissolved H_2 sensor. However, the new liquid path required additional components which increased the system complexity. The submerged probe setup required less modification of the in-house dissolved CO measurement system since the dissolved H_2 sensor (the H_2 detection probe) was installed in the (liquid) sample container of the system. However, the operating procedures for the dissolved CO measurement system need to be modified to include the dissolved H_2 sensor. Previous tests of the dissolved H_2 sensor demonstrated that the submerged probe setup was more appropriate than the flow-through setup. After the method to integrate the dissolved H_2 sensor was determined, the dissolved CO/H_2 measurement system was assembled and tested. The overall objective was to evaluate the

performance of the integrated dissolved CO/H_2 measurement system. The specific objectives were:

1) To integrate the dissolved H_2 sensor with the dissolved CO measurement system to establish an integrated dissolved CO/H_2 measurement system;

2) To evaluate the performance of the integrated measurement system.

8.2 Materials and Methods

8.2.1 Integrated dissolved CO/H_2 measurement system

The integrated dissolved CO/H_2 measurement system was established by integrating the dissolved H_2 sensor with the dissolved CO measurement system (Fig.8-1), which included a dissolved gas extraction system and a mid-infrared (MIR) CO sensor. The two probes of the dissolved H_2 sensor, the H_2 sensing probe and pH/temperature probe, were integrated into the dissolved gas extraction system as the setup described in Section 7.2.2. The H_2 sensing probe was installed into the sample container of the dissolved gas extraction system. The pH/temperature probe was placed in a nearby vessel with H_2-free water. Two outlet ports were added to the dissolved gas extraction system for the cleanup of the H_2 sensing probe. The remaining part of the CO measurement system was not changed. The details of the CO measurement system setup and the dissolved H_2 sensor installation were described in the Chapters 5 and 7, respectively.

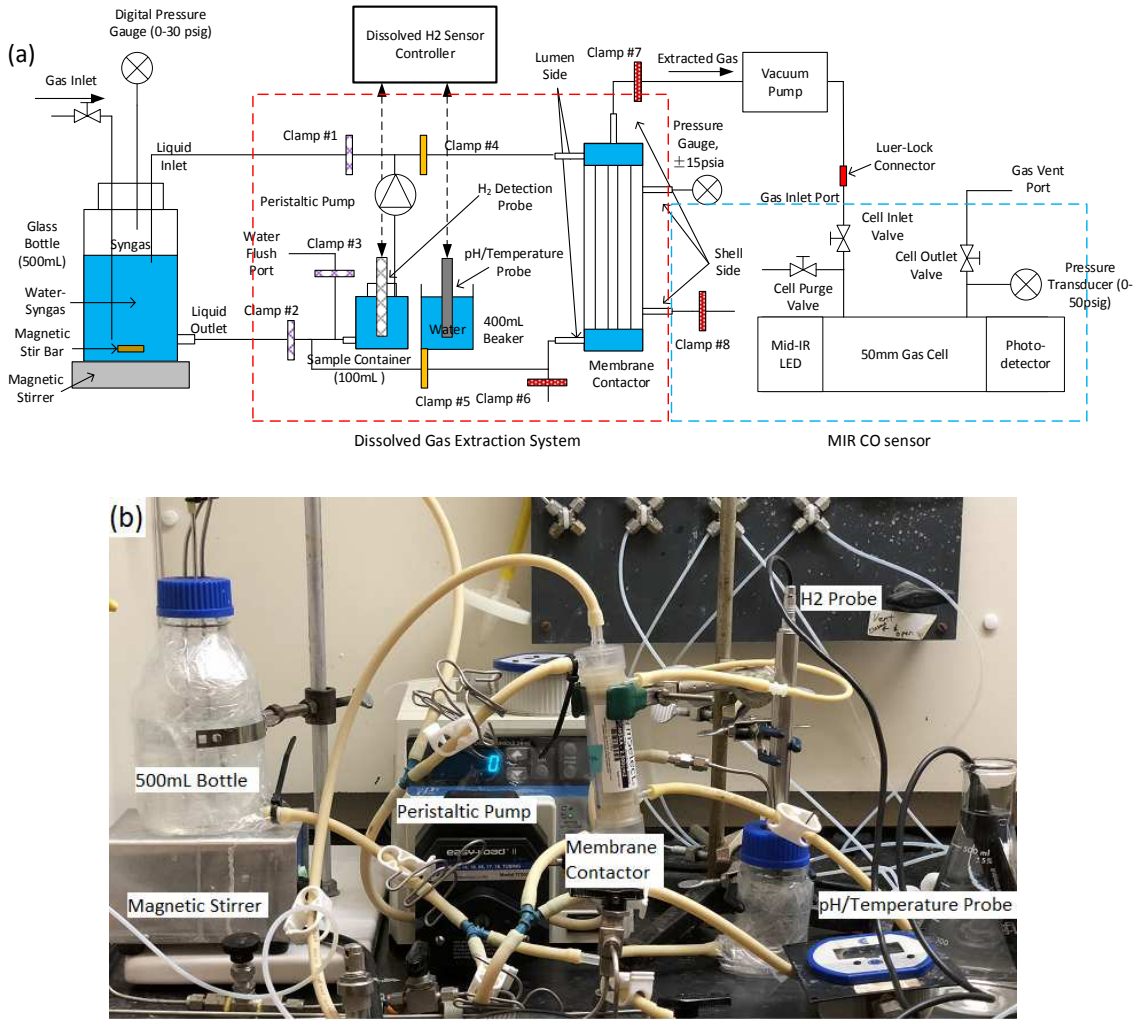

Fig.8-1 Illustration of the integrated dissolved CO/H_2 measurement system: a) the schematic diagram of the measurement system; b) the assembled measurement system in the laboratory (The MIR CO sensor was not shown).

The data acquisition (DAQ) system for the integrated dissolved CO/H_2 measurement system was modified based on the developed DAQ system for the MIR CO sensor (Fig.8-2). A serial connection (RS-232) was used between the host computer and the dissolved H_2 sensor to collect the H_2 concentration data.

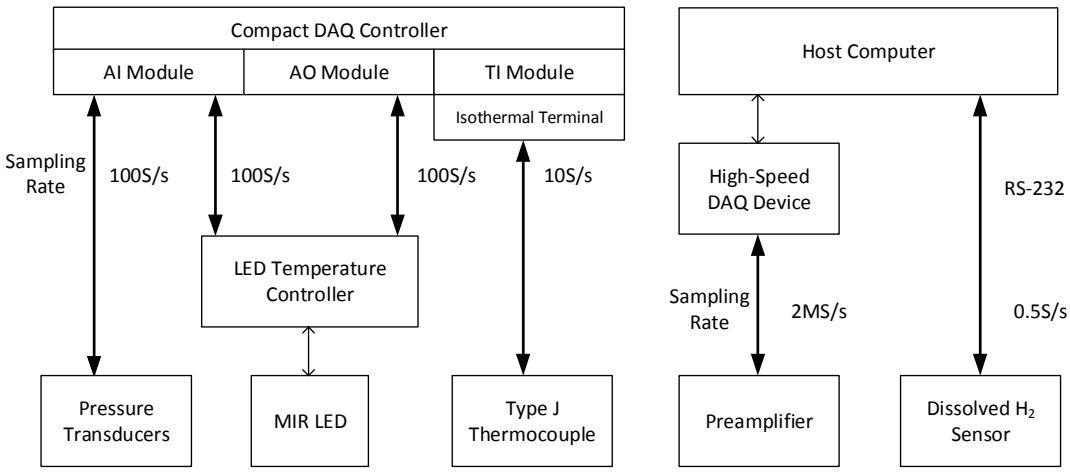

Fig.8-2 Diagram of the data acquisition system of the integrated dissolved CO/H_2 measurement system (MS/s was the abbreviation of million sample per second. S/s was the abbreviation of sample per second.).

The high-speed DAQ device and the dissolved H_2 sensor were connected to the same host computer in the DAQ system. The previously developed LabVIEW® programs were running simultaneously to record CO and H_2 measurement results. The compact DAQ controller operated separately to control the MIR CO sensor with its specific LabVIEW® program. The details and the settings of these three DAQ devices were described in the Chapters 6 and 7, respectively.

The same parameters of the dissolved CO measurement system and the dissolved H_2 sensor were used in the integrated CO/H_2 measurement system. Some primary settings of the MIR CO sensor were listed in Table.8-1. The detailed settings of the MIR CO sensor and the dissolved gas extraction system were described in Section 4.3.1 and Section 5.2.1, respectively. The settings of the dissolved H_2 sensor were described in Section 7.2.2.2.

Table.8-1 Primary settings of the MIR CO sensor (MIR LED and preamplifier) in the integrated measurement system

LED Driving Settings			Preamplifier Settings		
LED Current	Pulse Frequency	Pulse Width	1st stage transimpedance resistance	Frequency bandwidth	Preamplifier gain
0.6 A	2 kHz	20 μs	High (5 kΩ)	Low (150 kHz)	124 (~ 37.5 V/V)

8.2.2 Experiment setup

8.2.2.1 Liquid sample preparation

Liquid samples with dissolved CO and H_2 were prepared with the same method described in Section 5.2.2.2 and Section 7.2.2.1 by using reverse osmosis (RO) water and pressurized syngas (40% CO, 30% CO_2, and 30% H_2 in molar percentage). The dissolved CO and H_2 concentrations in the liquid sample were calculated using the Henry's law. The details of the calculation method were described in above sections. The pressures of CO and H_2, respectively, for the calculation were obtained when the dissolved and gas phase syngas reached an equilibrium. Two methods, the circulation method and the stirring method, were used to shorten the time to reach equilibrium. The detailed descriptions of these two methods were described in Section 7.2.2.2.

The syngas in the headspace of the 500 mL bottle was pressurized to three initial pressure levels, 3 psig, 6 psig, and 9 psig, to obtain liquid samples with three levels of dissolved CO and H_2 concentrations. Totally 18 sets of liquid samples were prepared for the experiment. For each pressure, three samples were prepared with the circulation method and another three samples were prepared with the stirring method.

8.2.2.2 Experiment procedures

The following experiment procedures were designed based on the procedures of the previous experiments on dissolved CO (Section 5.2.2) and H_2 measurements (Section 7.2.2.3).

1) Measurement system initialization

   The initialization of the measurement system included following steps: prepare the MIR CO sensor for gas phase CO measurements, prepare the dissolved gas extraction system, and start the polarization of the dissolved H_2 sensor.

   The setup of the MIR CO sensor included following steps in sequence (details described in Section 4.2.2): components warm-up, gas cell clean-up, components setting control, and measurement of original infrared signal strength. The preparation of the dissolved gas extraction system was proceeded by purge the system with N_2 firstly, then add 500 mL RO water into the system (details described in Section 5.2.2). The polarization of the dissolved H_2 sensor was performed after the preparation of dissolved gas extraction system (details described in Section 7.2.2.3).

2) Liquid sample preparation

   The preparation of liquid samples included following major steps: purge the 500 mL bottle with syngas, pressurize the headspace to desired pressure, and prepare liquid samples with equilibrated dissolved syngas (details described in Section 7.2.2.3).

3) CO/H_2 concentration measurements

   Measurement of the dissolved H_2 concentration started when the dissolved H_2 sensor polarization was completed and the liquid samples were introduced to the sample container (details described in Section 7.2.2). Measurement of CO concentration included following steps (described in Section 5.2.2 and Section 6.2.3): circulate (60 mL/min) a liquid sample in the sample container through a hollow fiber membrane (HFM) contactor

to degas the sample, perform the designed three-cycle gas extraction method to obtain accumulated gas phase CO concentration, and calculate the dissolved CO concentration.

4) System cleanup

   The system cleanup included following aspects: measure the after-experiment infrared emission intensity (details in Section 5.2.2), clean-up the dissolved H_2 sensor, and remove water/syngas from the system (details in Section 7.2.2.3).

8.2.3 Performance evaluation of the integrated dissolved CO/H_2 measurement system

The performance of the integrated dissolved CO/H_2 measurement system was mainly evaluated by its accuracy on the measurement of the dissolved CO/H_2 concentrations. The differences between the measured and the prepared concentrations were used to determine the accuracy of the measurement system.

The prepared dissolved CO and H_2 concentrations, C_{CO}^{aq} (mg/L) and C_{H}^{aq} (mg/L), were calculated from the Henry's law through their partial pressures and the adjusted Henry's law constants according to the liquid sample temperature. The measured dissolved CO concentration, C_{CO} (mg/L), was calculated from the gas phase CO concentration C_G (mg/L), the volume (L) of the gas cell V_G, and the volume (L) of the liquid sample $V_L$as:

$$C_{CO} = C_G V_G / V_L \tag{8.1}$$

The details of the calculation was stated in Section 5.2.2.2 and Section 7.2.2.1, respectively. The volume V_L was measured with the same method described in Section 5.2.2.1 before the experiment, which was 132.33mL (The volume was slightly different than that in Chapter 5 due to the replacement of rubber tubing). The measured dissolved H_2 concentration, C_H (mg/L), was obtained directly from the dissolved H_2 sensor. The mean absolute percentage error (MAPE) and

the root-mean-square error (RMSE) were used to evaluate the performance of the developed measurement system. The definition of the above two values were described in Section 4.2.2.2.

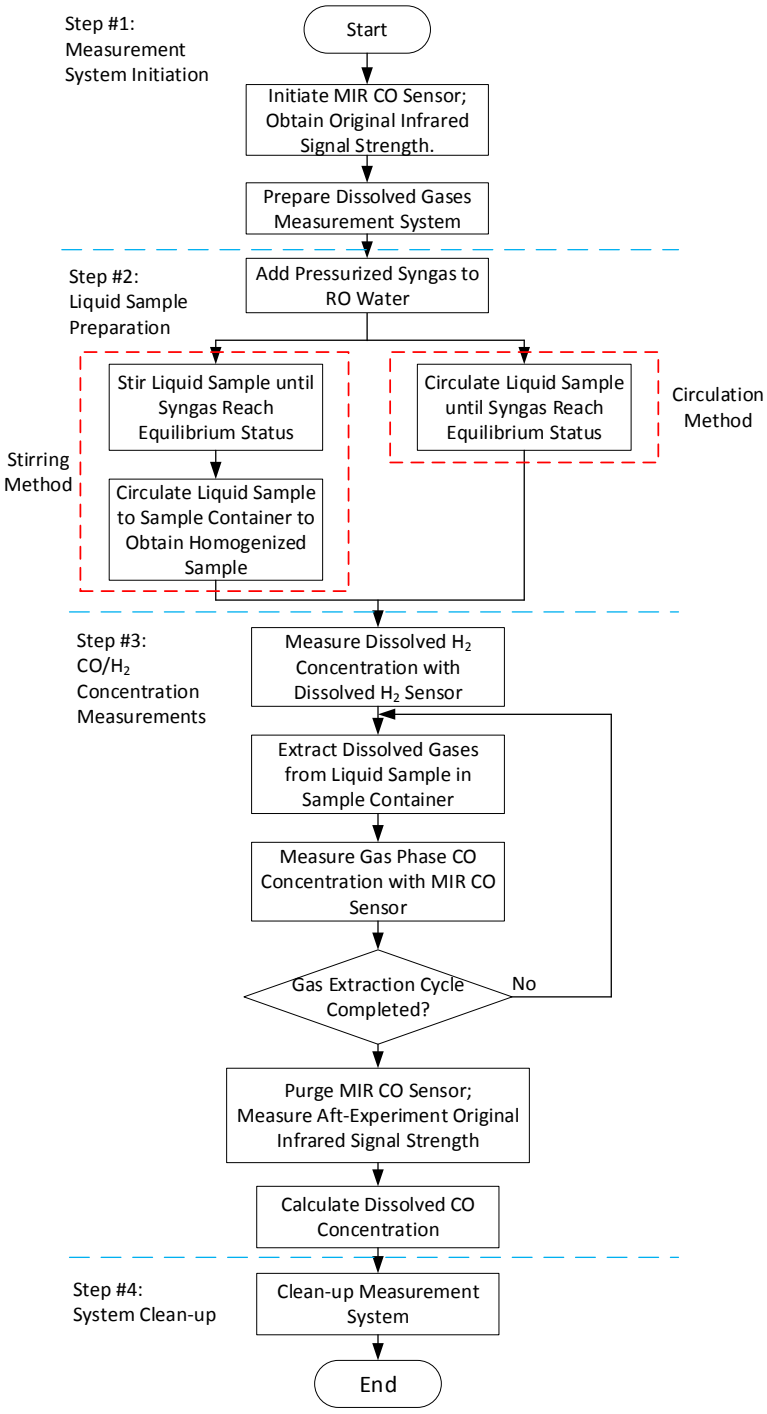

Fig.8-3 Flowchart of the dissolved CO and H_2 concentrations measurement procedures (blue dashed lines separated primary steps)

8.3 Results and Discussions

8.3.1 Dissolved CO concentration measurement

The results of the dissolved CO concentration measurements were shown in Fig.8-4. The x-axis represented the prepared dissolved CO concentration, C_{CO}^{aq} (mg/L), and the y-axis represented the measured dissolved CO concentration, C_{CO} (mg/L). The markers on the graph represented the measured and prepared dissolved CO concentration for a single measurement. A regression analysis (shown in dash-dot line) was performed on the entire nine data points to determine if the measurement had non-linear tendency across difference concentrations. The measurements on the liquid samples prepared with the circulation method and the stirring method were demonstrated separately to compare the two methods.

The comparison of the measurements suggested that the circulation method might have insufficient CO dissolution in the liquid samples. The measurements of the dissolved CO concentration with the circulation method were much lower than the results from liquid samples with the stirring method. Meanwhile, the RMSE of the measurements with the stirring method was close to that of previous dissolved CO measurement (1.40 mg/L to previously 0.83 mg/L). The comparison, along with the results from dissolved H_2 sensor tests stated in the Chapter 7, suggested that the circulation method might not have the syngas fully dissolved into the water.

Data analysis on the MAPE showed that the measured dissolved CO concentrations with the circulation method were about 41.21% to 45.84% lower than the corresponding prepared dissolved CO concentrations (Table.8-2). The measured dissolved CO concentrations with the stirring method were about 8.67% to 10.83% lower than the prepared dissolved CO concentrations. The RMSEs were about 6.16mg/L for the circulation method and 1.40mg/L for the stirring method. The regression analysis on the data points demonstrated that the linearity of the dissolved CO concentration measurement was better when using the stirring method to

prepare the liquid samples. The slope of the regression model was 0.9862, which was close to the ideal slope value of one. The slope from the regression model of the circulation method was 0.7373, which indicated that a higher CO concentration would have a higher measurement error.

Table.8-2 List of the mean absolute percentage error (MAPE) and root-mean-square error (RMSE) for the dissolved CO concentration measurements

No.	Initial Pressure (psig)	MAPE (C) (%)	MAPE S.D. (C) (%)	RMSE (C) (mg/L)	MAPE (S) (%)	MAPE S.D. (S) (%)	RMSE (S) (mg/L)
1	3	45.84	2.49	6.16	10.83	1.52	1.40
2	6	42.72	3.29		10.30	1.53	
3	9	41.21	2.29		8.67	1.78	

* “C” represented circulation method; “S” represented stirring method. S.D. was the abbreviation of standard deviation.

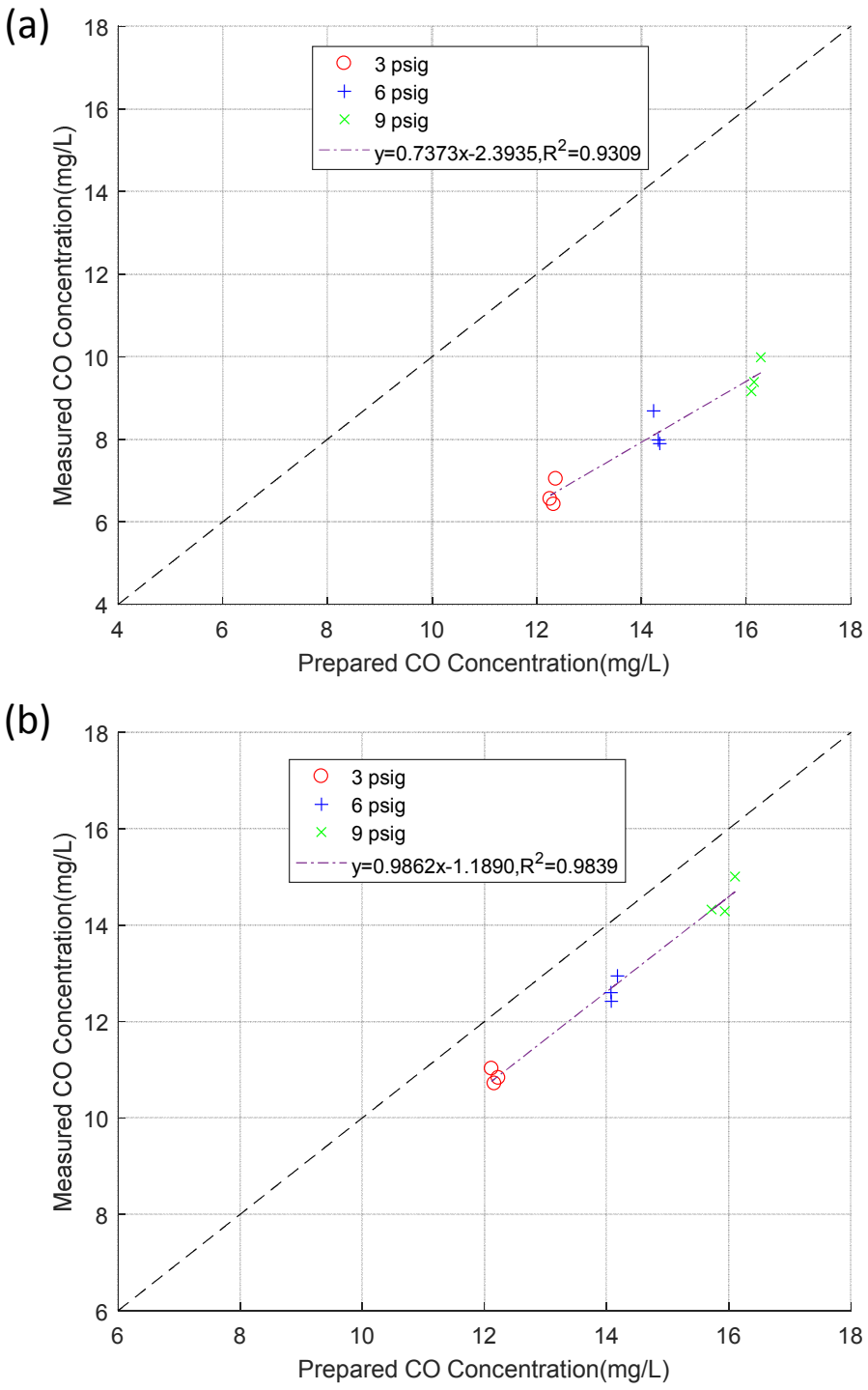

Fig.8-4 Comparison between the prepared and measured dissolved CO concentrations with the circulation method (a) and the stirring method (b) at initial gas pressure of 3 ("o" markers), 6 ("+" markers), and 9 psig ("X" markers). (Gas sample composition: 40% CO, 30% H_2, and 30% CO_2)

8.3.2 Dissolved H_2 concentration measurement

The results of the dissolved H_2 concentration measurements were shown in Fig.8-5 and Fig.8-6, respectively. The changing pattern of measured and prepared dissolved H_2 concentrations during the measurements were shown in these two graphs. The blue solid line was the average of the prepared dissolved H_2 concentration, $\bar{C}_H^{aq}$ (mg/L), calculated from the Henry's law. The average value was used to simplify the graph to demonstrate the differences between measured and prepared dissolved H_2 concentrations. The standard deviation of the three prepared dissolved H_2 concentrations was small than 0.05 mg/L. The dotted lines with markers were the measured dissolved H_2 concentrations in the three replicate measurements.

The results showed that both the stirring and the circulation method, which were used to shorten the time to reach equilibrium status, had great influence on the measurements. The circulation method resulted in underestimated measurements of the dissolved H_2 concentrations while the stirring method lead to overestimated measurements. Meanwhile, the circulation method was found to be more sensitive to the modification of the setup. The time to reach equilibrium was about one hour, which was longer than that time during the previous test of the dissolved H_2 sensor (around 30 to 40 minutes).

The stirring method, which used the magnetic stirrer to accelerate the syngas dissolution, had less impact from the modification of the system setup (Fig.8-6). However, it still generated a supersaturated H_2 in the liquid samples as the previous test.

The measurements of the dissolved H_2 concentrations would reach a steady status when the circulation method was used (Fig.8-5). The final measured dissolved H_2 concentrations were obtained when the steady status was reached after 60 to 90 minutes. The mean absolute percentage error (MAPE) of the measured dissolved H_2 concentrations was calculated as around 14.49% to 18.47% at the steady status (Table.8-3). A dissolved H_2 extraction ratio was also

calculated by comparing the dissolved H_2 concentration at the beginning and the ending of the gas extraction process. The ratio was calculated as about 94%, which showed most H_2 was removed from the liquid samples by the HFM contactor after three gas extraction cycles.

Table.8-3 List of the mean absolute percentage error (MAPE) and the dissolved H_2 extraction ratio for dissolved H_2 concentration measurements (with the stirring method).

No.	Initial Pressure (psig)	MAPE (%)	MAPE S.D. (%)	Dissolved H_2 Extraction Ratio (%)	Extraction Ratio S.D. (%)
1	3	18.47	2.34	94.76	0.23
2	6	14.49	3.76	93.33	0.41
3	9	15.90	0.53	94.68	0.83

*Measured dissolved H_2 concentrations were obtained at the elapsed time of 20 minutes (The end time of the measurements). S.D. was the abbreviation of standard deviation.

The measured dissolved H_2 concentrations had a tendency to decrease over time, when the stirring method was used. Therefore, it was difficult to determine when to report the measured dissolved H_2 concentrations. Since the dissolved CO measurements took around 20 minutes to report a dissolved CO concentration, a regression model was established for the change of the dissolved H_2 concentrations in the first 30 minutes to predict the overestimation (Fig.8-7). The data points used in the model were obtained when the measured dissolved H_2 concentrations began to decrease. The data from all three pressure levels were presented in different markers. The established regression model was:

$$y = -13.03x + 9608641.5, R^2 = 0.8543 \quad (8.2)$$

where y represented the overestimation ratio (%) and x represented the elapsed time (minute).

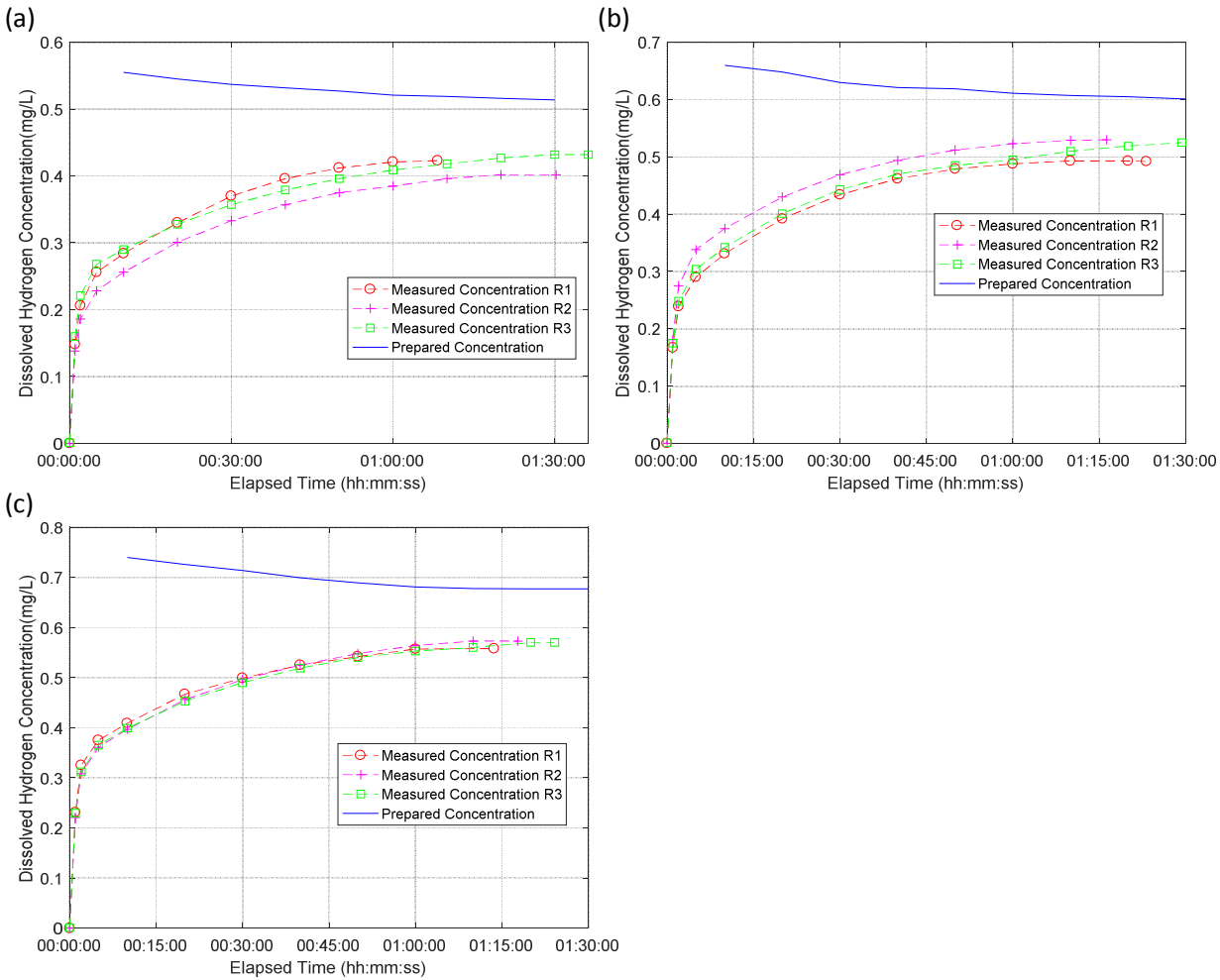

Fig.8-5 Measurements of the dissolved H_2 concentrations with the circulation method: a) 3 psig initial pressure; b) 6 psig initial pressure; c) 9 psig initial pressure (R1, R2, and R3 represented the three independent measurements. Gas sample composition: 40% CO, 30% H_2, and 30% CO_2).

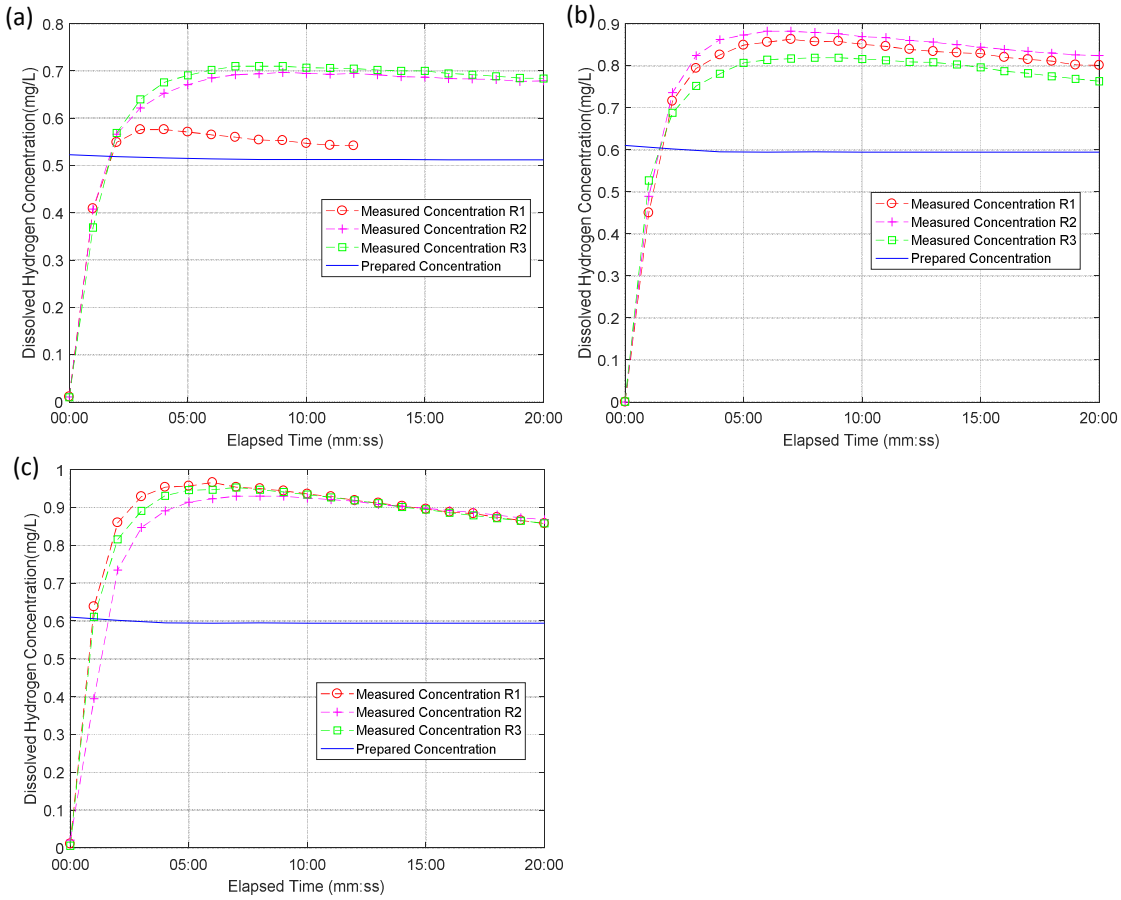

Fig.8-6 Measurements of the dissolved H_2 concentrations with the stirring method: a) 3 psig initial pressure; b) 6 psig initial pressure; c) 9 psig initial pressure (R1, R2, and R3 represented the three independent measurements. The replicate R1 of 3 psig samples had a different changing pattern due to the sample preparation mistake in the experiment. Gas sample composition: 40% CO, 30% H_2, and 30% CO_2).

The regression model demonstrated that the overestimation would decrease gradually after the prepared liquid samples were introduced to the sample container. The overestimation would be around 40% in 10 minutes and around 22% in 30 minutes.

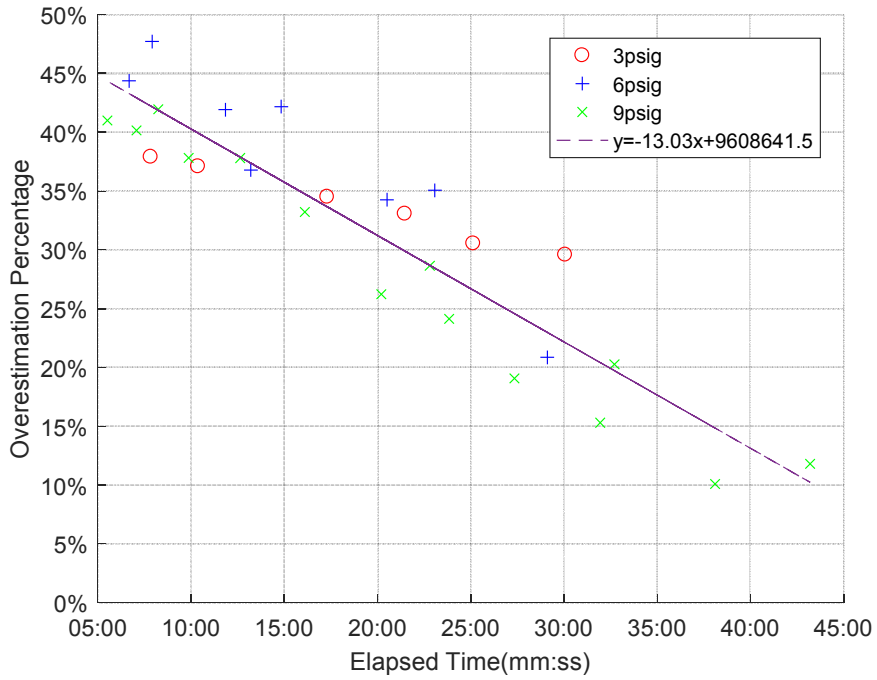

Fig.8-7 Regression analysis on the overestimation of the dissolved H_2 concentrations with the stirring method (Data points from 3, 6, and 9 psig initial pressure were shown in "o", "+", and "x" markers, respectively.).

8.3.3 Results discussion

The circulation method was determined as the method to prepare the liquid sample based on the dissolved H_2 sensor test in Chapter 7, because it would not generate a supersaturated dissolved H_2 in the sample. However, the measurements on the dissolved CO concentrations were not satisfactory in the integrated system. The measured CO concentrations were around 40% lower than the prepared ones. The regression analysis of the data showed that there was a systematical

error in the measurements of the dissolved CO concentrations, when the circulation method was used to prepare the liquid sample. The slope of the regression model also indicated that higher CO concentrations had larger measurement errors.

To address the problem of the lower than expected dissolved CO concentration, following possible causes were examined:

1) The calibration model of the MIR CO sensor;
2) The extraction efficiency of the HFM contactor; and
3) The problem with CO dissolution using the circulation method.

A validation test of the MIR CO sensor was performed after the measurements of dissolved CO/H_2 concentrations with the circulation method (Section 4.2.2.2). The validation test examined the difference between the measured and prepared CO concentrations (in gas phase) to determine whether the calibration model was still valid. The results of the validation test showed that the calibration of the mid-infrared CO sensor was valid; therefore, the measurements of gas phase CO concentrations were accurate.

It was known that the HFM contactor's gas extraction efficiency would deteriorate over time by clogging or membrane aging. Therefore, the capability of the HFM contactor was also examined to check if there was anything abnormal during the gas extraction process. Since there was no suitable tool for the evaluation of the CO extraction ratio. The dissolved H_2 extraction ratio was used to evaluate the gas extraction process (Table.8-3), which showed that the HFM contactor and the designed extraction method could reach a dissolved H_2 extraction ratio higher than 90%.

Therefore, the liquid sample preparation with the circulation method was the only cause of the abnormal CO concentrations. The results from the liquid samples prepared with the stirring method had normal measurement errors on the dissolved CO concentrations. Therefore, it was determined that the circulation method was not able to sufficiently dissolve CO in the water.

However, the circulation method generated supersaturated H_2 and made the measurements of dissolved H_2 concentrations unreliable. The future research should focus on the improvement of the dissolved H_2 concentration measurement, which might include the modification on the sensor installation and a device or procedure to eliminate the supersaturated H_2 before the measurement. It was also worthy to find a new method to prepare liquid samples, which could fully dissolve the syngas to the water and provide an accurate estimation on the dissolved syngas concentrations.

8.4 Conclusions

An integrated dissolved CO/H_2 measurement system was established based on the developed dissolved CO measurement system and a commercial dissolved H_2 sensor. Experiments were performed to evaluate the performance of the developed measurement system. The results showed the liquid preparation method had a great influence on the CO and H_2 measurements. The circulation method used to prepare liquid samples generated insufficient CO and H_2 dissolution and resulted in underestimated measurements. The stirring method, which used a magnetic stirrer, generated sufficient CO dissolution. However, it might generate supersaturated H_2 in liquid samples and affect the dissolved H2 concentration measurements.

The mean absolute percentage error (MAPE) of the dissolved CO concentrations was ranged between 8.67% and 10.83% with the stirring method to prepare liquid samples. The root-mean-square error (RMSE) of the dissolved CO concentration was 1.40 mg/L. The overestimation of the dissolved H_2 concentrations was around 40% in 10 minutes and around 22% in 30 minutes after the liquid samples were introduced to the dissolved H_2 sensor. Future research should focus on the improvements of the dissolved H_2 concentration measurement. New method for the liquid sample preparation was also necessary in the future research to overcome the opposite effect of stirring on CO and H_2 dissolution.

CHAPTER IX

CONCLUSIONS AND RECOMMENDATIONS

9.1 Conclusions

This research had following conclusions:

1) Literature reviews showed that the infrared detection method was the best method to detect dissolved CO in the syngas fermentation media. The preliminary results of FTIR experiment showed that it was feasible to measure CO concentrations in the gas phase syngas. However, the broad, strong liquid water interference was a challenge to measure dissolved CO in aqueous solution. Infrared CO measurements at mid-infrared (MIR) spectral range between 4.42 μm to 5 μm (2000 cm^{-1} and 2260 cm^{-1} in wavenumber) were free of interference from other chemicals in syngas and fermentation medium.
2) Two methods could be used to measure dissolved CO concentrations with infrared spectroscopic technology: a) directly measure dissolved CO concentrations with a powerful infrared radiation source, such as a quantum cascade laser; b) extract dissolved CO from the liquid sample then measure the gas phase CO with an infrared sensor. The latter method would not require a laser as the infrared radiation source, which could significantly reduce the cost and simplify the infrared CO sensing system.

3) A MIR CO sensor with MIR light emitting diode (LED) as the infrared radiation source was established. It was capable of measuring CO concentrations that in range for dissolved CO measurements. Dissolved CO concentrations could be measured from the designed indirect method with a dissolved gas extraction system and the developed MIR CO sensor. The maximal mean absolute percentage error in dissolved CO concentration measurements was 6.18% and the measurement time for one liquid sample was around 20 minutes. The designed dissolved gas extraction system could achieve a gas extraction ratio higher than 90% with specific operation procedures (three five-minute extraction cycles) for liquid samples (with around 130 mL volume).

4) The liquid preparation methods had a great influence of the CO and H_2 measurement results. The circulation method used to prepare liquid samples resulted in insufficient CO and H_2 dissolution and underestimated measurements. The stirring method, which used a magnetic stirrer, generated sufficient CO dissolution. However, it might resulted in supersaturated H_2 in liquid samples.

5) When the stirring method was used to prepare the liquid sample, the mean absolute percentage error of the dissolved CO concentrations was ranged between 8.67% and 10.83%. The root-mean-square error of the dissolved CO concentration was 1.40 mg/L. The overestimation of dissolved H_2 concentrations was around 40% in 10 minutes and around 22% in 30 minutes after liquid samples were introduced to the dissolved H_2 sensor.

9.2 Recommendations

The recommendations for future research involved following aspects:

1) Due to the limitation of funding and time, the gas cell of the developed MIR CO sensor was not specially optimized for the application. The current gas cell had a large volume and did not have inner surface coating to reflect the infrared light. The gas cell can be further improved by using a small volume, inner-coated customized cell. The optical pathlength can also be extended when the infrared radiation can be reflected in the inner surface. The improvement of the gas cell will further improve the sensitivity of the MIR CO sensor.

2) A reference channel can be added to simplify the operation procedures of the MIR CO sensor. The current method obtained the infrared emission intensity of the LED by measuring pure N_2 in the gas cell, which might not be available in actual applications. Therefore, it will be useful to establish a reference channel for real-time measurement of the infrared emission intensity of the LED . The reference channel could be introduced by adding another optical path and photodetector to directly measure the infrared emission. It could also be achieved by adding a correlation cell with gas samples with known CO concentration (Koppius, 1951).

3) The future improvement of the dissolved CO/H_2 measurement system should involve the automation of the dissolved gas extraction system. An automatic system will be helpful for the revision of the current method with multiple gas extraction cycles, which will improve the repeatability and reduce the measurement time of the system.

4) The volume of the liquid samples could also be adjusted to reduce the measurement time. The volume used in this research, around 130mL, required about 20 minutes for one measurement. With the improvement of the MIR CO sensor, it is possible to use smaller volume of liquid samples for a faster measurement.

5) New method for the liquid sample preparation is necessary in future research to overcome the contradiction between CO and H_2 dissolution in current method. An online gas chromatography method may be added to measure the CO and H_2 percentage changes during the liquid sample preparation process. A longer liquid sample preparation may be introduced to ensure the sufficient dissolution of CO/H_2 as well.

REFERENCES

Abell, J., Kim, C. S., Bewley, W. W., Merritt, C. D., Canedy, C. L., Vurgaftman, I., … Kim, M. (2014). Mid-infrared interband cascade light emitting devices with milliwatt output powers at room temperature. *Applied Physics Letters*, *104*(26). https://doi.org/10.1063/1.4886394

Adessi, A., Torzillo, G., Baccetti, E., De Philippis, R. (2012). Sustained outdoor H_2 production with Rhodopseudomonas palustris cultures in a 50 L tubular photobioreactor. *International Journal of Hydrogen Energy*, *37*(10), 8840–8849. https://doi.org/10.1016/j.ijhydene.2012.01.081

Alberti, G., Casciola, M., Palombari, R. (1993). Amperometric sensor for carbon monoxide based on solid state protonic conduction. *Solid State Ionics*, *61*(1–3), 241–244.

Alder, J. F., McCallum, J. J. (1983). Piezoelectric crystals for mass and chemical measurements. A review. *Analyst*, *108*(1291), 1169–1189. https://doi.org/10.1039/AN9830801169

Alexandrov, S. E., Gavrilov, G. A., Kapralov, A. A., Karandashev, S. A., Matveev, B. A., Sotnikova, G. Y., Stus', N. M. (2002). Portable optoelectronic gas sensors operating in the mid-IR spectral range (λ=3 5 μm). *Proc. SPIE 4680*, *4680*(February), 188. https://doi.org/10.1117/12.454676

Alexandrov, S., Gavrilov, G., Karandashev, S., Matveev, B., Sotnikova, G., Stus', N. (2002). Portable optoelectronic gas sensors operating in the mid-IR spectral range (λ=3~5 μm). In *Second International Conference on Lasers for Measurement and Information Transfer* (Vol. 4680, pp. 188–195). International Society for Optics and Photonics. https://doi.org/10.1117/12.454676

Ando, M., Kobayashi, T., Haruta, M. (2000). Optical recognition of CO and H_2 by use of gas-sensitive Au – Co_3O_4 composite films. *Journal of Materials Chemistry*, *7*(9), 1779-1783.

Ando, M., Kobayashi, T., Haruta, M. (1995). Optical CO detection by use of CuO/Au composite films. *Sensors and Actuators: B. Chemical*, *25*(1–3), 851–853. https://doi.org/10.1016/0925-4005(95)85187-9

Ando, M., Kobayashi, T., Haruta, M., Haruta, M. (1997). Combined effects of small gold particles on the optical gas sensing by transition metal oxide films. *Catalysis Today*, *36*(96), 135–141.

Ansari, Z. a, Ansari, S. G., Ko, T., Oh, J. (2002). Effect of MoO_3 doping and grain size on SnO_2-enhancement of sensitivity and selectivity for CO and H_2 gas sensing. *Sensors and Actuators B: Chemical*, *87*(1), 105–114. https://doi.org/10.1149/1.2054687

Arshak, K., Moore, E., Lyons, G. M., Harris, J., Clifford, S. (2004). A review of gas sensors employed in electronic nose applications. *Sensor Review*, *24*(2), 181–198. https://doi.org/10.1108/02602280410525977

Atiyeh, H. K., Phillips, J. R., Huhnke, R. L. (2017). Fermentation control for optimization of syngas utilization. U.S. Patent Application No. 15/526,558.

B'Hymer, C. (2003). Residual solvent testing: A review of gas-chromatographic and alternative techniques. *Pharmaceutical Research*, *20*(3), 337–344. https://doi.org/10.1023/A:1022693516409

Bacsik, Z., Mink, J., Keresztury, G. (2004). FTIR spectroscopy of the atmosphere. I. Principles and methods. *Applied Spectroscopy Reviews*, *39*(3), 295–363. https://doi.org/10.1081/ASR-200030192

Bai, H., Shi, G. (2007). Gas Sensors Based on Conducting Polymers. *Sensors*, *7*(3), 267–307.

Barron-Jimenez, R., Caton, J. A., Anderson, T. N., Lucht, R. P., Walther, T., Roy, S., … Gord, J. R. (2006). Application of a difference-frequency-mixing based diode-laser sensor for carbon monoxide detection in the 4.4-4.8 μm spectral region. *Applied Physics B: Lasers and Optics*, *85*(2–3), 185–197. https://doi.org/10.1007/s00340-006-2281-3

Barsan, N., Weimar, U. (2003). Understanding the fundamental principles of metal oxide based gas sensors; the example of CO sensing with SnO_2 sensors in the presence of humidity. *Journal of Physics: Condensed Matter*, *15*(20), R813–R839. https://doi.org/10.1088/0953-8984/15/20/201

Bay, H. W., Blurton, K. F., Sedlak, J. M., Valentine, A. M. (1974). Electrochemical technique for the measurement of carbon monoxide. *Anal Chem*, *46*(12), 1837–1839. Retrieved from http://www.ncbi.nlm.nih.gov/entrez/query.fcgi?cmd=Retrieve&db=PubMed&dopt=Citation&list_uids=4413204

Benito-Garagorri, D., Puchberger, M., Mereiter, K., Kirchner, K. (2008). Stereospecific and reversible CO binding at iron pincer complexes. *Angewandte Chemie - International Edition*, *47*(47), 9142–9145. https://doi.org/10.1002/anie.200803665

Björnsson, L., Hornsten, E. G., Mattiasson, B. (2001). Utilization of a Palladium – Metal Oxide Semiconductor (Pd-MOS) Sensor for On-Line Monitoring of Dissolved. *Biotechnology and Bioengineering*, *73*(1), 35–43.

Blyth, D. J., Aylott, J. W., Richardson, D. J., Russell, D. A. (1995). Sol-Gel Encapsulation of Metalloproteins for the Development of Optical Biosensors for Nitrogen-Monoxide and Carbon-Monoxide. *Analyst*, *120*(11), 2725–2730.

Boreman, G. D. (2001). A Users Guide to IR Detectors. *Proceedings of SPIE*, *4420*, 79–90. https://doi.org/10.1117/12.439218

Borisov, S. M., Wolfbeis, O. S. (2008). Optical biosensors. *Chemical Reviews*, *108*(2), 423–461. https://doi.org/10.1021/cr068105t

Boulart, C., Connelly, D. P., Mowlem, M. C. (2010). Sensors and technologies for in situ dissolved methane measurements and their evaluation using Technology Readiness Levels. *TrAC - Trends in Analytical Chemistry*, *29*(2), 186–195. https://doi.org/10.1016/j.trac.2009.12.001

Bozóki, Z., Pogány, A., Szabó, G. (2011). Photoacoustic instruments for practical applications: Present, potentials, and future challenges. *Applied Spectroscopy Reviews*, *46*(1), 1–37. https://doi.org/10.1080/05704928.2010.520178

Bredwell, M. D., Srivastava, P., Worden, R. M. (1999). Reactor Design Issues for Synthesis-Gas Fermentation. *Biotechnology Progress*, *15*, 834–844. https://doi.org/10.1021/bp990108m

Brix, O. (1981). A modified Van Slyke apparatus. *Journal of Applied Physiology: Respiratory, Environmental and Exercise Physiology*, *50*(5), 1093–7. Retrieved from http://www.ncbi.nlm.nih.gov/pubmed/7228760

Buerck, J., Roth, S., Kraemer, K., Scholz, M., Klaas, N. (2001). Application of a fiber-optic NIR-EFA sensor system for in situ monitoring of aromatic hydrocarbons in contaminated groundwater. *Journal of Hazardous Materials*, *83*(1–2), 11–28. https://doi.org/10.1016/S0304-3894(00)00335-6

Burke, C. S., Markey, A., Nooney, R. I., Byrne, P., McDonagh, C. (2006). Development of an optical sensor probe for the detection of dissolved carbon dioxide. *Sensors and Actuators, B: Chemical*, *119*(1), 288–294. https://doi.org/10.1016/j.snb.2005.12.022

Burt, R., Minkoff, G. J. (1956). The infra-red spectrometer as a non-dispersive instrument. *Journal of Scientific Instruments*, *33*(7), 283.

Butler, J. H., Elkins, J. W. (1991). An automated technique for the measurement of dissolved N_2O in natural waters. *Marine Chemistry*, *34*(1–2), 47–61. Retrieved from http://www.sciencedirect.com/science/article/pii/030442039190013M

Cai, T., Gao, G., Chen, W., Liu, G., Gao, X. (2011). Simultaneous measurements of CO_2 and CO using a single distributed-feedback (DFB) diode laser near 1.57 μm at elevated temperatures. *Applied Spectroscopy*, *65*(1), 108–112. https://doi.org/10.1366/10-06074

Cantalini, C., Post, M., Buso, D., Guglielmi, M., Martucci, A. (2005). Gas sensing properties of nanocrystalline NiO and Co3O4 in porous silica sol–gel films. *Sensors and Actuators B: Chemical*, *108*(1–2), 184–192. https://doi.org/10.1016/j.snb.2004.11.073

Capasso, F., Gmachl, C., Sivco, D. L., Cho, A. Y. (1999). Quantum cascade lasers. *Physics World*, *12*(6), 27–33. https://doi.org/10.1063/1.1485582

Chan, D. L. C., Soljačić, M., Joannopoulos, J. D. (2006). Thermal emission and design in 2D-periodic metallic photonic crystal slabs. *Optics Express*, *14*(19), 8785–8796. https://doi.org/10.1364/OE.14.008785

Chen, T., Yuan, H., Sun, Z. (2009). Photoacoustic method to detect CO and soot particles generated by fire. *2009 International Conference on Measuring Technology and Mechatronics Automation, ICMTMA 2009*, *1*, 304–307. https://doi.org/10.1109/ICMTMA.2009.14

Childers, J. W., Thompson, E. L., Harris, D. B., Kirchgessner, D. A., Clayton, M., Natschke, D.

F., Phillips, W. J. (2001). Multi-pollutant concentration measurements around a concentrated swine production facility using open-path FTIR spectrometry. *Atmospheric Environment*, *35*(11), 1923–1936. https://doi.org/10.1016/S1352-2310(00)00545-8

Choi, U. S., Sakai, G., Shimanoe, K., Yamazoe, N. (2005). Sensing properties of Au-loaded SnO2-Co3O4 composites to CO and H2. *Sensors and Actuators, B: Chemical*, *107*(1 SPEC. ISS.), 397–401. https://doi.org/10.1016/j.snb.2004.10.033

Chu, C. S., Lo, Y. L. (2010). Optical fiber dissolved oxygen sensor based on Pt(II) complex and core-shell silica nanoparticles incorporated with sol-gel matrix. *Sensors and Actuators, B: Chemical*, *151*(1), 83–89. https://doi.org/10.1016/j.snb.2010.09.044

Chung, K. E., Lan, E. H., Davidrron, M. S., Dunn, B. S., Valentine, J. S., Zinkt, J. I. (1995). Measurement of Dissolved Oxygen in Water Using glass-encapsuled myoglobin. *Analytical Chemistry*, *67*(9), 1505–1509. https://doi.org/10.1021/ac00105a004

Cohen, Y. (1977). Shipboard measurement of dissolved nitrous oxide in sea water by electron capture gas chromatography. *Analytical Chemistry*, *49*(8), 1238–1240.

Collison, H. A., Rodkey, F. L., O'Neal, J. D. (1968). Determination of carbon monoxide in blood by gas chromatography. *Clinical Chemistry*, *14*(2), 162–171.

Cord-ruwisch, R., Mercz, T. I., Hoh, C.-Y., Strong, G. E. (1997). Dissolved hydrogen concentration as an on-line control parameter for the automated operation and optimization of anaerobic digesters. *Biotechnology and Bioengineering*, *56*(6), 626–634.

Cosgrove, B. A., Walkley, J. (1981). Solubilities of gases in H2O and 2H2O. *Journal of Chromatography A*, *216*, 161–167.

Courbat, J., Pascu, M., Gutmacher, D., Briand, D., Wöllenstein, J., Hoefer, U., … De Rooij, N. F. (2011). A colorimetric CO sensor for fire detection. *Procedia Engineering*, *25*, 1329–1332. https://doi.org/10.1016/j.proeng.2011.12.328

Crawford, F. J. (1998). Electro-Optical Sensors Overview. *IEEE Aerospace and Electronic Systems Magazine*, (October), 17–24.

D'Amico, A., De Marcellis, A., Di Carlo, C., Di Natale, C., Ferri, G., Martinelli, E., … Stornelli, V. (2010). Low-voltage low-power integrated analog lock-in amplifier for gas sensor applications. *Sensors and Actuators, B: Chemical*, *144*(2), 400–406. https://doi.org/10.1016/j.snb.2009.01.045

Dakin, J. P., Gunning, M. J., Chambers, P., Xin, Z. J. (2003). Detection of gases by correlation spectroscopy. *Sensors and Actuators, B: Chemical*, *90*(1–3), 124–131. https://doi.org/10.1016/S0925-4005(03)00043-1

Daniell, J., Köpke, M., Simpson, S. D. (2012). *Commercial biomass syngas fermentation*. *Energies* (Vol. 5). https://doi.org/10.3390/en5125372

Davey, N. G., Krogh, E. T., Gill, C. G. (2011). Membrane-introduction mass spectrometry (MIMS). *TrAC - Trends in Analytical Chemistry*, *30*(9), 1477–1485. https://doi.org/10.1016/j.trac.2011.05.003

Davies, R., Meuli, G. (2010). Development of a digital lock-in amplifier for open-path light

scattering measurement. *ISIEA 2010 - 2010 IEEE Symposium on Industrial Electronics and Applications*, (Isiea), 50–55. https://doi.org/10.1109/ISIEA.2010.5679498

Devarapalli, M., Atiyeh, H. K. (2015). A review of conversion processes for bioethanol production with a focus on syngas fermentation. *Biofuel Research Journal*, *2*(3), 268–280. https://doi.org/10.18331/BRJ2015.2.3.5

Dinh, T. V., Choi, I. Y., Son, Y. S., Kim, J. C. (2016). A review on non-dispersive infrared gas sensors: Improvement of sensor detection limit and interference correction. *Sensors and Actuators, B: Chemical*, *231*, 529–538. https://doi.org/10.1016/j.snb.2016.03.040

Dixit, V., Misra, S. C. K., Sharma, B. S. (2005). Carbon monoxide sensitivity of vacuum deposited polyaniline semiconducting thin films. *Sensors and Actuators, B: Chemical*, *104*(1), 90–93. https://doi.org/10.1016/j.snb.2004.05.001

Dixon, P. K., Wu, L. (1989). Broadband digital lock-in amplifier techniques. *Review of Scientific Instruments*, *60*(10), 3329–3336. https://doi.org/10.1063/1.1140523

Dobos, K., Zimmer, G. (1985). Performance of carbon monoxide-sensitive MOSFET's with metal-oxide semiconductor gates. *IEEE Transactions on Electron Devices*, *32*(7), 1165–1169.

Downing, H. D., Williams, D. (1975). Optical constants of water in the infrared. *Journal of Geophysical Research*, *80*(12), 1656–1661.

Downs, C., Vandervelde, T. E. (2013). Progress in infrared photodetectors since 2000. *Sensors*, *13*(4), 5054–5098. https://doi.org/10.3390/s130405054

Duval, M. (2003). New techniques for dissolved gas-in-oil analysis. *IEEE Electrical Insulation Magazine*, *19*(2), 6–15. https://doi.org/10.1109/MEI.2003.1192031

Ebert, V., Giesemann, C., Koeth, J., Teichert, H., Köth, J., Teichert, H. (2004). New room-temperature 2.3μm DFB-diode lasers: First spectroscopic characterization and CO-detection. *Laser Applications to Chemical and Environmental Analysis*, *m*, 2003–2005. Retrieved from http://www.opticsinfobase.org/abstract.cfm?URI=LACEA-2004-TuF9

Emmons, R. B., Hawkins, S. R., Cuff, K. F. (1975). Infrared Detectors: An Overview. *Optical Engineering*, *14*(1), 21–30.

Eppeldauer, G. P., Martin, R. J. (2001). Photocurrent measurement of PC and PV HgCdTe detectors. *Journal of Research of the National Institute of Standards and Technology*, *106*(3), 577–587. https://doi.org/10.6028/jres.106.024

Fahrenfort, J. (1961). Attenuated total reflection. *Spectrochimica Acta*, *17*(7), 698–709. https://doi.org/10.1016/0371-1951(61)80136-7

Fanchenko, S., Baranov, A., Savkin, A., Sleptsov, V. (2016). LED-based NDIR natural gas analyzer. In *IOP Conference Series: Materials Science and Engineering* (Vol. 108, p. 012036). IOP Publishing. https://doi.org/10.1088/1757-899X/108/1/012036

Fergus, J. W. (2007). Solid electrolyte based sensors for the measurement of CO and hydrocarbon gases. *Sensors and Actuators, B: Chemical*, *122*(2), 683–693. https://doi.org/10.1016/j.snb.2006.06.024

Fietzek, P., Fiedler, B., Steinhoff, T., K??rtzinger, A. (2014). In situ quality assessment of a novel underwater pCO2 sensor based on membrane equilibration and NDIR spectrometry. *Journal of Atmospheric and Oceanic Technology*, *31*(1), 181–196. https://doi.org/10.1175/JTECH-D-13-00083.1

Formoso, M. A., Maclay, G. J. (1990). The effect of hydrogen and carbon monoxide on the interface state density in MOS gas sensors with ultra-thin palladium gates. *Sensors and Actuators B: Chemical*, *2*(1), 11–22.

Fouletier, J. (1982). Gas Analysis with Potentiometric Sensors A Review. *Sensors and Actuators*, *3*, 295–314.

Fukuda, H., Zohnishi, R., Nomura, S. (2001). Highly sensitive metal-insulator-semiconductor field-effect transistor sensors for detecting carbon monoxide gas using porous platinum and tungsten oxide thin films. *Japanese Journal of Applied Physics, Part 1: Regular Papers and Short Notes and Review Papers*, *40*(4 B), 2782–2786.

Fukushi, K., Hiiro, K. (1987). Determination of total carbon dioxide in seawater by capillary type isotachophoresis. *Fresenius' Zeitschrift Für Analytische Chemie*, *328*(3), 247–250.

Fung, Y. S., Wong, C. C. W. (2002). Determination of carbon monoxide in ambient air using piezoelectric crystal sorption detection. *Analytica Chimica Acta*, *456*(2), 227–239. https://doi.org/10.1016/S0003-2670(02)00013-2

Gabelman, A., Hwang, S.-T. (1999). Hollow fiber membrane contactors. *Journal of Membrane Science*, *159*(1–2), 61–106. https://doi.org/10.1016/S0376-7388(99)00040-X

Gaspar, J., Chen, S. F., Gordillo, A., Hepp, M., Ferreyra, P., Marques, C. (2004). Digital lock in amplifier: Study, design and development with a digital signal processor. *Microprocessors and Microsystems*, *28*(4), 157–162. https://doi.org/10.1016/j.micpro.2003.12.002

Gerbig, C., Kley, D., Volz-thomas, A., Kent, J., Dewey, K., McKenna, D. S. (1996). Fast response resonance fluorescence CO measurements aboard the C-130: Instrument characterization and measurements made during North Atlantic Regional Experiment 1993. *Journal of Geophysical Research: Atmospheres*, *101*(D22), 29229–29238.

Gerbig, C., Schmitgen, S., Kley, D., Volz-thomas, A., Dewey, K., Haaks, D. (1999). An improved fast-response vacuum-UV resonance fluorescence CO instrument. *Journal of Geophysical Research: Atmospheres*, *104*(D1), 1699–1704.

Gerlach, R., Amer, N. M. (1978). Sensitive optoacoustic detection of carbon monoxide by resonance absorption. *Applied Physics Letters*, *32*(4), 228–231.

Ghodselahi, T., Zahrabi, H., Saani, M. H., Vesaghi, M. A. (2011). COGas Sensor Properties of Cu@CuO Core Shell Nanoparticles Based on Localized Surface Plasmon Resonance. *The Journal of Physical Chemistry C*, *115*(45), 22126–22130.

Ghosh, S., Chowdhury, U., Roy, S., Bandyopadhyay, R. (2016). Detection of low ppm carbon monoxide with charge ordered LuFe2O4 gas sensor – A novel sensing mechanism. *Ceramics International*, *42*(13), 14944–14948.

Gmachl, C., Capasso, F., Sivco, D. L., Cho, a. Y. (2001). Recent progress in quantum cascade lasers and applications. *Report on Progress in Physics*, *64*, 1533–1601.

Godard, A. (2007). Infrared (2-12 μm) solid-state laser sources: a review. *Comptes Rendus Physique*, *8*(10), 1100–1128. https://doi.org/10.1016/j.crhy.2007.09.010

Gonzalez-valencia, R., Magana-rodriguez, F., Gerardo-nieto, O., Sepulveda-jauregui, A., Martinez-cruz, K., Anthony, K. W., … Thalasso, F. (2014). In situ measurement of dissolved methane and carbon dioxide in freshwater ecosystems by off-axis integrated cavity output spectroscopy. *Environmental Science & Technology*, *48*(19), 11421–11428.

Goto, T., Hyodo, T., Ueda, T., Kamada, K., Kaneyasu, K., Shimizu, Y. (2015). CO-sensing Properties of Potentiometric Gas Sensors Using an Anion-conducting Polymer Electrolyte and Au-loaded Metal Oxide Electrodes. *Electrochimica Acta*, *166*, 232–243.

Guimarães, O. M., Zaniquelli, M. E. D., Castro, J. R. M., Balbo, V. R., Andrade, J. F. (2006). Determination of carbon monoxide using a coated quartz crystal sensor. *Eclética Química*, *31*(4), 23–29.

Gurbuz, Y., Kang, W. P., Davidson, J. L., Kerns, D. V. (1999). A new diode-based carbon monoxide gas sensor utilizing Pt–SnO x/diamond. *Sensors and Actuators B: Chemical*, *56*(1), 151–154.

Haigh, M. K., Nash, G. R., Terakado, T., Bando, N., Yamagishi, Y., Smith, S. J., … Ashley, T. (2007). Mid-infrared AlxIn1-xSb components for gas sensing. In *Journal of Physics: Conference Series* (Vol. 76, p. 012003). IOP Publishing. https://doi.org/10.1088/1742-6596/76/1/012003

Hall, D. N., Aikens, R. S., Joyce, R., McCurnin, T. W. (1975). Johnson Noise Limited Operation of Photovoltaic InSb Detectors. *Applied Optics*, *14*(2), 450–453. https://doi.org/10.1364/AO.14.000450

Hara, N., Macdonald, D. D. (1997). Development of Dissolved Hydrogen Sensors Based on Yttria-Stabilized Zirconia Solid Electrolyte with Noble Metal Electrodes. *Journal of The Electrochemical Society*, *144*(12), 4152. https://doi.org/10.1149/1.1838158

Harren, F. J. M., Cotti, G., Oomens, J., Hekkert, S. te L. (2000). Photoacoustic Spectroscopy in Trace Gas Monitoring. *Encyclopedia of Analytical Chemistry*, 2203–2226. https://doi.org/10.1002/9780470027318.a0718

Hillman, K., Lloyd, D., Williams, A. G. (1985). Use of a portable quadrupole mass spectrometer for the measurement of dissolved gas concentrations in ovine rumen liquor in situ. *Current Microbiology*, *12*(6), 335–339.

Ho, M. H., Gullbault, G. G. (1982). Detection of carbon monoxide in ambient air with a piezoelectric crystal. *Analytical Chemistry*, *54*(12), 1998–2002.

Hodgkinson, J., Tatam, R. P. (2013). Optical gas sensing: a review. *Measurement Science and Technology*, *24*(1), 012004. https://doi.org/10.1088/0957-0233/24/1/012004

Hök, B., Blückert, A., Löfving, J. (2000). Acoustic gas sensor with ppm resolution. *Sensor Review*, *20*(2), 139–142. https://doi.org/10.1108/SR-05-2015-0073

Hurst, K. M., Lewis, R. S. (2010). Carbon monoxide partial pressure effects on the metabolic process of syngas fermentation. *Biochemical Engineering Journal*, *48*(2), 159–165. https://doi.org/10.1016/j.bej.2009.09.004

Inoue, T., De Zoysa, M., Asano, T., Noda, S. (2014). Filter-free nondispersive infrared sensing using narrow-bandwidth mid-infrared thermal emitters. *Applied Physics Express*, *7*(1), 012103. https://doi.org/10.7567/APEX.7.012103

Jacobs, M. B., Braverman, M. M., Hochheiser, S. (1959). Continuous Determination of Carbon Monoxide and Hydrocarbons in Air by a Modified Infrared Analyzer. *Journal of the Air Pollution Control Association*, *9*(2), 110–114. https://doi.org/10.1080/00022470.1959.10467879

Jalbert, J., Gilbert, R., Tétreault, P. (2001). Simultaneous determination of dissolved gases and moisture in mineral insulating oils by static headspace gas chromatography with helium photoionization pulsed discharge detection. *Analytical Chemistry*, *73*(14), 3382–3391. https://doi.org/10.1021/ac010063f

Jang, N., Yasin, M., Kang, H., Lee, Y., Park, G. W., Park, S., Chang, I. S. (2018). Bubble coalescence suppression driven carbon monoxide (CO) - water mass transfer increase by electrolyte addition in a hollow fiber membrane bioreactor (HFMBR) for microbial CO conversion to ethanol. *Bioresource Technology*, *263*, 375–384. https://doi.org/10.1016/j.biortech.2018.05.012

Jeroschewski, P., Steuckart, C., Kühl, M. (1996). An Amperometric Microsensor for the Determination of H2S in Aquatic Environments. *Analytical Chemistry*, *68*(24), 4351–4357. https://doi.org/10.1021/ac960091b

Johnson, K. M., Hughes, J. E., Donaghay, P. L., Sieburth, J. M. (1990). Bottle-Calibration Static Head Space Method for the Determination of Methane Dissolved in Seawater. *Analytical Chemistry*, *62*(21), 2408–2412.

Kaiser, H. (1978). Foundations for the critical discussion of analytical methods. *Spectrochimica Acta Part B: Atomic Spectroscopy*, *33*(9), 551–576.

Kampbell, D. H., Vandegrift, S. A. (1998). Analysis of dissolved methane, ethane, and ethylene in ground water by a standard gas chromatographic technique. *Journal of Chromatographic Science*, *36*(5), 253–256.

Karim, A., Andersson, J. Y. (2013). Infrared detectors: Advances, challenges and new technologies. In *IOP Conference Series: Materials Science and Engineering* (Vol. 51, p. 012001). https://doi.org/10.1088/1757-899X/51/1/012001

Kaye, W. (1955). Near infrared spectroscopy: Instrumentation and technique. *Spectrochimica Acta*, *7*, 181–204.

Khoshhesab, Z. M. (2012). Reflectance IR Spectroscopy. In T. Theophanides (Ed.), *Infrared Spectroscopy - Materials Science, Engineering and Technology*. InTech. https://doi.org/10.5772/37180

Kikuchi, K., Takeda, H., Rabolt, B., Okaya, T., Ogumi, Z., Saihara, Y., Noguchi, H. (2001). Hydrogen particles and supersaturation in alkaline water from an Alkali–Ion–Water electrolyzer. *Journal of Electroanalytical Chemistry*, *506*(1), 22–27. https://doi.org/10.1023/A:1013824220007

Kobayashi, T., Haruta, M., Sano, H., Nakane, M. (1988). A selective CO sensor using Ti-doped α-Fe2O3 with coprecipitated ultrafine particles of gold. *Sensors and Actuators*, *13*(4), 339–

349.

Koppius, O. G. (1951). Analysis of Mixtures with Double-Beam Nondispersive Infrared Instrumen. *Analytical Chemistry*, *23*(4), 554–559.

Kosterev, A. A., Bakhirkin, Y. A., Tittel, F. K. (2005). Ultrasensitive gas detection by quartz-enhanced photoacoustic spectroscopy in the fundamental molecular absorption bands region. *Applied Physics B: Lasers and Optics*, *80*(1), 133–138. https://doi.org/10.1007/s00340-004-1619-y

Kosterev, A. A., Tittel, F. K. (2002). Chemical sensors based on quantum cascade lasers. *IEEE Journal of Quantum Electronics*, *38*(6), 582–591. https://doi.org/10.1109/JQE.2002.1005408

Kraemer, J. T., Bagley, D. M. (2006). Supersaturation of Dissolved H2 and CO2 During Fermentative Hydrogen Production with N2 Sparging. *Biotechnology Letters*, *28*(18), 1485–1491. https://doi.org/10.1007/s10529-006-9114-7

Krämer, H., Conrad, R. (1993). Measurement of dissolved H2 concentrations in methanogenic environments with a gas diffusion probe. *FEMS Microbiology Ecology*, *12*(3), 149–158.

Kundu, S., Premer, S. A., Hoy, J. A., Trent, J. T., Hargrove, M. S. (2003). Direct Measurement of Equilibrium Constants for High-Affinity Hemoglobins. *Biophysical Journal*, *84*(6), 3931–3940. https://doi.org/10.1016/S0006-3495(03)75121-2

Kuo, C. W., Shih, J. S. (2005). Cryptand/metal ion coated piezoelectric quartz crystal sensors with artificial back propagation neural network analysis for nitrogen dioxide and carbon monoxide. *Sensors and Actuators, B: Chemical*, *106*(1 SPEC. ISS.), 468–476. https://doi.org/10.1016/j.snb.2004.09.009

Kuroda, K., Silveira, R. G., Nishio, N., Sunahara, H., Nagai, S. (1991). Measurement of dissolved hydrogen in an anaerobic digestion process by a membrane-covered electrode. *Journal of Fermentation and Bioengineering*, *71*(6), 418–423.

Kuusela, T., Peura, J., Matveev, B. A., Remennyy, M. A., Stus', N. M. (2009). Photoacoustic gas detection using a cantilever microphone and III-V mid-IR LEDs. *Vibrational Spectroscopy*, *51*(2), 289–293. https://doi.org/10.1016/j.vibspec.2009.08.001

Lammers, S., Suess, E. (1994). An improved head-space analysis method for methane in seawater. *Marine Chemistry*, *47*(2), 115–125. https://doi.org/10.1016/0304-4203(94)90103-1

Leonard, C., Liu, H.-F., Brewer, S., Sacks, R. (1998). High-speed gas extraction of volatile and semivolatile organic compounds from aqueous samples. *Analytical Chemistry*, *70*(16), 3498–3504.

Li, G.-L., Sui, Y., Dong, M., Ye, W.-L., Zheng, C.-T., Wang, Y.-D. (2015). A carbon monoxide detection device based on mid-infrared absorption spectroscopy at 4.6 μm. *Applied Physics B*, *119*, 287–296. https://doi.org/10.1007/s00340-015-6056-6

Li, N., Tan, T. C., Zeng, H. C. (1993). High-Temperature Carbon Monoxide Potentiometric Sensor. *Journal of The Electrochemical Society*, *140*(4), 1068. https://doi.org/10.1149/1.2056199

Lim, Y. C., Parker, S. R. (1983). FIR Filter Design Over a Discrete Powers-of-Two Coefficient Space. *IEEE Transactions on Acoustics, Speech, and Signal Processing*, *31*(3), 583–591. https://doi.org/10.1109/TASSP.1983.1164085

Lin, S. Y., Moreno, J., Fleming, J. G. (2003). Three-dimensional photonic-crystal emitter for thermal photovoltaic power generation. *Applied Physics Letters*, *83*(2), 380–382. https://doi.org/10.1063/1.1592614

Liu, C., Noda, Z., Sasaki, K., Hayashi, K. (2012). Development of a polyaniline nanofiber-based carbon monoxide sensor for hydrogen fuel cell application. *International Journal of Hydrogen Energy*, *37*(18), 13529–13535.

Liu, Y., Tang, Y., Barashkov, N. N., Irgibaeva, I. S., Lam, J. W. Y., Hu, R., … Tang, B. Z. (2010). Fluorescent Chemosensor for Detection and Quantitation of Carbon Dioxide Gas. *J. Am. Chem. Soc.*, *132*, 13951–13953. https://doi.org/10.1021/ja103947j

Lobnik, A., Wolfbeis, O. S. (1998). Sol-gel based optical sensor for dissolved ammonia. *Sensors and Actuators B: Chemical*, *51*(1–3), 203–207. https://doi.org/10.1016/S0925-4005(98)00189-0

Long, G. L., Winefordner, J. D. (1983). Limit of Detection: A Closer Look at the IUPAC Definition. *Analytical Chemistry*, *55*(7), 712A–724A. https://doi.org/10.1021/ac00258a001

Loose, B., Stute, M., Alexander, P., Smethie, W. M. (2009). Design and deployment of a portable membrane equilibrator for sampling aqueous dissolved gases. *Water Resources Research*, *45*(4). https://doi.org/10.1029/2008WR006969

Lovley, D. R., Goodwin, S. (1988). Hydrogen concentrations as an indicator of the predominant terminal electron accepting reaction sin aquatic sediments. *Geochimica Et Cosmochimica Acta*, *52*(12), 2993–3003.

MacIsaac, D., Kanner, G., Anderson, G. (1999). Basic physics of the incandescent lamp (lightbulb). *The Physics Teacher*, *37*(9), 520–525. https://doi.org/10.1119/1.880392

Maclay, G. J., Jelley, K. W., Nowroozi-Esfahani, S., Formosa, M. (1988). The response of MOS sensors with ultrathin palladium gates to carbon monoxide and methane. *Sensors and Actuators*, *14*(4), 331–348.

Maddipati, P., Atiyeh, H. K., Bellmer, D. D., Huhnke, R. L. (2011). Ethanol production from syngas by Clostridium strain P11 using corn steep liquor as a nutrient replacement to yeast extract. *Bioresource Technology*, *102*(11), 6494–6501. https://doi.org/10.1016/j.biortech.2011.03.047

Marín-Hernández, C., Toscani, A., Sancenón, F., Wilton-Ely, J. D. E. T., Martínez-Máñez, R. (2016). Chromo-fluorogenic probes for carbon monoxide detection. *Chem. Commun.*, *52*(35), 5902–5911. https://doi.org/10.1039/C6CC01335J

Matkovich, K. M., Thorne, L. M., Wolf, M. O., Pace, T. C. S., Bohne, C., Patrick, B. O. (2006). Luminescence of Ruthenium Halide Complexes Containing a Hemilabile Phosphine Pyrenyl Ether Ligand. *Inorganic Chemistry*, *45*(12), 4610–4618.

Matsumiya, M., Qiu, F., Shin, W., Izu, N., Matsubara, I., Murayama, N., Kanzaki, S. (2004). Thermoelectric CO Gas Sensor Using Thin-Film Catalyst of Au and Co3O4. *Journal of The*

Electrochemical Society, *151*(1), H7–H10. https://doi.org/10.1149/1.1630810

Matsumoto, T., Han, L. F., Jaklitsch, M., Aggarwal, P. K. (2013). A Portable Membrane Contactor Sampler for Analysis of Noble Gases in Groundwater. *GroundWater*, *51*(3), 461–468. https://doi.org/10.1111/j.1745-6584.2012.00983.x

McDonagh, C., Burke, C. S., MacCraith, B. D. (2008). Optical chemical sensors. *Chemical Reviews*, *108*(2), 400–422.

McEvoy, A. K., McDonagh, C. M., MacCraith, B. D. (1996). Dissolved Oxygen Sensor Based on Fluorescence Quenching of Oxugen-Sensitive Ruthenium Complexes Immobilized in Sol-Gel-derived Porous Silica Coatings. *Analyst*, *121*(June), 785–788.

Michaelian, K. H. (2010). *Photoacoustic IR Spectroscopy: Instrumentation, Applications and Data Analysis* (2nd ed.). John Wiley & Sons. https://doi.org/3527633219

Michel, B. W., Lippert, A. R., Chang, C. J. (2012). A Reaction-Based Fluorescent Probe for Selective Imaging of Carbon Monoxide in Living Cells Using a Palladium-Mediated Carbonylation. *Journal of the American Chemical Society*, *134*(38), 15668–15671.

Miller, J. H., Elreedy, S., Ahvazi, B., Woldu, F., Hassanzadeh, P. (1993). Tunable diode-laser measurement of carbon monoxide concentration and temperature in a laminar methane-air diffusion flame. *Applied Optics*, *32*(30), 6082–6089.

Mills, A., Chang, Q. (1994). Colorimetric polymer film sensors for dissolved carbon dioxide. *Sensors and Actuators B*, *21*(2), 83–89. https://doi.org/10.1016/0925-4005(94)80008-1

Mirabella, F. M. (1998). Attenuated Total Reflection Spectroscopy. In F. M. Mirabella (Ed.), *Modern Techniques in Applied Molecular Spectroscopy.* (1st ed., pp. 127–185). Wiley-Interscience.

Mislov, D., Cifrek, M., Krois, I., Dzapo, H. (2015). Measurement of dissolved hydrogen concentration with clark electrode. In *Sensors Applications Symposium (SAS), 2015 IEEE* (pp. 1–5). https://doi.org/10.1109/SAS.2015.7133656

Misra, S. C. K., Mathur, P., Srivastava, B. K. (2004). Vacuum-deposited nanocrystalline polyaniline thin film sensors for detection of carbon monoxide. *Sensors and Actuators, A: Physical*, *114*(1), 30–35. https://doi.org/10.1016/j.sna.2004.02.026

Miyazaki, H. T., Ikeda, K., Kasaya, T., Yamamoto, K., Inoue, Y., Fujimura, K., … Kitagawa, S. (2008). Thermal emission of two-color polarized infrared waves from integrated plasmon cavities. *Applied Physics Letters*, *92*(14), 141114. https://doi.org/10.1063/1.2906375

Miyazaki, H. T., Kasaya, T., Iwanaga, M., Choi, B., Sugimoto, Y., Sakoda, K. (2014). Dual-band infrared metasurface thermal emitter for CO2 sensing. *Applied Physics Letters*, *105*(12), 1–5. https://doi.org/10.1063/1.4896545

Mizaikoff, B. (1999). Mid-infrared evanescent wave sensors - A novel approach for subsea monitoring. *Measurement Science and Technology*, *10*(12), 1185–1194. https://doi.org/10.1088/0957-0233/10/12/310

Mocak, J., Bond, A. M., Mitchell, S., Scollary, G. (1997). A statistical overview of standard (IUPAC and ACS) and new procedures for determining the limits of detection and

quantification: application to voltammetric and stripping techniques (technical report). *Pure and Applied Chemistry*, *69*(2), 297–328.

Moragure, M. E., Esteban, J., Ros-Lis, J. V., Martinez-Máñez, R., Marcos, M. D., Martínez, M., … Sancenón, F. (2011). Sensitive and selective chromogenic sensing of carbon monoxide via reversible axial CO coordination in binuclear rhodium complexes. *Journal of the American Chemical Society*, *133*(39), 15762–15772.

Morrison, S. R. (1953). Changes of Surface Conductivity of Germanium with Ambient. *The Journal of Physical Chemistry*, *57*(8), 860–863. https://doi.org/10.1021/j150509a025

Morrison, S. R. (1982). Semiconductor gas sensors. *Sensors and Actuators*, *2*, 329–341. https://doi.org/10.1016/0250-6874(81)80054-6

Muller, B., Hauser, P. C. (1996). Fluorescence optical sensor for low concentrations of dissolved carbon dioxide. *Analyst*, *121*(3), 339–343. https://doi.org/10.1039/an9962100339

Munasinghe, P. C., Khanal, S. K. (2010). Biomass-derived syngas fermentation into biofuels: opportunities and challenges. *Bioresource Technology*, *101*(13), 5013–5022. https://doi.org/10.1016/B978-0-12-385099-7.00004-8

Nagai, D., Nakashima, T., Nishibori, M., Itoh, T., Izu, N., Shin, W. (2013). Thermoelectric gas sensor with CO combustion catalyst for ppm level carbon monoxide detection. *Sensors and Actuators B: Chemical*, *182*, 789–794.

Nam, H., Sasaki, T., Koshizaki, N. (2006). Optical CO gas sensor using a cobalt oxide thin film prepared by pulsed laser deposition under various argon pressures. *The Journal of Physical Chemistry B*, *110*(46), 23081–23084.

Nei, L., Compton, R. G. (1996). An improved Clark-type galvanic sensor for dissolved oxygen. *Sensors and Actuators, B: Chemical*, *30*(2), 83–87. https://doi.org/10.1016/0925-4005(95)01754-J

Noij, T., Es, A. Van, Cramers, C., Rijks, J. (1987). Selective Removal of Water in Purge and Cold-Trap Capillary Gas Chromatographic Analysis of Volatile Organic Traces in. *Journal of Separation Science*, *10*(2), 60–66.

Norton, P. (2002). HgCdTe Infrared Detectors. *Opto-Electronics Review*, *10*(3), 159–174. Retrieved from http://bib.convdocs.org/docs/11/10867/conv_2/file2.pdf

Nudelman, S. (1962). The detectivity of infrared photodetectors. *Applied Optics*, *1*(5), 627–636.

Okamoto, H., Obayashi, H., Kudo, T. (1980). Carbon monoxide gas sensor made of stabilized zirconia. *Solid State Ionics*, *1*(3–4), 319–326.

Pagel, B. R., Petritz, R. L. (1961). Noise in InSb photodiodes. *Journal of Applied Physics*, *32*(10), 1901–1904. https://doi.org/10.1063/1.1728260

Pandey, P., Chauhan, R. S. (2001). Membranes for gas separation. *Progress in Polymer Science*, *26*(6), 853–893. https://doi.org/10.1016/S0079-6700(01)00009-0

Pandey, S. (2016). Highly sensitive and selective chemiresistor gas/vapor sensors based on polyaniline nanocomposite: a comprehensive review. *Journal of Science: Advanced Materials and Devices*, *1*(4), 431–453.

Park, H., Kim, K., Chung, Y. K. (2014). Re I–Ir I bimetallic complexes based on a bis (chelating) ligand composed of 1, 10-phenanthroline and N-heterocyclic carbene: Coordination chemistry and their application for optical indicator of CO gas. *Inorganica Chimica Acta*, *410*, 214–220.

Park, J. Y., Song, S. J., Wachsman, E. D. (2010). Highly sensitive/selective miniature potentiometric carbon monoxide gas sensors with titania-based sensing elements. *Journal of the American Ceramic Society*, *93*(4), 1062–1068. https://doi.org/10.1111/j.1551-2916.2009.03500.x

Patimisco, P., Scamarcio, G., Tittel, F. K., Spagnolo, V. (2014). Quartz-enhanced photoacoustic spectroscopy: A review. *Sensors*, *14*(4), 6165–6206. https://doi.org/10.3390/s140406165

Pauss, A., Samson, R., Guiot, S., Beauchemin, C. (1990). Continuous measurement of dissolved H2 in an anaerobic reactor using a new hydrogen/air fuel cell detecto. *Biotechnology and Bioengineering*, *35*(5), 492–501.

Peng, Z. G., Lee, S. H., Zhou, T., Shieh, J. J., Chung, T. S. (2008). A study on pilot-scale degassing by polypropylene (PP) hollow fiber membrane contactors. *Desalination*, *234*(1–3), 316–322. https://doi.org/10.1016/j.desal.2007.09.100

Peter, C., Gutmacher, D., Schumacher, I., Schmitt, K., Wöllenstein, J. (2012). 8.5.3 Colorimetric CO and NO2 Gas Sensors for Fire Detection. *Proceedings IMCS*, 732–735. https://doi.org/10.5162/IMCS2012/8.5.3

Phillips, J. R., Huhnke, R. L., Atiyeh, H. K. (2017). Syngas Fermentation: A Microbial Conversion Process of Gaseous Substrates to Various Products. *Fermentation*, *3*(2), 28. https://doi.org/10.3390/fermentation3020028

Popov, A. ., Sherstnev, V. V., Yakovlev, Y. P., Baranov, A. N., Alibert, C. (1997). Powerful mid-infrared light emitting diodes for pollution monitoring. *Electronics Letters*, *33*(1), 86–88.

Potter, R. F., Eisenman, W. L. (1962). Infrared Photodetectors: A Review of Operational Detectors. *Applied Optics*, *1*(5), 567–574. https://doi.org/10.1364/AO.1.000567

Pralle, M. U., Moelders, N., McNeal, M. P., Puscasu, I., Greenwald, A. C., Daly, J. T., … Biswas, R. (2002). Photonic crystal enhanced narrow-band infrared emitters. *Applied Physics Letters*, *81*(25), 4685–4687. https://doi.org/10.1063/1.1526919

Pratt, K. F., Pawliszyn, J. (1992). Water Monitoring System Based on Gas Extraction with a Single Hollow Fiber Membrane and Gas Chromatographic Cryotrapping. *Analytical Chemistry*, *64*(18), 2107–2110. https://doi.org/10.1021/ac00042a015

Ram, M. K., Yavuz, Ö., Lahsangah, V., Aldissi, M. (2005). CO gas sensing from ultrathin nano-composite conducting polymer film. *Sensors and Actuators, B: Chemical*, *106*(2), 750–757. https://doi.org/10.1016/j.snb.2004.09.027

Ramamoorthy, R., Dutta, P. K., Akbar, S. A. (2003). Oxygen sensors : Materials , methods , designs, *8*, 4271–4282.

Ramieri, A., Jatlow, P., Seligson, D. (1974). New method for rapid determination of carboxyhemoglobin by use of double-wavelength spectrophotometry. *Clinical Chemistry*, *20*(2), 278–281.

Razeghi, M., Wei, Y., Gin, A. V., Brown, G. J., Johnstone, D. (2002). Type II InAs/GaSb superlattices and detectors with λc > 18 μm. In *Photodetector Materials and Devices VII* (Vol. 4650, pp. 111–117). International Society for Optics and Photonics. https://doi.org/10.1117/12.467673

Revsbech, N. P. (2005). Analysis of microbial communities with electrochemical microsensors and microscale biosensors. *Methods in Enzymology*, *397*(2003), 147–166. https://doi.org/10.1016/S0076-6879(05)97009-2

Revsbech, N. P., Nielsen, L. P., Christensen, P. B., Sorensen, J. (1988). Combined Oxygen and Nitrous Oxide Microsensor for Denitrification Studies. *Appl. Envir. Microbiol.*, *54*(9), 2245–2249. Retrieved from http://aem.asm.org/content/54/9/2245.short

Riggs, S. S., Heindel, T. J. (2006). Measuring carbon monoxide gas-liquid mass transfer in a stirred tank reactor for syngas fermentation. *Biotechnology Progress*, *22*(3), 903–906. https://doi.org/10.1021/bp050352f

Robbins, G. A., Wang, S., Stuart, J. D. (1993). Using the Static Headspace Method to Determine Henry's Law Constants. *Analytical Chemistry*, *65*(21), 3113–3118. https://doi.org/10.1021/ac00069a026

Roessler, D. M. (1965). Kramers-Kronig analysis of reflection data. *British Journal of Applied Physics*, *16*(8), 1119–1123.

Rogalski, A. (2002). Infrared detectors: an overview. *Infrared Physics & Technology*, *43*(3–5), 187–210.

Rogalski, A. (2005). HgCdTe infrared detector material: History, status and outlook. *Reports on Progress in Physics*, *68*(10), 2267–2336. https://doi.org/10.1088/0034-4885/68/10/R01

Rogalski, A. (2011). Recent progress in infrared detector technologies. *Infrared Physics and Technology*, *54*(3), 136–154. https://doi.org/10.1016/j.infrared.2010.12.003

Rogalski, A. (2012). History of infrared detectors. *Opto-Electronics Review*, *20*(3), 279–308. https://doi.org/10.2478/s11772

Rogers, C. W., Wolf, M. O. (2002). Drastic Luminescence Response to Carbon Monoxide from a RuII Complex Containing a Hemilabile Phosphane Pyrene Ether. *Angewandte Chemie International Edition*, *41*(11), 1898–1900.

Salehi, A., Jamshidi Kalantari, D. (2007). Characteristics of highly sensitive Au/porous-GaAs Schottky junctions as selective CO and NO gas sensors. *Sensors and Actuators, B: Chemical*, *122*(1), 69–74. https://doi.org/10.1016/j.snb.2006.05.004

Salehi, A., Nikfarjam, A. (2004). Room temperature carbon monoxide sensor using ITO/n-GaAs Schottky contact. *Sensors and Actuators, B: Chemical*, *101*(3), 394–400. https://doi.org/10.1016/j.snb.2004.04.013

Salonen, K. (1981). Rapid and precise determination of total inorganic carbon and some gases by high temperature combustion. *Water Research*, *15*(15), 403–406.

Sander, R. (2015). Compilation of Henry's law constants (version 4.0) for water as solvent. *Atmospheric Chemistry and Physics*, *15*(8), 4399–4981. https://doi.org/10.5194/acp-15-

4399-2015

Sanford, E., Shropshire, R. G., Solomon, D. K. (1996). Dissolved gas tracers in groundwater: Simplified injection, sampling, and analysis. *Water Resources Research*, *32*(6), 1635–1642.

Saptari, V. (2003). *Fourier transform spectroscopy instrumentation engineering*. SPIE Optical Engineering Press.

Schaden, S., Haberkorn, M., Frank, J., Baena, J. R., Lendl, B. (2004). Direct determination of carbon dioxide in aqueous solution using mid-infrared quantum cascade lasers. *Applied Spectroscopy*, *58*(6), 667–670. https://doi.org/10.1366/000370204872971

Scharffe, D., Slemr, F., Brenninkmeijer, C. A. M., Zahn, A. (2012). Carbon monoxide measurements onboard the CARIBIC passenger aircraft using UV resonance fluorescence. *Atmospheric Measurement Techniques*, *5*(7), 1753–1760. https://doi.org/10.5194/amt-5-1753-2012

Schelter, M., Zosel, J., Oelßner, W., Mertig, M. (2014). A novel method for measuring dissolved gases in liquids. *Sensors and Actuators B: Chemical*, *193*, 113–120.

Schiavon, G., Zotti, G., Toniolo, R., Bontempelli, G. (1991). Amperometric monitoring of sulphur dioxide in liquid and air samples of low conductivity by electrodes supported on ion-exchange membranes. *The Analyst*, *116*(8), 797–801. https://doi.org/10.1039/AN9911600797

Schiff, H. I., Mackay, G. I., Bechara, J. (1994). The Use of Tunable Diode-Laser Absorption-Spectroscopy for Atmospheric Measurements. *Research on Chemical Intermediates*, *20*(3–5), 525–556. https://doi.org/10.1163/156856794X00441

Schiff, H. I., Mackay, G. I., Bechara, J., and Bechara, J. (1994). The use of tunable diode laser absorption spectroscopy for atmospheric measurements. *Air Monitoring by Spectroscopic Techniques*, *20*(3), 239–333.

Schrader, B. (Ed.). (1994). *Infrared and Raman Spectroscopy-Methods and Applications*. VCH Verlagsgesellschaft mbH. https://doi.org/10.1016/0924-2031(00)00065-5

Sclar, N. (1984). Properties of doped silicon and Germanium infrared detectors. *Progress in Quantum Electronics*, *9*(3), 149–257. https://doi.org/10.1016/0079-6727(84)90001-6

Scofield, J. H. (1994). Frequency-domain description of a lock-in amplifier. *American Journal of Physics*, *62*(2), 129–133. https://doi.org/10.1119/1.17629

Sen, T., Shimpi, N. G., Mishra, S. (2016). Room temperature CO sensing by polyaniline/Co3O4 nanocomposite. *Journal of Applied Polymer Science*, *133*(42), 4–11. https://doi.org/10.1002/app.44115

Sengupta, A., Peterson, P. A., Miller, B. D., Schneider, J., Fulk, C. W. (1998). Large-scale application of membrane contactors for gas transfer from or to ultrapure water. *Separation and Purification Technology*, *14*(1–3), 189–200. https://doi.org/10.1016/S1383-5866(98)00074-4

Severinghaus, J. W., Freeman, B. A. (1958). Electrodes for blood pO2 and pCO2 determination. *Journal of Applied Physiology*, *13*(3), 515–520.

Shine, K. P., Campargue, A., Mondelain, D., McPheat, R. A., Ptashnik, I. V., Weidmann, D. (2016). The water vapour continuum in near-infrared windows – Current understanding and prospects for its inclusion in spectroscopic databases. *Journal of Molecular Spectroscopy*, *327*, 193–208. https://doi.org/10.1016/j.jms.2016.04.011

Silver, J. A., Chen, S.-J. (2006). Carbon monoxide sensor for combustion feedback control. In *44th AIAA Aerospace Sciences Meeting and Exhibit* (pp. 9–12).

Skoog, D. A., Holler, F. J., Crouch, S. R. (2017). *Principles of Instrumental Analysis* (7st ed.). Cengage Learning. Retrieved from https://books.google.com/books/about/Principles_of_Instrumental_Analysis.html?id=D13EDQAAQBAJ

Smith, S. D., Hardaway, H. R., Crowder, J. G. (2002). Recent developments in the applications of mid-infrared lasers, LEDs, and other solid state sources to gas detection. In *Novel In-Plane Semiconductor Lasers* (Vol. 4651, pp. 157–173). International Society for Optics and Photonics. https://doi.org/10.1117/12.467944

Smith, S. W. (1999). *The scientist and engineer's guide to digital signal processing*. *California Technical Publishing* (2nd ed.). California Technical Publishing,San Diego,CA. https://doi.org/10.1109/79.826412

Sonnaillon, M. O., Bonetto, F. J. (2005). A low-cost, high-performance, digital signal processor-based lock-in amplifier capable of measuring multiple frequency sweeps simultaneously. *Review of Scientific Instruments*, *76*(2). https://doi.org/10.1063/1.1854196

Sorita, R., Kawano, T. (1997). A highly selective CO sensor using LaMnO3 electrode-attached zirconia galvanic cell. *Sensors And Actuators*, *40*(96), 29–32. https://doi.org/10.1016/S0925-4005(97)80195-5

Sotnikova, G. Y., Gavrilov, G. a., Aleksandrov, S. E., Kapralov, A. a., Karandashev, S. a., Matveev, B. a., Remennyy, M. a. (2010). Low Voltage CO2-Gas Sensor Based on III-V Mid-IR Immersion Lens Diode Optopairs: Where we Are and How Far we Can Go? *IEEE Sensors Journal*, *10*(2), 225–234. https://doi.org/10.1109/JSEN.2009.2033259

Stangelmayer, A., Klimant, I., Wolfbeis, O. S. (1998). Optical sensors for dissolved sulfur dioxide. *Instrumentation*, 73–76. https://doi.org/10.1007/s002160051037

Stefanski, P., Lewicki, R., Tarka, J., Ma, Y., Jahjah, M., Tittel, F. K. (2013). Sensitive Detection of Carbon Monoxide using a Compact High Power CW DFB-QCL based QEPAS Sensor. In *CLEO: QELS_Fundamental Science. Optical Society of America* (p. JW2A.68). https://doi.org/10.1364/CLEO_AT.2013.JW2A.68

Stetter, J. R., Li, J. (2008). Amperometric Gas Sensors: A Review. *Chemical Reviews*, *108*(2), 352–366.

Stuart, B. H. (2004). *Infrared Spectroscopy: Fundamentals and Applications*. Chichester, West Sussex, England ; Hoboken, NJ :J. Wiley. https://doi.org/10.1002/0470011149

Sweet, W. J., Houchins, J. P., Rosen, P. R., Arp, D. J. (1980). Polarographic Measurement of H2 in Aqueous Solutions. *Anal. Biochem.*, *107*, 337–340.

Swinehart, D. F. (1962). The Beer-Lambert Law. *Journal of Chemical Education*, *39*(7), 333.

https://doi.org/10.1021/ed039p333

Swinnerton, J. W., Linnenbom, V. J., Cheek, C. H. (1962). Determination of Dissolved Gases in Aqueous Solutions by Gas Chromatography. *Analytical Chemistry*, *34*(4), 483–485.

Swinnerton, J. W., Linnenbom, V. J., Cheek, C. H. (1962). Revised Sampling Procedure for Determination of Dissolved Gases in Solution by Gas Chromatography. *Analytical Chemistry*, *34*(11), 1509. https://doi.org/10.1021/ac60191a047

Tacke, M. (2003). New developments and applications of tunable IR lead salt lasers. *Solid-State Mid-Infrared Laser Sources*, *89*(1), 447–463.

Takeda, H., Ueda, T., Kamada, K., Matsuo, K., Hyodo, T., Shimizu, Y. (2015). CO-sensing properties of a NASICON-based gas sensor attached with Pt mixed with Bi2O3 as a sensing electrode. *Electrochimica Acta*, *155*, 9–15.

Tam, A. C. (1986). Applications of photoacoustic sensing techniques. *Reviews of Modern Physics*, *58*(2), 381.

Thermo Nicolet Corporation. (2002). FT-IR vs. Dispersive Infrared: Theory of Infrared Spectroscopy Instrumentation. Retrieved from http://www.thermo.com/eThermo/CMA/PDFs/Product/productPDF_21611.pdf

Thomas, R. F., Booth, R. L. (1973). Selective Electrode Measurement of Ammonia in Water and Wastes. *Environmental Science and Technology*, *7*(6), 523–526. https://doi.org/10.1021/es60078a006

Tirado-Acevedo, O., Chinn, M. S., Grunden, A. M. (2010). Production of biofuels from synthesis gas using microbial catalysts. *Advances in Applied Microbiology*, *70*(December 2010), 57–92. https://doi.org/10.1016/S0065-2164(10)70002-2

Tittel, F. K., Richter, D., Fried, A. (2003). Mid-infrared laser applications in spectroscopy. In I. T. Sorokina & K. T. Vodopyanov (Eds.), *Solid-State Mid-Infrared Laser Sources* (pp. 458–529). Springer-Verlag Berlin Heidelberg. https://doi.org/10.1007/3-540-36491-9_11

Torrent, J., Barrón, V. (2008). Diffuse reflectance spectroscopy. In *Methods of Soil Analysis Part 5—Mineralogical Methods. SSSA Book Ser. 5.5.* (pp. 367–385). Madison, WI: Soil Science Society of America. https://doi.org/10.2136/sssabookser5.5.c13

Toscani, A., Marín-Hernández, C., Moragues, M. E., Sancenõn, F., Dingwall, P., Brown, N. J., … Wilton-Ely, J. D. E. T. (2015). Ruthenium(II) and Osmium(II) Vinyl Complexes as Highly Sensitive and Selective Chromogenic and Fluorogenic Probes for the Sensing of Carbon Monoxide in Air. *Chemistry - A European Journal*, *21*(41), 14529–14538. https://doi.org/10.1002/chem.201501843

Tsai, M. W., Chuang, T. H., Meng, C. Y., Chang, Y. T., Lee, S. C. (2006). High performance midinfrared narrow-band plasmonic thermal emitter. *Applied Physics Letters*, *89*(17), 96–99. https://doi.org/10.1063/1.2364860

Tsurushima, N., Watanabe, S., Tsunogai, S. (1999). Determination of light hydrocarbons dissolved in seawater. *Talanta*, *50*(3), 577–583. https://doi.org/10.1016/S0039-9140(99)00144-7

Twiss, S. B., Teague, D. M., Bozek, J. W., Sink, M. V. (1955). Application of infrared spectroscopy to exhaust gas analysis. *Journal of the Air Pollution Control Association*, *5*(2), 75–83. https://doi.org/10.1080/00966665.1955.10467692

Ungerman, A. J., Heindel, T. J. (2007). Carbon monoxide mass transfer for syngas fermentation in a stirred tank reactor with dual impeller configurations. *Biotechnology Progress*, *23*(3), 613–620. https://doi.org/10.1021/bp060311z

van der Wal, P. ., de Rooij, N. ., Koudelka-Hep, M. (1996). Extremely stable Nafion based carbon monoxide sensor. *Sensors and Actuators B: Chemical*, *35*(1–3), 119–123. https://doi.org/10.1016/S0925-4005(97)80040-8

Van Slyke, D. D., Neill, J. M. (1924). The determination of gases in blood and other solutions by vacuum extraction and manometric measurement. *Journal of Biological Chemistry*, *61*(2), 523–573.

Varlet, V., De Croutte, E. L., Augsburger, M., Mangin, P. (2013). A new approach for the carbon monoxide (CO) exposure diagnosis: Measurement of total co in human blood versus carboxyhemoglobin (HbCO). *Journal of Forensic Sciences*, *58*(4), 1041–1046. https://doi.org/10.1111/1556-4029.12130

Varlet, V., Lagroy De Croutte, E., Augsburger, M., Mangin, P. (2012). Accuracy profile validation of a new method for carbon monoxide measurement in the human blood using headspace-gas chromatography-mass spectrometry (HS-GC-MS). *Journal of Chromatography B: Analytical Technologies in the Biomedical and Life Sciences*, *880*(1), 125–131. https://doi.org/10.1016/j.jchromb.2011.11.028

Vashist, S. K., Zheng, D., Al-Rubeaan, K., Luong, J. H. T., Sheu, F. S. (2011). Advances in carbon nanotube based electrochemical sensors for bioanalytical applications. *Biotechnology Advances*, *29*(2), 169–188. https://doi.org/10.1016/j.biotechadv.2010.10.002

Volz, A., Kley, D. (1985). A resonance-fluorescence instrument for the in-situ measurement of atmospheric carbon monoxide. *Journal of Atmospheric Chemistry*, *2*, 345–357.

Voss, R. F., Clarke, J. (1976). Flicker (1/f) noise: Equilibrium temperature and resistance fluctuations. *Physical Review B*, *13*(2), 556.

Waich, K., Mayr, T., Klimant, I. (2008). Fluorescence sensors for trace monitoring of dissolved ammonia. *Talanta*, *77*(1), 66–72. https://doi.org/10.1016/j.talanta.2008.05.058

Wang, C., Yin, L., Zhang, L., Xiang, D., Gao, R. (2010). Metal oxide gas sensors: Sensitivity and influencing factors. *Sensors*, *10*(3), 2088–2106. https://doi.org/10.3390/s100302088

Wang, J., Maiorov, M., Jeffries, J. B., Garbuzov, D. Z., Connolly, J. C., Hanson, R. K. (2000). A potential remote sensor of CO in vehicle exhausts using 2.3 μm diode lasers. *Measurement Science and Technology*, *11*(11), 1576–1584. https://doi.org/10.1088/0957-0233/11/11/306

Wang, Z., Peng, X., Huang, C., Chen, X., Dai, W., Fu, X. (2017). CO gas sensitivity and its oxidation over TiO2 modified by PANI under UV irradiation at room temperature. *Applied Catalysis B: Environmental*, *219*, 379–390.

Werle, P. (1998). A review of recent advances in semiconductor laser based gas monitors. *Spectrochimica Acta Part A: Molecular and Biomolecular Spectroscopy*, *54*(2), 197–236.

https://doi.org/10.1016/S1386-1425(97)00227-8

Werle, P., Popov, A. (1999). Application of antimonide lasers for gas sensing in the 3-4um range. *Applied Optics*, *38*(9), 1494–1501. https://doi.org/10.1364/AO.38.001494

Werle, P., Slemr, F., Maurer, K., Kormann, R., Mücke, R., Jänker, B. (2002). Near- and mid-incrared laser-optical sensors for gas analysis. *Optics and Lasers in Engineering*, *37*(2–3), 101–114.

Widdop, B. (2002). Analysis of carbon monoxide. *Annals of Clinical Biochemistry*, *39*(4), 378–391.

Wiesenburg, D. A., Guinasso Jr, N. L. (1979). Equilibrium solubilities of methane, carbon monoxide, and hydrogen in water and sea water. *Section Title: Water*, *24*(4), 356–360. https://doi.org/10.1021/je60083a006

Wilkins, M. R., Atiyeh, H. K. (2011). Microbial production of ethanol from carbon monoxide. *Current Opinion in Biotechnology*, *22*(3), 326–330. https://doi.org/10.1016/j.copbio.2011.03.005

Williams, B. S., Kumar, S., Hu, Q., Reno, J. L. (2006). High-power terahertz quantum-cascade lasers. *Electronics Letters*, *42*(2), 89–91.

Williams, P., Norris, K. (2001). *Near-infrared technology in the agricultural and food industries.* (2nd ed.). American Association of Cereal Chemists, Inc.

Wolfbeis, O. S., Kovács, B., Goswami, K., Klainer, S. M. (1998). Fiber-optic fluorescence carbon dioxide sensor for environmental monitoring. *Mikrochimica Acta*, *188*, 181–188. https://doi.org/10.1007/BF01244739

Wu, R. J., Chang, W. C., Tsai, K. M., Wu, J. G. (2009). The Novel CO sensing material CoOOH-WO3 with Au and SWCNT performance enhancement. *Sensors and Actuators, B: Chemical*, *138*(1), 35–41. https://doi.org/10.1016/j.snb.2009.02.014

Wu, R. J., Hu, C. H., Yeh, C. T., Su, P. G. (2003). Nanogold on powdered cobalt oxide for carbon monoxide sensor. *Sensors and Actuators, B: Chemical*, *96*(3), 596–601. https://doi.org/10.1016/S0925-4005(03)00646-4

Wu, R. J., Wu, J. G., Tsai, T. K., Yeh, C. T. (2006). Use of cobalt oxide CoOOH in a carbon monoxide sensor operating at low temperatures. *Sensors and Actuators, B: Chemical*, *120*(1), 104–109. https://doi.org/10.1016/j.snb.2006.01.053

Wu, R. J., Wu, J. G., Yu, M. R., Tsai, T. K., Yeh, C. T. (2008). Promotive effect of CNT on Co3O4-SnO2 in a semiconductor-type CO sensor working at room temperature. *Sensors and Actuators, B: Chemical*, *131*(1), 306–312. https://doi.org/10.1016/j.snb.2007.11.033

Xu, T., Huang, H., Luan, W., Qi, Y., Tu, S. tung. (2008). Thermoelectric carbon monoxide sensor using Co-Ce catalyst. *Sensors and Actuators, B: Chemical*, *133*(1), 70–77. https://doi.org/10.1016/j.snb.2008.01.064

Xu, Y. H., Mitra, S. (1994). Continuous monitoring of volatile organic compounds in water using on-line membrane extraction and microtrap gas chromatography system. *Journal of Chromatography A*, *688*(1–2), 171–180. https://doi.org/10.1016/0021-9673(94)00944-9

Yamaura, H., Moriya, K., Miura, N., Yamazoe, N. (2000). Mechanism of sensitivity promotion in CO sensor using indium oxide and cobalt oxide. *Sensors and Actuators, B: Chemical*, *65*(1), 39–41. https://doi.org/10.1016/S0925-4005(99)00456-6

Yamaura, H., Nakaoka, M., Yahiro, H. (2008). Effect of Supported Transition Metal on CO Sensing Performance Using SnO_2 in Reducing Atmosphere. *Advanced Materials Research*, *47–50*, 1518–1521. https://doi.org/10.4028/www.scientific.net/AMR.47-50.1518

Yamazoe, N., Sakai, G., Shimanoe, K. (2003). Oxide semiconductor gas sensors. *Catalysis Surveys from Asia*, *7*(1), 63–75.

Yan, H., Liu, C. (1994). A solid polymer electrolyte-based electrochemical carbon monoxide sensor. *Sensors and Actuators B: Chemical*, *17*(2), 165–168.

Yan, T., Chen, J., Wu, S., Mao, Z., Liu, Z. (2014). A Rationally Designed Fluorescence Chemosensor for On-Site Monitoring of Carbon Monoxide in Air. *Organic Letters*, *16*(12), 3296–3299.

Zhao, Y., Strong, K., Kondo, Y., Koike, M., Matsumi, Y., Irie, H., … Murata, I. (2002). Spectroscopic measurements of tropospheric CO, C2H6, C2H2, and HCN in northern Japan. *Journal of Geophysical Research*, *107*(D18), 4343. https://doi.org/10.1029/2001JD000748

Zheng, K., Lin, W., Tan, L., Chen, H., Cui, H. (2014). A unique carbazole–coumarin fused two-photon platform: development of a robust two-photon fluorescent probe for imaging carbon monoxide in living tissues. *Chemical Science*, *5*(9), 3439. https://doi.org/10.1039/C4SC00283K

APPENDICES

I. Illustration of circuits and program for the MIR CO sensor

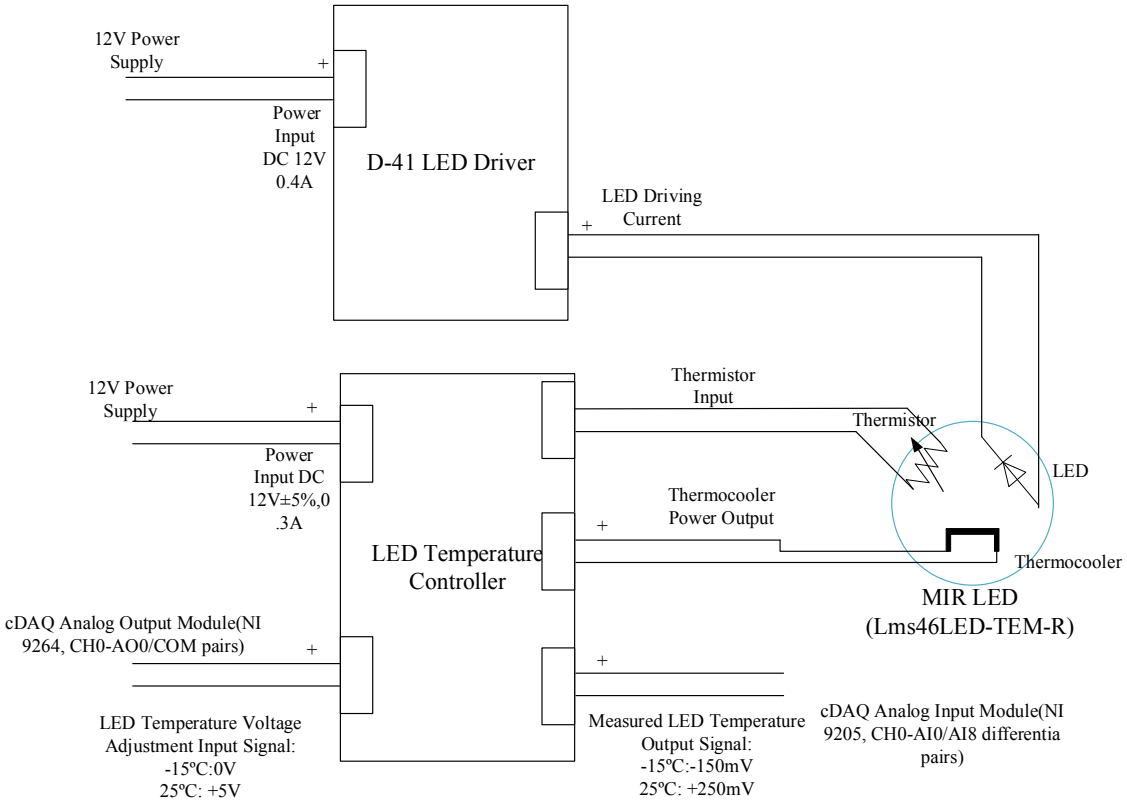

Fig.A-1 Illustration of the connections between the MIR LED, the LED driver, and the LED temperature controller

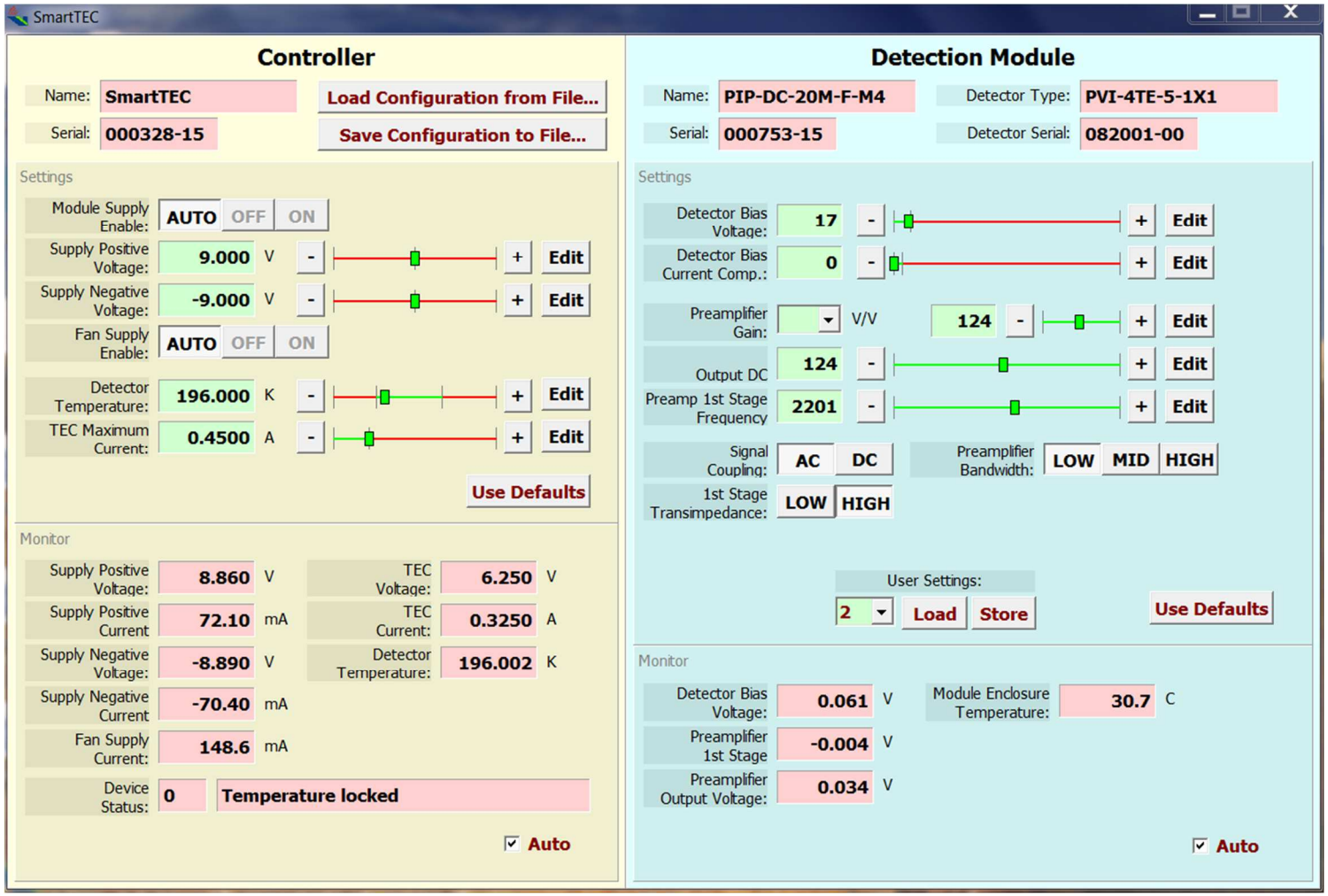

Fig.A-2 Screen shot of the preamplifier settings (in preamplifier management software)

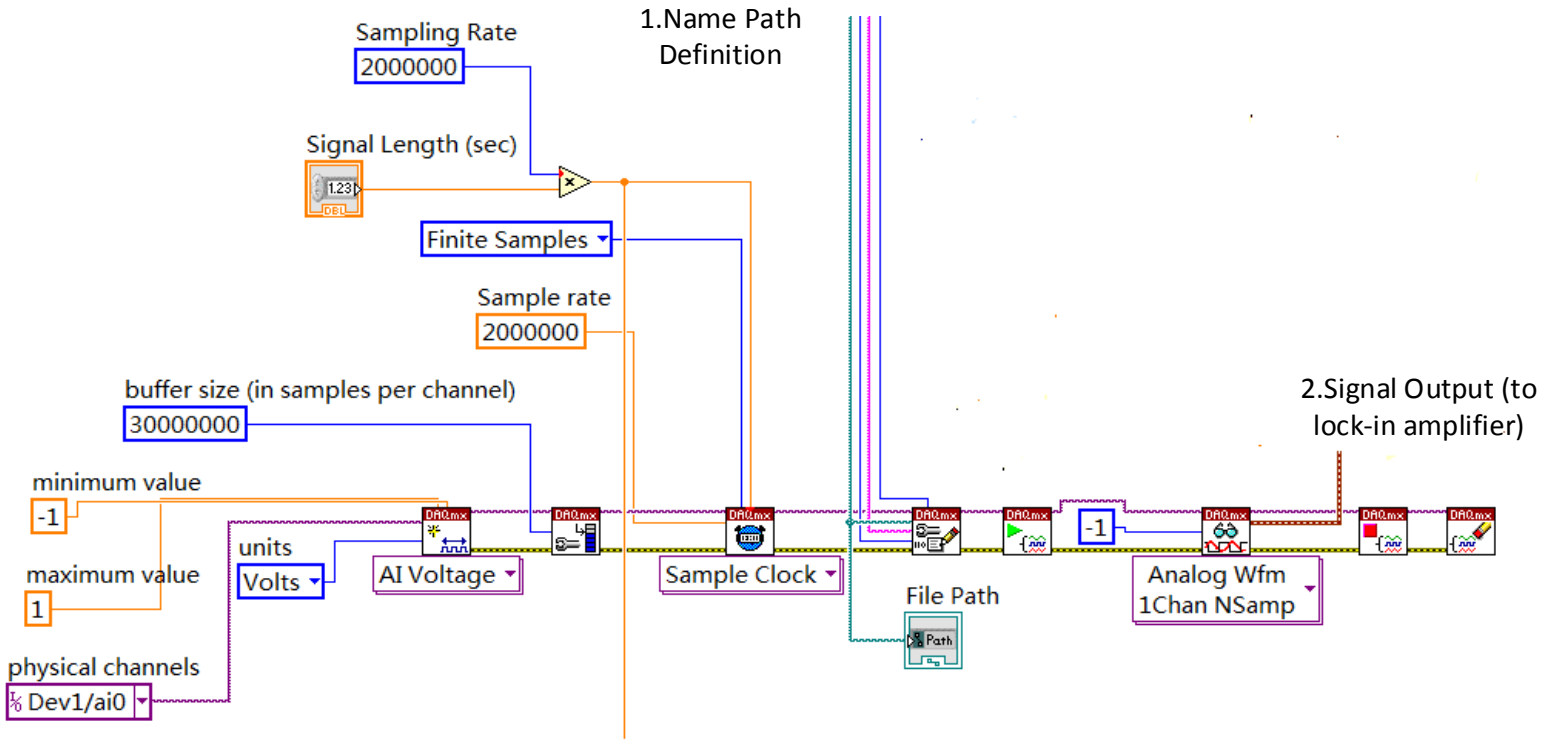

Fig.A-3 Data acquisition program for the MIR CO sensor

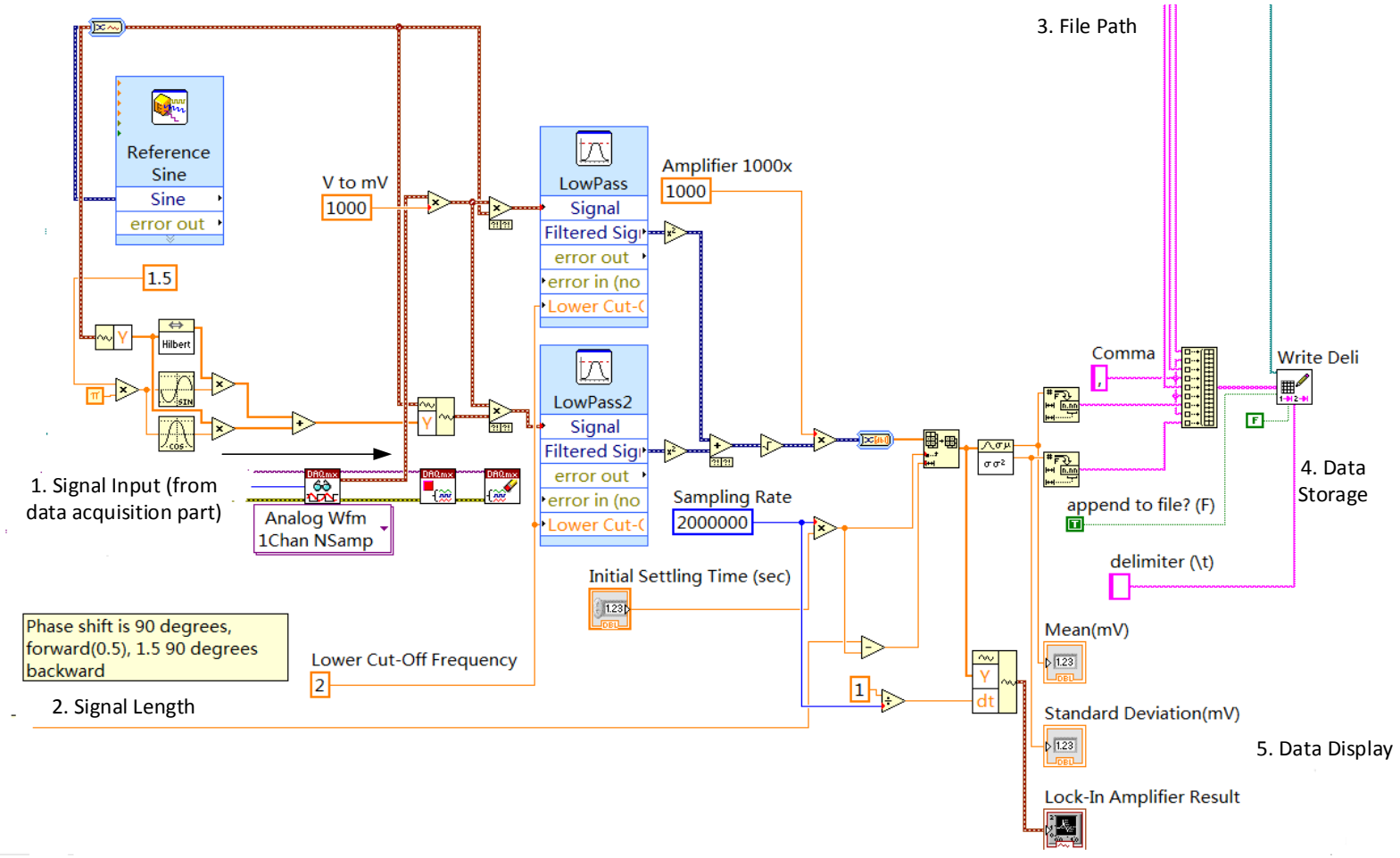

Fig. A-4 Digital lock-in amplifier in the data acquisition program for MIR CO sensor

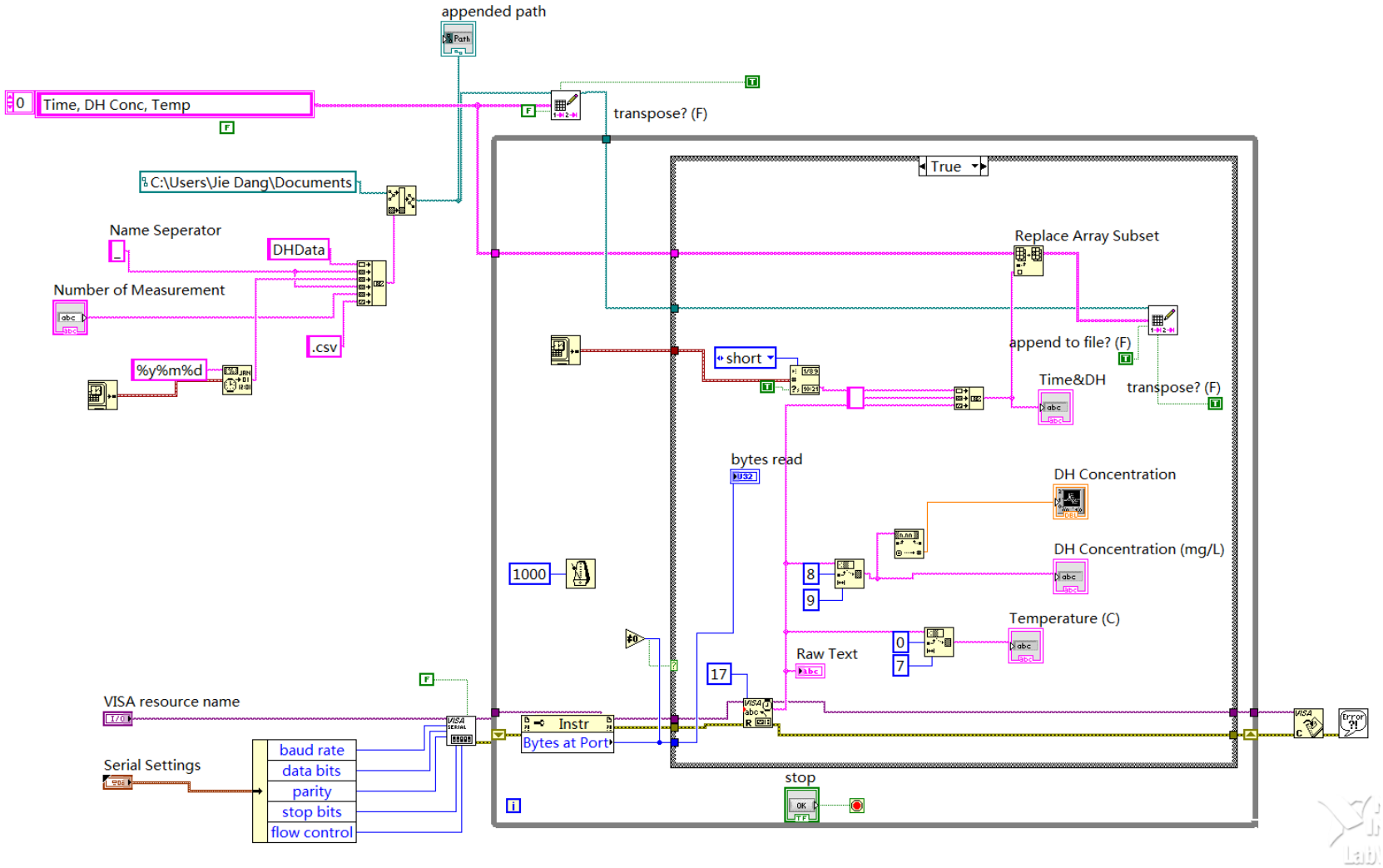

Fig. A-5 Data acquisition program for dissolved H_2 sensor

II. MATLAB programs for signal analysis

1. Infrared absorbance analysis for FTIR measurement results

```
clc;
clear;
%05072018, MATLAB program to draw the regression curve for CO
FTIR gas
%experiment data
C = [2.58352045 2.629246476 2.581759265 2.796900573 2.853980176
2.787386109 3.65558834 3.630262784 3.660575767 3.970028492
3.727909543 4.209599177 4.771637493 5.334461152 4.747838803
8.3785 8.1403 8.1623 10.3498 10.5967 10.93132 33.20940177
30.98463511 27.9347507 54.68225846 52.6393888 54.52779736
97.05377572 95.78021663 89.52855224 112.1448 104.5453 110.4761
160.3839 160.7422 163.9771 308.3984309 306.5703594 306.5703594
447.2645279 452.6302568 456.7803109 531.1462753 527.1446191
528.082463 926.3397021 927.7443186 920.3633121];
%CO concentration (mg/L)
Res1 = [0.1002 0.0887 0.0823 0.1129 0.1215 0.1136 0.1455 0.1281
0.1434 0.1533 0.1432 0.1704 0.1926 0.2062 0.1894 0.2931 0.2996
0.2885 0.3424 0.3570 0.3518 0.2834 0.2692 0.2825 0.4145 0.3999
0.4149 0.6462 0.6480 0.6346 0.7429 0.7484 0.7470 0.9272 0.9126
0.9118 1.4410 1.4457 1.4412 1.6082 1.6978 1.7410 1.9265 1.8319
1.9190 2.9505 2.8239 2.8595];
%CO absorbance, 2161.864cm-1
Res2= [5.0696 4.9091 2.0876 5.9983 6.5027 6.0132 8.3055 7.1935
8.0944 9.1887 5.5786 7.7692 11.0667 10.8091 11.3131 18.3525
19.0255 18.6253 22.7970 23.6459 23.3360 18.5221 17.1744 18.2908
29.1010 27.8017 29.1077 49.5558 50.0450 49.1739 58.4829 62.0740
58.8719 76.9663 68.0005 76.0265 115.4047 115.5847 115.0528
149.9981 160.0800 163.7206 183.9246 172.6291 183.5224 292.2719
288.9843 290.0360];
%CO absorbance over area

figure(1)
scatter(C,Res1,'ro')
hold on
p = polyfit(C,Res1,1)
Rsquare = Rsquarecalc(C,Res1,p)
f = polyval(p,C);
% y = 0.003x+0.251,R^2 = 0.9724
plot(C,f,'b-.')
grid on
%title('Regression Analysis on Single Line (2161cm^-^1)
Absorbance Data')
xlabel('CO concentration(mg/L)')
ylabel('Absorbance')
legend('Data points','Regression: y=0.0030x+0.2510,R^2=.9724')

figure(2)
```

```
scatter(C,Res2,'ro')
hold on
p2 = polyfit(C,Res2,1)
Rsquare2 = Rsquarecalc(C,Res2,p2)
f2 = polyval(p2,C);
% y = 0.3098x+13.483,R^2 = 0.9909
plot(C,f2,'b-.')
grid on
%title('Regression Analysis on Absorbance in Total CO Absorption
Band')
xlabel('CO concentration(mg/L)')
ylabel('Absorbance')
legend('Data points','Regression: y=0.3098x+13.4829,R^2=.9909')
```

2. Preamplifier/lock-in amplifier output signal spectrum analysis

```
clc;
clear;
%Calculate the FFT spectrum and display the Preamplifier Output
signal

filename = 'PDData63R.mat';
rawMat = load(filename,'ConvertedData');
%Read data from TDMS levels
rawDataStruct = rawMat.ConvertedData.Data.MeasuredData(1,3);
rawData = rawDataStruct.Data;
Fs = 2000000;

%2MSa/s data's sampling rate
[F,P] = DFT_Dec(rawData,Fs);
figure()%FFT spectrum
plot(F,P)
axis([0 20000 0 inf])
title('Single-Sided Amplitude Spectrum 1.5A,2kHz,10\mus' )
xlabel('f (Hz)')
ylabel('|P(f)|')
grid off

figure()%PO signal in time domain

tS = 0.2;%Length of displayed signal
inputData = rawData(1:tS*Fs);
t = 1/Fs;
k = t:t:tS;
z = 1000;%change time unit to ms
plot(1000*k,1000*inputData)
xlabel('Time (ms)')
ylabel('Signal Amplitude (mV)')
title('Time Domain Signal 1.5A,2kHz,10\mus' )
```

VITA

Jie Dang

Candidate for the Degree of

Doctor of Philosophy

Dissertation: DEVELOPMENT OF A DIRECT MONITORING APPROACH OF CO/H_2 IN BIOREACTORS FOR SYNGAS TO BIOFUEL CONVERSION

Major Field: Biosystems and Agricultural Engineering

Biographical:

Education:

Completed the requirements for the Doctor of Philosophy in Biosystems and Agricultural Engineering at Oklahoma State University, Stillwater, Oklahoma in May, 2019.

Completed the requirements for the Master of Science in Control Science and Engineering at Xi'an Jiaotong University, Xi'an, Shaanxi, China in 2013.

Completed the requirements for the Bachelor of Science in Automation at Xi'an Jiaotong University, Xi'an, Shaanxi, China in 2010.

Experience:

Research Assistant, Department of Biosystems and Agricultural Engineering, Oklahoma State University, Stillwater, Oklahoma, USA, January 2014 to August 2017

Professional Memberships:

American Society of Agricultural and Biological Engineers (ASABE)